Beam Loading in High-Charge Laser Wakefield Accelerators

Johannes Peter Götzfried

Munich 2023

Meinen Eltern

Beam Loading in High-Charge Laser Wakefield Accelerators

Johannes Peter Götzfried

Dissertation
an der Fakultät für Physik
der Ludwig-Maximilians-Universität
München

vorgelegt von
Johannes Peter Götzfried
aus Schwabmünchen

München, den 2. Mai 2023

Erstgutachter: Prof. Dr. Stefan Karsch
Zweitgutachter: Prof. Dr. László Veisz
Tag der mündlichen Prüfung: 13. Juni 2023

Zusammenfassung

Bei lasergetriebenen Plasmabeschleunigern, den sogenannten *Laser wakefield accelerators (LWFAs)*, treibt ein hochintensiver ultrakurzer Laserpuls eine Plasmawelle. Die dadurch hervorgerufene Ladungsseparation generiert beschleunigende Felder von mehreren hundert $\mathrm{GV\,m^{-1}}$. Diese übertreffen damit jegliche auf konventionelle Art erzeugten Felder um etwa vier Größenordnungen. Durch deren Ausnutzung zur Beschleunigung von geladenen Teilchen können die Größe und somit auch die Kosten für zukünftige Teilchenbeschleuniger drastisch gesenkt werden. Hiermit beschleunigte Elektronenpakete führen durch ihre inhärent kurze Dauer von einigen Femtosekunden zu extrem hohen Spitzenströmen von etlichen 10 kA. Zusammen mit den in dieser Arbeit vorgestellten beschleunigten Gesamtladungen von bis zu 0.7 nC stellen LWFAs mittlerweile einen vielversprechenden Kandidaten für zukünftige Beschleunigerkonzepte dar [1]. Aufgrund ihrer ultrakurzen Elektronenpakete sind sie zum einen eine hervorragende Quelle für hochbrillante Röntgenpulse über Betatronstrahlung [2, 3] bzw. Thomson-Rückstreuung und zum anderen ein möglicher Treiber für Freie-Elektronen-Laser (FELs) [4, 5]. Um die hierfür nötigen Teilchenstromdichten zu erzeugen, müssen die Beschleuniger im sog. „beam-loading Regime“ arbeiten. Dort überlagern die elektrostatischen Felder der beschleunigten Teilchenpakete die beschleunigenden Felder des Plasmas und modifizieren die Dynamik des Beschleunigungsprozesses dadurch signifikant. Es ist daher überaus wichtig, ein tieferes Verständnis für dieses kritische Regime zu entwickeln.

In dieser Doktorarbeit werden beam-loading Effekte in quasi-monoenergetischen LWFAs der nanocoulomb-Klasse systematisch untersucht. Ein lokal und zeitlich eng begrenzter Injektionsmechanismus führt dabei zu hoher Schuss-zu-Schuss Stabilität. Bisher für diese Laserklasse unerreichte Gesamtladungen, spektrale Ladungsdichten und geringe Divergenzen werden präsentiert. Diese Eigenschaften ermöglichen den Vorstoß in ein bisher nur spärlich untersuchtes Regime: den Übergang vom laser- zum teilchengetriebenen Plasmabeschleuniger. Beam-loading Effekte dominieren dieses Regime und wirken sich auf die spektrale Form der beschleunigten Elektronenpakete aus. Diese Effekte werden untersucht und deren Wirkung sowohl auf die beschleunigten Elektronen, als auch auf ein nachfolgend injiziertes Teilchenpaket, erklärt. In einer Pump-Probe-Konfiguration können damit nicht nur die effektiven beschleunigenden Felder, sondern auch die Auswirkungen des Beam-loadings auf die Teilchendynamik des Plasmas untersucht werden.

Die auf umfangreiche Simulationen gestützten Studien führen zu einem tiefen Verständnis der zugrunde liegenden Wechselwirkungsmechanismen. Hierauf basierend wird gezeigt werden, dass beam-loading Effekte zu einer nichtlinearen zeitlichen Änderung der Elektronenenergie („Chirp“) im Phasenraum führen. Diese Nichtlinearität kann durch Einführung eines neuen Parameters – der sogenannten Schiefe („skewness“) – beschrieben werden und stellt eine einfache Messgröße zur Ermittlung der Stärke des Beam-loadings für diese Beschleunigerklasse dar. Letztendlich kann diese Nichtlinearität im Phasenraum ausgenutzt werden, um die spektrale Bandbreite der Elektronen signifikant zu verbessern.

Das mit diesen Studien erlangte tiefe Verständnis der Teilchendynamik bildet die Basis für die zukünftige Ausnutzung von beam-loading Effekten, um die Qualität der Elektronenpakete signifikant zu verbessern und bildet den Ausgangspunkt für ein neues, hybrides Beschleunigerkonzept.

Beam Loading in High-Charge Laser Wakefield Accelerators

Johannes Peter Götzfried

Dissertation
Faculty of Physics
at Ludwig-Maximilians-Universität
Munich

presented by
Johannes Peter Götzfried
born in Schwabmünchen

Munich, May 2, 2023

1st Referee: Prof. Dr. Stefan Karsch
2nd Referee: Prof. Dr. László Veisz
Date of oral exam: June 13, 2023

Abstract

In laser-driven plasma accelerators, so-called laser wakefield accelerators (LWFAs), an ultra-short high-intensity laser pulse drives a plasma wave. The charge separation induced by the driving laser pulse generates fields on the order of several hundred $\mathrm{GV\,m^{-1}}$. These fields surpass any conventionally generated ones by four orders of magnitude. Applying these fields for particle acceleration promises to significantly reduce the size and cost of future accelerators. Due to their inherent short duration of a few femtoseconds, the accelerated electron bunches feature extremely high peak currents of several 10 kA. Together with the accelerated total charges up to 0.7 nC presented in this thesis, LWFAs are currently regarded as promising candidates for future accelerator concepts [1]. Due to their ultra-short electron bunches, they are on the one hand an excellent source for highly-brilliant X-ray pulses via betatron emission [2, 3] or Thomson backscattering [6] and on the other hand, a candidate driver for Free-Electron Lasers (FELs) [4, 5]. To generate the required peak current densities, the accelerators have to be operated in the so-called "beam loading regime". Here the self-fields of the accelerated particle bunches superimpose the accelerating fields of the plasma and thus modify the acceleration dynamics significantly. Therefore, it is of great importance to gain a deeper understanding of this critical regime.

In this doctoral thesis, beam loading effects in quasi-monoenergetic nanocoulomb-class LWFAs are studied systematically. A locally and temporally sharply confined injection mechanism leads to high shot-to-shot stability. Peak charges, spectral charge densities, and low divergences unprecedented for this laser class are presented. These properties allow for the advance to a regime only scarcely studied yet: the transition from laser- to beam-driven plasma accelerators. Beam loading effects dominate this regime and affect the final spectral shape of the accelerated electron bunches. These effects are studied and their influence on accelerated as well as subsequently injected particle bunches is explained. In pump-probe configurations, not only the effective fields but also the effects of beam loading on the plasma dynamics can be studied.

Elicited by extensive simulations, these studies lead to a profound understanding of the underlying interaction mechanisms. Based on these simulations, it is shown that beam loading causes a nonlinear chirp in the electrons' phase space. This nonlinearity can be parametrized by introducing a new quantity – the so-called "skewness" – and constitutes

an easily accessible parameter to determine the strength of beam loading for this class of accelerators. Ultimately, this nonlinearity in phase space can be utilized to significantly improve the spectral bandwidth of the electron bunches.

This comprehensive study of the particle dynamics not only forms the cornerstone for future experiments exploiting beam loading effects to significantly improve the quality of the electron bunches but also forms the starting point for the development of a new, hybrid accelerator concept.

Contents

Chapter 1

Introduction

Accelerators generating ultra-relativistic particles are not only a key tool for fundamental research in particle physics but also widely used in industrial and medical applications. In 1919, Ernest Rutherford proposed "atomic projectiles" with energies beyond those provided by natural radioactive sources for "probing the inner structure of the atoms and all elements" [7]. First particle accelerators using direct current (DC) voltages like the Cockcroft-Walton generator [8] or the Van de Graaff generator [9] were invented in the early 1930s. The accelerated particles were limited to energies around one MeV by the maximum breakdown field gradients these machines could handle. Nevertheless, John Douglas Cockcroft and Ernest Walton were able to use their accelerator to perform the first artificial nuclear disintegration in 1932, which won them the Nobel Prize in 1951 [10]. In order to reach even higher energies, Rolf Wideröe proposed a scheme of multiple, resonantly driven radio frequency (RF) drift tubes [11]. This concept led to the invention of the cyclotron technology few years later and still is the fundamental principle of high-energy particle acceleration nowadays. Based on Wideröe's ideas, the very first cyclotron was invented by Ernest O. Lawrence in 1930 [12], for which he was awarded the Nobel Prize in 1939 [13]. With these machines, unprecedented proton energies beyond one MeV became feasible. The rapid accelerator development producing higher and higher particle energies led to many discoveries in the field of particle physics, culminating in the observation of the Higgs boson in 2012 at the Large Hadron Collider (LHC) operated by the European Organization for Nuclear Research (CERN) [14].

Based on RF cavity resonators, these conventional accelerators are nowadays reaching a fundamental limit: depending on the cavity's surface quality, the vacuum breakdown limit is reached when the accelerating fields exceed $250\,\mathrm{MV\,m^{-1}}$ at the maximum[1] [19]. At this point, the local field strengths are high enough to expel electrons from the solid surface into the vacuum. An exponentially growing cascade of electrons is generated upon each subsequent RF field reversal – a phenomenon called "multipactor effect" – which

[1] Reliably operating accelerators typically apply accelerating field gradients up to around $100\,\mathrm{MV\,m^{-1}}$ [15–18].

ultimately leads to a breakdown of the accelerating field (see, e.g., [16, 20]). Hence, in common high-energy accelerators, the particles are either forced on circular orbits to pass the same accelerating stages multiple times ("synchrotrons") or they are subjected to a series of accelerating cavities along a linear beamline ("linear accelerators"). In the first case, electromagnetic radiation emitted via synchrotron emission and necessary magnetic field strengths to bend the particles' trajectories limit the final kinetic energy. Based on current accelerator technology, the particles' energies can only be boosted by increasing the sheer size of the accelerators, namely the total length of the linear accelerator or the radius of curvature for synchrotrons. To reduce the costs and to make ultra-relativistic particles more accessible for applications, a new accelerator technology not subjected to the above limits is necessary.

Wakefield accelerators are widely considered a promising candidate as a future high-gradient accelerator concept. Here, either an ultra-high intense laser pulse (LWFAs) or a dense ultra-relativistic bunch of charged particles (plasma wakefield accelerators (PWFAs)) expels electrons from its path of propagation through the plasma target by its electromagnetic field. Therefore, behind the driver, a void of electrons forms. Since the ions are orders of magnitude heavier, they are almost unaffected by the fields of the driver and do not move. This charge separation constitutes a three-dimensional field structure in the form of a co-propagating wake behind the driver, the so-called *plasma wave*, which offers longitudinal and transverse electromagnetic fields that may accelerate and focus charged particles. The plasma wave is not prone to the vacuum breakdown limit and hence, field gradients beyond $100\,\mathrm{GV\,m^{-1}}$ are feasible. This allows the reduction of the overall accelerator size and its costs by orders of magnitude.

The underlying concepts were theoretically proposed by Tajima and Dawson in 1979 [21] for LWFAs and Chen *et al.* [22] in 1985 for PWFAs. Due to the complementary but different driver technology, both types of wakefield accelerators used to be treated separately. Nevertheless, their development went hand-in-hand as the physics at stake is very similar. The feasibility of laser wakefield acceleration by simulations was shown by Joshi *et al.* [23] in 1984. Laser technology at that time could not produce fields strong enough to self-inject plasma electrons into the accelerating structure, but they were sufficient to trap externally injected electrons [24]. It was in the early 90s when energy gain of externally injected electrons into a beat-wave-driven plasma wave was first demonstrated [25, 26]. The invention of chirped pulse amplification (CPA) [27] in 1985 made sub-picosecond, multi-TW laser pulses available within the next decade which gave a new impetus to the field of LWFA [28, 29] and finally led to the first laser wakefield accelerated electrons in 1998 [30]. The next milestone in LWFA was reached in 2002 when Pukhov and Meyer-ter-Vehn [31] found a new, highly nonlinear regime in which

the driving laser pulse blows out all electrons on its path forming a solitary *bubble-like structure* behind the driver. This bubble acts as an accelerating cavity with the potential of delivering monoenergetic electron bunches. Nowadays, all wakefield accelerators aim at operating in this highly nonlinear regime. Exploiting the advantages of this new regime combined with sophisticated titanium-sapphire (Ti:Sa) laser technology, three groups simultaneously achieved a breakthrough in this respect in 2004. In their so-called *Dream Beam Papers* they demonstrated for the first time the full potential of laser wakefield acceleration by producing quasi-monoenergetic electron beams beyond 100 MeV with tens of pC charge [32–34]. Two years later, the goal of accelerating electrons to 1 GeV in a single LWFA stage was demonstrated [35].

With current laser technology, beam intensities around $5.5 \times 10^{22}\,\mathrm{W\,cm^{-2}}$ can be reached [36] and electron acceleration up to 7.8 GeV is feasible [37]. Moreover, controlled injection mechanisms have been developed to ensure reproducible and monoenergetic electron beams with charges beyond 1 nC [38]. Such laser plasma accelerators (LPAs) may induce currents beyond 100 kA due to their short particle bunch length. However, at such high currents, the self-fields of the trapped charges start to superimpose the accelerating fields of the wake, which causes a local moderation of the accelerating force. This so-called *beam loading effect* becomes stronger with increasing bunch charge and can finally alter the key parameters of the accelerator. As we will see in the course of this work, the charge separation induced by the optical driver is caused by the ponderomotive force, a second-order effect that is proportional to the gradient of the spatially inhomogeneous oscillating electromagnetic field. Beam loading effects, however, originate from the unipolar space charge field of the particle driver and in that sense, are much more efficient in interacting with the surrounding plasma [39]. Therefore, proper control of the beam loading effect and the understanding of its influence on the beam characteristics is crucial for operating LPAs in the highly-loaded regime, which is a prerequisite for driving high-brightness X-ray sources or FELs.

The first theoretical studies of beam loading in the linear regime were published by Katsouleas *et al.* [40] in 1987, who described the effective accelerating field as a superposition of the electron bunch's wakefield with the one of the driver. Only the discovery of the highly nonlinear regime fifteen years later and the advent of electron beams in the kA range triggered further research on this effect. Based on the theoretical advances in the first decade of the 21st century [41], Tzoufras *et al.* [42, 43] extended this mathematical framework to beam loading in the nonlinear regime. They even found that trapezoidal beam currents with the appropriate total charge may flatten the accelerating fields in a LWFA via beam loading. In the following year, Rechatin *et al.* [44] conducted the first experimental studies on beam loading effects and – albeit their particle beams were limited

to some tens of pC – established the charge-energy correlation as characteristic feature of beam loading. In their follow-up paper, Rechatin *et al.* [45] discuss the generation of electron bunches with low energy spread and present first experimental data on the optimal loading regime. Simulations suggest that peak charges around 20 pC even out the inherent longitudinal field gradient via beam loading. Corresponding experimental data is in good agreement, as a scan of the peak charge in the range of 0 pC to 140 pC reveals a minimal relative energy spread on the order of 10 % for the suggested charge. Within the following decade advanced injection techniques like self-truncated ionization injection (STII) [46, 47] or shock injection [48] matured and reproducibly delivered quasi-monochromatic electron beams in the kA range corresponding to beam charges of hundreds of pC [38, 49]. With these particle bunches, first explorations of the intermediate regime between laser-driven (LWFA) and purely particle-driven wakefield acceleration (PWFA) became feasible as the self-fields of such high-current beams become non-negligible.

Systematic studies for highly-loaded beams were conducted by Guillaume *et al.* [50] a few years ago, who examined the acceleration of ionization-injected, highly-charged electron beams with charges up to 250 pC. They present the beam charge and energy spectrum in relation to either the laser energy or gas density. Based on these experiments, Couperus *et al.* [49] expanded this field to quasi-monoenergetic bunches in heavily loaded wakefields. In this regime, the accelerated charge and corresponding self-fields are high enough to significantly alter the accelerating fields and hereby determine the acceleration dynamics. The employed tailored STII ([46, 47]) injection scheme offers the possibility to adjust the injected charge by varying the doping concentration of nitrogen as the high-Z gas component. In this way, the parameters of the driving laser pulse and the plasma density remain unchanged. Hence, differences in energy spread may be traced back to beam loading effects alone. In their paper, Couperus *et al.* [49] demonstrated that beam loading effects can be employed to improve the performance of the LWFA. Based on theoretical predictions by Tzoufras *et al.* [42, 43], they identified an optimal loading condition where the final energy spread is minimized. For a laser pulse of 64 TW the measured relative energy spread reached its minimum with $\sim 15\,\%$ (full width at half maximum (FWHM)) at a bunch charge of ~ 300 pC

To assess the strength of beam loading, i.e. to determine the interaction strength of the particle bunch with the wakefield structure, a multi-shot data set is necessary to reveal charge-energy correlations. In the course of the work at hand, the skewness of the electron spectrum is identified as a scalar, single-shot parameter, which allows for the quantification of beam loading for shock front accelerators. PIC simulations support the finding that this experimentally observed skewness is directly induced by beam loading and ensues from a nonlinear chirp in the phase space of the accelerated electron bunch.

In addition, Rechatin *et al.* [45] observed in their experiments a reduction in the background current the higher the charge trapped in the first wakefield bucket. This effect is theoretically expected, as the load in the leading plasma cavity dampens the fields in the trailing periods. However, due to their experimental setup, Rechatin *et al.* [45] were not able to quantitatively measure this effect. By tailoring the gas density profile of the shock-injected Advanced Titanium Sapphire Laser System (ATLAS)-300 LWFA, we gain the possibility of injecting two electron bunches into subsequent plasma buckets in a "driver-witness" configuration. This dual shock injection scheme allows for the probing of the effective accelerating fields in the second wakefield cavity and will be used to study "inter-cavity" beam loading effects. The two particle beams may be differentiated in the experimental data by their final energies. Therefore, we may quantitatively examine correlations between charges and final energies of both electron bunches in the data analysis below. Extensive particle-in-cell (PIC) simulations with varying bunch charges in the first and second cavity support our experimental finding that the charge trapped in the second wakefield period indeed positively correlates with the final energy of the leading electron bunch.

However, up to now, beam loading effects between two different electron bunches were restricted to particles sitting in locally separated buckets of the wakefield. With the only recently presented technique of adding a second, independent injection event [51], beam loading studies within the same wakefield bucket become feasible and are presented in the work at hand. Modifications to the target to incorporate an additional optical injector grant the opportunity to create two longitudinally separated electron bunches as driver-witness pair in the leading wakefield cavity itself ("intra-cavity beam loading"). As in the aforementioned setup, correlations between the charges and final energies of these two electron bunches are extracted from the experimental data and discussed below. Besides the dependencies typical for beam loading, we again find a significant influence of the first bunch on the second one. This manifests itself as a correlation between the first bunch's charge and the energy of the latter. Again, the experimental data is in good agreement with simulations, which indeed show a growing suppression of the accelerating field behind the leading bunch the higher its charge.

This thesis aims at delivering a detailed and systematic study of beam loading effects for single and dual-energy electron bunches. To do so, the work at hand is structured as follows:

Chapter 2 covers the underlying physics of wakefield excitation and electron acceleration. It lays the foundation to explain the influence of beam loading effects on the acceleration process inherent to the experimental data presented in the following chapters. From basic principles, the interaction between a driver and the gaseous target is discussed and theoretically examined for the combination of both laser and

particle drivers. The creation of wakefields behind the driver is deduced and various wakefield regimes are debated. Methods to inject particles into the accelerating phase of the wake are introduced and acceleration limits, as well as scaling laws, are derived. This section is followed by a mathematical treatment of beam loading for different regimes. The chapter is concluded by a comprehensive, tabular overview of important LPA parameters and their specific values for the ATLAS-300 LWFA.

Chapter 3 gives a brief introduction to PIC simulations and presents the key concepts of the code "Fourier-Bessel Particle-In-Cell (FBPIC)" [52]. General simulation parameters are discussed here, whereas their specific values to model the ATLAS-300 accelerator are transferred to the appendix.

Chapter 4 covers the basic setup and technical details of the experiment. A short overview of the ATLAS is given, as well as a comprehensive overview of the gas target and electron diagnostics system.

Chapter 5 is dedicated to the presentation and analysis of experimental and theoretical data. Three different measuring campaigns and four theoretical parameter scans are discussed. Based on these data, not only the stability of the ATLAS-300 accelerator is deduced but also correlations between charge and energy on the one hand, and laser and target parameters, on the other hand, are revealed. These findings are employed in the following chapter to specifically tailor the characteristics of electron bunches for beam loading studies.

Chapter 6 describes beam loading effects for shock front LWFAs. An experimental data set with high shot-to-shot variations is examined for beam loading. With the help of PIC simulations, the skewness of the electron spectrum is identified as a key signature and parameterized to quantify the strength of beam loading. The second part of this chapter deals with beam loading effects in longitudinally separated electron bunches. The combination of two injection events enables the generation of dual-energy electron bunches. Two experimental campaigns dedicated to inter- and intra-cavity beam loading effects are analyzed and corresponding PIC simulations are discussed. We hereby systematically extend our previous analysis to beam loading effects between two longitudinally separated electron bunches.

Chapter 7 concludes this thesis by summarizing the main results and by giving an outlook on the development of new types of LPAs. By employing beam loading effects, hybrid acceleration schemes may be realized which are capable of delivering particle beams of supreme quality.

Chapter 2

Laser-Matter-Interaction

The interaction of light with charged particles is governed by electromagnetic forces which are described by the theory of electrodynamics. Being the strongest infinitely ranged fundamental force, it was studied for centuries. In the second half of the 19th century, the physical environment and mathematical apparatus were evolved enough to formulate a consistent electrodynamic theory. At the core of this theory stand four coupled partial differential equations discovered by and named after James Clerk Maxwell who published them in the 1860s [53]. Together with the Lorentz force, they cover the complete range of electric and magnetic phenomena and accordingly also stand at the beginning of our theoretical treatment of LPAs.

In this chapter, the theoretical framework for plasma wakefield acceleration is set up. Starting from the basic description of electromagnetic waves, the motion of a charged particle in a plane wave is derived. Afterward, the ponderomotive force is introduced and a brief overview of plasma physics is given. The interaction of electromagnetic waves with a plasma is treated in the succeeding section. On this basis, fundamental equations of LWFA and PWFA are derived and beam loading effects for different regimes are examined. We study the self-fields of the accelerated particle bunch, which eventually superimpose with the main accelerating fields and – if the bunch's current is large enough – may significantly modify the particle dynamics during the acceleration process. In the last section, crucial quantities for LPAs are summed up and their respective values for our experiments are given. These are either measured or derived in the theoretical context of this chapter.

2.1. Description of Electromagnetic Waves

The theoretical concepts compiled in this chapter can be found in [54–57]. A much deeper treatment with detailed elaborations is for example given in [56, 58, 59].

In the following, we assume the electromagnetic waves to propagate in a vacuum. Therefore, the relative permittivity $\varepsilon_r := 1 + \chi_e$ as well as the relative permeability $\mu_r := 1 + \chi_m$ equal 1, as both material parameters the electric χ_e and magnetic susceptibility χ_m vanish in vacuum. Hence, the refractive index defined by $n := \sqrt{\varepsilon_r \mu_r}$ equals 1 and will be neglected in the following formalism.

The behavior of electromagnetic radiation is fully governed by Maxwell's equations [53]

$$\nabla \cdot \boldsymbol{E} = \frac{\rho}{\varepsilon_0}, \qquad \text{(Gauss's law)} \tag{2.1}$$

$$\nabla \times \boldsymbol{E} = -\frac{\partial \boldsymbol{B}}{\partial t}, \qquad \text{(Faraday's law of induction)} \tag{2.2}$$

$$\nabla \cdot \boldsymbol{B} = 0, \qquad \text{(Gauss's law for magnetism)} \tag{2.3}$$

$$\nabla \times \boldsymbol{B} = \frac{1}{c^2}\frac{\partial \boldsymbol{E}}{\partial t} + \mu_0 \boldsymbol{j}. \qquad \text{(Ampère's law)} \tag{2.4}$$

Here, $\boldsymbol{E}$ and $\boldsymbol{B}$ are the electric and magnetic fields, whereas ρ stands for the charge density and $\boldsymbol{j}$ is the electric current density. μ_0 and ε_0 denote the vacuum permeability and the vacuum permittivity, respectively. Both constants are linked to the speed of light via $c = 1/\sqrt{\mu_0 \varepsilon_0}$.

Conservation of charge is a direct consequence of Maxwell's equations. Taking the divergence on both sides of Eq. (2.4) and using the identity of Eq. (2.1) leads to the continuity equation

$$\frac{\partial \rho}{\partial t} + \nabla \boldsymbol{j} = 0. \tag{2.5}$$

For convenience, the vector and scalar potential $\boldsymbol{A}$ and ϕ are introduced, exploiting the fact that $\nabla \cdot (\nabla \times \boldsymbol{V}) = 0$ for all vector fields $\boldsymbol{V}$

$$\boldsymbol{B} = \nabla \times \boldsymbol{A}. \tag{2.6}$$

From Eq. (2.6) and Eq. (2.2) follows, that $(\boldsymbol{E} + \partial \boldsymbol{A}/\partial t)$ can be expressed as gradient of a scalar potential ϕ

$$\boldsymbol{E} = -\frac{\partial \boldsymbol{A}}{\partial t} - \nabla \phi. \tag{2.7}$$

ϕ is an integration constant that is often set to zero in the case of absent charges with the Coulomb gauge $\nabla \cdot \boldsymbol{A} = 0$.

These potentials are constructed such that the homogeneous Maxwell equations (Eq. (2.2) and Eq. (2.3)) are automatically fulfilled. The inhomogeneous equations (Eq. (2.1) and Eq. (2.4)) can be rewritten using the identity $\nabla \times (\nabla \times \boldsymbol{A}) = \nabla(\nabla \cdot \boldsymbol{A}) - \nabla^2 \boldsymbol{A}$ in the second case. The two relations then transform into the well-known electromagnetic wave equations

$$\left(\nabla^2 - \frac{1}{c^2}\frac{\partial^2}{\partial t^2}\right)\phi = -\frac{\rho}{\varepsilon_0}, \tag{2.8}$$

$$\left(\nabla^2 - \frac{1}{c^2}\frac{\partial^2}{\partial t^2}\right)\boldsymbol{A} = -\mu_0 \boldsymbol{j}, \tag{2.9}$$

where we have applied the Lorenz gauge $\nabla \cdot \boldsymbol{A} = -1/c^2 \partial\phi/\partial t$ to decouple the second order partial differential equations. Eq. (2.8) and Eq. (2.9) are fully equivalent to the four equations initially introduced [58].

Analogous wave equations for the electric and magnetic field can either be derived from these two equations or by taking the time derivative of Eq. (2.4) and inserting Eq. (2.2) and Eq. (2.1) together with the above-mentioned vector identity. In any case, one obtains

$$\left(\nabla^2 - \frac{1}{c^2}\frac{\partial^2}{\partial t^2}\right)\boldsymbol{E} = \frac{1}{\varepsilon_0}\nabla\rho + \mu_0 \frac{\partial \boldsymbol{j}}{\partial t}. \tag{2.10}$$

If charges and currents are absent, this expression reduces to the homogeneous wave equation

$$\left(\nabla^2 - \frac{1}{c^2}\frac{\partial^2}{\partial t^2}\right)\boldsymbol{E} = 0. \tag{2.11}$$

The wave equation for the magnetic field is obtained similarly

$$\left(\nabla^2 - \frac{1}{c^2}\frac{\partial^2}{\partial t^2}\right)\boldsymbol{B} = -\mu_0 \nabla \times \boldsymbol{j} \tag{2.12}$$

and the homogeneous form reads

$$\left(\nabla^2 - \frac{1}{c^2}\frac{\partial^2}{\partial t^2}\right)\boldsymbol{B} = 0. \tag{2.13}$$

These two homogeneous equations describe electromagnetic radiation in a vacuum as an electric and magnetic wave propagating with speed c.

The general solution to Eq. (2.11) and Eq. (2.13) is a linear superposition of plane waves with complex amplitudes $c_{\boldsymbol{k}}$ and $\psi \in [\boldsymbol{E},\boldsymbol{B}]$,

$$\psi(\boldsymbol{r},t) = \int c_{\boldsymbol{k}} e^{i(\boldsymbol{k}\cdot\boldsymbol{r}-\omega t+\phi)}\,\mathrm{d}\boldsymbol{k} + \text{c.c.}. \tag{2.14}$$

ϕ represents an absolute phase offset, whereas the angular frequency ω is related to the wave vector $\boldsymbol{k}$ via $\omega(\boldsymbol{k}) = c|\boldsymbol{k}|$. The complex conjugate is abbreviated by c.c..

From Eq. (2.1) and Eq. (2.3) follows the perpendicularity of the fields on the wave vector

$$\boldsymbol{k} \perp \boldsymbol{B}, \tag{2.15}$$
$$\boldsymbol{k} \perp \boldsymbol{E}, \tag{2.16}$$

and Eq. (2.4) leads to

$$\boldsymbol{E} \perp \boldsymbol{B}, \tag{2.17}$$
$$|\boldsymbol{E}| = c|\boldsymbol{B}|\,. \tag{2.18}$$

The intensity I of an electromagnetic wave is given by the cycle averaged Poynting vector[1] $\boldsymbol{S}$ and can be expressed as

$$I := \left\langle|\boldsymbol{S}|\right\rangle = \varepsilon_0 c\,\langle \boldsymbol{E}^2\rangle\,. \tag{2.19}$$

2.2. Single Electron in a Plane Wave

To derive the concept of the ponderomotive force, a closer look at the basic effects of electromagnetic fields acting upon a single charged particle is necessary. The classical and relativistic treatment of this interaction process is given in the following.

[1] Details are given in the appendix section A.1.

2.2.1. Classical Treatment

The equation of motion for a charged particle in an electromagnetic field is given by Newton's second law

$$\frac{\mathrm{d}\boldsymbol{p}}{\mathrm{d}t} = \boldsymbol{F}_\mathrm{L} = q\left(\boldsymbol{E} + \boldsymbol{v} \times \boldsymbol{B}\right). \tag{2.20}$$

where $\boldsymbol{p}$ stand for the momentum of the particle and $\boldsymbol{F}_\mathrm{L}$ for the Lorentz force acting upon the particle with charge q. According to Eq. (2.18) the second term on the right-hand side may be neglected in the classical treatment, where $|\boldsymbol{v}| \ll c$. Therefore, the equation of motion becomes

$$\frac{\mathrm{d}\boldsymbol{p}}{\mathrm{d}t} = \boldsymbol{F}_\mathrm{L} = q\boldsymbol{E}. \tag{2.21}$$

By integrating this equation, approximating the electromagnetic field by a plane wave $E(x,t) = E_\mathrm{max}\sin(kx - \omega t)$ and assuming the particle to be an electron ($q = -e$, where e is the elementary charge) that is initially at rest, we obtain

$$\begin{aligned} v = \int \frac{\mathrm{d}v}{\mathrm{d}t}\,\mathrm{d}t = -\int \frac{1}{m_\mathrm{e}} eE(x,t)\,\mathrm{d}t = &\frac{eE_\mathrm{max}}{m_\mathrm{e}} \int \sin(kx - \omega t)\,\mathrm{d}t = \frac{eE_\mathrm{max}}{m_\mathrm{e}\omega}\cos(kx - \omega t) \\ \Rightarrow v_\mathrm{max} = &\frac{eE_\mathrm{max}}{m_\mathrm{e}\omega} = ca_0. \end{aligned} \tag{2.22}$$

In the last step, we have used the *normalized vector potential* a_0 defined via

$$\boldsymbol{a} \coloneqq \frac{e\boldsymbol{A}}{m_\mathrm{e}c}, \tag{2.23}$$

$$a_0 \coloneqq \frac{eA_0}{m_\mathrm{e}c} = \frac{eE_\mathrm{max}}{m_\mathrm{e}c\omega} = \frac{eE_\mathrm{max}\lambda}{2\pi m_\mathrm{e}c^2}, \tag{2.24}$$

where E_max is the amplitude of the electric field, and $E_\mathrm{max} = \omega A_0$ according to Eq. (2.7) was used. $\boldsymbol{a}^2$ is often called *normalized laser intensity*. It is convenient to normalize the electric field of electromagnetic waves according to Eq. (2.24) by giving their field strength $\boldsymbol{E}$ in units of $m_\mathrm{e}c\omega/e$.

For $a_0 \gtrsim 1$ the classical description of electron acceleration in electromagnetic field breaks completely down (cf. Eq. (2.22)) and a relativistic treatment is necessary. Therefore, it

turns out that a_0 is a convenient quantity to distinguish between non-relativistic ($a_0 \ll 1$) and relativistic regimes ($a_0 \gtrsim 1$)[1].

In the plane wave approximation, the electromagnetic field of a laser pulse can be calculated by measuring the intensity of the focal laser spot via Eq. (2.19)

$$I = \varepsilon_0 c \left\langle E^2 \right\rangle = \frac{\varepsilon_0 c}{2} E_{\max}^2, \tag{2.25}$$

For convenience, one often makes use of Eq. (2.24) and writes

$$I = \frac{2\pi m_e^2 c^5 \varepsilon_0}{e^2} \frac{a_0^2}{\lambda^2} \approx 1.38 \times 10^{10}\,\mathrm{W}\frac{a_0^2}{\lambda^2} = 1.38 \times 10^{18}\,\mathrm{W\,cm^{-2}} \frac{a_0^2}{\left(\lambda\,[\mu\mathrm{m}]\right)^2}, \tag{2.26}$$

with m_e being the mass of the electron and λ the wavelength of the plane wave.

A typical parameter for ATLAS-300 during experimental campaigns was a vacuum peak intensity around $I \approx 5.5 \times 10^{18}\,\mathrm{W\,cm^{-2}}$ at a central wavelength of $\lambda = 0.8\,\mu\mathrm{m}$ (for more details see section 4.1). This corresponds to a normalized vector potential of $a_{0,\mathrm{vac}} \approx 1.6$ and a peak electric field strengths around $E_{\max} \approx 6.4\,\mathrm{TV\,m^{-1}}$ (cf. Table 2.2 at the very end of this chapter for a compilation of all key parameters). Hence, a relativistic description of our experiments is inevitable[2].

Since the mass of the proton – as the lightest possible ion which may form the plasma background – is ~ 1836 times larger than the mass of the electron, the intensity of the laser pulse needs to increase by a factor of $\sim 1836^2$ (according to Eq. (2.26)) to reach the relativistic threshold for protons. This would imply a laser intensity I of

$$I \approx 1836^2 \times 1.38 \times 10^{18}\,\mathrm{W\,cm^{-2}}/0.8^2 \approx 7.3 \times 10^{24}\,\mathrm{W\,cm^{-2}}, \tag{2.27}$$

which is two orders of magnitude beyond current laser technology [36]. Therefore, the motion of the ionic plasma background induced by the laser pulse can be fully neglected and, hence, the assumption of an immobile ion background is justified.

[1] As will be shown later (in section 2.6), for efficient particle acceleration, LWFAs are operated in the nonlinear $a_0 > 1$ regime.

[2] Note that this laser peak intensity is measured in vacuum. The corresponding normalized vector potential is therefore denoted by $a_{0,\mathrm{vac}}$. Effects of laser-plasma-interaction – as discussed in section 2.5 – lead to much higher intensities in th experiment. The normalized vector potential denoted by a_0 takes these effects into account. An estimate for a_0 is given in Eq. (2.68).

2.2.2. Relativistic Treatment

In the relativistic case, the electron's momentum is given by

$$\frac{\mathrm{d}\boldsymbol{p}}{\mathrm{d}t} = \frac{\mathrm{d}}{\mathrm{d}t}\left(\gamma m_\mathrm{e}\boldsymbol{v}\right) = \boldsymbol{F}_\mathrm{L} = -e\left(\boldsymbol{E} + \boldsymbol{v}\times\boldsymbol{B}\right) \tag{2.28}$$

with

$$\gamma := \frac{1}{\sqrt{1-\frac{v^2}{c^2}}} = \sqrt{1+\left(\frac{\boldsymbol{p}}{m_\mathrm{e}c}\right)^2} \tag{2.29}$$

being the relativistic Lorentz factor. In contrast to the classical treatment, both terms on the right-hand side of Eq. (2.28) contribute to the Lorentz force and none can be neglected.

The electron's equation of motion can be solved for a linearly polarized electromagnetic wave (a detailed derivation is given in the appendix, c.f. section A.2) leading to the typical figure-8 motion in the co-moving frame (parametrized by the coordinates x', y' and τ')

$$kx' = \frac{a_0^2}{8}\sin(2\omega\tau'), \tag{2.30}$$

$$ky' = a_0\cos(\omega\tau'), \tag{2.31}$$

which is plotted in Figure 2.1.

Figure 2.2 shows the electron dynamics during interaction with a plane wave. All key parameters of the electron and their evolution during the interaction process are depicted.

The acceleration in the forward direction is due to the term $\boldsymbol{v}\times\boldsymbol{B}$ which transforms the transverse velocity into a forward force. Since this force is always perpendicular to the trajectory, the electron can only gain energy from the transverse electric field. Assuming a laser pulse of finite duration, the electron would have the exact same energy before and after the interaction with the electromagnetic pulse[1]. A net energy transfer onto the particle is only possible with a non-vanishing spatial intensity gradient of the driver. An electron initially placed close to the propagation axis of the laser pulse will be displaced by the electric field and pushed into regions of lower light intensity. Here the restoring force is smaller such that the electron cannot return to its initial position and therefore a net displacement is achieved. Averaging over the oscillating movement leads to a drift motion to regions of lower laser intensity. This effective force is called *ponderomotive force* and will be discussed in the following.

[1] The generalization of this finding is subsumed under the *Lawson-Woodward theorem*

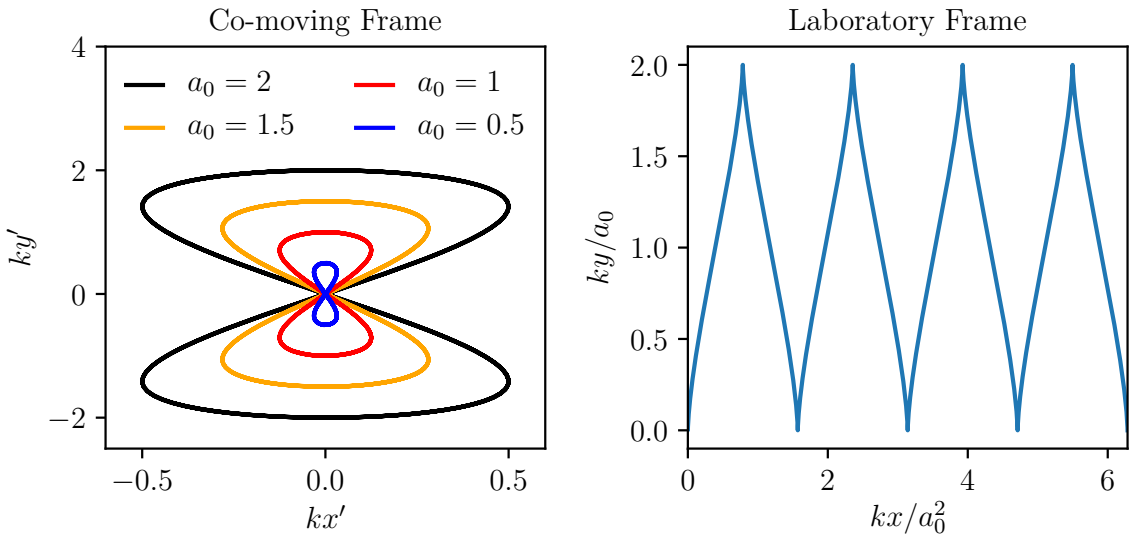

Figure 2.1.: *Trajectory of an electron interacting with a plane wave. In the co-moving frame (left) the particle follows a characteristic figure-8 motion. A stronger laser driver leads to a longitudinally more stretched trajectory. In the laboratory frame (right) the electron is pushed forward periodically by the* $\boldsymbol{v} \times \boldsymbol{B}$ *term.*

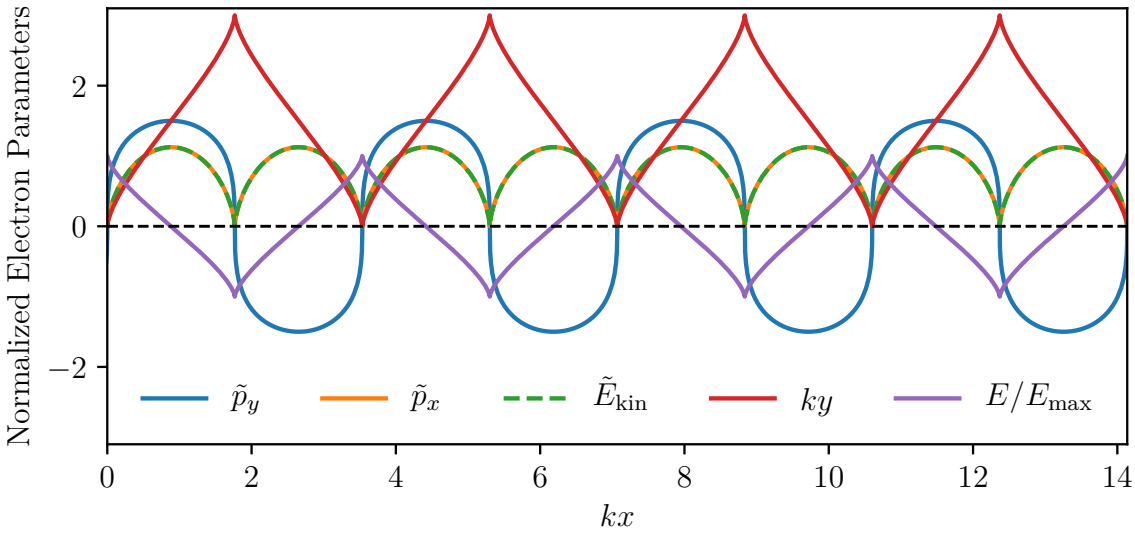

Figure 2.2.: *Electron dynamics in a plane wave. The evolution of electron parameters during interaction with a plane wave laser field ($a_0 = 1.5$) with electric field strength E is shown. $\tilde{p}$ denotes momenta normalized by $m_e c$ and the energy $\tilde{E}_{kin}$ is normalized by $m_e c^2$.*

2.3. Ponderomotive Force

The ponderomotive force is the net force that a charged particle experiences after averaging over the fast oscillation cycles. In case of an electron this may be expressed as

$$\boldsymbol{F}_{\mathrm{Pond}} := m_{\mathrm{e}} \left\langle \mathrm{d}v/\mathrm{d}t \right\rangle . \tag{2.32}$$

A derivation of the ponderomotive force taking into account relativistic effects is demanding and beyond the scope of this work. A full treatment may be found in [60–62] and results in

$$\boldsymbol{F}_{\mathrm{Pond}} = -\frac{m_{\mathrm{e}}c^2}{2\langle\gamma\rangle}\nabla\langle\boldsymbol{a}^2\rangle = -\frac{m_{\mathrm{e}}c^2}{4+a_0^2}\nabla a_0^2 = -\frac{e^2}{4\langle\gamma\rangle m_{\mathrm{e}}\omega^2}\nabla\tilde{\boldsymbol{E}}^2, \tag{2.33}$$

where $\tilde{E}$ stands for the spatial component of the electric field[1].

Since the ponderomotive force is conservative, a potential ϕ_{Pond} fulfilling $\boldsymbol{F}_{\mathrm{Pond}} = -\nabla\phi_{\mathrm{Pond}}$ can be found

$$\phi_{\mathrm{Pond}} = \frac{e^2}{4\langle\gamma\rangle m_{\mathrm{e}}\omega^2}\tilde{\boldsymbol{E}}^2. \tag{2.34}$$

F_{Pond} is proportional to the negative gradient of the laser intensity ∇I and the laser wavelength squared λ^2. It drives electrons away from regions of higher to regions of lower field strengths.

2.4. Plasma Physics

So far, the interaction of a single electron with a laser pulse has been described. To extend this analysis to electromagnetic waves propagating in and interacting with a gas of charged particles, plasmas need to be introduced and physically defined. The following sections are based upon [57, 63] and address this task.

[1] Nevertheless, by a perturbative ansatz the ponderomotive force can be derived easily to leading order as shown in the appendix in section A.3. The result deviates from the general expression given in Eq. (2.33) above only by missing the $1/\langle\gamma\rangle$ factor.

2.4.1. Basic Plasma Properties

Plasma is often called the fourth state of matter since its properties and behavior differ significantly from those of the other three states. It typically consists of a gas of positively charged ions and free electrons. The parameters and mechanisms introduced in the following are suitable tools to characterize and describe this mixture of charged particles.

In the following, n_e denotes the electron density, Z_i and n_i stand for the charge and density of the ions. λ_D stands for the Debye length which will be introduced in the next section.

Plasmas are defined by the following three properties:

- The physical size L of the plasma is much larger than the Debye length $L \gg \lambda_D$.
- The number of charge carriers N_D in a sphere of radius λ_D (Debye sphere) around a given charged particle is large, i.e., $N_D = n_e \times 4\lambda_D^3\pi/3 \gg 1$.
- The plasma frequency is large compared to the particle collision frequency.

The first point ensures that edge effects at the boundary of the plasma are negligible. The second point means that collective electrostatic interactions mediated by the electrostatic fields within the Debye sphere dominate over pairwise interactions (collision or scattering). The last criterion guarantees that electrostatic interactions are far superior to the effects of ordinary gas kinetics.

A plasma is called *quasi-neutral* when the plasma appears electrically neutral on scales much larger than the Debye length

$$\frac{n_e - Z_i n_i}{n_e} \ll 1.$$

In the so-called *plasma approximation* it is set $n_e = Z_i n_i$ [63].

Debye Shielding

The Coulomb force of an electric test charge acts upon the particles of the surrounding plasma. The freely moving charged components follow the electric field lines and lead to a shielding of the test charge. The typical distance at which the electric potential is significantly suppressed, the so-called Debye length, is given by [63]

$$\lambda_D = \sqrt{\frac{\varepsilon_0 k_B T}{n_e e^2}}, \tag{2.35}$$

and the Coulomb potential screened by this effect reads

$$\phi(r) = -\frac{e}{4\pi\varepsilon_0 r}\exp\left(-\frac{\sqrt{2}r}{\lambda_\mathrm{D}}\right). \tag{2.36}$$

Here, T stands for the temperature and k_B denotes the Boltzmann constant. Note that ϕ is composed of the normal Coulomb potential which is multiplied by a shielding term that depresses the potential exponentially with increasing radius. Both expressions are derived in the appendix in section A.4.

Plasmas used in LWFAs with $n_\mathrm{e} \approx 3 \times 10^{18}\,\mathrm{cm}^{-3}$ and temperatures according to Eq. (A.29) in the range of some MeV have a Debye length on the order of microns. Hence, the Debye sphere is densely populated and the collective behavior of the charged particles dominates. It is therefore justified to talk of "plasma" accelerators.

2.4.2. Plasma Frequency

In the section above, we have established that electric fields in an unperturbed plasma are effectively shielded on the scale of the Debye sphere. Nevertheless, external fields may disturb this equilibrium and entice a dynamic reaction of the plasma particles. In the following, we will discuss how electrons react to these fields. Due to the ~ 2000 times higher mass of the ions forming the positively charged background, their motion can be neglected in the following.

Deviations from quasi-neutrality result in an electric field $\boldsymbol{E}$ entailing a force $\boldsymbol{F} = -e\boldsymbol{E}$ upon the electron. Ensuing from Newton's second law and Eq. (2.1), the equation of motion for the electron reads

$$m_\mathrm{e}\frac{\mathrm{d}^2 x}{\mathrm{d}t^2} = -\frac{n_\mathrm{e}e^2}{\varepsilon_0}x. \tag{2.37}$$

This harmonic oscillator has the eigenfrequency

$$\omega_\mathrm{p} = \sqrt{\frac{n_\mathrm{e}e^2}{m_\mathrm{e}\varepsilon_0}}. \tag{2.38}$$

Once displaced by external fields, the free electrons oscillate with frequency ω_p against the ion background. If this quivering motion becomes relativistic, the electron mass m_e has to be replaced by $\langle\gamma\rangle\, m_\mathrm{e}$.

The corresponding wavelength is called *plasma wavelength* and is given by[1]

$$\lambda_\mathrm{p} = \frac{2\pi c}{\omega_\mathrm{p}} \approx 33.4\,\mu\mathrm{m} \times \frac{1}{\sqrt{n_\mathrm{e}[10^{18}\,\mathrm{cm}^{-3}]}}. \tag{2.39}$$

2.5. Electromagnetic Waves in Plasma

Atoms exposed to external electric fields are easier to ionize since the Coulomb potential binding the electrons to the nucleus is reduced. At laser intensities commonly used in LWFA experiments ($I > 10^{18}\,\mathrm{W\,cm^{-2}}$) the inner-atomic fields are suppressed below the electron's ground state potential such that electrons can leave the binding potential even without the need to tunnel through the Coulomb barrier [59]. This so-called barrier-suppression ionization (BSI) affects all but the most strongly bound inner electrons [57]. For hydrogen gas used in our experiments, even the pedestal of the main laser pulse is intense enough to ionize the atoms.

In this section, we will examine the properties of electromagnetic waves propagating in plasmas. Beginning with Maxwell's equation, the dispersion relation and refractive index of plasmas are derived.

2.5.1. Dispersion Relation and Refractive Index

Let's assume a plane electromagnetic wave with $\boldsymbol{E}(\boldsymbol{r},t) = \mathrm{Re}\left[\boldsymbol{E}_{\boldsymbol{k}} \mathrm{e}^{\mathrm{i}(\boldsymbol{k}\boldsymbol{r}-\omega t)}\right]$ where $\omega = 2\pi c/\lambda$. Taking the curl of Eq. (2.2) and exploiting the identity $\boldsymbol{j} = -e n_\mathrm{e} \boldsymbol{v}$, we get

$$\nabla \times (\nabla \times \boldsymbol{E}) = -\frac{1}{c^2}\partial_t^2 E + \mu_0 e n_\mathrm{e} \partial_t \boldsymbol{v} \tag{2.40}$$

Inserting $\boldsymbol{E}$ and Eq. (2.21) the above expression becomes

$$\boldsymbol{k} \times (\boldsymbol{k} \times \boldsymbol{E}) = \left(\frac{\omega^2}{c^2} - \mu_0 \frac{e^2 n_\mathrm{e}}{m_\mathrm{e}}\right) \boldsymbol{E}. \tag{2.41}$$

[1] See Table 2.2 for specific experimental values.

By exploiting the perpendicularity of Eq. (2.16) we obtain the dispersion relation [64]

$$\begin{aligned} \boldsymbol{k}^2 &= \frac{\omega^2}{c^2} - \frac{1}{c^2}\frac{e^2 n_\mathrm{e}}{\varepsilon_0 m_\mathrm{e}} \\ \Rightarrow \boldsymbol{k}^2 c^2 &= \omega^2 - \omega_\mathrm{p}^2, \end{aligned} \tag{2.42}$$

where we have used Eq. (2.38) in the last step.

The group velocity defined by $v_\mathrm{gr} := \partial\omega/\partial k$ and phase velocity $v_\mathrm{ph} := \omega/k$ follow directly

$$v_\mathrm{gr} = \frac{\partial\omega}{\partial k} = \frac{ck}{\omega}c =: \eta c < c, \tag{2.43}$$

$$v_\mathrm{ph} = \frac{\omega}{k} = \frac{\omega}{ck}c =: \frac{1}{\eta}c > c. \tag{2.44}$$

The refractive index in plasma therefore is

$$\eta = \frac{ck}{\omega} = \sqrt{1 - \frac{\omega_\mathrm{p}^2}{\omega^2}}. \tag{2.45}$$

If the angular frequency ω of the incident light is smaller than the plasma frequency ω_p, the refractive index becomes imaginary. This means, that electromagnetic waves of this frequency cannot propagate in such plasmas. The physical reason behind this behavior is the following: when distorted by an external field of frequency ω, the electrons shield deviations from quasi-neutrality if $\omega < \omega_\mathrm{p}$. For laser frequencies above ω_p, the plasma electrons are too slow to follow the oscillating electromagnetic field and the wave cannot be shielded. This has direct consequences for the penetration of electric fields in plasmas. Electromagnetic waves with frequencies below ω_p are reflected by plasmas, whereas for frequencies above ω_p plasmas become transparent.

Analogously to Eq. (2.38), it is convenient to define the critical plasma density for incident light of angular frequency ω according to[1]

$$n_\mathrm{crit} := \frac{\omega^2 m_\mathrm{e}\varepsilon_0}{e^2} = \frac{\omega^2}{\omega_\mathrm{p}^2} n_\mathrm{e}. \tag{2.46}$$

Hence, the refractive index becomes

$$\eta = \sqrt{1 - \frac{n_\mathrm{e}}{n_\mathrm{crit}}}. \tag{2.47}$$

[1] See Table 2.2 for specific experimental values.

Light of frequency ω can only propagate in plasmas with densities $n_e < n_{crit}$. Such plasmas are called *underdense*, whereas plasmas with $n_e > n_{crit}$ are called *overdense* and reflect incident light. The critical density for Ti:Sa laser systems centered around 800 nm is $n_{crit} \approx 1.7 \times 10^{21}\,\mathrm{cm}^{-3}$, whereas typical plasma densities used in LWFAs are on the order of $n_e \approx 3.0 \times 10^{18}\,\mathrm{cm}^{-3}$. Hence, such plasmas are underdense and the driving laser pulse can propagate through the gaseous target medium.

In the focus of a highly intense laser pulse, the driving potential is large enough to accelerate plasma electrons to relativistic energies. In this nonlinear regime, the electron's rest mass m_e has to be replaced by the relativistic mass $m_e \to \langle\gamma\rangle m_e$.

The plasma frequency, refractive index and critical density then have to be corrected accordingly which leads to the definition of the respective relativistic quantities, denoted with an additional 'n' (for 'nonlinear')

$$\omega_p \to \sqrt{\frac{n_e e^2}{\langle\gamma\rangle m_e \varepsilon_0}} = \frac{\omega_p}{\sqrt{\langle\gamma\rangle}} =: \omega_{p,n}, \tag{2.48}$$

$$\eta \to \sqrt{1 - \frac{\omega_p^2}{\langle\gamma\rangle \omega^2}} =: \eta_n, \tag{2.49}$$

$$n_{crit} \to \frac{\omega^2 \langle\gamma\rangle m_e \varepsilon_0}{e^2} = \langle\gamma\rangle n_{crit} =: n_{crit,n}. \tag{2.50}$$

The plasma frequency and the refractive index now not only depend on the plasma density n_e and laser frequency ω but also on a via Eq. (A.27). These dependencies give rise to a plethora of interesting effects in the nonlinear regime like ionization defocusing, relativistic self-focusing, self-phase modulation, pulse compression or self-induced transparency [65–71]. The effects relevant for LWFAs will be treated in the following.

2.5.2. Laser Pulse Evolution

Through Eq. (2.49) and its dependencies on the plasma density and laser intensity, the plasma influences the propagation of the laser pulse. In the following sections, the different effects which are relevant for LWFAs will be discussed.

The refractive index in Eq. (2.49) depends on three parameters: the plasma density n_e, the laser wavelength ω and $\langle\gamma\rangle$. Assuming the pulse to propagate in a relativistically underdense plasma $\omega_p/\langle\gamma\rangle \ll \omega$, the refractive index can be simplified

$$\eta = \sqrt{1 - \frac{\omega_p^2}{\langle\gamma\rangle\,\omega^2}} \approx 1 - \frac{1}{2}\frac{\omega_p^2}{\langle\gamma\rangle\,\omega^2}, \tag{2.51}$$

$$\frac{1}{\eta} \approx 1 + \frac{1}{2}\frac{\omega_p^2}{\langle\gamma\rangle\,\omega^2}. \tag{2.52}$$

Small perturbations of the laser wavelength and the plasma density lead to

$$\frac{\partial\eta}{\partial\omega}\,\mathrm{d}\omega = \frac{1}{2}\frac{\omega_p^2}{\langle\gamma\rangle\,\omega^2}2\frac{\mathrm{d}\omega}{\omega}, \tag{2.53}$$

$$\frac{\partial\eta}{\partial n_e}\,\mathrm{d}n_e = -\frac{1}{2}\frac{\omega_p^2}{\langle\gamma\rangle\,\omega^2}\frac{\mathrm{d}n_e}{n_e}. \tag{2.54}$$

With $\langle\gamma\rangle = 1 + a_0^2/4$ from Eq. (A.27)[1] in the plane wave approximation, the refractive index changes with varying a_0 as

$$\frac{\partial\eta}{\partial a_0}\,\mathrm{d}a_0 = \frac{1}{2}\frac{\omega_p^2}{\langle\gamma\rangle\,\omega^2}\frac{1}{2}\frac{a_0}{1 + a_0^2/4}\,\mathrm{d}a_0. \tag{2.55}$$

In the non-relativistic regime $a_0 \ll 1$ this can be further simplified

$$\frac{\partial\eta}{\partial a_0}\,\mathrm{d}a_0 \approx \frac{1}{2}\frac{\omega_p^2}{\langle\gamma\rangle\,\omega^2}\frac{1}{2}a_0\,\mathrm{d}a_0 = \frac{1}{2}\frac{\omega_p^2}{\langle\gamma\rangle\,\omega^2}\frac{1}{4}\mathrm{d}a_0^2. \tag{2.56}$$

With these identities, the refractive index can be expanded via the total differential as [57]

$$\begin{aligned}\eta + \mathrm{d}\eta &= \eta + \frac{\partial\eta}{\partial n_e}\,\mathrm{d}n_e + \frac{\partial\eta}{\partial\omega}\,\mathrm{d}\omega + \frac{\partial\eta}{\partial a_0}\,\mathrm{d}a_0 \\ &= 1 - \frac{1}{2}\frac{\omega_p^2}{\omega^2}\left(1 + \frac{\mathrm{d}n_e}{n_e} - 2\frac{\mathrm{d}\omega}{\omega} - \frac{\mathrm{d}a_0^2}{4}\right).\end{aligned} \tag{2.57}$$

[1] A general expression for $\langle\gamma\rangle$ in the case of a linearly polarized laser is given in [56, 72] and reads $\langle\gamma\rangle = \sqrt{1 + a^2/2}$

These dependencies transfer to the group and phase velocity via Eq. (2.43) and Eq. (2.44) accordingly

$$v_{\mathrm{gr}} + \mathrm{d}v_{\mathrm{gr}} = c\left(1 - \frac{1}{2}\frac{\omega_{\mathrm{p}}^2}{\omega^2}\left(1 + \frac{\mathrm{d}n_{\mathrm{e}}}{n_{\mathrm{e}}} - 2\frac{\mathrm{d}\omega}{\omega} - \frac{\mathrm{d}a_0^2}{4}\right)\right), \tag{2.58}$$

$$v_{\mathrm{ph}} + \mathrm{d}v_{\mathrm{ph}} = c\left(1 + \frac{1}{2}\frac{\omega_{\mathrm{p}}^2}{\omega^2}\left(1 + \frac{\mathrm{d}n_{\mathrm{e}}}{n_{\mathrm{e}}} - 2\frac{\mathrm{d}\omega}{\omega} - \frac{\mathrm{d}a_0^2}{4}\right)\right), \tag{2.59}$$

where we have used Eq. (2.52) in the latter case. Therefore, it is clear that the phase and group velocity can be modulated by changing the density, laser frequency or intensity [73]. These effects were first predicted by theory in the 60s and 70s of the last century [74–76] and shall be discussed in the following.

Density Dependent Focusing Effects

The spatial and temporal Gaussian shape of a focused laser pulse leads to inhomogeneities in the constant background plasma density which directly affect the group and phase velocity of the laser beam [77]. On the one hand, the intensity peaks on the axis, thus the medium here ionizes first and the leading edge of the laser pulse experiences a higher electron density on the axis. On the other hand, the ponderomotive force expels electrons from the central regions of the beam generating a lower electron density on the axis. Both effects influence the propagation of the laser as they either force the beam to diverge or converge. These effects will be treated in the following in more detail.

Ionization Defocusing As the higher light intensity on the axis ionizes the medium first, a higher electron density on the axis is induced. Therefore, the term $\mathrm{d}n_{\mathrm{e}}/n_{\mathrm{e}}$ in Eq. (2.57) modifying the refractive index increases towards the axis. Hence, this induced density perturbation leads to a transverse non-vanishing gradient of the refractive index with a higher phase velocity on the axis according to Eq. (2.59). The further away from the axis the lower the phase velocity. Overall, these modulations of the radial phase velocity lead to a defocusing of the driving laser pulse termed *ionization defocusing* [78]. However, in the case of hydrogen gas ionized with high-intensity laser pulses, this effect is of minor importance since the ionization threshold is orders of magnitudes below the ionization potential of the laser pulse. Ionization defocusing therefore only plays a role at the leading edge of the pulse's pedestal.

Ponderomotive Self-focusing The ponderomotive force counteracts ionization defocusing as it pushes electrons away from the center region of the laser beam. According to Eq. (2.34), the ponderomotive potential is proportional to the laser intensity $\phi_{\mathrm{Pond}} \propto I$, therefore n_e decreases towards the axis and the term $\mathrm{d}n_\mathrm{e}/n_\mathrm{e}$ in Eq. (2.59) becomes negative [79].

For a Gaussian laser profile $a^2 = a_0^2 \exp(-2r^2/r_0^2)$ with $a^2 \ll 1$ this density perturbation to the background plasma density n_0 can be calculated [56]

$$n_\mathrm{e}(r) = n_0 - \frac{4a_0^2 \varepsilon_0 m_\mathrm{e} c^2}{e^2 r_0^2} \left(1 - \frac{2r^2}{r_0^2}\right) \exp\left(-\frac{2r^2}{r_0^2}\right). \tag{2.60}$$

As a lower plasma density decreases the phase velocity, such variations in the plasma background force the laser beam to converge.

Relativistic Self-focusing

The previously studied effect modifies the phase velocity by directly acting upon the plasma density. In contrast, the last term in Eq. (2.59) addresses the plasma electrons by considering their relativistic mass increase due to acceleration. In summary, the gradient of a_0 in the transverse direction leads to a reduced phase velocity on-axis causing the so-called *relativistic self-focusing*. This effect only depends on the power P of the laser pulse and overcompensates diffraction if the critical power P_crit is surpassed [29, 72, 80][1]

$$P > P_\mathrm{crit} := 8\pi\varepsilon_0 c \left(\frac{m_\mathrm{e} c^2}{e}\right)^2 \frac{\omega^2}{\omega_\mathrm{p}^2} \approx 17.4 \frac{\omega^2}{\omega_\mathrm{p}^2} [\mathrm{GW}]. \tag{2.62}$$

In practical units, this expression may be rewritten as

$$P_\mathrm{crit}[\mathrm{TW}] \approx 19.5 \lambda[\mu\mathrm{m}]^{-2} n_\mathrm{e}[10^{18}\,\mathrm{cm}^{-3}]^{-1}. \tag{2.63}$$

[1] If both relativistic *and* ponderomotive self-focusing are taken into account, the threshold for guiding P_L is lowered to [80]

$$P_\mathrm{L} = 16.2 \frac{\omega^2}{\omega_\mathrm{p}^2} [\mathrm{GW}]. \tag{2.61}$$

Due to diffraction, the waist of a Gaussian beam $w(z)$ evolves according to

$$\frac{w(z)}{w_0} = \sqrt{1 + \left(\frac{z}{z_\mathrm{R}}\right)^2}, \tag{2.64}$$

where $w_0 \coloneqq w(0)$ denotes the radius of the beam at the focal spot ($z = 0$). z_R is the so-called *Rayleigh length* defined by $z_\mathrm{R} \coloneqq \pi w_0^2/\lambda$. Taking into account relativistic self-focusing, the beam waist evolves in first order according to [56]

$$\frac{w(z)^2}{w_0^2} = 1 + \left(1 - \frac{P}{P_\mathrm{crit}}\right)\frac{z^2}{z_\mathrm{R}^2}. \tag{2.65}$$

For $P > P_\mathrm{crit}$, higher-order corrections prevent the laser pulse to focus down to an infinitely and therefore nonphysically small spot size [72].

Simulations show that guiding over several Rayleigh lengths with a stable spot size w_0 is reached, if [41]

$$w_0 \approx w_\mathrm{match} \coloneqq 2\frac{\sqrt{a_0}}{k_\mathrm{p}}. \tag{2.66}$$

w_match is called *matched beam spot size*. In this case, self-focusing balances the natural diffraction and the laser pulse can maintain its driving potential over several Rayleigh lengths. Nevertheless, the very front of the laser pulse where the power is lower than P_crit will diffract which leads to *head erosion* of the laser pulse. This effect ultimately limits the propagation distance of a laser pulse with matched beam spot size [81].

With Eq. (2.62) and Eq. (2.26) the power P may be expressed as

$$P = w_0^2 \pi \frac{a_0^2 \omega_\mathrm{p}^2}{16\pi^2 c^2} P_\mathrm{crit}. \tag{2.67}$$

Hence, the above condition Eq. (2.66) for a stable guiding of the laser pulse can be reformulated as [41]

$$\left(\frac{P_\mathrm{match}}{P_\mathrm{crit}}\right)^{\frac{1}{3}} \approx \frac{a_0}{2}. \tag{2.68}$$

For laser powers around P_crit the pulse dynamics in plasmas is governed by the relativistic mass increase of the electrons [56]. In contrast, for laser powers typical in LWFA ex-

periments with $P \gg P_{\text{crit}}$, density perturbations due to the ponderomotive force play the dominant role [80].

In our experiments with $n_e = 3.0 \times 10^{18}\,\text{cm}^{-3}$ the critical power is $P_{\text{crit}} \approx 10.1\,\text{TW}$. With $P \approx 75\,\text{TW}$, the corresponding matched normalized vector potential is ~ 3.9 with a matched spot size of $w_{\text{match}} \approx 12\,\mu\text{m}$. According to PIC simulations (cf. Figure 2.3) focusing effects in the plasma increase a_0 from ~ 1.8 – its vacuum value – to ~ 3 leading to a matched power of $\sim 60\,\text{TW}$, which is in good agreement with the measured pulse power at the target in our experiments.

Temporal Pulse Compression

The above-mentioned focusing effects were based on transverse variations of the refractive index. Of course, also longitudinal plasma inhomogeneities alter the pulse propagation. As mentioned above, the front of the pulse already completely ionizes the gas medium, but the ponderomotive force of the main peak pushes electrons forward and to the side. Therefore, the back of the laser pulse travels in a plasma of lower density and increased γ, which both increase η and hence also the group velocity according to Eq. (2.58). Therefore, the tail of the pulse travels at a higher group velocity than the front part. The pulse gets longitudinally compressed resulting in an effect called *temporal pulse compression* [82]. This has the advantageous effect that the power of the driving laser pulse stays relatively constant even though energy from the driver is transferred to the plasma electrons to form the wakefield [83].

Let us consider two points of a laser pulse initially separated by $c\tau_0$. The pulse itself travels through a plasma of length l having an unperturbed density n_e. Due to laser-plasma interactions, these two points have different group velocities $v_{\text{gr},1}$ and $v_{\text{gr},2}$. The temporal separation of these two points after propagation in z direction over the distance Δl changes by

$$\Delta\tau = \left(v_{\text{gr},2} - v_{\text{gr},1}\right)\frac{\Delta l}{c^2} = \left(\eta_2 - \eta_1\right)\frac{\Delta l}{c} = \Delta\eta\,\frac{\Delta l}{c}, \tag{2.69}$$

where we made use of Eq. (2.43).

$\Delta\eta$ of course is difficult to determine as it depends on the properties of the laser pulse which influences the plasma density and the electron's Lorentz factor γ according to Eq. (2.49).

But for $n_e \ll \gamma n_{crit}$ the refractive index can be approximated by Eq. (2.51)

$$\eta = \sqrt{1 - \frac{n_e}{\gamma n_{crit}}} \approx 1 - \frac{n_e}{2\gamma n_{crit}}. \tag{2.70}$$

Hence,

$$\Delta\eta \approx \eta_{max} - \eta_{min} \approx 1 - \left(1 - \frac{n_e}{2n_{crit}}\right) = \frac{n_e}{2n_{crit}}, \tag{2.71}$$

where we assumed a highly intense laser pulse $a \gg 1$ such that $\eta_{max} \approx 1$ for large γ and $\eta_{min} \approx 1 - n_e/(2n_{crit})$.

Therefore, the temporal distance τ between the two points at the end of the plasma can be estimated by [84][1]

$$\tau = \tau_0 - \Delta\tau \approx \tau_0 - \frac{n_e l}{2n_{crit} c}. \tag{2.72}$$

In our experiments with $n_e = 3.0 \times 10^{18}\,\mathrm{cm}^{-3}$, $l = 2.5\,\mathrm{mm}$ and $n_{crit} = 1.7 \times 10^{21}\,\mathrm{cm}^{-3}$, the temporal duration of the laser pulse reduces according to this estimation by $\Delta\tau \approx 7.4\,\mathrm{fs}$, which is in good agreement with simulations (cf. Figure 2.3(d)).

Figure 2.3 shows a full PIC simulation of the three most relevant laser parameters and their evolution in vacuum (dashed lines) and plasma (solid line). Figure 2.3(a) depicts the corresponding profiles of the plasma density. Self-focusing (c) and temporal pulse compression (d) indeed significantly take place as soon as the plasma density has reached its plateau. This increases the intensity of the laser pulse, which in turn raises the laser's normal vector potential a_0 (d).

All these above-mentioned effects arise from the coupling of the electron background to the refractive index and thus also increase or decrease a_0, which has significant influences on the wakefield forming behind the laser driver as will be seen in the following section.

[1] Of course various effects like dispersion, the limited bandwidth of the pulse, etc. prevent τ from becoming infinitely small.

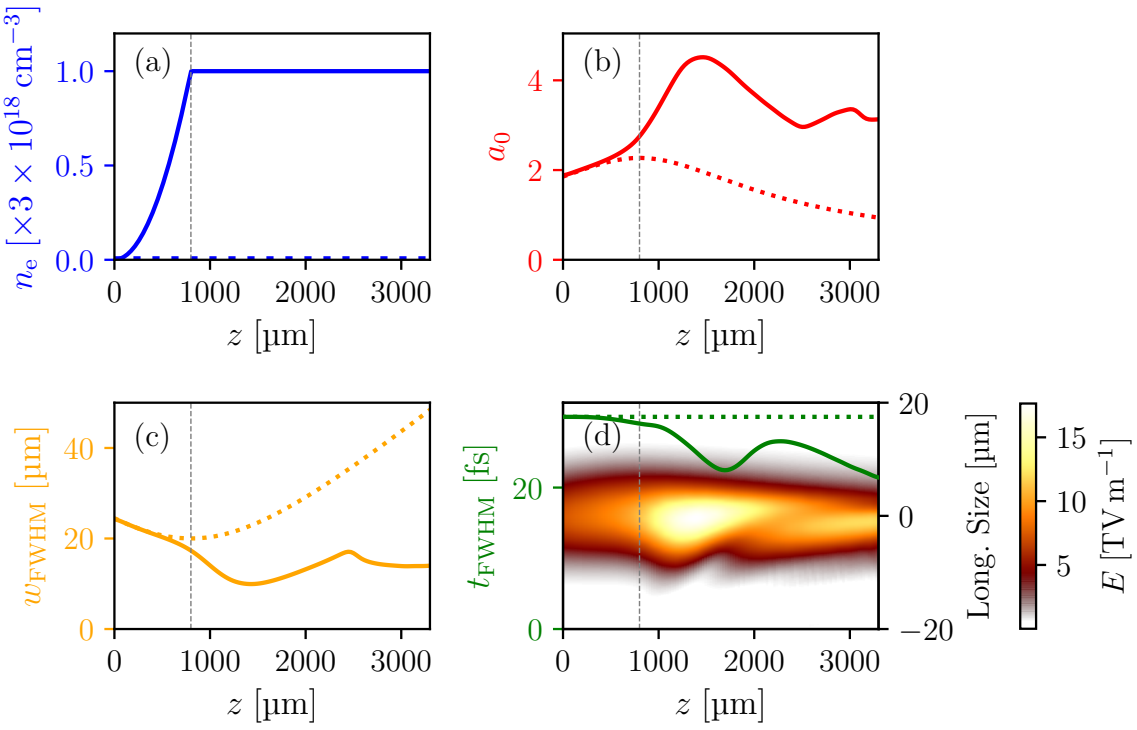

Figure 2.3.: *Evolution of several laser parameters while propagating through a plasma. A typical hydrogen gas density profile generated by a gas nozzle with plateau density $3.0 \times 10^{18} cm^{-3}$ is plotted in (a). The driving laser pulse ($P = 50 TW$, $\tau_{FWHM} = 30 fs$) is focused to a spot size of $w = 20\,\mu m$ at the beginning of the gas plateau ($z = 800\,\mu m$), indicated by the dashed gray vertical line. The interaction with the plasma increases the laser intensity (b) due to transverse focusing (c) and temporal (longitudinal) compression effects. The latter is plotted in (d) together with the longitudinal on-axis envelope of the laser pulse. The solid lines in each plot are results from PIC simulations, whereas dashed lines represent the evolution of these parameters assuming Gaussian beam propagation in a vacuum.*

2.6. Laser Wakefield Acceleration

At the beginning of this chapter, we studied the interaction of a single electron with an electromagnetic wave to derive its trajectory and established the ponderomotive force exerted by a high-intensity laser pulse on charged particles. In the following sections, we examine the collective effects of plasma electrons as a response to a general driving potential. In pure LWFA this driving potential is composed of a solitary high-intensity laser pulse. On the opposite side, for pure PWFA, a relativistic particle beam drives the wakefield. We are interested in the intermediary regime between these two extreme cases. Here the particle beam becomes non-negligible compared to the laser driver and beam loading effects emerge. Consequently, both potentials are essential for our analysis and, thus, none can be neglected in the following derivations.

To incorporate these beam loading effects, we analyze the response of the plasma to a general driving force (be it a laser or particle beam or the combination of both) for 3D linear and 1D nonlinear regimes. To do so, we first derive the general relativistic equation of motion in plasmas. Note that the force on the electrons exerted by electromagnetic fields can now be influenced by charge distributions *and* currents in the plasma – as opposed to the equation of motion for a single electron [85].

2.6.1. General Equation of Motion in Plasmas

Taking into account that $\boldsymbol{p}^2 = m_\mathrm{e}^2 c^2(\gamma^2 - 1)$ – which follows from the expression $\beta\gamma = \sqrt{\gamma^2 - 1}$ – and using the relation Eq. (A.13) together with Eq. (A.14), the equation of motion given in Eq. (2.28),

$$\frac{\mathrm{d}\boldsymbol{p}}{\mathrm{d}t} = \frac{\mathrm{d}}{\mathrm{d}t}\left(\gamma m_\mathrm{e}\boldsymbol{v}\right) = -e\left(\boldsymbol{E} + \boldsymbol{v}\times\boldsymbol{B}\right), \tag{2.73}$$

can be simplified to

$$\begin{aligned}
\frac{\partial \boldsymbol{p}}{\partial t} &= -e\boldsymbol{E} - e\boldsymbol{v}\times\boldsymbol{B} - (\boldsymbol{v}\cdot\nabla)\boldsymbol{p} && (2.74)\\
&= -e\boldsymbol{E} - e\boldsymbol{v}\times\boldsymbol{B} - \frac{1}{2m_\mathrm{e}\gamma}\nabla\boldsymbol{p}^2 + v\times(\nabla\times\boldsymbol{p}) && (2.75)\\
&= -e\boldsymbol{E} - m_\mathrm{e}c^2\nabla\gamma - \boldsymbol{v}\times(e\boldsymbol{B} - \nabla\times\boldsymbol{p}). && (2.76)
\end{aligned}$$

With Eq. (2.6) this can further be expressed as [86]

$$\frac{\partial \boldsymbol{p}}{\partial t} = -e\boldsymbol{E} - m_\mathrm{e}c^2\nabla\gamma - \boldsymbol{v}\times\left(\nabla\times(e\boldsymbol{A}-\boldsymbol{p})\right). \tag{2.77}$$

The last term of this equation vanishes, since replacing $\boldsymbol{E} = -\dfrac{\partial \boldsymbol{A}}{\partial t} - \nabla\phi$ (cf. Eq. (2.7)) and taking the curl on both sides yields

$$\frac{\partial}{\partial t}\left(\nabla\times(\boldsymbol{p}-e\boldsymbol{A})\right) = \nabla\times\left(\boldsymbol{v}\times\left(\nabla\times(\boldsymbol{p}-e\boldsymbol{A})\right)\right). \tag{2.78}$$

Before the arrival of the driver, the electrons are unperturbed and at rest. With this initial condition, $\nabla\times(\boldsymbol{p}-e\boldsymbol{A}) = 0$ for all time [87].

Therefore, the *general equation of motion in plasmas* becomes [59]

$$\frac{\partial \boldsymbol{p}}{\partial t} = -e\boldsymbol{E} - m_\mathrm{e}c^2\nabla\gamma. \tag{2.79}$$

In the following, we solve this equation. Replacing $\boldsymbol{E}$ – as above – with the corresponding potentials yields

$$\frac{\partial \boldsymbol{p}}{\partial t} = e\frac{\partial \boldsymbol{A}}{\partial t} + e\nabla\phi - m_\mathrm{e}c^2\nabla\gamma. \tag{2.80}$$

The first term on the right-hand side of this equation describes the laser field, the second term the electrostatic force induced by the charge separation in the plasma, and the third term is the plasma pressure.

Rearranging this equation leads to [79]

$$\frac{\partial}{\partial t}(\boldsymbol{p}-e\boldsymbol{A}) = \nabla\left(e\phi - m_\mathrm{e}c^2\gamma\right), \tag{2.81}$$

which has a trivial solution, when the electrostatic force $\boldsymbol{F}_\mathrm{E} = e\nabla\phi$ is balanced by the ponderomotive force $\boldsymbol{F}_\mathrm{Pond,N} = -m_\mathrm{e}c^2\nabla\gamma$,

$$e\nabla\phi = m_\mathrm{e}c^2\nabla\gamma \tag{2.82}$$

$$\Rightarrow \boldsymbol{p} = e\boldsymbol{A}, \tag{2.83}$$

with the boundary condition, that the electrons are initially (i.e., prior to the passage of the laser pulse) at rest. $\boldsymbol{F}_\mathrm{Pond,N}$ is often called *generalized nonlinear ponderomotive force*

as it generalizes the ponderomotive force for a single electron in a laser field derived in section 2.3 ([55, 56]).

From Eq. (2.83) follows with Eq. (2.23) [85, 86]

$$\begin{aligned} \boldsymbol{a} &= \frac{e\boldsymbol{A}}{m_e c} = \frac{\boldsymbol{p}}{m_e c} = \gamma\beta \\ \Rightarrow a^2 &= (\gamma\beta)^2 = \gamma^2 - 1 \\ \Rightarrow \gamma &= \sqrt{a^2+1} \end{aligned} \tag{2.84}$$

The ponderomotive force in a plasma is therefore given by

$$\boldsymbol{F}_{\mathrm{Pond,N}} = -m_e c^2 \nabla\gamma = -m_e c^2 \nabla\sqrt{a^2+1}. \tag{2.85}$$

The corresponding ponderomotive potential follows directly

$$\phi_{\mathrm{Pond,N}} = m_e c^2 (\gamma - 1) = m_e c^2 \left(\sqrt{a^2+1} - 1\right). \tag{2.86}$$

Note, that these expressions, as well as the relation for γ derived in Eq. (2.84), differ from the expressions given for a single electron in a plane wave (cf. section 2.2 and section 2.3) as we are dealing here with effects emerging from collective electron motion[1].

2.6.2. Wakefield Generation

High intensity laser pulses or relativistic particle beams excite collective electron motion when propagating through a plasma. This response of the plasma manifested by a plasma wave is caused by the ponderomotive and electrostatic potential of the driver. The derivation of the equations describing these plasma waves will be given in the following, starting out with the continuity equation, Gauss's law and the general equation of motion which have already been introduced in previous sections above (Eq. (2.5), Eq. (2.1) and Eq. (2.79))

- Continuity Equation: $\frac{\partial\rho}{\partial t} + \nabla\boldsymbol{j} = 0$
- Gauss's law: $\nabla\cdot\boldsymbol{E} = \frac{\rho}{\varepsilon_0}$,
- Equation of Motion in Plasmas: $\frac{\partial\boldsymbol{p}}{\partial t} = -e\boldsymbol{E} - m_e c^2\nabla\gamma$.

[1] The ponderomotive force treated in this context has its origin in the collective motion of charged particles, whereas the ponderomotive force derived in section 2.3 originates from the motion of a single particle. Therefore, the expressions for the ponderomotive force and γ differ. For more details see [62, 85].

In the following, the electrons are treated as a fluid with zero temperature and with the density and velocity distribution $n_e(\boldsymbol{r},t)$ and $\boldsymbol{v}(\boldsymbol{r},t)$, respectively. The positively charged ion background with density n_i is assumed to be immobile ($\boldsymbol{v}_i = 0$) which is justified due to the much higher mass of the ions (cf. section 2.2). In the following, we denote the unperturbed electron plasma density by n_0. In the case of hydrogen gas, we therefore have $n_i = n_0$. The density of the plasma wave n_e can hence be expressed by $n_e = n_0 + \delta n$. The laser is described by its normalized intensity a^2 and the driving, non-evolving electron beam with speed $\boldsymbol{v}_b$ by its charge density n_b. The following derivation is based on the works of [54–56, 59, 79, 86].

Linear Wakefields

In the 3D linear non-relativistic regime, we assume a weak laser driver with $a_0 \ll 1$ in combination with a particle beam as an additional driver. Moreover, the particle beam density and perturbations to the plasma density are assumed to be small, i.e., $n_b/n_0 \ll 1$ and $\delta n/n_0 \ll 1$. The fundamental equations above can then be simplified by linearization, as carried out in the following [40].

Using the relations $\rho = -e(n_e + n_b - n_0)$ and $\boldsymbol{j} = -e(n_e\boldsymbol{v} + n_i\boldsymbol{v}_i + n_b\boldsymbol{v}_b)$, the continuity equation can be rewritten. For that, we harness the assumptions of an immobile ion background to deduce the linearized form of the continuity equation by omitting small higher-order contributions

$$\frac{\partial\,\delta n}{\partial t} + n_0 \nabla\cdot\boldsymbol{v} = 0. \tag{2.87}$$

Gauss's law can be transformed accordingly

$$\nabla\cdot\boldsymbol{E} = -\frac{e}{\varepsilon_0}\left(n_b + \delta n\right). \tag{2.88}$$

The ponderomotive force given in Eq. (2.85) can also be simplified considering that Eq. (2.84) transforms as $\gamma = \sqrt{a^2+1} \approx 1$ for $a \ll 1$

$$\boldsymbol{F}_{\mathrm{Pond,N}} = -m_e c^2 \nabla\gamma = -m_e c^2 \nabla\sqrt{a^2+1} \approx -m_e c^2 \nabla\frac{a^2}{2}, \tag{2.89}$$

where we have used Eq. (2.84) and $\nabla\gamma = (\nabla a^2)/(2\gamma) \approx \nabla a^2/2$.

The ponderomotive potential simplifies as well

$$\phi_{\mathrm{Pond,N}} = m_\mathrm{e}c^2\left(\gamma - 1\right) = m_\mathrm{e}c^2\left(\sqrt{a^2+1} - 1\right) \approx m_\mathrm{e}c^2\frac{a^2}{2}. \tag{2.90}$$

Inserting Eq. (2.84) into the equation of motion, Eq. (2.79), together with $\gamma \approx 1$ in the linear regime, we get

$$\frac{\partial \boldsymbol{v}}{\partial t} = -\frac{e\boldsymbol{E}}{m_\mathrm{e}} - c^2\nabla\frac{a^2}{2}. \tag{2.91}$$

The wave equation describing a plasma density perturbation induced by an external driving potential directly follows from equations Eq. (2.87), Eq. (2.88), and Eq. (2.91).

To start off, we take the time derivative of Eq. (2.87), which yields

$$\frac{\partial^2}{\partial t^2}\frac{\delta n}{n_0} = -\frac{\partial}{\partial t}\left(\nabla\cdot\boldsymbol{v}\right). \tag{2.92}$$

The divergence on both sides of Eq. (2.91) leads to

$$\nabla\frac{\partial \boldsymbol{v}}{\partial t} = -\frac{e}{m_\mathrm{e}}\nabla\cdot\boldsymbol{E} - c^2\nabla^2\frac{a^2}{2}. \tag{2.93}$$

Plugging both relations into Eq. (2.88), we get

$$-\frac{e^2 n_0}{m_\mathrm{e}\varepsilon_0}\frac{n_\mathrm{b}+\delta n}{n_0} = \frac{e}{m_\mathrm{e}}\nabla\boldsymbol{E} = -\nabla\frac{\partial \boldsymbol{v}}{\partial t} - c^2\nabla^2\frac{a^2}{2} = \frac{\partial^2}{\partial t^2}\frac{\delta n}{n_0} - c^2\nabla^2\frac{a^2}{2}. \tag{2.94}$$

Rearranging and inserting the plasma frequency, Eq. (2.38), leads to the *wave equation for linear wakefields* [79]

$$\left(\frac{\partial^2}{\partial t^2} + \omega_\mathrm{p}^2\right)\frac{\delta n}{n_0} = c^2\nabla^2\frac{a^2}{2} - \omega_\mathrm{p}^2\frac{n_\mathrm{b}}{n_0}. \tag{2.95}$$

With Eq. (2.90), the right-hand side can be further simplified to

$$\left(\frac{\partial^2}{\partial t^2} + \omega_\mathrm{p}^2\right)\frac{\delta n}{n_0} = \frac{1}{m_\mathrm{e}}\Delta\phi_{\mathrm{Pond,N}} - \frac{1}{m_\mathrm{e}}\frac{e^2 n_\mathrm{b}}{\varepsilon_0}. \tag{2.96}$$

The very last term on the right-hand side is related to the electric potential of the particle beam ϕ_b via

$$\Delta\phi_\mathrm{b} = \frac{e}{\varepsilon_0} n_\mathrm{b}. \tag{2.97}$$

Hence, with $q = -e$, the wave equation can be rewritten

$$\left(\frac{\partial^2}{\partial t^2} + \omega_\mathrm{p}^2\right) \frac{\delta n}{n_0} = \frac{1}{m_\mathrm{e}} \Delta \left(\phi_\mathrm{Pond,N} + q\phi_\mathrm{b}\right), \tag{2.98}$$

which we recognize as an undamped driven harmonic oscillator [83]. The driving potential on the right-hand side is a linear superposition of the ponderomotive potential generated by the laser pulse and the electrostatic potential provoked by the particle beam. Their interaction with the plasma particles displaces electrons which then start to oscillate.

In the co-moving frame, with $\zeta = z - ct \Rightarrow \partial/\partial t = -c\partial/\partial\zeta$, $\partial/\partial z = \partial/\partial\zeta$, this wave equation can be solved analytically assuming that the drive beam is non-evolving, which means it has no direct time dependence (so-called quasi-static approximation) and therefore the partial time derivatives vanish. The corresponding electric field can be calculated from Eq. (2.88).

Solutions to Eq. (2.95) in the case of a purely laser-driven wakefield ($n_\mathrm{b} = 0$) with arbitrary lengths of the driver are difficult to find and were subject to theoretical studies for many years [28, 81, 88–90]. Nevertheless, with a driver of transverse Gaussian and longitudinal sine-squared-like normalized intensity profile,

$$a(r,z)^2 = a_0^2 \exp\left(-\frac{2r^2}{w(z)^2}\right) \sin^2\left(\pi\zeta/L\right) \quad \text{for } 0 < \zeta < L, \tag{2.99}$$

and 0 elsewhere, an exact solution was given by Sprangle *et al.* [91]. Their expression indicates that the wake is driven resonantly for laser pulse lengths $L \approx \lambda_\mathrm{p}$, i.e.,

$$L_\mathrm{FWHM} \approx \lambda_\mathrm{p}/2, \tag{2.100}$$

and that the radial extent of the wake is on the order of the laser spot size w_0. However, the exact pulse length to resonantly drive a wake in the linear case depends on the exact shape of the driving pulse [56].

Analogous to the definition of the normalized field of electromagnetic waves with frequency ω given by Eq. (2.23) $a = E/\tilde{E}_0$ with $\tilde{E}_0 = (m_\mathrm{e} c\omega)/e$, we introduce the normalized electric

field strength of the wakefield E_z/E_0 with $E_0 = (m_e c \omega_p)/e$. E_0 will play an important role in the following subsection 2.6.3.

For a linearly polarized laser pulse of resonant length, the normalized axial electric field E_z/E_0 and normalized density perturbation $\delta n/n_0$ of the wake behind the driver are given by [79]

$$\frac{E_z}{E_0} = -\frac{\pi}{4}\frac{a_0^2}{2}\exp\left(-\frac{2r^2}{w(z)^2}\right)\cos\left(k_p\zeta\right), \tag{2.101}$$

$$\frac{\delta n}{n_0} = -\frac{\pi}{4}\frac{a_0^2}{2}\left(1+\frac{8}{k_p^2 w(z)^2}\left(1-\frac{2r^2}{w(z)^2}\right)\right)\exp\left(-\frac{2r^2}{w(z)^2}\right)\sin\left(k_p\zeta\right). \tag{2.102}$$

By the Panofsky-Wenzel theorem, the radial electric field can be calculated from E_z [79] which leads to $E_r \propto r\exp(-2r^2/w(z)^2)\sin\left(k_p\zeta\right)$. Hence, in the linear regime, the accelerating electric fields as well as the density perturbation behind the driver follow a sinusoidal shape and are phase-shifted with respect to each other by $\pi/2$. The electrostatic fields and density perturbation are periodic with wavelength λ_p. Due to the changing sign in the trigonometric functions, the structure of the wake provides regions with decelerating and accelerating forces, and the radial electric fields display focusing and defocusing effects on the accelerated particle bunch induced by the r dependence [56]. Due to their respective phase difference, an off-axis electron will simultaneously experience axial acceleration and radial focusing forces only for a region of $\left|\Delta\zeta\right| = \pi/(2k_p)$ (which differs from the non-linear case as we will see later) [92]. It is this phase of the wake that is favorable for electron injection and acceleration.

Typical LWFAs are operated in the nonlinear regime, where $a_0 > 1$. Therefore, the above assumptions cannot be maintained and the theoretical description of wakefield acceleration has to be extended to the much more complicated case of nonlinear wakefields, where only a one-dimensional theoretical description exists. The study of the general three-dimensional non-linear case requires numeric methods like PIC simulations (cf. chapter 3). Nevertheless, the one-dimensional theory already covers a wide range of nonlinear effects and scaling laws which may directly be transferred to the general 3D case. Justified by this fact, the fully relativistic one-dimensional description of plasma wakefields shall briefly be treated.

Nonlinear Wakefields

When entering the relativistic regime $a_0 > 1$, the above assumptions of small density perturbations and $\gamma \approx 1$ cannot be kept up. The response of the plasma becomes highly nonlinear, which makes the linearization of the underlying equations impossible. Nevertheless, the way of proceeding stays the same. Using the Coulomb gauge $\nabla \cdot \boldsymbol{A} = 0$ and the relation for the plasma frequency given in Eq. (2.38), Gauss's law can be reformulated to the Poisson equation

$$\nabla^2 \varphi = k_\mathrm{p}^2 \left(\frac{n_\mathrm{e}}{n_0} + \frac{n_\mathrm{b}}{n_0} - 1 \right), \tag{2.103}$$

where

$$\varphi := \phi / (m_\mathrm{e} c^2) \tag{2.104}$$

is the normalized electric potential.

As in the linear case, the equation of motion and continuity equation are used to derive the *one-dimensional general wakefield equation* in the co-moving frame in the quasi-static approximation [54, 79, 93][1]

$$\frac{1}{k_\mathrm{p}^2} \frac{\partial^2 \varphi}{\partial \zeta^2} = \pm \frac{n_\mathrm{b}}{n_0} + \gamma_\mathrm{p}^2 \left(\beta_\mathrm{p} \left(1 - \frac{1 + a^2/2}{\gamma_\mathrm{p}^2 (1+\varphi)^2} \right)^{-\frac{1}{2}} - 1 \right). \tag{2.105}$$

Here we have used the relativistic factor for the plasma wave $\gamma_\mathrm{p} = (1 - \beta_\mathrm{p}^2)^{-1/2}$ and $\beta_\mathrm{p} = v_\mathrm{p}/c$, with v_p being the phase velocity of the plasma wave. The $+$ sign covers the case of an electron driver, the $-$ sign a positron driver. Note, that Eq. (2.105) breaks down for $\varphi = \sqrt{1 + a^2/2}/\gamma_\mathrm{p} - 1$. The corresponding electric field $E_\mathrm{B}/E_0 = \sqrt{2\sqrt{1+a^2/2}(\gamma_\mathrm{p} - 1)}$ is a generalization of the cold relativistic wave breaking limit *including* effects of a laser field [93], as will be discussed later in subsection 2.6.3.

[1] In mathematical expressions for the wakefield and related equations, typically a circularly polarized laser pulse is assumed. However, as we are dealing with a linearly polarized driver in our experiments, all equations in this chapter assume linear polarization. They can be translated to circularly polarized light by substituting $a^2/2$ with a^2.

The normalized axial electric field behind the driver is given by[1]

$$\frac{E_z}{E_0} = -\frac{1}{E_0}\frac{\partial \phi}{\partial z} = -\frac{e}{m_e c \omega_p}\frac{m_e c^2}{e}\frac{\partial \varphi}{\partial \zeta} = -\frac{c}{\omega_p}\frac{\partial \varphi}{\partial \zeta} = -\frac{1}{k_p}\frac{\partial \varphi}{\partial \zeta}. \tag{2.106}$$

In the ultra-relativistic limit $\gamma_p \gg 1$ we can expand both the innermost expression

$$\left(1 - \frac{1+a^2/2}{\gamma_p^2(1+\varphi)^2}\right)^{-\frac{1}{2}} \approx 1 + \frac{1+a^2/2}{(1+\varphi)^2}\frac{1}{2\gamma_p^2} \tag{2.107}$$

and

$$\beta_p = \sqrt{1-\gamma_p^{-2}} \approx 1 - \frac{1}{2\gamma_p^2} \tag{2.108}$$

to simplify Eq. (2.105), which directly leads to [79]

$$\frac{1}{k_p^2}\frac{\partial^2 \varphi}{\partial \zeta^2} = \pm\frac{n_b}{n_0} + \frac{1+a^2/2}{2(1+\varphi)^2} - \frac{1}{2}. \tag{2.109}$$

Eq. (2.105) and Eq. (2.109) imply that the plasma wavelength increases with a, i.e., $\lambda_{p,n} > \lambda_p$ [79], where $\lambda_{p,n}$ stands for the plasma wavelength in the nonlinear regime. This is due to the relativistic mass increase of the accelerated background plasma electrons which leads to a reduced plasma frequency according to Eq. (2.48).

In the case of a linearly polarized laser pulse of square axial profile with length L, the normalized axial electric field given in Eq. (2.106) is maximized when [56]

$$L \approx \lambda_{p,n}/2. \tag{2.110}$$

Assuming further the group velocity of the driver to approach the speed of light, Eq. (2.109) can be solved analytically. Under these conditions, the maximum normalized wakefield quantities under the constraint $E_z < E_B$ are then given by [89, 94]

$$\left.\frac{E_z}{E_0}\right|_{max} = \frac{a_0^2/2}{\sqrt{1+a_0^2/2}}, \tag{2.111}$$

$$\varphi_{max} = a_0^2/2. \tag{2.112}$$

[1] Mathematical expressions for the plasma fluid quantities can be found in [56].

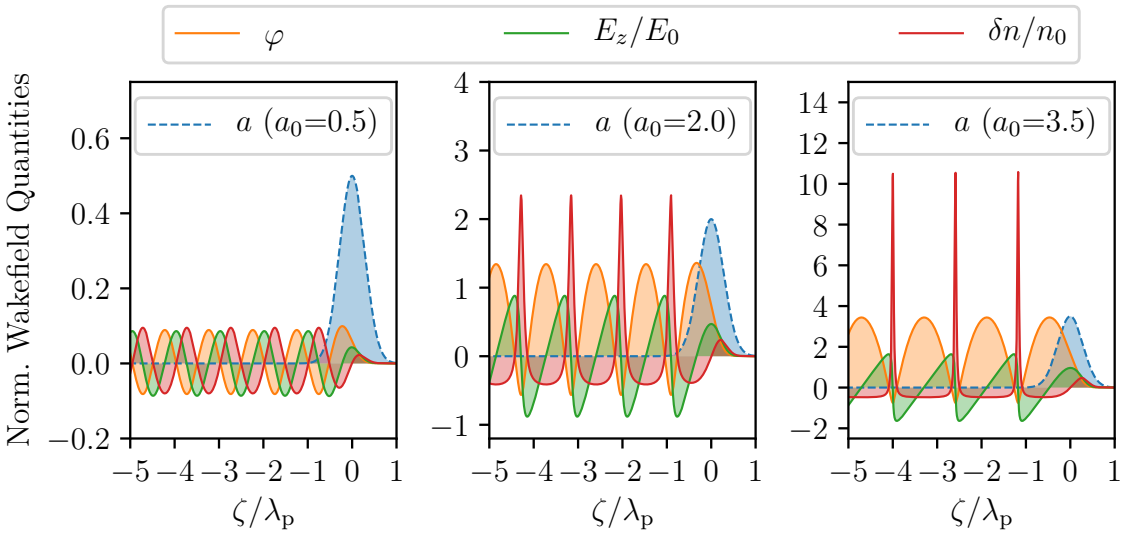

Figure 2.4.: *Normalized wakefield quantities derived from numerical solutions to the one-dimensional general wakefield equation Eq. (2.105) for different normalized vector potentials of the driving laser pulse. A possibly additional particle driver is neglected, i.e., $n_b = 0$. ζ_0 of the driving Gaussian laser pulse has been set to $0.4\lambda_p$, which corresponds to a FWHM (intensity) time duration of ~ 26 fs at typical plasma densities of $3.0 \times 10^{18} cm^{-3}$. Three different regimes are plotted: the linear regime with $a_0 \ll 1$ (left), the relativistic regime $a_0 > 1$ (middle) and highly relativistic regime with $a_0 \gg 1$ (right). Note the different scales on the vertical axes.*

In the linear limit, $|\varphi| \ll 1$, it is $(1+\varphi)^{-2} \approx 1 - 2\varphi$, which reverts to the one-dimensional form of the linear wakefield equation given in Eq. (2.95) [79].

The general wakefield equation Eq. (2.105) solved numerically for a Gaussian laser pulse as the sole driver (i.e., $n_b = 0$) with $a(\zeta) = a_0 \exp\left(-\zeta^2/\zeta_0^2\right)$ is plotted in Figure 2.4 for different a_0. ζ_0 stands for the length of the laser pulse.

The time duration of its FWHM intensity is given by $\sqrt{2\ln 2}\zeta_0/c$. The normalized electric field E_z/E_0 is obtained via Eq. (2.106) and the normalized charge density $\delta n/n_0$ is given by Eq. (2.103). Moreover, the electric field having a sinusoidal shape in the linear regime takes on a sawtooth-like profile in the relativistic regime with almost constant field gradients between its maxima. In contrast to the sinusoidal oscillation in the linear regime, the plasma wave expressed by the electron density adopts sharper spikes the greater a_0. The

above-mentioned elongation of the plasma wavelength λ_p is clearly visible and can be approximated by [56]

$$\lambda_{\mathrm{p,n}} = \lambda_\mathrm{p} \begin{cases} 1 + \frac{3}{16}\left(\frac{E_\mathrm{max}}{E_0}\right)^2, & \frac{E_\mathrm{max}}{E_0} \ll 1, \\ \frac{2}{\pi}\left(\frac{E_\mathrm{max}}{E_0} + \frac{E_0}{E_\mathrm{max}}\right), & \frac{E_\mathrm{max}}{E_0} \gg 1, \end{cases} \tag{2.113}$$

where E_max/E_0 is the normalized peak electric field strength of the plasma wave which is given by Eq. (2.111)

$$\frac{E_\mathrm{max}}{E_0} \approx \begin{cases} \frac{a_0^2}{2}, & a_0 \ll 1, \\ \frac{a_0}{\sqrt{2}}, & a_0 \gg 1, \end{cases} \tag{2.114}$$

for a linear polarized laser pulse with a square axial profile and optimal length according to Eq. (2.110). In this case, the nonlinear plasma wavelength $\lambda_{\mathrm{p,n}}$ then scales as

$$\lambda_{\mathrm{p,n}}(a_0) \approx \lambda_\mathrm{p} \begin{cases} 1 + \frac{3}{64}a_0^4, & a_0 \ll 1, \\ \frac{\sqrt{2}a_0}{\pi}, & a_0 \gg 1. \end{cases} \tag{2.115}$$

In the nonlinear regime $E_\mathrm{max}/E_0 \gg 1$, the optimal length L to resonantly drive a wakefield for a square laser pulse according to Eq. (2.110) is therefore given by [94]

$$L \stackrel{!}{=} \frac{\lambda_{\mathrm{p,n}}}{2} \approx \frac{a_0}{\sqrt{2}\pi}\lambda_\mathrm{p}. \tag{2.116}$$

For other axial profiles of the driving laser pulse, this optimal length changes and even becomes independent of a_0 in the case of a Gaussian laser pulse [56, 95].

Note that these scaling laws only hold true in the one-dimensional case. 3D PIC simulations not only suggest an additional dependence on the laser pulse's width and length but also disagree with this scaling law for $a_0 \gg 1$ [96]. Nevertheless, the dependence of $\lambda_{\mathrm{p,n}}$ on the normalized vector potential has strong implications on the appearance of the three-dimensional nonlinear plasma wave in LWFA experiments. Since the intensity of the laser pulse typically peaks on the axis and has a (super-)Gaussian radial profile, the plasma wavelength is maximum on the axis and decreases farther away from the axis. This dependence of $\lambda_{\mathrm{p,n}}$ on the radius causes the plasma wave to become curved like a horseshoe (cf. Figure 4.9(b)).

2.6.3. Wave Breaking

Naturally, the question arises about the maximum field E_z the plasma wave can sustain before wave breaking occurs. This happens when the velocity of the electrons forming the wake exceeds the phase velocity of the wake itself [59]. In the three-dimensional linear case, the electric field on axis follows a cosine-like shape $E_z = E_{\max}\cos(k_p(z-ct))$ according to Eq. (2.101). $E_{\max}$ can be estimated via Gauss's law Eq. (2.88) [56, 97]

$$\begin{aligned}\frac{\partial E_z}{\partial z} &= -\frac{e}{\varepsilon_0}\delta n = -E_{\max}k_{\mathrm{p}}\sin(k_p(z-ct)) \\ \Rightarrow E_{\max} &= \frac{\omega_{\mathrm{p}}m_{\mathrm{e}}c}{e}\left.\frac{\delta n}{n_0}\right|_{\max}.\end{aligned} \tag{2.117}$$

Assuming a maximum density perturbation $\delta n/n_0 = 1$ we obtain the so-called *cold non-relativistic wave breaking field*

$$E_0 = \frac{\omega_{\mathrm{p}}m_{\mathrm{e}}c}{e} = \sqrt{\frac{c^2 n_0 m_{\mathrm{e}}}{\varepsilon_0}} \approx 96\sqrt{n_0[10^{18}\,\mathrm{cm}^{-3}]}\,\mathrm{GV\,m^{-1}}, \tag{2.118}$$

which is exactly the factor we used to apply to normalize the electric field strength in wakefields (cf. section 2.6.2).

Based on Dawson [97], an illustrative picture of wave breaking can be derived. By Gauss's law and from the electric field E_z above follows directly the electron displacement from the equilibrium position $d(z)$ in one dimension

$$d(z) = d_{\max}\cos\left(k_{\mathrm{p}}(z-ct)\right), \tag{2.119}$$

with the maximum deflection $d_{\max} = E_{\max}\varepsilon_0/(n_{\mathrm{e}}e)$. If the electric field reaches the wave breaking limit $E_{\max} = E_0$, the maximum displacement becomes

$$d_{\max} = \frac{\omega_{\mathrm{p}}m_{\mathrm{e}}c\varepsilon_0}{e^2 n_{\mathrm{e}}} = \frac{c}{\omega_{\mathrm{p}}} = k_{\mathrm{p}}^{-1}. \tag{2.120}$$

Therefore, in the wave breaking limit, the displacement grows so large, that it becomes comparable to the plasma wavelength. The electrons' oscillation amplitude becomes larger

than k_p^{-1} and the wave breaks longitudinally. Hence, for $E_\mathrm{max} > E_0$, the linear description of wakefields breaks down [1][2].

Comparing these fields needed to achieve wave breaking with the ones derived in section 2.6.2, it becomes obvious that wave breaking cannot be achieved in the linear regime, where $a_0 \ll 1$ since according to Eq. (2.101), the fields are much smaller than the wave breaking limit

$$\left|\frac{E_{z,\mathrm{max}}}{E_0}\right| = \frac{\pi}{8} a_0^2 \ll 1. \tag{2.121}$$

The above estimation for the wave breaking field only holds true in the non-relativistic linear case. Using the one-dimensional nonlinear cold fluid equations, the maximum attainable field amplitude E_WB, the so-called *cold relativistic wave breaking field* can be derived [59, 98]

$$E_\mathrm{WB} = E_0 \sqrt{2(\gamma_\mathrm{p} - 1)}, \tag{2.122}$$

where $\gamma_\mathrm{p} = (1 - v_\mathrm{p}^2/c^2)^{-1/2}$ denotes the Lorentz factor of the phase velocity v_p of the plasma wave. Since the latter is approximately given by the group velocity of the laser pulse, it is (applying Eq. (2.43) and Eq. (2.47))

$$\gamma_\mathrm{p} \approx \sqrt{\frac{n_\mathrm{crit}}{n_\mathrm{e}}} = \frac{\omega}{\omega_\mathrm{p}} \gg 1 \tag{2.123}$$

and therefore

$$E_\mathrm{WB} \approx E_0 \sqrt{2\left(\frac{\omega}{\omega_\mathrm{p}} - 1\right)} \approx E_0 \sqrt{2\frac{\omega}{\omega_\mathrm{p}}}. \tag{2.124}$$

Including effects from the driving laser field, the cold relativistic wave breaking field changes to [93]

$$E_\mathrm{B} = E_0 \sqrt{2\sqrt{1 + a^2/2}(\gamma_\mathrm{p} - 1)}, \tag{2.125}$$

[1] This closely corresponds to the acceleration of particles in electromagnetic fields. Here, the classical description breaks down for $a = E/\tilde{E}_0 > 1$ with $\tilde{E}_0 = (m_\mathrm{e} c\omega)/e$. In the case of wakefields, the linear description breaks down for $E_z/E_0 > 1$ with $E_0 = (m_\mathrm{e} c\omega_\mathrm{p})/e$.

[2] See Table 2.2 for specific experimental values.

as we have seen in the discussion of Eq. (2.105). E_B converges to E_{WB} for negligible laser intensity $a \to 0$.

Compared to the non-relativistic case, the wave breaking field E_{WB} is much higher[1]. To reach this threshold in the relativistic regime, either the laser intensity is significantly increased or measures are taken to force wave breaking. Both methods are described in detail in subsection 2.6.6.

Technically, the above-mentioned limits only hold true in the case of low-temperature plasma waves. Thermal effects not only change this maximum attainable amplitude [56, 59, 99–101] but also make a concise definition of wave breaking problematic [102] since the electron distribution is now spread around its mean velocity. Expressions for the warm relativistic wave breaking limit in the case of relativistic drivers ($\gamma_p \sim 10 - 100$, typical for laser-driven plasma waves) can be found in [103] and in the case of ultra-relativistic drivers (typical for particle-driven plasma waves) in [101].

In the multidimensional case, the transverse plasma oscillations couple to the longitudinal ones which makes a general treatment of wave breaking in the three-dimensional relativistic regime much more complicated [104] and gives rise to additional effects like *transverse wave breaking* [105].

2.6.4. Blow-out and Bubble Regime

In the previous sections, we have investigated plasma wakefields in the 1D regime as well as in the 3D linear regime under the constraint of a non-evolving drive beam. These models can be treated analytically. Nevertheless, a fully relativistic analytic theory of wakefields in three dimensions does not exist and therefore a realistic description depends on numerical simulations. Here, the underlying partial differential equations that couple charged particles to the electromagnetic fields are usually solved in discrete time steps while the electromagnetic fields are evaluated on a computational grid. This kind of numerical treatment is called particle-in-cell (PIC) simulation and is further detailed in chapter 3. The vast number of necessary particles to initialize and the required resolutions in time and space to accurately model the plasma and light wave make a numerical treatment computationally extremely expensive (cf. Figure 2.5). This is why the 3D nonlinear regime was not studied until 1991 by Rosenzweig *et al.* [106] for PWFA and more than a decade later for LWFA by Pukhov & Meyer-ter-Vehn [31]. These so-called *blow-out* or *bubble* regimes are characterized by a complete expulsion of plasma electrons behind the driver triggered by its ponderomotive potential. A cavity void of electrons forms in the trail of

[1] See Table 2.2 in section 2.8

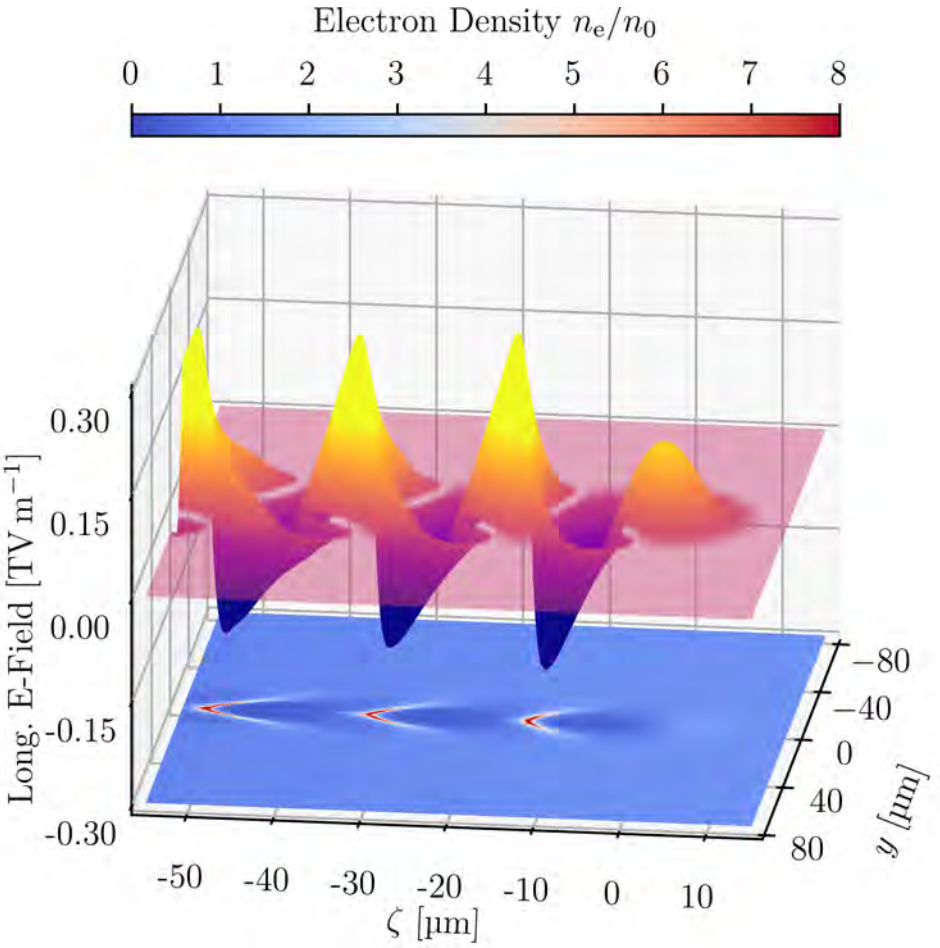

Figure 2.5.: *Three-dimensional rendering of a PIC simulation showing a wakefield with $a_0 = 2.6$ and $n_0 = 3.0 \times 10^{18} cm^{-3}$. The relative electron density n_e/n_0 is plotted as false color at the bottom, whereas the longitudinal electric field is portrayed by the three-dimensional surface plot. For greater clarity, the driving laser pulse with its peak intensity located at $\zeta = 0$ is not shown.*

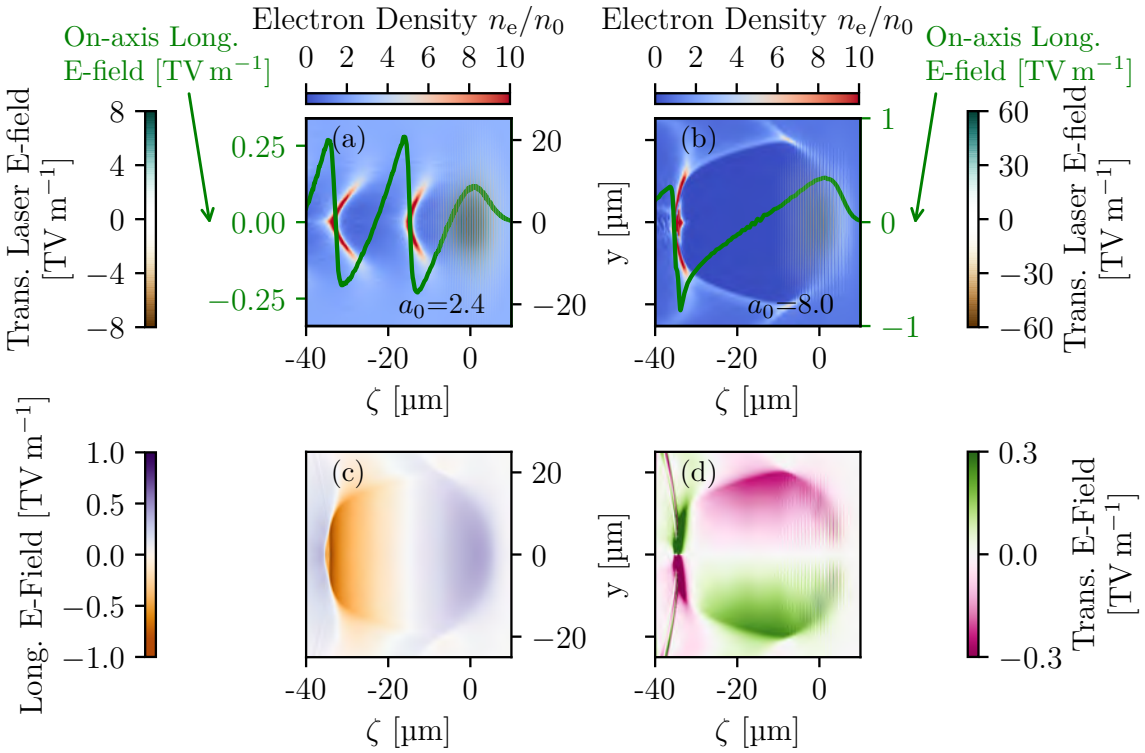

Figure 2.6.: *Two-dimensional plots of PIC simulations showing nonlinear wakefields and their properties. In (a) the electron density behind a relativistic laser driver is shown. The electric fields of the driver as well as the longitudinal accelerating field on the axis forming behind the driver (green line) are plotted. In comparison, (b) shows the fully broken blow-out regime with a highly relativistic driver ($P \approx 1000\,TW$). The accelerating and focusing fields inside this bubble are plotted in (c) and (d). The simulation from (b-d) is the same as in Figure 2.8.*

the driver surrounded by a thin sheath of expelled electrons (see Figure 2.6). The plasma electrons are pulled back as soon as the driver has passed and oscillate around their initial position with their plasma frequency forming the elongated wakefield structure behind the driver. Depending on the strength of the laser driver in the fully relativistic case, one distinguishes between the fully broken "bubble regime" ($a_0 \gtrsim 4$) and the partially broken "blow-out regime" ($2 \lesssim a_0 \lesssim 4$) [41]. In the latter, blow-out still occurs and the shape of the leading cavity slightly deviates from a sphere [41]. Nevertheless, in contrast to the bubble regime, the collective motion of the electrons forming the wake is still coherent enough to form a stable structure behind the driver. A train of plasma buckets follows the leading cavity (cf. Figure 2.7). In the fully broken bubble regime, however, the potential of the driver is large enough ($a_0 \gtrsim 4$) to induce nonlinearities that lead to electron trajectory crossings [31, 106]. The electron motion becomes nonlaminar which smears out and finally

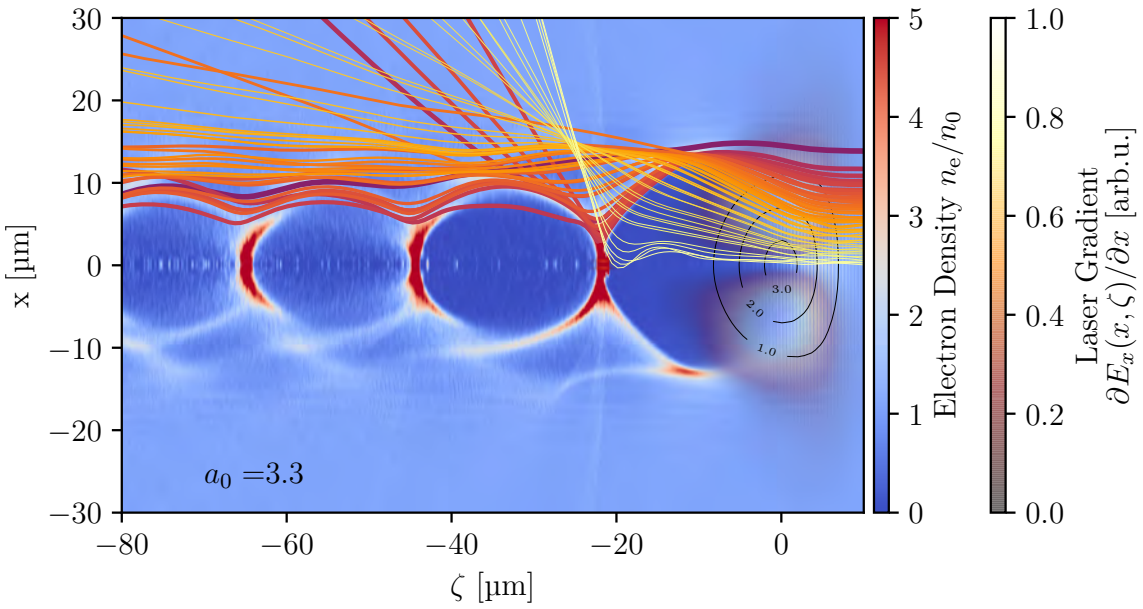

Figure 2.7.: *PIC simulation of a LWFA in the partially broken regime with $a_0 \approx 3.3$ and $n_0 = 3.0 \times 10^{18} cm^{-3}$. The contour lines of the laser's electric field as well as its directional derivative are also plotted. The wakefield behind the driver forms a chain of bubbles. Some electron trajectories color-coded by their initial radial distance from the laser propagation axis are plotted to illustrate how this structure is created. Their respective line thickness depicts the corresponding relative charge ("weight") of the macroparticle.*

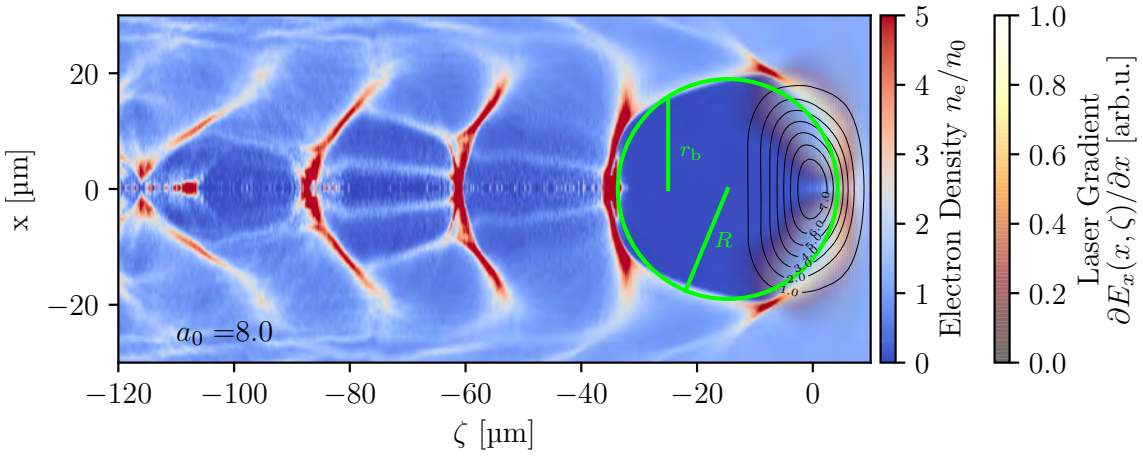

Figure 2.8.: *PIC simulation of a LWFA in the fully broken bubble regime with $a_0 \approx 8.0$ and $n_0 = 3.0 \times 10^{18} cm^{-3}$. The contour lines of the laser's electric field as well as its directional derivative are also plotted. The plasma density takes over a circular shape ("bubble") behind the laser driver with radius R. The transverse extent of this cavity is denoted by $r_b(\zeta)$. For better clarity, only the laser gradient is shown here.*

erases the typical wake structure behind the leading cavity [97, 107]. Effectively, behind the driver, a solitary blow-out region, the so-called "bubble", is formed (cf. Figure 2.8). Analogously, for PWFA the nonlinear regime occurs for $n_\mathrm{b}/n_0 > 1$, $k_\mathrm{b}\sigma_z < 1$ and $k_\mathrm{b}\sigma_r < 1$, where σ_z and σ_r denote the axial and radial (RMS) bunch lengths.

In both the blow-out and bubble regime, the shape of the bubble can be approximated by [108, 109]

$$r_\mathrm{b}\frac{\mathrm{d}^2 r_\mathrm{b}}{\mathrm{d}\xi^2} + 2\left(\frac{\mathrm{d}r_\mathrm{b}}{\mathrm{d}\xi}\right)^2 + 1 \approx \frac{4\lambda_\mathrm{c}(\xi)}{r_\mathrm{b}^2}, \tag{2.126}$$

where

$$\xi \coloneqq \zeta + \lambda_\mathrm{p,n}/2 \tag{2.127}$$

is defined such that the center of the bubble is approximately located at $\xi = 0$ (whereas $\zeta = 0$, as defined above, is the position of the laser's peak intensity in the co-moving frame). r_b depends on ξ and stands for the local transverse radius of the blow-out cavity. The bubble propagates in the co-moving frame in ξ direction. Accelerated charges inside the bubble act on the electrons forming the sheath by their Coulomb potential. Hence, a loaded cavity has a different shape. This effect is taken into account by the right-hand side of this equation. λ_c, given in normalized units, denotes the charge per unit length of the load, i.e. the electron beam [42].

In the case of an unloaded wake (meaning no accelerated electron beam inside the bubble or no particle driver) Eq. (2.126) then simplifies to

$$r_\mathrm{b}\frac{\mathrm{d}^2 r_\mathrm{b}}{\mathrm{d}\xi^2} + 2\left(\frac{\mathrm{d}r_\mathrm{b}}{\mathrm{d}\xi}\right)^2 + 1 \approx 0. \tag{2.128}$$

Considering the equation for a circle (with radius 1 and ξ,$r_\mathrm{b}(\xi)$ being the x,y components), which can be rewritten as

$$0 = r_\mathrm{b}^2 + \xi^2 - 1 = r_\mathrm{b}\frac{\mathrm{d}^2 r_\mathrm{b}}{\mathrm{d}\xi^2} + \left(\frac{\mathrm{d}r_\mathrm{b}}{\mathrm{d}\xi}\right)^2 + 1, \tag{2.129}$$

we recognize Eq. (2.128) as a circle plus an additional $(\mathrm{d}r_\mathrm{b}/\mathrm{d}\xi)^2$ term which leads to a stronger bending of the radius at the rear part of the bubble than compared to a circle.

In the unloaded case, the radius of the blowout cavity R which is the maximum bubble radius is approximately given by the matched spot size of the driving laser pulse. It depends

on the plasma wavelength and the normalized laser vector potential (which changes during propagation through the plasma, cf. Figure 2.3). With Eq. (2.66) we may estimate [41][1]

$$R \approx w_{\mathrm{match}} \approx 2\sqrt{a_0}/k_\mathrm{p} = \lambda_\mathrm{p}\sqrt{a_0}/\pi. \tag{2.130}$$

The longitudinal on-axis accelerating fields inside the bubble are given by [109]

$$E_z(\xi) = -\frac{en_\mathrm{e}}{2\varepsilon_0} r_\mathrm{b} \frac{\mathrm{d}r_\mathrm{b}}{\mathrm{d}\xi}. \tag{2.131}$$

As $\left|\mathrm{d}r_\mathrm{b}/\mathrm{d}\xi\right|$ increases rapidly at the very end of the cavity, the accelerating field E_z shows a sharp spike there, whereas in the middle of the bubble, where $r_\mathrm{b} \approx R$ and $\left|\mathrm{d}r_\mathrm{b}/\mathrm{d}\xi\right| \ll 1$, the field is almost linear (see Figure 2.6(c)) and may be approximated by [56, 110]

$$\frac{E_z}{E_0} \approx \frac{en_\mathrm{e}}{2\varepsilon_0 E_0}\xi = k_\mathrm{p}\frac{\xi}{2}, \tag{2.132}$$

since with Eq. (2.128) follows

$$\frac{\mathrm{d}E_z}{\mathrm{d}\xi} = -\frac{en_\mathrm{e}}{2\varepsilon_0}\left[\left(\frac{\mathrm{d}r_\mathrm{b}}{\mathrm{d}\xi}\right)^2 + r_\mathrm{b}\left(\frac{\mathrm{d}^2 r_\mathrm{b}}{\mathrm{d}\xi^2}\right)\right] = \frac{en_\mathrm{e}}{2\varepsilon_0}\left[1 + \left(\frac{\mathrm{d}r_\mathrm{b}}{\mathrm{d}\xi}\right)^2\right] \approx \frac{en_\mathrm{e}}{2\varepsilon_0}. \tag{2.133}$$

This approximation for the on-axis accelerating field can be extrapolated and reaches its maximum at $\xi = R$. Therefore, with Eq. (2.130) [56]

$$E_{z,\mathrm{max}} = E_0\frac{k_\mathrm{p}R}{2} = E_0\sqrt{a_0}. \tag{2.134}$$

The radial electric field as well as the magnetic field can be derived accordingly [108, 111]

$$\frac{E_r}{E_0} \approx k_\mathrm{p}\frac{r}{4}, \tag{2.135}$$

$$\frac{B_\theta}{E_0} \approx k_\mathrm{p}\frac{r}{4}. \tag{2.136}$$

Note that in this regime, the region where both the longitudinal fields are accelerating and the radial fields are focusing extends over half the bubble radius. Hence, the phase

[1] Note that the expression for the nonlinear plasma wavelength in three dimensions given here differs from the one-dimensional expression by a factor of $\sqrt{a_0/2}$ since in the latter theory it is $2R \approx \lambda_{\mathrm{p,n}} = \lambda_\mathrm{p} a_0\sqrt{2}/\pi$ according to Eq. (2.115).

favorable for particle acceleration ($E_z(\xi) < 0$, $E_r(\xi) > 0$) extends over π as opposed to linear wakefields (cf. section 2.6.2).

According to Eq. (2.135) and Eq. (2.136), the electromagnetic fields inside the cavity are linear and aligned radially. Thus, the transverse field components effectively focus the accelerated particles (see Figure 2.6(d)). Since the forces are linear, the normalized emittance of an accelerated electron bunch remains unchanged which makes this regime ideal for LWFA [56].

Many experiments, however, operate in an intermediary regime between linear perturbation and bubble regime, which currently lacks a consistent theory. In this case, we are obliged to completely rely on PIC simulations. The majority of electron data presented in this thesis stem from LWFAs driven in the transition range between blowout and bubble regime. Taking self-focusing into account, the normalized vector potential a_0 of the driving laser pulse delivered by the ATLAS-300 system stays between ~ 2 and ~ 7 when propagating through the plasma according to PIC simulations (e.g., Figure 2.3(b)). Details on such PIC simulations that enable the study of this intermediary regime are given in chapter 3.

As discussed above, the wakefield structure examined in this chapter and its inherent accelerating fields can be utilized to accelerate electrons. To do so, the charged particles must be *injected into* this accelerating structure and extracted again before deceleration due to dephasing happens. The following sections are dedicated to these processes.

2.6.5. Trapping and Acceleration

Trapping of injected particles naively occurs when the plasma electrons' velocities eventually match or surpass the phase velocity of the plasma wave. The latter is given by the group velocity of the driving laser pulse (for non-evolving wake drivers). Hence, the energy injected electrons need to reach to be trapped can be estimated by requiring $\gamma > \gamma_{\text{thres}} :\approx \gamma_{\text{p}}$. According to Eq. (2.123), this threshold may be calculated as

$$\gamma_{\text{thres}} \approx \sqrt{\frac{n_{\text{crit}}}{n_{\text{e}}}} = \frac{\omega}{\omega_{\text{p}}}. \tag{2.137}$$

In the following, we will examine the phase space of plasma electrons exposed to an external driving potential. From that, we gain a more profound insight into the trapping and acceleration dynamics. Furthermore, a brief outline of how to derive a thorough mathematical expression for γ_{thres} will be given.

As soon as the electrons are trapped within the potential of the wakefield, they are accelerated by the longitudinal electric fields of this structure. The electron dynamics can be illustrated by examining their trajectories in phase space. To do so, we consider the corresponding Hamiltonian in the one-dimensional theory in the co-moving frame, average over the fast laser oscillations, use the normalized quantities introduced in section 2.6 and assume the initial transverse momentum of the electron to be small ($p_\perp \ll 1$) [112]

$$h(\zeta, p_\parallel) = \sqrt{1 + p_\parallel^2 + a(\zeta)^2/2} - (\varphi(\zeta) + \beta_\mathrm{p} p_\parallel) = h_0, \tag{2.138}$$

where $p_\parallel$ is the longitudinal momentum of the electron normalized by $m_\mathrm{e}c$. h as the sum of potential (terms inside the bracket) and kinetic energy (square root) in the co-moving frame does not explicitly depend on time and therefore, energy is conserved. Hence, the trajectory is specified by its initial energy h_0. Eq. (2.138) describes closed (which we call *trapped*) and open (*untrapped*) orbits in phase space determined by h_0 and can be solved analytically [93]

$$p_\parallel = \beta_\mathrm{p}\gamma_\mathrm{p}^2(h_0 + \varphi) \pm \gamma_\mathrm{p}\sqrt{\gamma_\mathrm{p}^2(h_0 + \varphi)^2 - 1 - a^2/2}. \tag{2.139}$$

A color-coded graphical depiction of the Hamiltonian is plotted in Figure 2.9 for the longitudinal phase space. Some contour lines representing individual particle trajectories of equal energies are highlighted (bold lines) and differentiated by their initial energy (color-coded). The directional movement on these trajectories is indicated by arrows. Trajectories with lower initial energy form closed orbits (d). Electrons following these trajectories in the direction of the arrows are trapped in the wake's potential and periodically gain and lose kinetic energy. The separatrix (a) with initial energy h_s separates these orbits from open (untrapped) trajectories. If the initial energy of the electron is too high or low, it simply overtakes the wake (b) or moves backward in the co-moving frame (f) following the wave's motion. These electrons and their periodic oscillation form the plasma wave itself (cf. Figure 2.7). As the first bucket of the wake is influenced by the laser potential, the separatrix is modified and gives rise to so-called runaway electrons (c) with energies below h_s. They gain enough kinetic energy to finally overtake the driving laser field. These runaway electrons are separated by the runaway separatrix (e) from the electrons which are trapped in the first bucket or reflected by the driver's potential [54].

The separatrix h_s is characterized as the solution to Eq. (2.138) with maximum initial energy for closed orbits. In this special case, the closed trajectories intersect at one singular

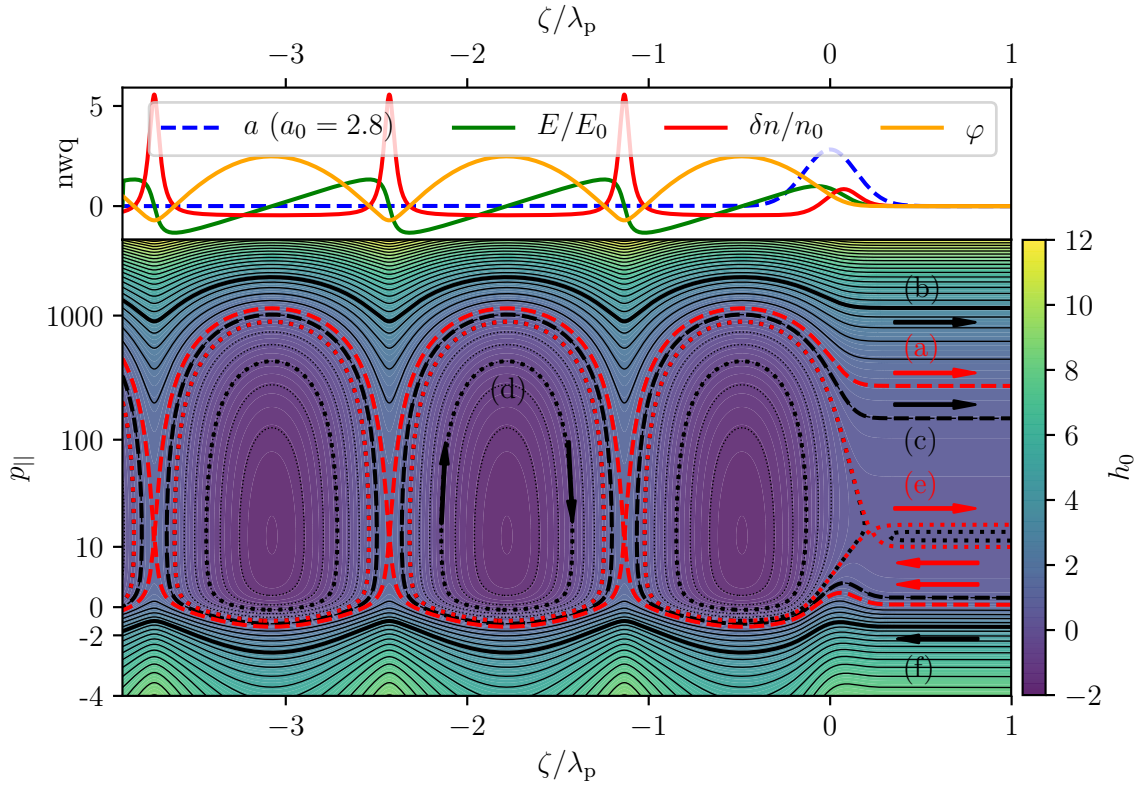

Figure 2.9.: *Longitudinal phase space of the wakefield structure. The upper part of the plot shows the normalized wakefield quantities (nwq.) similar to Figure 2.4 with $a_0 = 2$ and $\zeta_{FWHM} \approx 0.33\lambda_p$. The lower part shows the color-coded Hamiltonian with $\gamma_p \approx 13.2$ depending on the normalized position in the co-moving frame and the longitudinal momentum $p_{||}$. Exemplary trajectories (bold) in this phase space with different initial energies are highlighted in red and black. The highlighted orbits are either closed (d) or opened (b). The trajectory separating these phase space areas is the so-called separatrix (red dashed line labeled (a)). Red lines separate regions with different particle behavior. Solid lines represent trajectories outside the separatrix, dashed lines mark trajectories between the separatrix and runaway separatrix (e). Dotted lines stand for closed orbits resp. reflected particles. Details and characteristics of exemplary orbits or trajectories are given in the main text.*

point ζ_i. Therefore, for this special orbit, the square root in Eq. (2.139) has to vanish and a condition for h_s can be derived with $\varphi_\mathrm{min} := \varphi(\zeta_\mathrm{i})$

$$\gamma_\mathrm{p}^2(h_\mathrm{s}+\varphi_\mathrm{min})^2 - 1 - a^2/2 \stackrel{!}{=} 0 \Rightarrow h_\mathrm{s} = \frac{\sqrt{1+a^2/2}}{\gamma_\mathrm{p}} - \varphi_\mathrm{min}. \tag{2.140}$$

With this expression, $p_\parallel$ can be minimized under the condition $h = h_\mathrm{s}$ to find the minimum momentum $p_{\parallel,\mathrm{min}}$ required to trap electrons [93]. This trapping threshold depends on the potential φ respectively on the corresponding longitudinal fields E/E_0. For a field strength E corresponding to the generalized cold relativistic wave breaking field (including laser effects) (cf. section 2.6.2) $E/E_0 = E_\mathrm{B}/E_0 = \sqrt{2\sqrt{1+a^2/2}(\gamma_\mathrm{p}-1)}$, the threshold becomes $p_{\parallel,\mathrm{min}} = \gamma_\mathrm{p}$ [93, 113], which confirms our naive picture above leading to Eq. (2.137).

From Figure 2.9 it also becomes clear, that of all possible trajectories, trapped particles gain the highest kinetic energy, until they reach the decelerating phase of the wake where their kinetic energy gets lost again. For a LWFA to work most efficiently, the acceleration process of trapped electrons therefore needs to be terminated when the particles reach $\zeta \approx -\lambda_\mathrm{p,n}/2$.

In the following sections, several mechanisms to inject electrons into the accelerating phase of the wakefield structure are discussed.

2.6.6. Injection Mechanisms

In order to accelerate charged particles in a plasma wakefield, they must be brought into the accelerating phase of the wakefield (i.e. $-\lambda_\mathrm{p,n}/2 < \xi < 0$, since here $E_z < 0$ according to Eq. (2.132), respectively $-\lambda_\mathrm{p,n} < \zeta < -\lambda_\mathrm{p,n}/2$, cf. Eq. (2.127)), where they follow the trajectories described in the previous section. This can be achieved either passively by driving the wake into the highly relativistic regime, where wave breaking occurs, or by controlled injection. The first technique is known as *self-injection mechanism* and happens more or less automatically as soon as the driver is strong enough owing to the laser pulse evolution in plasma (cf. subsection 2.5.2). The latter, however, has experienced growing attention in the last two decades. These advanced techniques generally aim at a localized injection. Here all injected particles are accelerated over the same distance which ideally leads to a smaller final energetic bandwidth (cf. chapter 5).

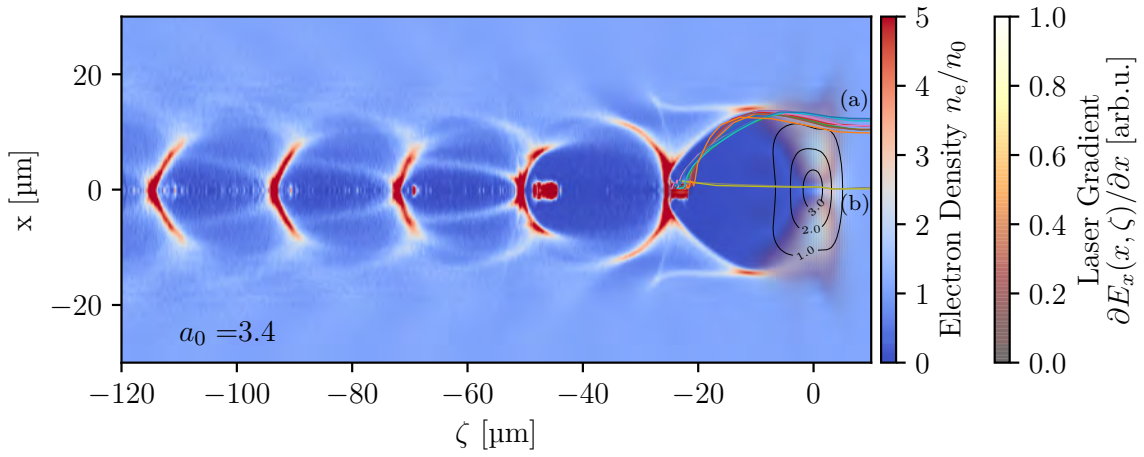

Figure 2.10.: *Depiction of longitudinal and transverse self-injection. Transverse self-injection (a): Electrons located approximately one laser waist away from the axis circumvent the laser pulse and travel to the back of the bubble, where they are injected. Longitudinal injection (b): Electrons close the laser propagation axis pass through the laser pulse and the bubble. When entering the latter half of the wakefield, they are accelerated and gain energy. If their energy exceeds the injection threshold, they are eventually injected.*

Self-injection

If the driver is highly relativistic ($a_0 \gg 1$ for laser drivers or $n_b/n_0 \gg 1$ for particle drivers) plasma waves exceeding the wave breaking limit can be driven. As shown in subsection 2.6.3 the velocity of the electrons constituting the sharp density spike now exceeds the phase velocity of the wake itself. The electrons which are fast enough to overcome this threshold can slip into the accelerating phase of the preceding wakefield period. As highlighted in Figure 2.10, this either happens longitudinally, where the trajectory of an injected electron only has a negligible radial distance from the laser axis (Figure 2.10(b)), or transversely, where the electrons are pushed away by the ponderomotive force of the laser pulse. The remaining ion background pulls these electrons back to the propagation axis where they reach the back of the bubble (Figure 2.10(a)) [114]. Since the laser driver evolves when propagating through an underdense plasma and self-focuses, for a laser driver of sufficient power (cf. Eq. (2.62)), self-injection naturally takes place as shown in the following.

A thorough analysis conducted in [115] and [116] leads to an analytical expression for self-injection to occur in the bubble regime, when

$$k_\mathrm{p} R > 2\sqrt{\ln\left(\frac{2n_\mathrm{crit}}{3n_\mathrm{e}}\right) - 1}. \tag{2.141}$$

With Eq. (2.130) this condition for self-injection becomes

$$a_0 > a_{0,\mathrm{si}} := \ln\left(\frac{2n_\mathrm{crit}}{3n_\mathrm{e}}\right) - 1, \tag{2.142}$$

which is routinely fulfilled in experimental conditions when taking the evolution of the normalized vector potential into account during propagation through a plasma, since typical LWFA parameters ($n_\mathrm{e} = 3\times10^{18}\,\mathrm{cm}^{-3}$, $\lambda = 800\,\mathrm{nm} \rightarrow n_\mathrm{crit} \approx 1.7\times10^{21}\,\mathrm{cm}^{-3}$) lead to $a_{0,\mathrm{si}} \approx 5$ [116]. Self-injection due to wave breaking in the relativistic regime, therefore, is an inherent feature of LWFA. Note that by adjusting the plasma density n_e in the experiment, self-injection can be deliberately turned on or off.

As such, no sophisticated target design is necessary to accelerate electrons via self-injection, as opposed to the injection mechanisms presented below that require complex target designs. The drawback of this rather primitive scheme is its strong dependence on the driving laser pulse and its persistent injection into the back of the bubble over a wide propagation distance in the plasma. Due to this continuous process, early injected particles are accelerated over a longer distance than compared to later ones. Therefore, a large energetic bandwidth of the accelerated particles is inherent to this injection scheme. Moreover, due to the highly nonlinear process of wave breaking even small variations in the driver cause significant changes to the acceleration parameters which makes this injection mechanism very unstable. Improved injection schemes aim at decoupling the injection from the laser pulse evolution. These externally controlled mechanisms not only lead to a much higher shot-to-shot stability but may also restrict injection to a very localized point in space and time, which ultimately leads to a small energetic spread of the accelerated particles.

Controlled Injection

Over the last two decades, many different controlled injection schemes have been invented and studied to meet the aim of high charge quasi-monoenergetic electron bunches with decent shot-to-shot stability (e.g., ponderomotive injection [117], density down ramp injection [118], self-truncated ionization injection [46]). Subtle adjustments and fine-

tuning of the parameter range offered by these controlled injection mechanisms allow for tailored quasi-monoenergetic electron bunches. Three of these injection schemes will be described in further detail since they were either employed in the experiments presented in this work or serve as benchmarks concerning stability, charge, and energetic bandwidth.

Ionization Injection The basic principle of this method is the excitation of a wakefield in a plasma created from a mixture of gases of high and low atomic numbers. By that, electron energy levels with very different binding potentials are provided which are ionized by different laser intensities. To avoid ionization defocusing (cf. section 2.5.2) the concentration of the high Z gas component needs to be kept below some percent. As low atomic number gas, typically hydrogen or helium are used, whereas the high Z component is mostly made up of oxygen or nitrogen. In this case, the leading edge of the ultrashort laser pulses fully ionizes the low Z gas and only strips the nitrogen/oxygen from its outer electrons. These are the electrons that create the accelerating structure of the wakefield. They constitute the plasma wave and do not gain any significant momentum by the ponderomotive force. The remaining inner electrons are tunnel ionized (cf. section 2.5) by the peak intensity of the driver [119]. These electrons are "born" inside the potential well of the first wakefield period. Being at rest initially, they slip back into the accelerating phase of the wake where they gain kinetic energy. If these newborn electrons reach the phase velocity of the plasma wave $\gamma_\mathrm{p} = \gamma_\mathrm{thres}$ before they are overtaken by the wake, they are trapped [120]. This injection mechanism is continuous if a homogeneous mixture of light and heavy gas atoms is used. It therefore suffers the same drawbacks as self-injection [57].

Shock Front Injection The shock front injection technique nowadays arguably carries the greatest potential for stable, high charge monochromatic LWFAs. Here, a supersonic gas flow emitted by a de Laval nozzle is perturbed by a sharp object, typically a razor blade. This creates a sharp density down ramp (cf. subsection 4.2.1). The sudden drop in plasma density leads to a prompt increase of the bubble radius $R \propto \sqrt{a_0/n_\mathrm{e}}$ according to Eq. (2.130). This elongation of the accelerating structure leads to the injection of electrons into the accelerating phase of the wakefield [48, 121]. Figure 2.11 shows three snapshots of the electron density depicting the evolution of the first bucket when passing through the sharp density down ramp. Fine-tuning the plasma density such that no self-injection occurs before and after the shock front (e.g., via Eq. (2.142)), the injection is locally well-confined. Depending on this temporal and local confinement, all the injected electrons ideally now experience the same accelerating force for the same acceleration distance and therefore their stability and energy spread are greatly improved. Simulations like the one shown in Figure 2.12 suggest that the vast majority ($\sim 99\,\%$) of shock-injected electrons stem from

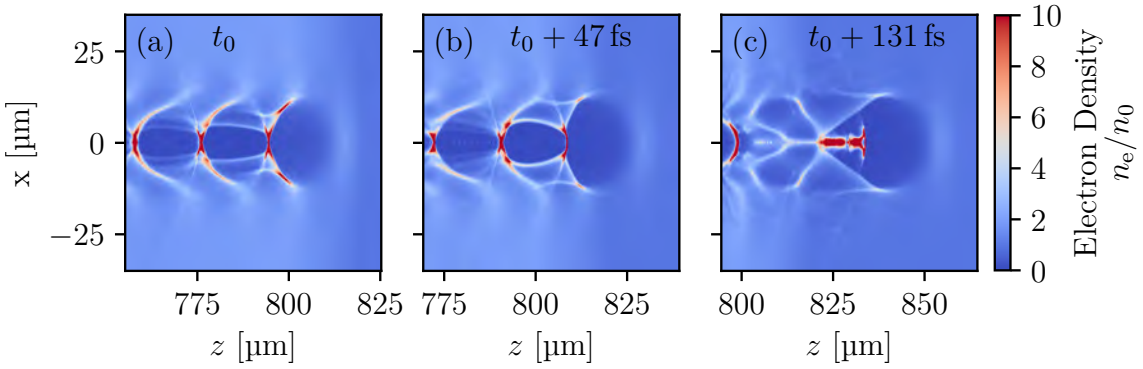

Figure 2.11.: *Evolution of a laser-driven wakefield during propagation through a sharp density down ramp with $a_0 \approx 3.7$. Due to the higher plasma density in (a), the bubble expands when passing through a sharp density down ramp, here located at $\sim 800\,\mu m - 819\,\mu m$ (b). Within $19\,\mu m$ the plasma density drops from $6.0 \times 10^{18} cm^{-3}$ to $3.0 \times 10^{18} cm^{-3}$. The hereby associated elongation of the plasma wavelength leads to the injection of electrons into the accelerating phase of the wakefield (c).*

hydrogen atoms longitudinally located less than $\lambda_p/2$ away from the density down ramp with a radial distance to the laser propagation axis of $0.3\,\lambda_p$ to $0.6\,\lambda_p$[1]. The shock injection technique therefore clearly favors transverse injection (cf. Figure 2.10). Modifications to the shock front parameters such as the backing pressure, shock front angle, or blade position give further access to crucial bunch properties like energy spread, pointing [122] and peak energy.

The first experimental demonstration of shock front injection was performed by Schmid *et al.* [123] a decade ago. From then on, shock-front-driven LWFAs have shown their great potential in delivering unprecedented total electron bunch charges and charge densities at superior shot-to-shot stability, as will be presented in later parts of this work (cf. chapter 5) [38].

Colliding Pulse Injection Another method to control injection requires a second laser pulse counterpropagating and colliding with the main pulse. Depending on the exact conditions, the interference of both pulses creates a beat wave pattern [124]. This beat wave gives background electrons a momentum kick by heating them. This pre-acceleration facilitates their injection [125–128]. In the highly nonlinear regime, so-called optical

[1] When simulating shock-injected LWFA we take advantage of this well-confined region. The macroparticle sampling rate is adjusted for different plasma regions according to their relevance for simulating the injected charge. With this adaptive mechanism, the PIC code runs one to two orders of magnitude faster without losing accuracy for the simulated charge. Details on the implementation of this adaptive sampling rate are given in the appendix in section B.1

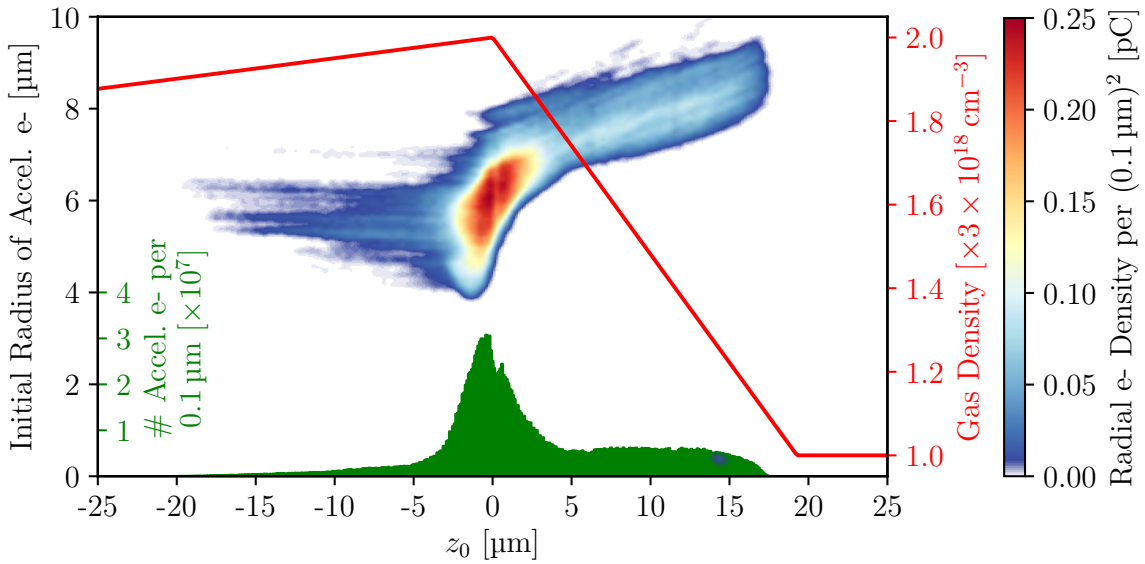

Figure 2.12.: *Initial position of shock-injected and accelerated electrons. By tracking the accelerated electrons their initial spatial coordinates can be retraced. Together with their radial density, the heat map visualizes this information. The plasma density is plotted in red and the number of accelerated electrons per 0.1 µm in green. Plasma around the gas density shock contributes more than 99 % of all the electrons to the acceleration process. To be injected and accelerated, the particles have to be located less than roughly half a plasma wavelength away from the axis. For this specific simulation, the peak gas density corresponds to a plasma wavelength of* $\sim 13.6\,\mu m$. *At the density plateau it is* $\lambda_p \approx 19.3\,\mu m$. *The laser power is initialized with 50 TW and the peak vacuum vector potential at the beginning of the shock front is set to* $a_0 \approx 2.3$.

transverse injection dominates the injection process [129]. Although this specific mechanism has not been investigated experimentally yet, PIC simulations suggest that in this regime the bubble size decreases during the pulse collision by reducing the efficiency of the ponderomotive force. After the pulse collision, the bubble recovers its original shape by expanding to its previous size. Hence, this mechanism closely resembles shock front injection in its underlying physics.

Both shock front injection and colliding pulse injection share the capability of producing ultrashort quasi-monoenergetic electron bunches. The energy of these particle bunches furthermore can be tuned by adjusting the total acceleration length, e.g., by manipulating the position of the shock front or by shifting the collision point. Limits to the acceleration mechanism and corresponding scaling laws will be the subject of the following section.

2.6.7. Acceleration Limits and Scalings

The particles' energy gain in a LPA is limited by the amount of energy the driver can transfer to the plasma in its wake. The energy flow to excite the wake eventually drains the driving potential. Moreover, in the case of LWFAs, the electrons finally leave the phase favorable for acceleration (cf. subsection 2.6.5). These constraints fundamentally limit the energy gain of plasma accelerators.

Dephasing Length

As the group velocity of the laser pulse is reduced in plasmas according to Eq. (2.43) the trapped and accelerated electrons slip forward in the wakefield. When the electrons pass $\xi \approx \lambda_{\mathrm{p,n}}/2$ (cf. Eq. (2.115)), they enter the decelerating phase of the wake since the longitudinal electric field now changes its sign. The slope of the phase space trajectory becomes negative and the electrons lose kinetic energy (cf. Figure 2.9). The total distance in the laboratory frame the electrons have traveled until they reach the decelerating phase is called *dephasing length* L_{d}. To maximize the kinetic energy, this is the point in LWFA where the plasma should end to stop the acceleration process. An expression for L_{d} can be derived in the one-dimensional theory by exploiting the condition

$$L_{\mathrm{d}}\left(1-\frac{v_{\mathrm{gr}}}{c}\right)=\frac{\lambda_{\mathrm{p,n}}}{2}. \tag{2.143}$$

With Eq. (2.43) and Eq. (2.45) this becomes

$$L_{\mathrm{d}}=\frac{1}{2(1-\eta)}\lambda_{\mathrm{p,n}}\approx\frac{\omega^2}{\omega_{\mathrm{p}}^2}\lambda_{\mathrm{p,n}}. \tag{2.144}$$

Substituting the nonlinear plasma wavelength according to Eq. (2.115), we get [130]

$$L_{\mathrm{d}}\approx\frac{\omega^2}{\omega_{\mathrm{p}}^2}\lambda_{\mathrm{p}}\begin{cases}1, & a_0\ll 1,\\ \frac{\sqrt{2}a_0}{\pi}, & a_0\gg 1.\end{cases} \tag{2.145}$$

Note that this dephasing limit is one of the major limitations for energy gain in LWFA and can hardly be circumvented. Methods to overcome dephasing involve creating a plasma density up ramp after the injection such $\lambda_{\mathrm{p,n}}$ becomes smaller the longer the acceleration distance, imprinting advantageous space-time correlations on the laser pulse ("flying focus" [131, 132]) or staging the accelerator [130]. Yet, some of these concepts are very ambitious and their experimental implementation is still under research [133, 134]. Of

course, replacing the driver with a particle beam (PWFA) that is not subject to the reduced group velocity also overcomes the dephasing limit, but suffers other problems (e.g., limited transformer ratio [135], etc.).

Pump Depletion and Etching

The excitation of a plasma wave constantly transfers energy from the driver to the wake. The acceleration process ceases when a significant fraction of the driving potential is consumed. For LWFAs, the corresponding acceleration length – the so-called *pump depletion length* L_{pd} – can be calculated by equating the laser pulse energy to the energy left behind in the wake. In one dimension and for a flattop laser pulse of optimal length, this leads to [95, 130]

$$L_{\mathrm{pd}} = \frac{\omega^2}{\omega_{\mathrm{p}}^2}\lambda_{\mathrm{p}} \begin{cases} \frac{2}{a_0^2}, & a_0 \ll 1, \\ \frac{\sqrt{2}a_0}{\pi}, & a_0 \gg 1. \end{cases} \tag{2.146}$$

Assuming a laser pulse of Gaussian shape, the depletion length can be approximated by [95]

$$L_{\mathrm{pd}} = \frac{\omega^2}{\omega_{\mathrm{p}}^2}\lambda_{\mathrm{p}} \begin{cases} \frac{2.8}{\pi a_0^2}, & a_0 \ll 1, \\ \frac{4.4}{\pi}, & a_0 \gg 1. \end{cases} \tag{2.147}$$

Note that the pump depletion length in the highly relativistic regime is independent of a_0 for a Gaussian laser pulse as opposed to the flattop case. This is due to the fact, that the optimal length to resonantly drive the wakefield scales as $\sim a_0$ in the latter case, whereas for a Gaussian laser pulse the optimal length is independent of a_0 (see section 2.6.2) [95].

In the linear regime $a_0 \ll 1$ the electron energy gain is limited by the dephasing length ($L_{\mathrm{d}} < L_{\mathrm{pd}}$), whereas in the nonlinear regime ($a_0 \gg 1$) $L_{\mathrm{pd}} \lesssim L_{\mathrm{d}}$. Therefore, when tapering the density profile to avoid electron dephasing in the relativistic regime, one has to take pump depletion into account. Again, staging the acceleration process circumvents both limits by replacing the drained driver with a new one in addition to readjusting the phase relation of the laser pulse to the particle bunch [136]. However, the experimental implementation of this technique is still under research and remains extremely challenging [134].

As the very front of the laser pulse interacts with the highest electron density, this part of the driver is exposed to the highest energy loss and by that slowly erodes. An expression for

this so-called etching velocity is given in [137], $v_{\text{etch}} \approx c\omega_p^2/\omega^2$, which can be translated to a depletion length in three dimensions $L_{\text{pd,3D}}$ as follows. The time it takes to 'etch away' a pulse of length $c\tau_{\text{FWHM}}$ is denoted by $t_{\text{pd,3D}}$. Up to this point, the laser has traveled the distance $L_{\text{pd,3D}} = ct_{\text{pd,3D}}$. Therefore, this depletion length in three dimensions is given by [41]

$$L_{\text{pd,3D}} = ct_{\text{pd,3D}} = c\frac{c\tau_{\text{FWHM}}}{v_{\text{etch}}} = \frac{\omega^2}{\omega_p^2} c\tau_{\text{FWHM}}. \tag{2.148}$$

The etching velocity in turn reduces the group velocity of the driving laser pulse, such that the electrons enter dephasing earlier [41]. The dephasing length in three dimensions $L_{\text{d,3D}}$ is therefore given by [41]

$$\begin{aligned} L_{\text{d,3D}}\left(1 - \frac{v_{\text{gr}}}{c} + \frac{v_{\text{etch}}}{c}\right) &= L_{\text{d,3D}}\frac{3\omega_p^2}{2\omega^2} = \frac{\lambda_{\text{p,n}}}{2} \\ \Rightarrow L_{\text{d,3D}} = \frac{\omega^2}{3\omega_p^2}\lambda_{\text{p,n}} \approx \frac{\omega^2}{3\omega_p^2} 2R &\approx \frac{2\omega^2}{3\omega_p^2}\frac{2\sqrt{a_0}}{k_p} = \frac{\omega^2}{\omega_p^2}\lambda_p\frac{2\sqrt{a_0}}{3\pi}, \end{aligned} \tag{2.149}$$

where we have applied Eq. (2.130) and expanded the refractive index η given in Eq. (2.45) for $\omega_p^2/\omega^2 \ll 1$ according to

$$\frac{v_{\text{gr}}}{c} - \frac{v_{\text{etch}}}{c} = \eta - \frac{\omega_p^2}{\omega^2} = \sqrt{1 - \frac{\omega_p^2}{\omega^2}} - \frac{\omega_p^2}{\omega^2} \approx 1 - \frac{3\omega_p^2}{2\omega^2}. \tag{2.150}$$

In practical units, this length can be calculated by

$$L_{\text{d,3D}}[\text{mm}] \approx 21 \times \lambda\,[0.8\,\mu\text{m}]^{-\frac{5}{3}} n_e[10^{18}\,\text{cm}^{-3}]^{-\frac{4}{3}} P[100\,\text{TW}]^{\frac{1}{6}} \tag{2.151}$$

and typically lies in the range of one to few millimeters. Specific values for the pump depletion and dephasing length are summed up in Table 2.2 presented in section 2.8.

Ideal Energy Gain

The optimal energy gain is composed of the mean accelerating field $\bar{E}$ times the acceleration distance L_{acc} until dephasing/pump depletion:

$$W = e\bar{E}L_{\text{acc}}. \tag{2.152}$$

For $E_z < E_{\mathrm{WB}}$ and an ideal acceleration length of $L_{\mathrm{acc}} \approx L_{\mathrm{d}}$ (linear case), resp. $L_{\mathrm{acc}} \approx L_{\mathrm{pd}}$ (nonlinear case), we can estimate in the one-dimensional case [56, 113]

$$W_{\max} = e\frac{E_{\max}}{E_0}E_0 \begin{cases} L_{\mathrm{d}} \\ L_{\mathrm{pd}} \end{cases} = m_{\mathrm{e}}c^2\frac{\omega^2}{\omega_{\mathrm{p}}^2} \begin{cases} \pi a_0^2, & a_0 \ll 1, \\ 4.4\sqrt{2}a_0, & a_0 \gg 1, \end{cases} \tag{2.153}$$

where we have used the identity $E_0 = (2\pi m_{\mathrm{e}}c^2)/(e\lambda_{\mathrm{p}})$ and $E_{\max}$ which has already been calculated in Eq. (2.111).

Of course, this one-dimensional theoretical estimation neither includes laser pulse evolution effects like self-focusing nor accounts for laser-plasma instabilities or guiding effects.

A more accurate estimation in three dimensions is given by Lu *et al.* [41] who combined analytical theory for the bubble regime with PIC simulations to obtain the following scaling laws. The maximum longitudinal electric field in the blow-out regime can be estimated by Eq. (2.134). Since the electric field is quasi-linear, the average electric field that the electrons experience until dephasing is then approximately half the maximum and hence given by

$$\bar{E} \approx E_0\frac{\sqrt{a_0}}{2}, \tag{2.154}$$

where we made use of Eq. (2.134).

Together with Eq. (2.149) we can simplify Eq. (2.152) according to [41]

$$W = e\bar{E}L_{\mathrm{acc}} \approx eE_0\frac{\sqrt{a_0}}{2}\frac{\omega^2}{\omega_{\mathrm{p}}^2}\lambda_{\mathrm{p}}\frac{2\sqrt{a_0}}{3\pi} = \frac{2}{3}\frac{\omega^2}{\omega_{\mathrm{p}}^2}m_{\mathrm{e}}c^2a_0 = m_{\mathrm{e}}c^2\left(\frac{8Pe^2}{27\pi\varepsilon_0 m_{\mathrm{e}}^2c^5}\right)^{\frac{1}{3}}\left(\frac{n_{\mathrm{crit}}}{n_{\mathrm{e}}}\right)^{\frac{2}{3}}, \tag{2.155}$$

where we have used $eE_0\lambda_{\mathrm{p}} = 2\pi m_{\mathrm{e}}c^2$, Eq. (2.68) and Eq. (2.62) in the final step.

When converting to practical units, we get [41]

$$\begin{aligned} W[\mathrm{GeV}] &\approx 0.38 \times \left(\lambda[\mu\mathrm{m}]\right)^{-2}\left(n_{\mathrm{e}}[10^{18}\,\mathrm{cm}^{-3}]\right)^{-1}a_0 \\ &\approx 0.29 \times \left(P[\mathrm{TW}]\right)^{\frac{1}{3}}\left(\lambda[\mu\mathrm{m}]\right)^{-\frac{4}{3}}\left(n_{\mathrm{e}}[10^{18}\,\mathrm{cm}^{-3}]\right)^{-\frac{2}{3}} \\ &\approx 1.8 \times \left(P[100\,\mathrm{TW}]\right)^{\frac{1}{3}}\left(\lambda[0.8\,\mu\mathrm{m}]\right)^{-\frac{4}{3}}\left(n_{\mathrm{e}}[10^{18}\,\mathrm{cm}^{-3}]\right)^{-\frac{2}{3}}. \end{aligned} \tag{2.156}$$

Table 2.1.: *Overview of the above derived scaling laws obtained from analytical theory for the one-dimensional case and corresponding quantities based upon the phenomenological theoretical framework for the three-dimensional nonlinear regime by [41].*

Regime	a_0	L_{acc}		$W_{\mathrm{max}}/(m_{\mathrm{e}}c^2)$	
Linear	< 1	$\frac{\omega^2}{\omega_{\mathrm{p}}^2}\lambda_{\mathrm{p}}$	Eq. (2.145)	$\pi\frac{\omega^2}{\omega_{\mathrm{p}}^2}a_0^2$	Eq. (2.153)
1D Nonlinear	> 1	$\frac{\omega^2}{\omega_{\mathrm{p}}^2}\lambda_{\mathrm{p}}\frac{4.4}{\pi}$	Eq. (2.147)	$\frac{\omega^2}{\omega_{\mathrm{p}}^2}4.4\sqrt{2}a_0$	Eq. (2.153)
3D Blow-out	> 2	$\frac{\omega^2}{\omega_{\mathrm{p}}^2}\lambda_{\mathrm{p}}\frac{2\sqrt{a_0}}{3\pi}$	Eq. (2.149)	$\frac{2}{3}\frac{\omega^2}{\omega_{\mathrm{p}}^2}a_0$	Eq. (2.155)

Note that reducing the plasma density n_{e} leads to higher beam energies W and the much stronger dependence of the beam energy on n_{e} than on the laser pulse power P.

In terms of the critical power for relativistic self-focusing, the above expression may be reformulated as [41]

$$W[\mathrm{GeV}] \approx 3.9 \left(\frac{P}{P_{\mathrm{crit}}}\right)^{-\frac{2}{3}} P[100\,\mathrm{TW}], \tag{2.157}$$

where we made use of Eq. (2.63) and Eq. (2.68). An overview of the above-derived scaling laws is given in Table 2.1.

Eq. (2.156) suggests a maximum energy gain for our experiments of $\sim 785\,\mathrm{MeV}$ per electron (see Table 2.2 in section 2.8) which agrees with experimental data (cf. chapter 5).

Accelerated Charge

From the energy balance, the total number N of accelerated electrons can be deduced. By integrating the field energies E_z, E_r and B_θ given in Eq. (2.132), Eq. (2.135) and Eq. (2.136), we get the total energy E_{tot} available to accelerate N particles [107]

$$E_{\mathrm{tot}} = \frac{1}{60}(k_{\mathrm{p}}R)^5 \frac{4\pi\varepsilon_0 m_{\mathrm{e}}^2 c^5}{e^2\omega_{\mathrm{p}}}. \tag{2.158}$$

Assuming each particle experiences an average field of $\bar{E}$ (cf. Eq. (2.154)), we finally obtain [41][1]

$$N \approx \frac{16}{15}\frac{\varepsilon_0}{e}\lambda\sqrt{\frac{P}{4\pi\varepsilon_0 c}} = 2.5\times10^9 \times \lambda[0.8\,\mu\mathrm{m}]\sqrt{P[100\,\mathrm{TW}]}. \tag{2.159}$$

In practical units, the total accelerated charge $Q_{\mathrm{tot}} = Ne$ is given by

$$Q_{\mathrm{tot}}[\mathrm{nC}] = 0.053 \times \lambda[\mu\mathrm{m}]\sqrt{P[\mathrm{TW}]} \tag{2.160}$$

$$= 0.41 \times \lambda[0.8\,\mu\mathrm{m}]\sqrt{P[100\,\mathrm{TW}]}. \tag{2.161}$$

Note that Q_{tot} is independent of the plasma density. For the ATLAS-300 laser we find $Q_{\mathrm{tot}} \approx 360\,\mathrm{pC}$ which is in good agreement with our experimental findings (cf. chapter 5) and nicely matches corresponding PIC simulations.

A simulation of the ATLAS-300 accelerator is shown in Figure 2.13, depicting the evolution of the electrons' energy spectrum during the acceleration process and the charge density. The accelerated charge in the first bucket amounts to $\sim 330\,\mathrm{pC}$, which nicely agrees with theoretical predictions. The maximum energy gain, however, differs by a factor of two compared to Eq. (2.156). We attribute this deviation mainly to beam loading effects which will be discussed in section 2.7.

Efficiency

An estimate for the efficiency Γ of the accelerator can be obtained by combining Eq. (2.156) and Eq. (2.159) to get the total energy W_{tot} transferred to the accelerated particles

$$W_{\mathrm{tot}}[\mathrm{J}] \approx 0.7 \times \lambda[0.8\,\mu\mathrm{m}]^{-\frac{1}{3}} P[100\,\mathrm{TW}]^{\frac{5}{6}} n_{\mathrm{e}}[10^{18}\,\mathrm{cm}^{-3}]^{-\frac{2}{3}}. \tag{2.162}$$

For the ATLAS-300 we calculate $W_{\mathrm{tot}} \approx 0.26\,\mathrm{J}$ which justifies the term "joule-class" LWFA for accelerators in a similar parameter range.

With a typical pulse energy of $E_{\mathrm{L}} \approx 2.1\,\mathrm{J}$, the three-dimensional theory predicts an efficiency of the whole acceleration process of

$$\Gamma = \frac{W_{\mathrm{tot}}}{E_{\mathrm{L}}} = \frac{0.26}{2.1} \approx 12\,\%. \tag{2.163}$$

[1] A very different approach to estimate the total number of accelerated electrons is pursued by [138]. Based on a scale-invariant reformulation of laser-plasma interaction, their similarity theory leads to the same scaling law with slightly different prefactors.

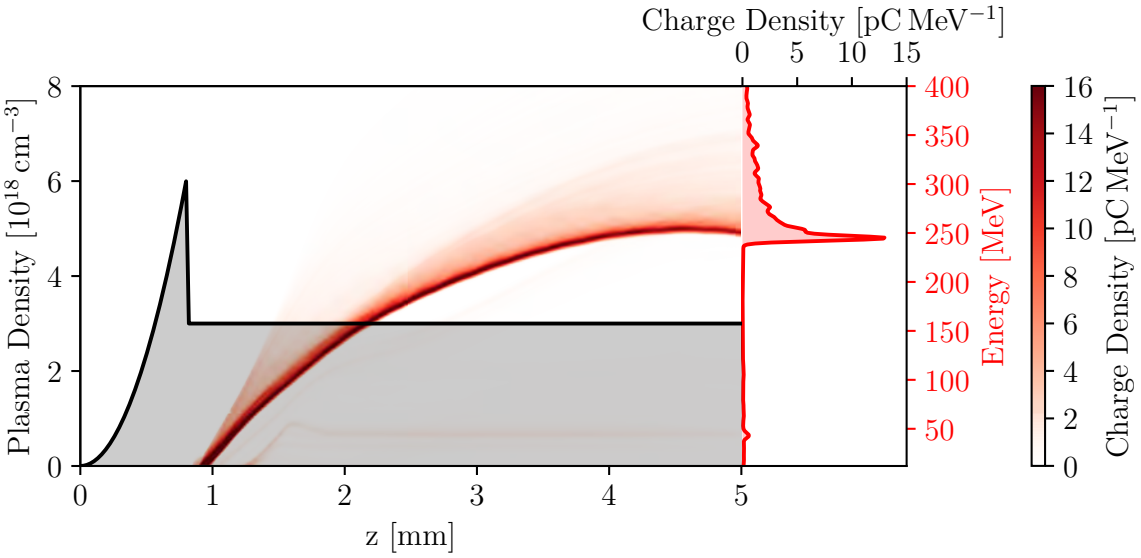

Figure 2.13.: *Electron energy vs. acceleration length based on a PIC simulation. The electrons are injected via shock front injection at $z \approx 800\,\mu m$ and accelerated for more than 4 mm. The plasma density profile is plotted in gray. The electrons start to dephase at $z \approx 4.5\,mm$ where they have reached more than $\sim 250\,MeV$. Only electrons above $\gamma_{thres} \approx 24$ are plotted. The driving laser pulse was initialized with a power of 50 TW resulting in a vacuum a_0 of ~ 1.5. The electron energy spectrum at the very end of the acceleration process is plotted in red. The accelerated charge in the first bucket is 332 pC.*

Assuming a roughly resonant length of the pulse ($c\tau \approx R \approx 2\sqrt{a_0}/k_p$), the laser pulse energy E scales as $E = P\tau \propto P\sqrt{a_0} \propto P^{\frac{7}{6}}$ (cf. Eq. (2.68)). Hence, the efficiency drops for higher laser powers [41]

$$\Gamma \propto \frac{P^{\frac{5}{6}}}{P^{\frac{7}{6}}} = P^{-\frac{1}{3}} \propto a_0^{-1}. \tag{2.164}$$

2.7. Beam Loading

Up to now, we have only considered the driver as the sole generator of the wakefield. However, as the injected and accelerated charge increases, the self-fields of the particle bunch become non-negligible. Coulomb interactions between both the accelerated charges themselves and with the surrounding electrons superimpose the accelerating fields which may alter the wakefield structure and change the acceleration dynamics significantly. Figure 2.14 for example depicts the wakefield of a shock front LWFA where the injected charge is large enough to significantly interact with the surrounding plasma and to deform

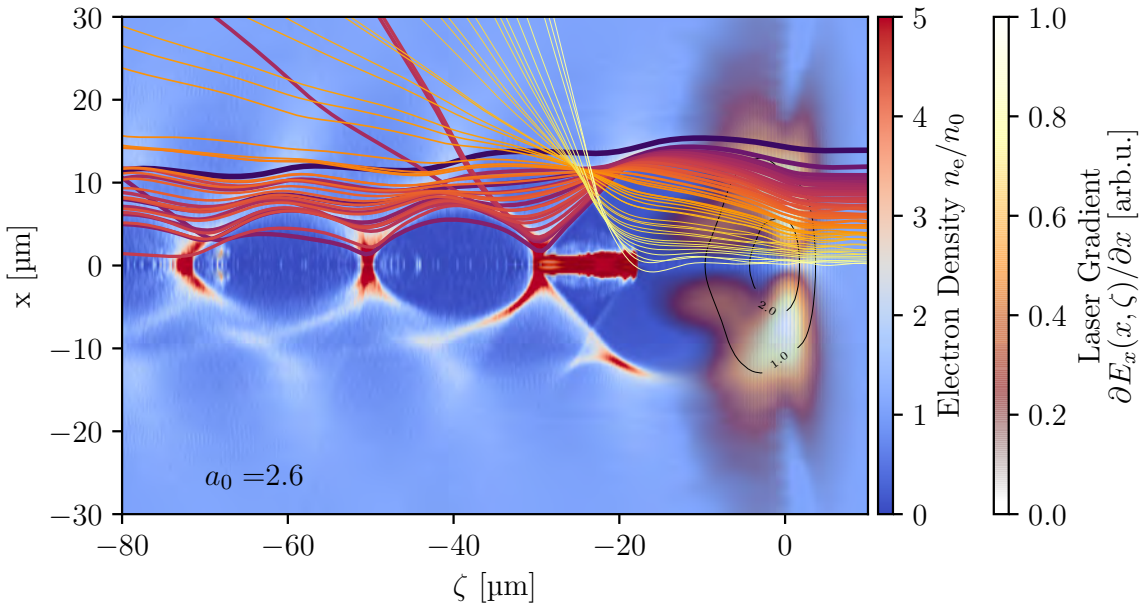

Figure 2.14.: *PIC simulation depicting the wakefield structure of a shock front LWFA in the partially broken regime with $a_0 \approx 2.6$ and $n_0 = 3.0 \times 10^{18} cm^{-3}$. The contour lines of the laser's electric field, as well as its directional derivative, are also plotted. The wakefield behind the driver forms a chain of bubbles. Some electron trajectories color-coded by their initial radial distance from the laser propagation axis are plotted to illustrate how this structure is created. Their respective line thickness depicts the corresponding relative charge of the macroparticle. The electrons in the leading bubble were injected via a sharp density shock front and constitute an accelerated charge of $\sim 750 pC$. Compared to Figure 2.7 one notices that the self-fields of these electrons not only deflect the trajectories of other electrons but also deform the shape of the back of the bubble to a triangle (cf. subsection 2.6.4).*

the shape of the leading cavity (in sharp contrast to Figure 2.7). As we have seen in subsection 2.6.2, the driving potentials of both the laser driver and the accelerated particle beam superimpose and consequently the accelerating dynamics is modified. This so-called *beam loading* effect can be exploited to flatten the fields along the bunch such that all electrons experience the same accelerating forces during the acceleration process. This effect allows for the generation of electron bunches of very low energy spread.

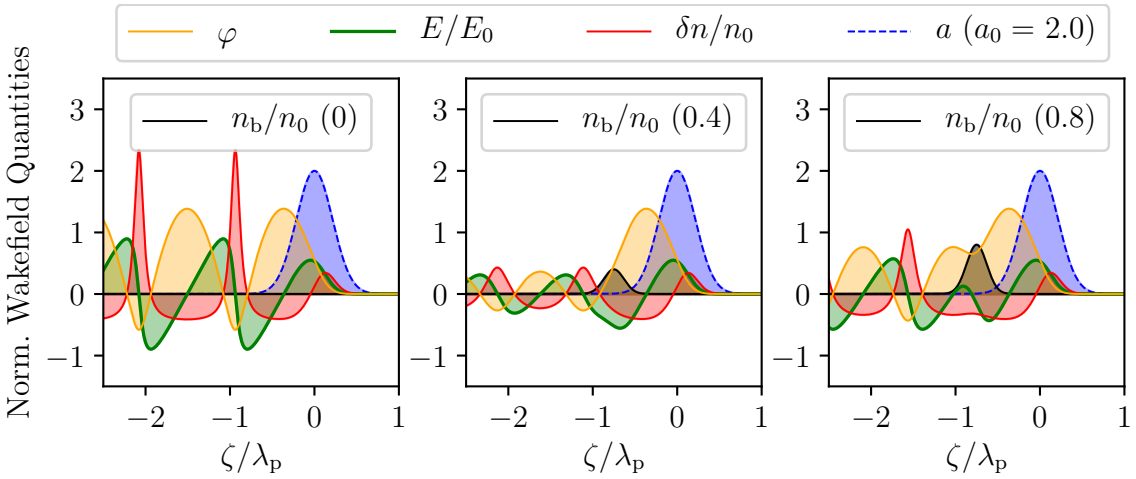

Figure 2.15.: *Beam loading effects on different wakefield quantities for relativistic laser drivers based on Eq. (2.165). The strength of beam loading is varied by changing the peak normalized density of the Gaussian electron beam from 0 to 0.4 and 0.8. The center of the electron beam is located at $\zeta/\lambda_p = -0.75$. Due to the presence of the particle beam, the accelerating field in bold green is changed significantly at the position of the electron beam (black line).*

2.7.1. Beam Loading in 1D

In the ultra-relativistic one-dimensional wakefield theory, beam loading can be treated fully analytically. Reverting to Eq. (2.109),

$$\frac{1}{k_\mathrm{p}^2}\frac{\partial^2\varphi}{\partial\zeta^2} = \pm\frac{n_\mathrm{b}}{n_0} + \frac{1+a^2}{2(1+\varphi)^2} - \frac{1}{2}, \tag{2.165}$$

it becomes clear that the wake's potential is composed of both the potential of the particle bunch and the potential of the driving laser pulse. If n_b/n_0 becomes comparable to the second term, the fields of a pure laser-driven wake are significantly changed.

The effect of beam loading on the wakefield quantities is illustrated in Figure 2.15 for varying charge densities and in Figure 2.16 for different distances of the electron beam to the laser pulse as the primary driver of the wake. When the beam is sitting in the second half of the wake bucket, its own wakefield interferes destructively with the main wake. The overall accelerating field is reduced and, thus, the maximum possible energy gain is lowered (cf. Figure 2.15). Hence, any bunch sitting in the accelerating phase of a wakefield directly influences the accelerating fields it experiences. Energy conservation, of course, dictates the reduction of the effective accelerating fields the higher the bunch charge. The interference of both wakes can be analyzed by changing the relative distance between the

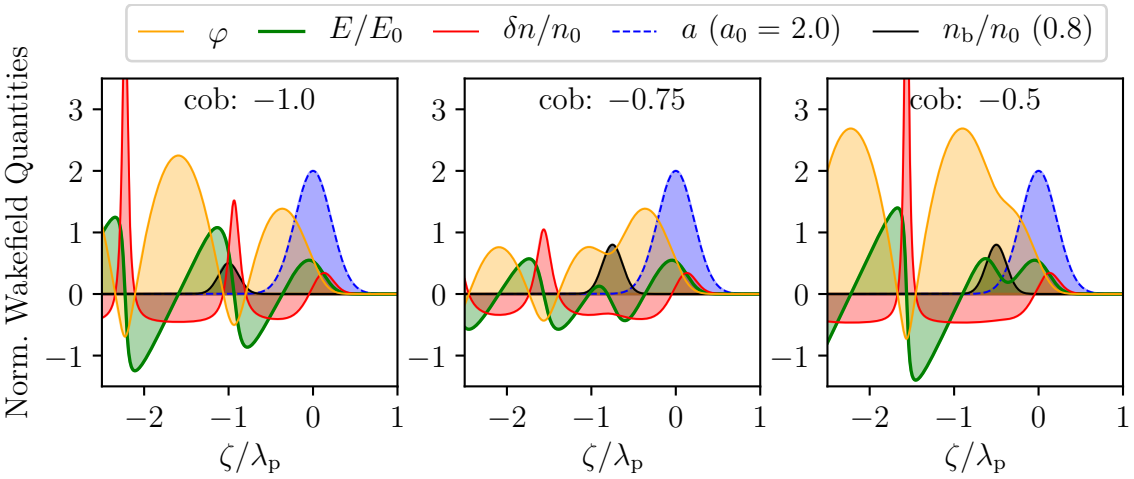

Figure 2.16.: *Beam loading for relativistic laser drivers depending on the longitudinal beam position according to Eq. (2.165). In contrast to Figure 2.16 the peak of the normalized density is kept constant whilst the position of the electron beam's center (cob) is varied from −1.0 to −0.75 and −0.5. The accelerating field in bold green is changed significantly at the position of the electron beam.*

drivers. The closer the two drivers, the more the individual wakefields get in phase and interfere constructively. Consequently, the effective wakefield quantities are enhanced as can be seen in Figure 2.16.

2.7.2. Beam Loading in 3D

From Eq. (2.165) one might conclude, that the bunch density distribution n_b is the essential parameter for beam loading. As explained in the following, in the purely beam-loaded regime, where the plasma blowout radius is larger than the lateral size of the bunch (as opposed to the beam-driven regime), the key parameter in this case actually is the beam current. The following arguments are based on [38].

For a relativistic electron beam, the transverse fields are enhanced, whereas the longitudinal ones are suppressed [58]. The fields of a highly relativistic electron bunch are therefore almost entirely oriented in the radial direction. This electron bunch can therefore be described by a charged cylinder with radius r_0 and length L.

Let us consider a charged particle in the electron sheath around the blowout having the coordinates (r,z), with $r > r_0$. A drawing of this coordinate system is given in Figure 2.17(a).

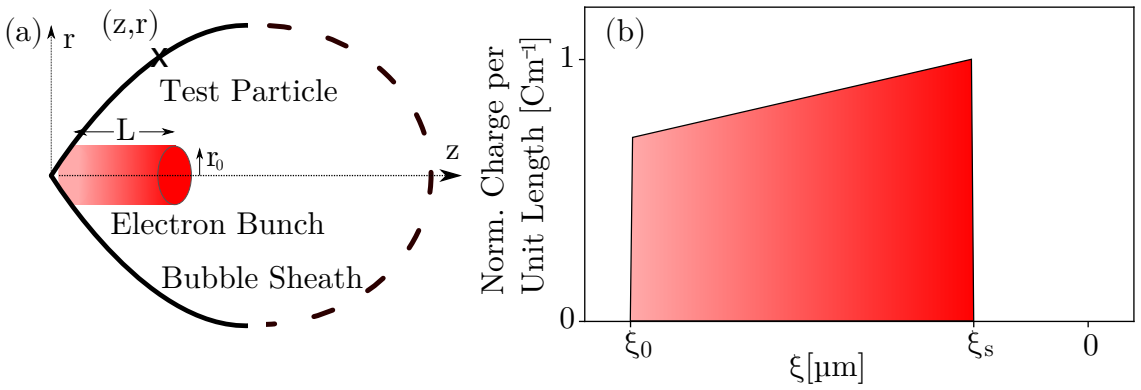

Figure 2.17.: *(a) Schematic drawing of the coordinate system used to calculate the influence of bunch particles on sheath electrons. A test particle located at (z,r) is located within this sheath and interacts with the particle bunch sitting in the rear half of the bubble. The bunch is approximated by a cylinder (red) with radius r_0 and length L. (b) shows the normalized current profile of an optimal beam load, i.e. an electron bunch which generates a constant longitudinal on-axis field E_s. At ξ_s the trapezoidal current profile reaches its maximum. ξ_0 denotes the location, where the electron sheath reaches the ξ-axis. Within the interval $\xi_0 < \xi < \xi_s$, the current profile is linear in ξ, whereas outside this interval, the optimal beam current vanishes.*

According to Gauss's law, the electric field at the position of the test particle is given by

$$\oint_A \boldsymbol{E} \cdot \mathrm{d}\boldsymbol{A} = \frac{Q}{\varepsilon_0}, \tag{2.166}$$

where Q is the total charge enclosed by the volume defined by the surface A. Exploiting the radial symmetry, we can simplify

$$E_r(r,z)2\pi r = \frac{2\pi}{\varepsilon_0}\int_0^r e n_\mathrm{b}(r',z)r'\mathrm{d}r'. \tag{2.167}$$

Since $r > r_0$ and $n_\mathrm{b}(\tilde{r},z) = 0$ for $\tilde{r} > r_0$, the upper integration limit can be replaced by r_0

$$E_r(r,z) = \frac{1}{r\varepsilon_0}\int_0^{r_0} e n_\mathrm{b}(r',z)r'\mathrm{d}r'. \tag{2.168}$$

The integral on the right-hand side simplifies to the electron beam current via

$$I(z) = \frac{\mathrm{d}Q}{\mathrm{d}z}\frac{\mathrm{d}z}{\mathrm{d}t} = 2\pi c\int_0^{r_0} e n_\mathrm{b}(r',z)r'\mathrm{d}r', \tag{2.169}$$

where we have used $z \approx ct$ for a relativistic electron beam.

Inserting into Eq. (2.168) leads to

$$E_r(r,z) = \frac{1}{2\pi c r \varepsilon_0} I(z). \tag{2.170}$$

The electric field E_r in the sheath of the bubble is therefore determined by the beam current $I(z)$. As the trajectories of the particles forming the electron sheath are governed by E_r, it follows, that in turn, the shape of the blowout depends on E_r. The longitudinal fields inside the cavity are again directly linked to the blowout shape via $E_z(\xi) \propto r\mathrm{d}r/\mathrm{d}\xi$ (cf. Eq. (2.131)). Hence, beam loading in this regime depends on the shape of the beam current [38].

To demonstrate this finding, we simulate electron bunches with identical total charges but different currents in the wake of a laser driver. Only the longitudinal or lateral dimensions of the bunches have been varied. Figure 2.18(a-c) shows three snapshots of these simulations. Here, the length of the bunches has been changed to adjust the beam current. Although the total charges are the same, the resulting shapes of the bubble and hence the fields E_z differ substantially (cf. Figure 2.18(e)). If total charge *and* beam current are kept equal by only changing the transverse size of the bunch (Figure 2.18(d)), the effect on the field is negligible (red vs. black line in Figure 2.18(e))[1].

As we did not measure the bunch durations in our experiments, we have to resort to simulations to conclude that their effect on the beam current is much smaller than the one by changes in the peak current itself (cf. chapter 6). This finding is supported by earlier coherent transition radiation (CTR) measurements in the self-injection regime, which show only small shot-to-shot fluctuations in the bunch duration [139]. It is therefore justified to assume that these fluctuations mainly affect the amplitude of the beam current. Under this assumption, the total charge is directly proportional to the beam current[2]. Hence, in the following, we will stick to the convention and consider beam loading to primarily depend on the total charge of the electron bunch.

2.7.3. Beam Loading in the Bubble Regime

Based on the phenomenological bubble theory detailed in [41], Tzoufras *et al.* [42, 43] examined the interaction of an electron bunch with the nonlinear plasma wave itself. They

[1] In the case of beam-driven wakefields, where $r \not\gg r_0$, the above derivation breaks down and the simplification made in Eq. (2.168) is not valid. As a result, the wakefield does not only depend on $I(z)$ anymore and changes with increasing bunch radius, as stated in [38].

[2] However, bunch length fluctuations certainly appear as "higher-order" corrections in our measurements (cf. [38]).

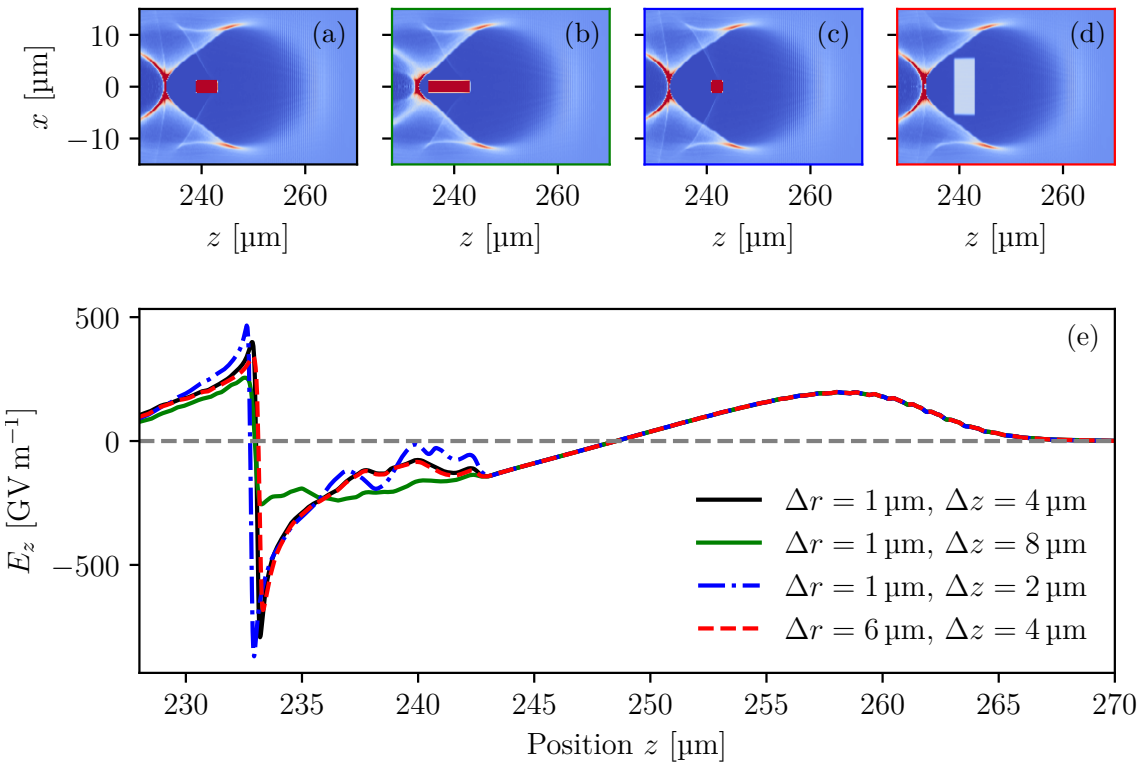

Figure 2.18.: *PIC simulations showing the difference in beam loading for electron bunches with the same charge (500 pC). In (a)-(c) the charge is kept equal, but the length of the electron bunch is varied, leading to different beam currents. Despite the same charge, the on-axis longitudinal fields E_z (as shown in (e)) differ significantly. However, keeping charge and current equal by only increasing the lateral bunch extension (d), the fields are unaffected. Simulations provided by courtesy of A. Döpp.*

found that a bunch load with trapezoidal current profile[1], cf. Figure 2.17(b), reshapes the bubble sheath according to Eq. (2.126), such that the accelerating on-axis field E_z becomes longitudinally constant (E_s) along the whole electron bunch. Hence, the energy spread on the beam is minimized for this current profile, and we may modify Eq. (2.131) to

$$E_z(\xi) = \frac{e n_e}{2\varepsilon_0} r_b \frac{\mathrm{d}r_b}{\mathrm{d}\xi} = \text{const} =: E_s. \tag{2.171}$$

[1]The charge per unit length linearly drops from the front to the back of the particle bunch. The slope of this current profile is proportional to E_s. For more details, see [42].

The maximum charge that can be accelerated while keeping the field constant is then given by [43]

$$Q_\mathrm{s} = \frac{1}{4^3}\left(k_\mathrm{p}R\right)^4 \frac{m_\mathrm{e}c^2}{r_\mathrm{e}}\frac{1}{E_\mathrm{s}}, \tag{2.172}$$

where $r_\mathrm{e} = e^2/(4\pi\varepsilon_0 m_\mathrm{e}c^2)$ is the classical electron radius. This equation can be converted into a practical formula [42]

$$Q_\mathrm{s}[\mathrm{nC}] \approx 0.0047 \times \frac{m_\mathrm{e}c\omega_\mathrm{p}}{eE_\mathrm{s}}\sqrt{n_\mathrm{e}[10^{18}\,\mathrm{cm}^{-3}]}\left(k_\mathrm{p}R\right)^4. \tag{2.173}$$

With Eq. (2.130) we can further replace the last bracket and simplify [42]

$$Q_\mathrm{s}[\mathrm{nC}] \approx 7.23 \times \frac{a_0^2}{E_\mathrm{s}[\mathrm{GV\,m}^{-1}]} \tag{2.174}$$

$$\approx 4.0 \times \lambda[\mu\mathrm{m}]^{\frac{4}{3}} n_\mathrm{e}[10^{18}\,\mathrm{cm}^{-3}]^{\frac{2}{3}} P[\mathrm{TW}]^{\frac{2}{3}} E_\mathrm{s}[\mathrm{GV\,m}^{-1}]^{-1}, \tag{2.175}$$

where Eq. (2.68) was used to replace the normalized vector potential in the last step. Generally, E_s is difficult to access and only attainable via experimental data. Nevertheless, $E_{z,\mathrm{max}}$ from Eq. (2.134) can be used as the upper limit for this parameter [140]. Hence, Eq. (2.174) transforms into a rough estimation for the charge necessary to flatten the accelerating fields

$$Q_\mathrm{s}[\mathrm{nC}] \approx 7.2 \times \frac{a_0^{\frac{3}{2}}}{E_0[\mathrm{GV\,m}^{-1}]} \tag{2.176}$$

$$\approx 0.048 \times \lambda[\mu\mathrm{m}]\sqrt{P[\mathrm{TW}]}. \tag{2.177}$$

Therefore, under the assumption of a trapezoidal current profile, the accelerating fields with $E_z \approx E_\mathrm{s} \approx E_{z,\mathrm{max}}$ become flat, when the cavity is loaded by $Q_\mathrm{s}/Q_\mathrm{tot} \approx 90\,\%$ (cf. Eq. (2.160)). For ATLAS-300 parameters, this leads to $Q_\mathrm{s} = 330\,\mathrm{pC}$ (cf. Table 2.2).

2.8. Overview of Important LWFA Parameters

Table 2.2 summarizes the most important LWFA parameters. Specific values for the ATLAS-300 laser and accelerator are given, as well as corresponding references to the preceding theoretical sections and equations.

Table 2.2.: *Key parameters of the ATLAS-300 wakefield accelerator and their specific values as determined by theoretical concepts introduced in this chapter.*

Quantity	Symbol	Value	Reference
Laser central wavelength	λ	800 nm	(measured)
Laser pulse energy on target	E_L	2.1 J	(measured)
Laser pulse duration (FWHM)	τ_FWHM	27 fs	(measured)
Laser peak focal intensity	I	$5.5 \times 10^{18}\,\mathrm{W\,cm^{-2}}$	(measured)
Plasma density	n_0	$3.0 \times 10^{18}\,\mathrm{cm^{-3}}$	(measured)
Laser central frequency	ω	$2.4 \times 10^{15}\,\mathrm{s^{-1}}$	$\omega = 2\pi c/\lambda$
Laser peak power on target	P	75 TW	$P \approx 0.94 E_\mathrm{L}/\tau_\mathrm{FWHM}$
Normalized vacuum vector potential	$a_{0,\mathrm{vac}}$	1.6	Eq. (2.26)
Plasma frequency	ω_p	$9.8 \times 10^{13}\,\mathrm{s^{-1}}$	Eq. (2.38)
Plasma wavelength	λ_p	19 µm	Eq. (2.39)
Critical plasma density	n_crit	$1.7 \times 10^{21}\,\mathrm{cm^{-3}}$	Eq. (2.46)
Critical laser power	P_crit	10 TW	Eq. (2.63)
Matched radial laser spot size	w_match	12 µm	Eq. (2.66)
Matched normalized vector potential	a_0	3.9	Eq. (2.68)
Cold non-relativistic wave breaking field	E_0	$170\,\mathrm{GV\,m^{-1}}$	Eq. (2.118)
Matched bubble radius	R	12 µm	Eq. (2.130)
Cold relativistic wave breaking field	E_WB	$1.1\,\mathrm{TV\,m^{-1}}$	Eq. (2.124)
Electron trapping threshold	γ_thres	24	Eq. (2.137)
Pump depletion length	$L_\mathrm{pd,3D}$	4.7 mm	Eq. (2.148)
Dephasing length	$L_\mathrm{d,3D}$	4.6 mm	Eq. (2.151)
Ideal accelerated electron energy	W	790 MeV	Eq. (2.156)
Accelerated charge	Q_tot	360 pC	Eq. (2.161)
Total particle beam energy	W_tot	0.26 J	Eq. (2.162)
Acceleration efficiency	Γ	12 %	Eq. (2.163)
Flat field beam loading charge	Q_s	330 pC	Eq. (2.177)

Chapter 3

Particle-in-Cell Simulations

Due to its complexity, the analytical framework for underdense laser plasma interaction is based on severe simplifications (reduction to one dimension or restriction to the linear regime). In addition, such key processes as electron injection completely elude a self-consistent analytical description. For accurate modeling, one has to resort to numerical solutions of Maxwell's equations [141, 142]. One way to numerically describe such complex systems is by dividing the time evolution into a finite number of small time steps. The size of these steps determines the temporal resolution of the simulation. The particle distribution is sampled by so-called macroparticles (also called quasi-particles) each representing many real particles. Since the Lorentz force determining the equation of motion is only sensitive to the charge-to-mass ratio, these macroparticles follow the same trajectory as real particles as long as scattering processes are negligible. The motion of the macroparticles is calculated for each time step by the so-called *particle pusher*. The resulting currents and charge imbalances leading to electromagnetic fields are calculated per time step by the *field solver* and react back to the macroparticles and their behavior. The continuous domain here is replaced with a discrete grid of points onto which the electric and magnetic fields are mapped [64]. Derivatives may then be approximated by differences between neighboring points of the grid.

At each time step, the following calculations are performed [59, 143]:

- Interpolate the $\boldsymbol{E}$ and $\boldsymbol{B}$ fields on the grid to the positions $\boldsymbol{x}_i$ of the macroparticles
- Perform the particle push in time (update $\boldsymbol{x}_i$ and $\boldsymbol{p}_i$ via Eq. (2.28) for the next time step)
- Calculate the corresponding charge ρ and current $\boldsymbol{j}$ densities from $\boldsymbol{x}_i$ and $\boldsymbol{v}_i$
- Update the fields $\boldsymbol{E}$ and $\boldsymbol{B}$ on the grid by solving Eq. (2.2) and Eq. (2.4)

Such kinds of numerical codes are called *particle-in-cell (PIC) simulations* [144, 145]. Since their introduction in the late 50s [146] and early 60s [147], they have become an indispensable tool in plasma physics. For both the particle pusher and field solver, many

different schemes have been developed since then and been implemented into a variety of different PIC codes [148]. The most relevant for the field of LPA are among others OSIRIS [149], EPOCH [150], WARP [151], CALDER-Circ [152], PIConGPU [153] and FBPIC [52]. All simulations in this work were done with FBPIC since it combines several advantages which are highly beneficial for simulating LPA. This is why the distinctive features of FBPIC shall be treated in the following.

3.1. FBPIC

The code FBPIC is a PIC algorithm for relativistic plasma physics specially developed for laser and plasma wakefield acceleration [52]. It combines the advantages of both a spectral 3D PIC code (robust against numerical artifacts) and the massive speedup of cylindrical algorithms in quasi-rotationally symmetric scenarios. Standard 3D PIC codes represent the fields on a generic Cartesian grid, which is computationally very expensive [143]. However, for quasi-rotationally symmetric scenarios, it is much more efficient to employ a cylindrical field representation and account for deviations from this symmetry by introducing higher-order field modes. In this way, the code uses vastly less memory and runs orders of magnitudes faster as in the two-dimensional case the number of grid points scales as $\sim m * N_r * N_l$ with m being the number of modes, N_r and N_l denoting the number of radial and longitudinal grid points. In the Cartesian case, however, the total number of grid points scales as $\sim N_y * N_r * N_l$, where N_y denotes the number of grid points in the third dimension. Depending on the physics at stake, m is on the order of $\sim 2-4$, which is orders of magnitudes lower than N_y and hence explains the much greater efficiency for quasi-symmetric scenarios. Moreover, common PIC codes usually solve Maxwell's equations by discretizing the spatial and time derivatives via finite differences on a discrete spatial grid. This technique suffers from spurious numerical dispersion, especially for objects traveling close to the speed of light (e.g., laser pulses or accelerated particle beams). This leads to substantial numerical artifacts if the time and spatial resolution are not chosen with great care [154–156] and for example adapted to the Courant limit [141, 157]. In FBPIC, however, the fields are decomposed into a discrete Fourier-Bessel series [158], a linear combination of orthonormal Bessel functions (of the first kind), which is where the name for this code is derived from. The fields are then solved in spectral space via Fourier-Hankel transformations (Fourier transformation along the longitudinal dimension z and Hankel transformation along the r-axis) allowing for the analytical integration of Maxwell's equations [52, 152]. These so-called *spectral algorithms* are free of numerical dispersion and hence conditions like the Courant limit to avoid numerical artifacts are irrelevant here [143]. Since LPA are quasi-rotational symmetric, the spectral cylindrical

decomposition chosen in FBPIC makes this code fast and accurate for our applications [143].

FBPIC can run on multi-core Central Processing Units (CPUs) or Graphics Processing Units (GPUs), where the latter is typically significantly faster. Exploiting the quasi-radial symmetry of typical LPA simulations, it is – as mentioned before – much more efficient to decompose the fields using a cylindrical grid rather than a 3D Cartesian grid. Simulations exploiting the radial symmetry are therefore sometimes referred to as *quasi-3D* or *quasi-cylindrical algorithms*. Due to this cylindrical representation, macroparticles that were initialized far away from the axis represent more electrons and hence have larger weight (cf. Figure 2.14). This weighting factor must be considered when evaluating the simulations.

All the parameters necessary for conducting a FBPIC simulation are defined in a separate input file which needs to be written by the user[1]. The quantities defined here can be separated into technical parameters which set up the framework for the simulation (like resolution in time and space, sampling rate, etc.) and physical ones, which directly influence the interaction processes (laser strength, gas density, etc.). Both types of quantities are briefly discussed in the following.

3.1.1. Resolution and Number of Macroparticles

In order to decently mimic the underlying physics of LPA, typically more than 10^6 macroparticles are required (for quasi-3D simulations; in full 3D simulations often more than 10^9 macroparticles are used) which makes such simulations very demanding as the particle pusher acts on each macroparticle separately. Hence, computer systems capable of performing a massive number of tasks in parallel (e.g., CPU-Clusters or special GPUs) are needed to keep the time expenditure for one LWFA simulation on the order of few hours. Not only the size of the simulation box but also the number of macroparticles per cell (defined by the sampling rate) as well as the temporal and spatial resolution (defined by setting the grid parameters) crucially determine the computational cost but also the accuracy of the simulation. Nevertheless, the spatial resolution in each dimension is restricted by the smallest length scale of interest to be resolved (e.g., the wavelength of the driving laser pulse for the longitudinal dimension). Consequently, for all these parameters a trade-off between computational cost and accuracy must be found which requires some experience with PIC simulations (details on the parameters chosen for simulations in this thesis can be found in section B.1). In particular, a decent prediction for the accelerated charge makes a high sampling of macroparticles necessary. Since the accelerated charges

[1] An example for such an input file is given in section B.4.

in our experiments are injected very localized around the shock front, it is sufficient for an accurate charge estimate to sample only the shock region finely. In all shock front simulations presented in this thesis, the macroparticle density was varied for different segments of the plasma target to achieve an adaptive sampling rate: particles from outer regions which do not contribute to the total accelerated charge are sampled less accurately than the region around the shock where injection happens. In this way, it was possible to unite high simulation accuracy with low computation time. Further details are given in section B.1.

3.1.2. Physical Parameters

Whereas the parameters discussed in the previous section settle the external framework for the simulation, the remaining quantities to define determine the strength of the physical laser-plasma interaction. For FBPIC simulations, these parameters characterize the laser pulse (laser amplitude, laser waist, laser duration, and position) as well as the gas target (gas density and profile). To tailor these simulations to our experiments, all these parameters have been measured and accordingly adopted to the simulations. Further details are given in Appendix B.

3.1.3. Simulation Analysis

The data generated by FBPIC is saved in the Hierarchical Data Format 5 (HDF5) at certain time steps determined by the input file. All the simulated data in this thesis was then analyzed and graphically processed with the help of python and the open standard for particle-mesh data files (openPMD) [159] framework. More details are given in Appendix B.

Chapter 4

Experimental Setup

The general setup for LWFA experiments can be divided into three parts: the high-power short-pulse laser system delivering the necessary energy to drive the wakefield, the gas target where the electrons are accelerated, and finally the particle diagnostics utilized to quantify the characteristic parameters of the particle bunch. These different parts will be discussed in the following by taking the example of the LPA operated in the Laboratory for EXtreme Photonics (LEX) driven by the ATLAS-300 laser system.

4.1. The ATLAS Laser System

As shown in the theory chapter, an adequate optical driver to efficiently accelerate electrons in an underdense plasma has to meet several requirements:

- the FWHM laser pulse length should be around $\tau_{\mathrm{FWHM}} \approx \lambda_{\mathrm{p}}/2c$ (cf. Eq. (2.100))
- the normalized vector potential should be large enough to enter the nonlinear regime, hence $a_0 > 1$ (cf. section 2.6)
- the focal spot radius should be around the matched beam spot size w_{match} (cf. Eq. (2.66))

Assuming $n_0 \approx 3 \times 10^{18}\,\mathrm{cm}^{-3}$, $a_0 \approx 2$ and $\lambda \approx 800\,\mathrm{nm}$, the above requirements set following rigid restraints to the laser system

$$\begin{aligned} \tau_{\mathrm{FWHM}} &\approx 30\,\mathrm{fs}, \\ w &\approx 10\,\mu\mathrm{m}, \\ E &\approx 1\,\mathrm{J} \end{aligned}$$

Hence, at typical gas densities, a femtosecond laser system capable of delivering at least tens of terawatts of output power is needed for LWFA experiments.

The Advanced Titanium Sapphire Laser System (ATLAS) has been built and constantly upgraded over the past two decades to specifically meet these requirements. This 300 TW system was located at the LEX in Garching during the time the experimental campaign took place. A complete layout for this CPA-based [27] high field laser is shown in Figure 4.1.

Titanium sapphire (Al_2O_3 doped with titanium ions typically around 0.1 %) laser crystals exhibit a broad gain bandwidth peaked around 800 nm, excellent thermal conductivity, as well as a wide range of possible pump wavelengths [160, 161]. Due to these unique properties, titanium sapphire is by far the most widely used gain medium for femtosecond laser systems and is also employed for each amplification stage in the ATLAS. The laser as such may be divided into three main parts, the so-called *front end*, where the femtosecond laser pulses are generated, stretched, cleaned, and spectrally shaped, the *main amplification stages*, where the energy of the stretched and chirped pulses is increased, and the final part, where the chirped laser pulses are compressed, diagnosed and sent to the experimental chambers. These three main parts shall briefly be discussed in the following. A more detailed description may be found in [162, 163].

At the very beginning of the laser chain, a commercially available Kerr-lens mode-locked Femtolasers Rainbow oscillator delivers a train of ~ 6 nJ, $\tau_{\mathrm{FWHM}} < 10$ fs pulses at a repetition frequency of 70 MHz, see Figure 4.1. From this pulse train, the so-called *pulse picker*, a Pockels cell with polarizers, selects a single pulse every 0.1 seconds. These selected pulses are then pre-stretched to about 3 ps by transmission through an SF-14 glass block and amplified to the mJ level in a circular multipass preamplifier (so-called *booster*). A subsequent saturable absorber prevents the transmission of amplified spontaneous emission (ASE) originating from the booster to increase the contrast.

The amplified pulses are then stretched to about 400 ps in a grating-based Öffner configuration stretcher setup [164]. A subsequently installed acousto-optic programmable dispersive filter (AOPDF) (commercially sold under the name "Dazzler", [165]) allows for the precompensation and fine-tuning of the pulses' dispersion. The losses introduced by these two elements are accounted for by a following high-gain regenerative amplifier which boosts the pulses' energies from some µJ to the mJ-level. This amplifier includes an additional acousto-optic programmable gain filter (commercially named "Mazzler", [166]) to pre-shape the pulses' spectrum to account for spectral distortions in the subsequent power amplifiers (gain narrowing, etc.). Thereby, a FWHM spectral bandwidth of ~ 50 nm can be maintained. The following two multipass amplifiers further increase the energy to 20 mJ. In total four Pockels cells ensure high temporal contrast and reduce the repetition rate to 5 Hz. The pulses have now been chirped, stretched, spectrally shaped and are energetic enough to enter the main amplifier chain, consisting of three multipass amplifiers pumped by commercially available neodymium-doped yttrium aluminum garnet (Nd:YAG) pump

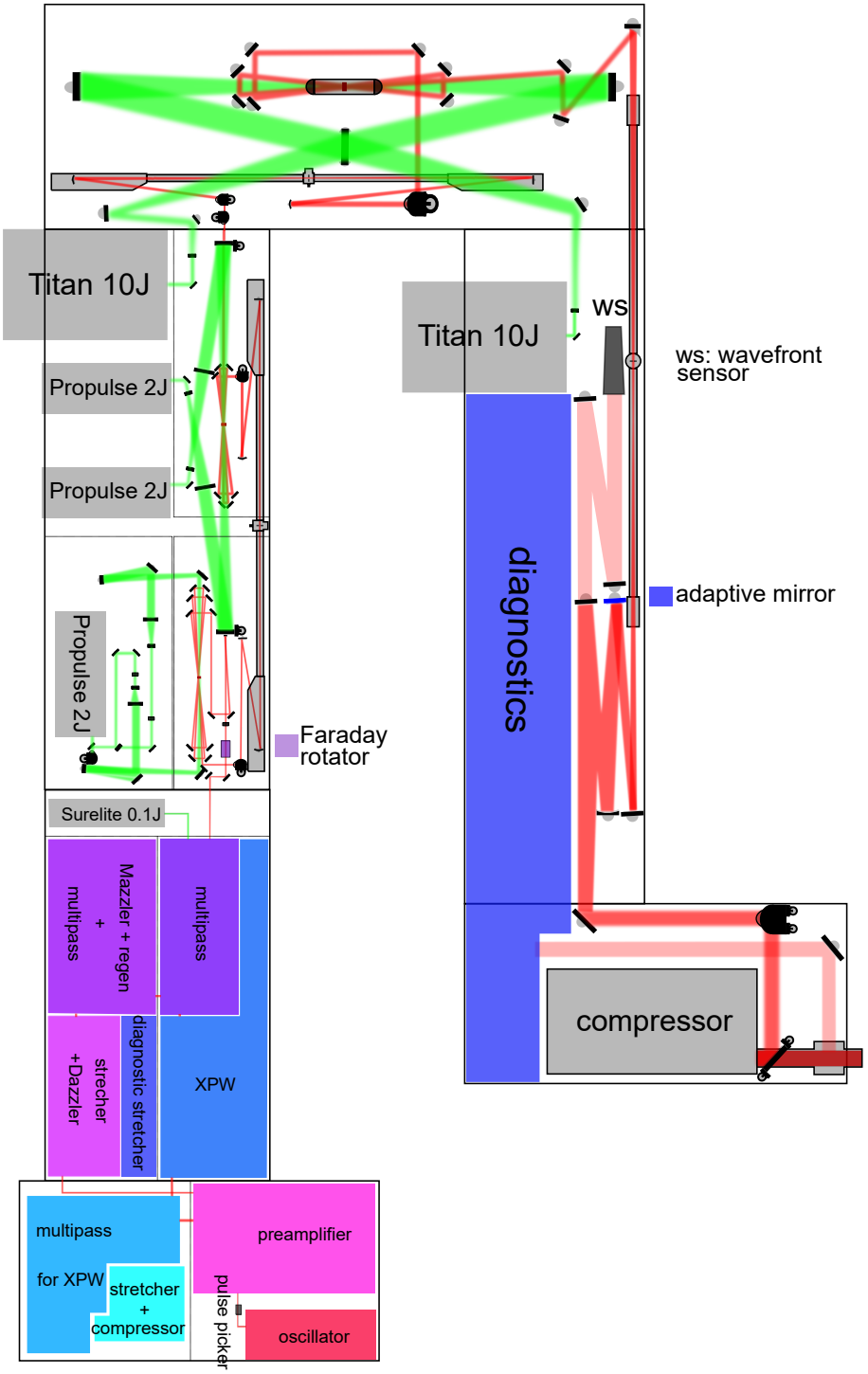

Figure 4.1.: *Layout of the ATLAS-300 laser system. Both front ends are depicted schematically on the lower left. For clarity, the complete beam paths for the seed (red) and the pumps (green) are only shown after the front end.*

lasers (sold by Amplitude Technologies [167]) at 532 nm and pulse energies of 2 J, 4 J and 20 J respectively. To reduce thermal effects, the final amplifier's crystal is cryogenically cooled. In total, the pulse energy is boosted by these three multipass amplifiers to 9 J with a shot-to-shot root mean square (RMS) stability below 0.7 %[1]. The multipass amplifiers themselves are separated by spatial filters to remove high spatial frequency modulations from the beam profile and expand the beam diameter to 10 cm.

Before being compressed by the grating compressor, the pulses' wavefronts are measured by a Shack-Hartmann sensor and appropriate corrections to a deformable mirror are applied such that the wavefront becomes flat (Phase PtV $\approx 0.2\lambda$, Phase RMS $\approx 0.03\lambda$). This closed-loop adaptive optics ensures a homogeneous intensity profile on the delicate compressor gratings and leads to a Strehl ratio above 0.9. The spatial intensity profile is constantly monitored by a CCD camera measuring the leakage through one of the dielectric mirrors. The recorded brightness of these images is cross calibrated to the pulse energy and also serves as an energy meter during the experiments.

After compression down to $\tau \approx 27$ fs, the pulses can either be guided to the experimental chamber or fed to a sophisticated diagnostics setup used to further characterize and accordingly adjust the pulses. Aiming at maximum focal peak intensity, the following pulse properties are examined:

- Pulse front tilt ([168])
- Temporal pulse compression, diagnosed with a Grenouille (a device from Swamp Optics [169])
- Temporal intensity contrast, measured with a third-order autocorrelator ("Sequoia", sold by Amplitude Technologies [170])
- Spectral phase and spectral intensity, retrieved via self-referenced spectral interferometry (SRSI) by a "Wizzler" (a device from Fastlite [171–173])

A closed feedback loop between Wizzler and Dazzler applies corrections and fine-tuning to the spectral phase allowing for pulse durations close to the Fourier limit of ~ 20 fs.

From the compressor, the pulses are sent to the experimental chambers through a pumped beamline. The total losses introduced by the compressor and limited transmission through the beamline reduce the pulse energy to 35 %. Hence, optical pulses at a repetition rate of 5 Hz with an energy of 2.0 J to 3.1 J arrive at the target, corresponding to 70 TW to 110 TW.

[1] Due to the lower than specified energy threshold of the compressor gratings, the laser energy had to be reduced during the experimental campaign to 6 J before compression.

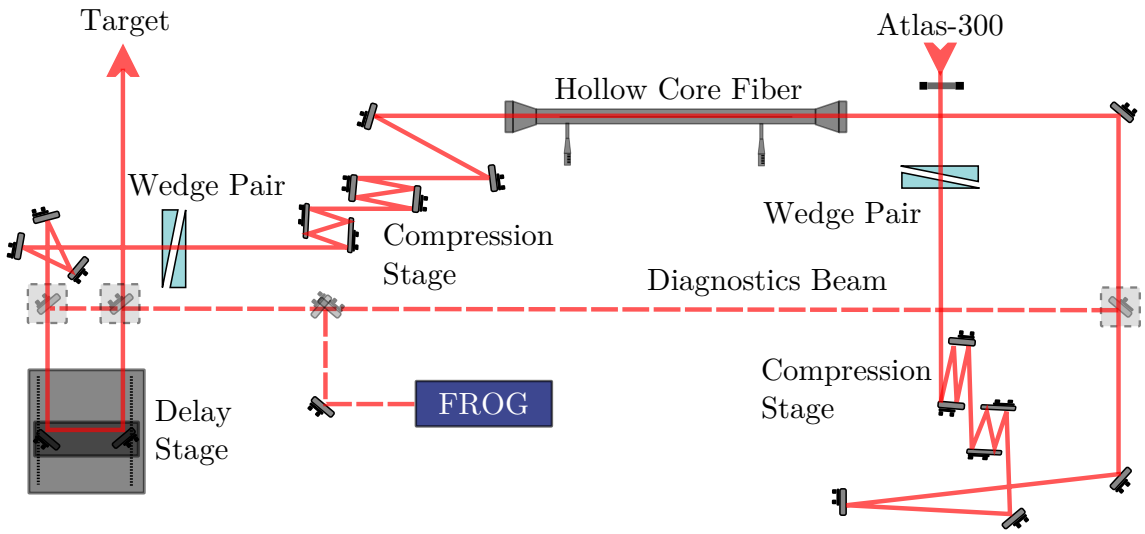

Figure 4.2.: *Schematic depiction of the probe setup. A small fraction ($\sim 2\,\%$) of the ATLAS beam is spectrally broadened in an argon-filled hollow-core fiber via SPM. A subsequent set of chirped mirrors in combination with a wedge pair creates a transform-limited pulse of less than 10 fs duration. The delay stage permits the temporal synchronization to the main laser pulse. The faintly drawn components are removable mirrors that are needed for probe alignment and probe diagnostics.*

When entering the chamber, a $1/2$" diameter beam part of the main laser is coupled out and reflected to the probe beam laser table [96, 174, 175]. A schematic depiction of this setup is given in Figure 4.2. Here, this pulse is spectrally broadened in an argon-filled hollow-core fiber via self-phase modulation (SPM) and further compressed to generate a few-cycle probe laser beam of less than 10 fs FWHM duration intended to transversely illuminate the target area. A delay stage compensates path differences to the main beam such that the probe beam is perfectly timed to record shadowgraphic snapshots of the laser-plasma interaction (cf. Figure 4.3) [96, 176]. These images are also used to retrieve the plasma density [177]. More details on these probe images are given in subsection 4.2.1).

An additional 1.5" mirror can be moved into the main beam path to generate a counter-propagating "injector" beam (cf. Figure 4.5 in section 4.2). The timing of this beam can be adjusted by an additional delay stage which changes the collider's beam path length. An $f/26$ off-axis parabolic mirror (OAP) focuses the colliding beam at an angle of 173° to the main beam. The timing and position of the focus are both chosen such that this counter-propagating pulse collides with the main laser pulse at the position of the gas target to optically inject particles (cf. section 2.6.6 and its application in section 6.2). The colliding beam has an energy of $\sim 0.3\,\mathrm{J}$, corresponding to a normalized vector potential of ~ 0.9. The main part of the laser pulse, however, is focused by an off-axis $f/25$ OAP to a

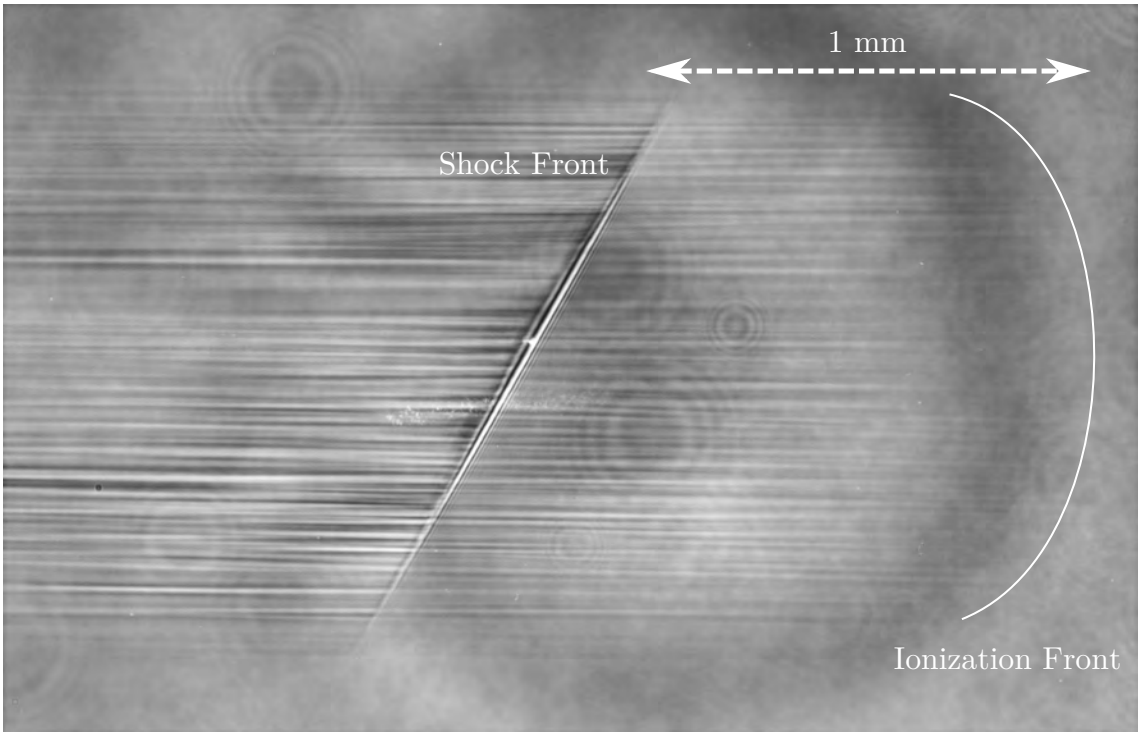

Figure 4.3.: *Shadowgraphic image of the gas shock front. The laser driver is propagating from left to right and ionizes the hydrogen gas. The beginning of the plasma filamentation marks the ionization front of the laser pulse. The shock front generated by a silicon wafer is clearly visible as well as injection radiation ([178]) in the center of the image. The circular diffraction rings are generated by dust particles on the imaging optics.*

FWHM spot size of $\sim 30\,\mu m$. A wedge can be moved into the attenuated beam to image the focal spot by a microscope objective onto a charge-coupled device (CCD) camera. An image of the focal spot of the main beam is given in Figure 4.4(a). The intensity for this focal spot is measured to peak at $\sim 8 \times 10^{18}\,W\,cm^{-2}$, which corresponds to a vacuum $a_0 \approx 1.9$ (according to Eq. (2.26)). Around 30 % of the pulse energy is concentrated in the spatial FWHM around the maximum intensity. A high dynamic range ($> 10^4$) image reconstructed from four different focal spot pictures with attenuations varying from ND0 to ND3 is given in Figure 4.4(b).

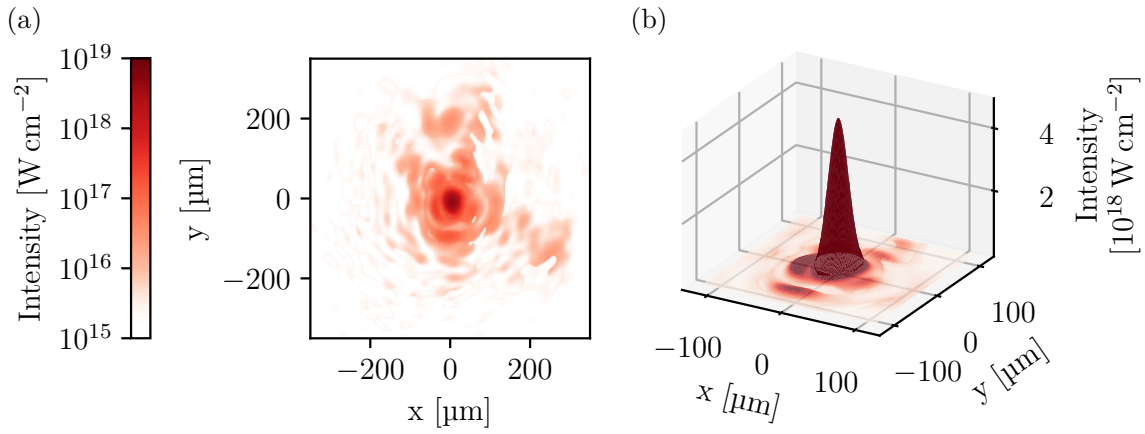

Figure 4.4.: *Focal intensity distribution of the ATLAS-300 laser. A logarithmic plot of the intensity profile in the focal plane is given in (a), whereas a linear surface plot showing the focal intensity profile in a close-up is shown in (b). These high dynamic range plots are composed of four single images of the focal spot with different but well-known attenuation. Detailed quantities are given in the main text.*

4.2. Experimental Chamber

Figure 4.5 shows a CAD drawing of the vacuum chamber used to perform the experiments. The major components besides the driving laser pulses, which have already been described above, are the target that provides the hydrogen gas, and where the laser-plasma interaction ultimately accelerates electrons. The electron spectrometer utilized to determine the accelerated bunch parameters is located at the very end of the chamber (right side in Figure 4.5). The following sections describe these key components in more detail.

4.2.1. Gas Target

Typical gas targets for LWFA are gas cells or supersonic gas jets. Whereas gas cells are mainly employed to examine self-injection in a turbulent-free environment, gas jets are used in our experiments to study advanced injection schemes, in particular shock front injection. A picture of the target area is shown in Figure 4.6.

Here, a de Laval nozzle with an orifice of 5 mm (Mach number ~ 6.3, [179]) was installed upon a hexapod to generate a supersonic gas jet into which a sharp edge of a silicon wafer projects (cf. Figure 4.7(a)). By interrupting the supersonic gas flow, it creates a shock front that introduces a sharp density down ramp which is used to inject plasma electrons into the wake structure (cf. section 2.6.6). The plateau gas density which follows the

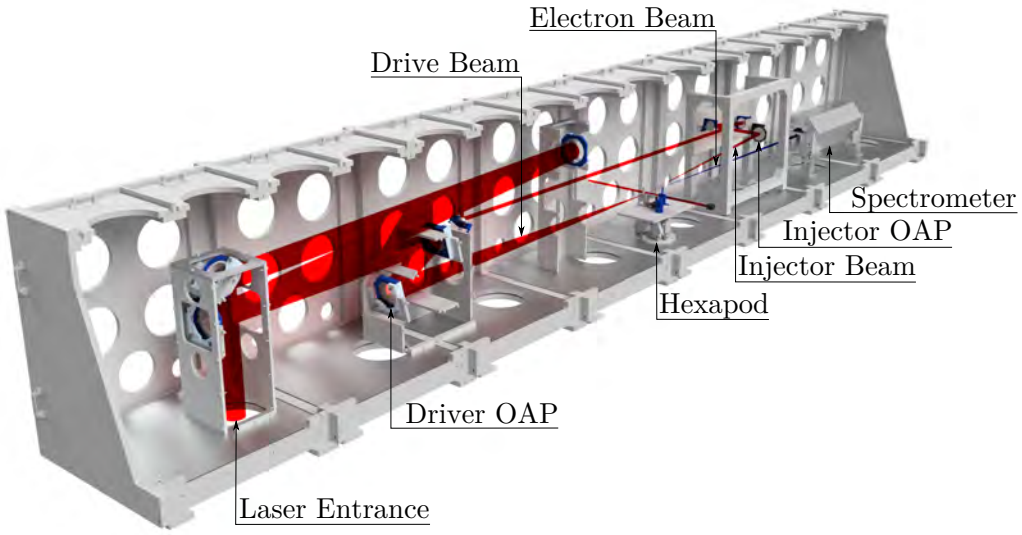

Figure 4.5.: *CAD drawing of the experimental chamber. The main laser and injector beam paths are shown in red. They are folded by mirrors which are mounted in aluminum towers. The gas target is placed on top of the hexapod together with the focus diagnostics. The electron spectrometer is situated at the very end of the chamber. Turbopumps (not shown here) attached to the bottom of the chamber extract the hydrogen gas. The total length of the chamber is 8 m.*

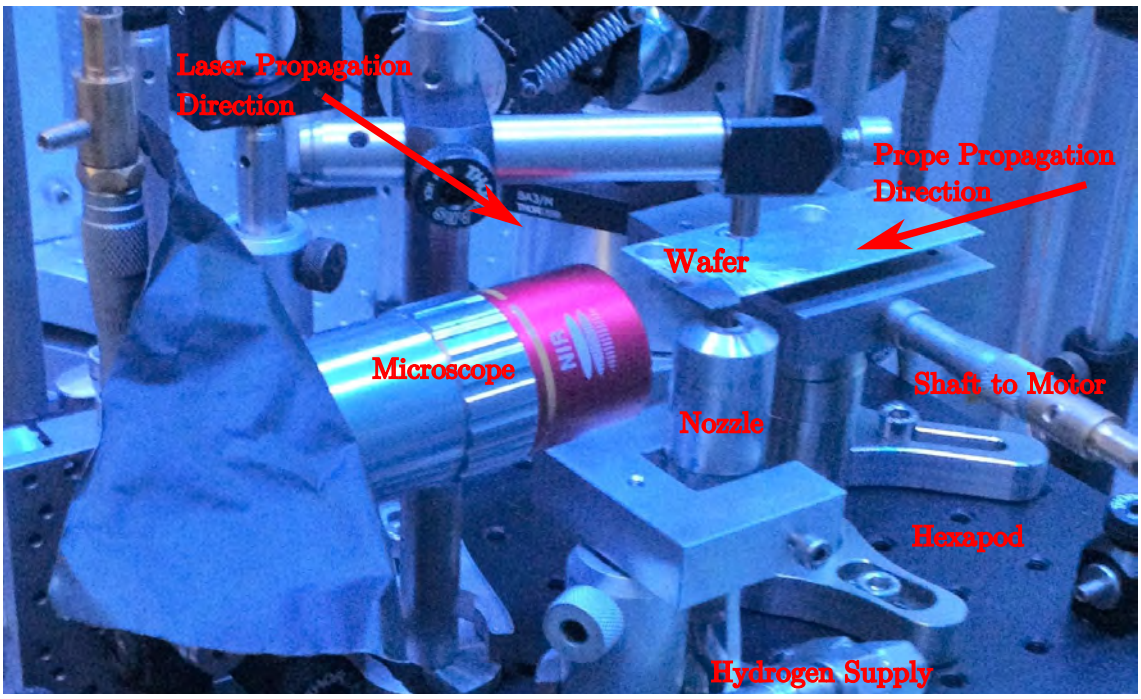

Figure 4.6.: *Picture of the target mounted on top of a hexapod. The major components are labeled. For reference: the diameter of the gas nozzle's orifice is 5 mm.*

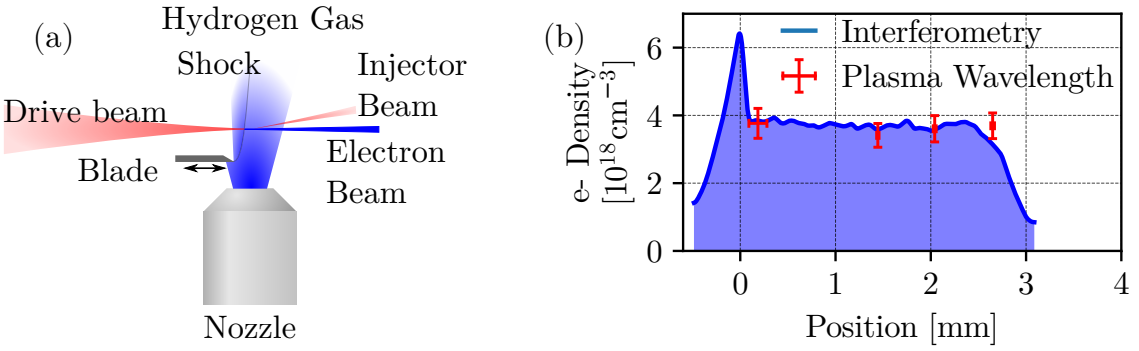

Figure 4.7.: *Schematic drawing of the target setup (a) and retrieved gas density profile (b). The 5 mm nozzle is mounted on a hexapod to be movable in all directions. A sharp knife edge protrudes into the supersonic gas jet to generate a shock – an abrupt jump in the gas density. The gas density profile in (b) is interferometrically retrieved (blue) by the setup described in Figure 4.8. The sharp density jump is followed by a density plateau of ∼ 2.5 mm length. The red data points mark spots where the density has also been determined by measuring plasma wavelengths. They represent the mean of seven to eleven distinct measurements at each marked position and are in good agreement with the interferometric density retrieval.*

sharp down ramp was adjusted to values between $3.0 \times 10^{18}\,\mathrm{cm}^{-3}$ to $4.0 \times 10^{18}\,\mathrm{cm}^{-3}$ for the experiments described below (cf. Figure 4.7). The ratio between the gas density of the shock and the plateau depends on the Mach number of the nozzle [180]. The gas jet is triggered ∼ 5 ms before the arrival of the laser pulse to establish a steady-state and reproducible gas flow. The hydrogen gas that floods the vacuum chamber is removed by four turbopumps. Depending on the gas pressure applied to the nozzle, the hydrogen load on the pumps limits the maximum shooting frequency to ∼ 2 Hz. The supersonic gas jet has been characterized interferometrically to determine the plasma density present during the interaction process, cf. Figure 4.7(b). To do so, a Nomarski-type interferometer was set up. A scheme of this setup is given in Figure 4.8. When passing through the target area, the phase shift induced by the plasma spatially distorts the probe beam. The latter is afterward split up into two orthogonally polarized pulses by a Wollaston prism. A subsequent polarizer aligns the polarization of both beams which are then recombined such that undisturbed parts from one beam overlap with disturbed ones from the other, resulting in a characteristic fringe pattern. This interference pattern is imaged onto a CCD. The imprinted phase shift results in a deformation of the uniform fringe pattern and can hence be extracted. By assuming rotational symmetry, the three-dimensional gas distribution and its density are retrieved via Abel inversion [179, 181, 182]. The resulting

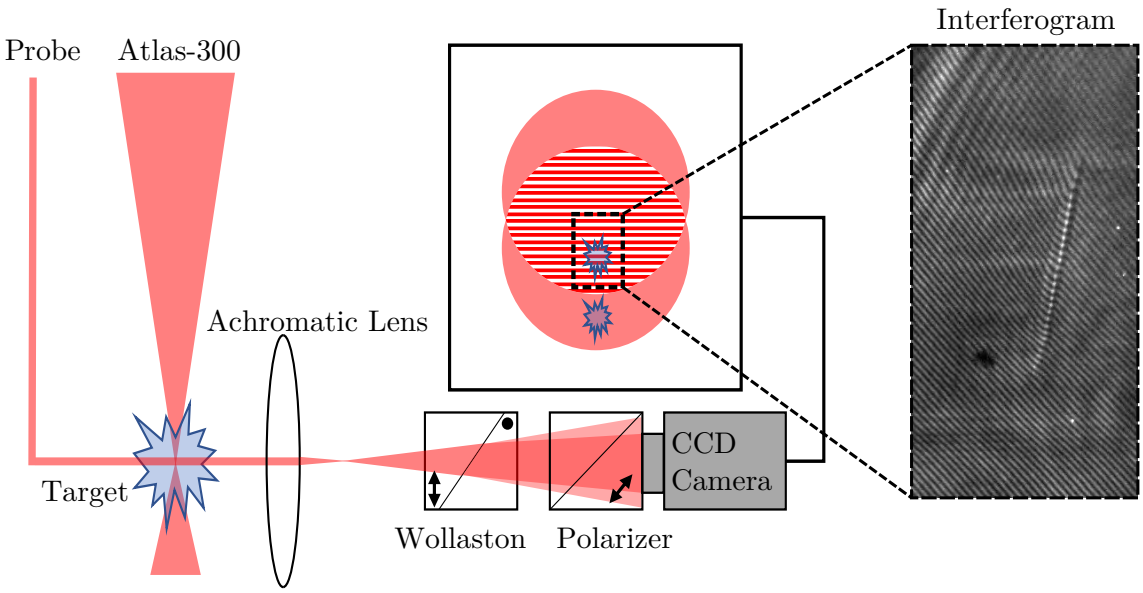

Figure 4.8.: *Sketch of the Nomarski-type interferometer setup. The probe beam illuminates the interaction of the main laser pulse with the hydrogen gas target. A Wollaston prism together with a polarizer creates two partially overlapping beams on a CCD. The gas density can be retrieved by distortions of the interference pattern. For clarity, several optical components (beam splitters, neutral-density filters, imaging optics) have been omitted in this drawing. Further details are given in the main text.*

gas density profile is plotted in Figure 4.7(b) and was adopted to set up PIC simulations (cf. section B.2).

Unfortunately, this method requires a sophisticated post-analysis of the shadowgraphic images and renders a live density retrieval inconvenient. Yet, a less accurate but much faster way to locally determine the gas density is provided by measuring the plasma wavelength on shadowgraphic snapshots of the laser-plasma interaction (cf. Figure 4.9). With the approximation $\lambda_{p,n}(a_0) \approx \lambda_p$ (cf. Eq. (2.115)), the electron density can be determined via Eq. (2.39). This however requires sharp, high-contrast images of the plasma wave. Nevertheless, both methods yield very similar results (cf. Figure 4.7(b))[1].

4.2.2. Electron Diagnostics

The accelerated electron bunch is characterized for each shot by a magnetic spectrometer located at the end of the vacuum chamber (cf. Figure 4.5). The distance between the nozzle and the entrance of the spectrometer amounts to 2.1 m. The spectrometer itself is composed

[1] More details about the interferometric gas density reconstruction may be found in [181–183].

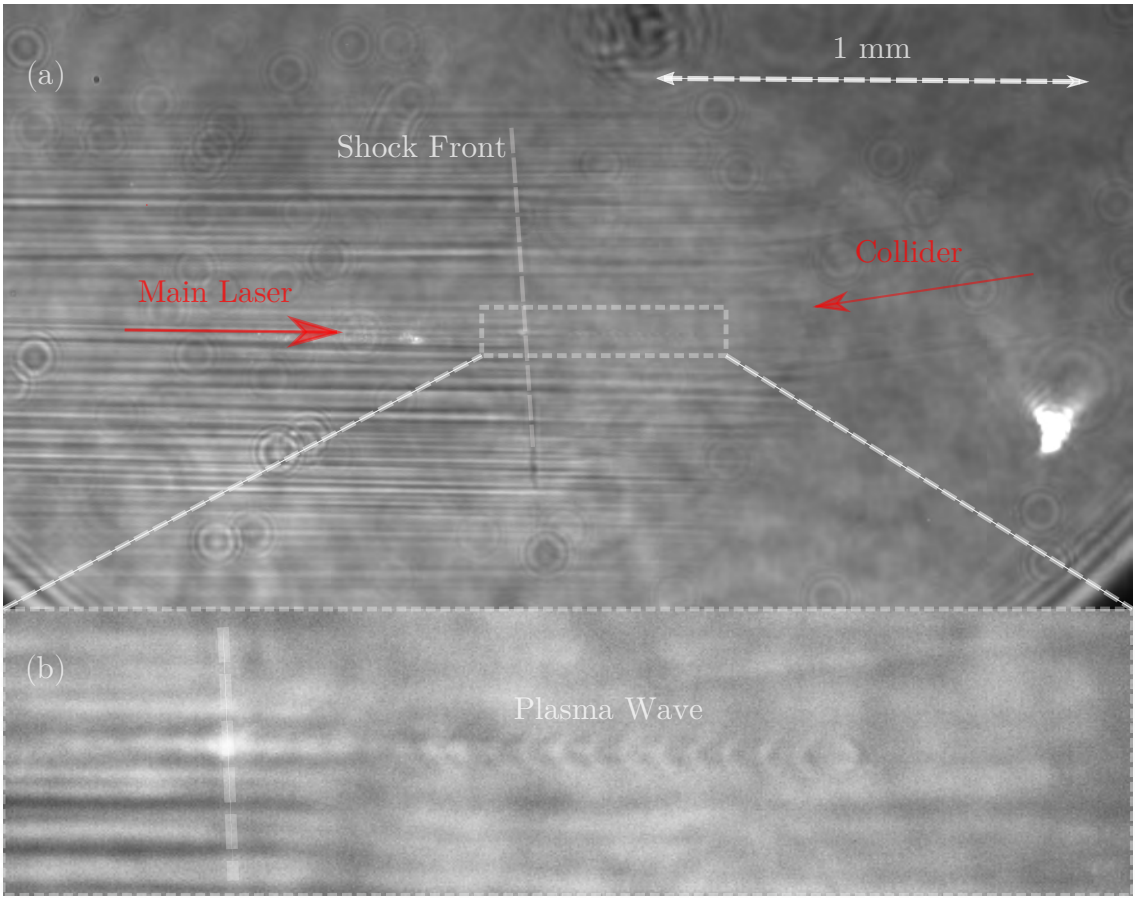

Figure 4.9.: *Shadowgraphic image of colliding pulse injection and a laser-driven plasma wave. (a) The main laser pulse is traveling from left to right, whereas the colliding beam propagates in the opposite direction. Plasma filamentation visible as horizontal dark and bright lines mark the laser beam path. A shock front forms at the very spot where both beams collide [184]. The plasma wave visible at the right of the shock front is magnified in (b). The pronounced ring structures are caused by diffraction at dust particles located in front of the CCD camera. Both images are unprocessed data.*

of eight permanent dipole magnets with 40 mm gaps, which are mounted with the same orientation and are firmly attached to a steel yoke. The accumulated length of these eight magnets sums up to 0.8 m. The magnetic field residing in the gap at an absolute height between 195 mm and 345 mm above the breadboard has been mapped by calibrated Hall probes and averages to 0.85 T. Scintillating screens (usually called "lanex") manufactured by CAWO and commercially sold under the specification "OG16" [185] are positioned at the entrance and beneath the magnets. Being hit by electrons the phosphorous materials which these screens contain, convert a fraction of the deposited particle energy into photons peaked around a wavelength of 546 nm. The corresponding fluorescence lifetime of ~ 1 ms [186] is short enough to support single shot diagnostics up to 1 kHz [187]. CCD cameras triggered by the laser system record and save images of these fluorescing lanex shot by shot. The accelerated electrons are detected on two different scintillating screens: Once before entering the spectrometer and after being deflected downwards by the spectrometer's magnetic field. The first screen is used to determine the pointing angle, the shot-to-shot pointing jitter and the divergence of the particle beam – hence its name "pointing lanex". It can be flipped in and out of the particle beam path and is located 1.8 m behind the target. The pointing angle determined by this screen is crucial for the energy determination of the particle beam, as the energy calibration of the spectrometer depends on the particles' incident angle. Images of the pointing lanex in false colors are shown in Figure 4.10. The second scintillator called "espec lanex" resolves the charge density and energy spectrum (cf. Figure 4.11). For this purpose, the electrons' trajectories through the magnetic field depending on their momentum and incident angle were traced (cf. Figure 4.12) and the spectrometer accordingly calibrated (cf. Figure 4.11(a))[1]. At a specific incident angle, the electron's point of intersection with the espec lanex is unique for a certain momentum. This energy-position relation is plotted for various incident pointing angles in Figure 4.13. The response for both lanex screens is linear for charge densities up to $\sim 33\,\mathrm{pC\,mm^{-2}}$ [189], which is around one order of magnitude above the maximum peak charge densities measured on the espec lanex in our experiments[2].

For several shots, the pointing lanex was moved out of the beam path as it increases the electrons' divergence by scattering and therefore decreases the energy resolution of the spectrometer. Comparing consecutive shots where the pointing lanex has been moved in and out of the beam path alternately, the FWHM divergence measured in the transverse direction on the espec lanex increases by ~ 2.1 mrad from $\sim (1.6 \pm 0.2)$ mrad (pointing

[1] The magnetic field was initialized according to the Hall probe measurements. The software used for tracking the particles through the magnet spectrometer is developed and maintained by Pulsar Physics [188]. For this work, the General Particle Tracer version 3.03 was used.

[2] Charge densities on the pointing lanex, however, may exceed this threshold leading to saturation. Therefore, only the espec lanex was used to determine bunch charges and charge densities.

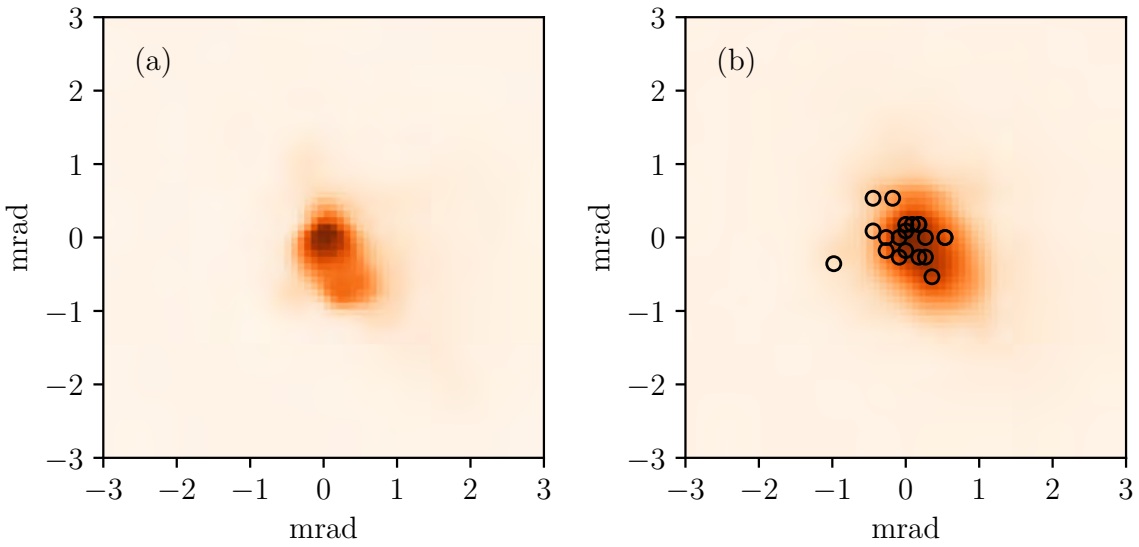

Figure 4.10.: *Image of the pointing lanex in false colors. In (a) an exemplary single shot is shown. In (b) the accumulated response of the scintillator for 20 consecutive shots is plotted. Their pointing jitters by ∼ 0.44 mrad (std). The position of maximum charge density for each shot is highlighted by black circles. Other parameters of the particle beams are given in the main text (cf. chapter 5).*

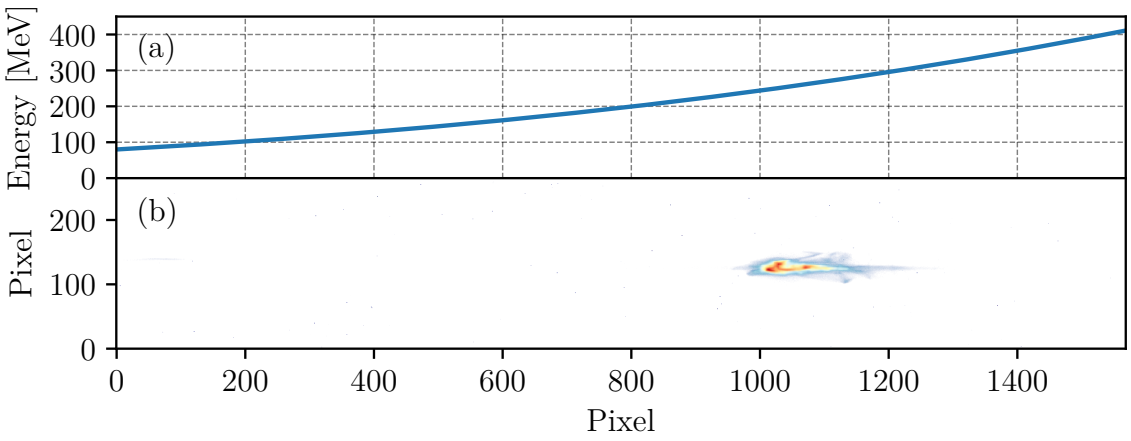

Figure 4.11.: *Energy calibration and raw data of the scintillating screen. In (a) the electron energy vs. pixel as determined by a particle tracker is plotted. The tracker simulates the electrons' trajectories through the magnetic field of the spectrometer depending on their energies. In (b) an exemplary shot as raw data on the energy lanex is presented (in false colors). Further analysis of this shot may be found in the next chapter (see Figure 5.2).*

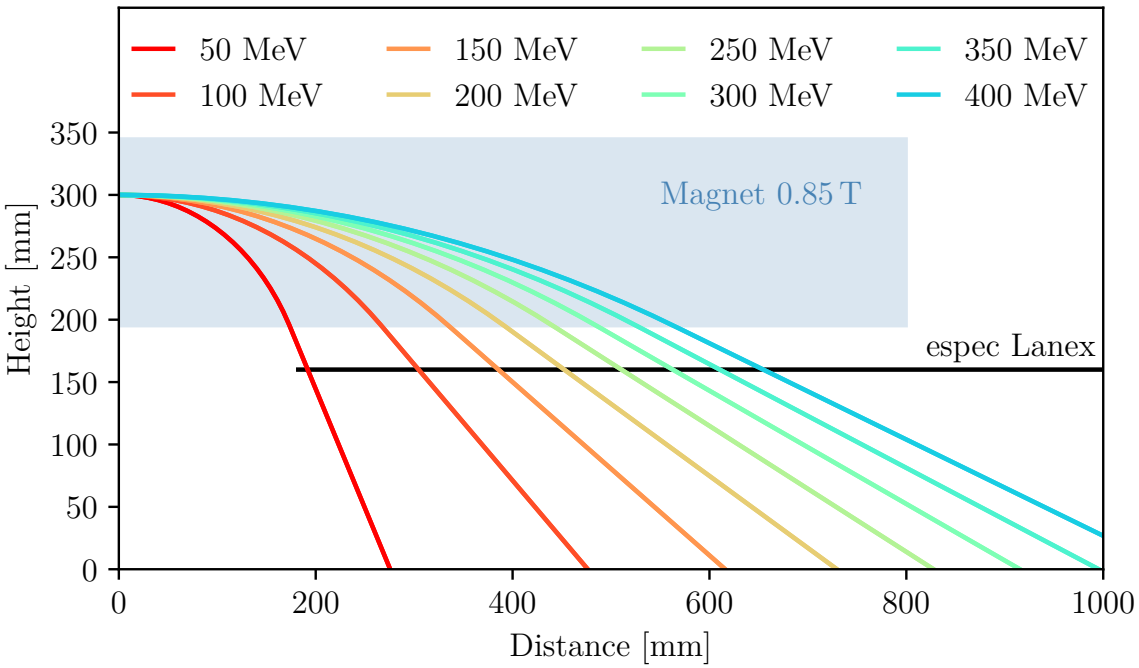

Figure 4.12.: *Energy calibration of the energy lanex. Assuming a horizontal beam path of the incident particles, the electrons enter the spectrometer at an absolute height of 300 mm. The magnetic fields deflect the charged particles on circular orbits. The radii of these orbits depend on the kinetic energies of the particles. Depending on this radius, the respective electrons leave the magnetic field at different longitudinal positions and hit the espec lanex after a free vacuum drift at an absolute height of 160 mm. Eight exemplary paths of electrons passing the spectrometer with energies between 50 MeV and 400 MeV are depicted. The respective longitudinal intersection of the trajectory with the lanex screen is characteristic for a certain kinetic energy allowing for a distance-energy correlation which is used to calibrate the espec lanex. Some calibration curves for different incident angles are given in Figure 4.13.*

lanex out) to $\sim (3.7 \pm 0.2)$ mrad (pointing lanex in). Provided the pointing lanex in front of the spectrometer is flipped into the beam path to determine the incident angle of the electrons, the energy calibration is adapted accordingly. Otherwise, the "0 mrad" curve in Figure 4.13 was applied for the energy calibration of the espec lanex. For the experimental campaigns, the electron spectrometer was set up to detect electrons in the range of 30 MeV to 500 MeV.

An absolute charge calibration of these screens was established by Buck *et al.* [189] and Kurz [190] and referenced to a light source which is glued onto the scintillating screens. From the recorded CCD images the relative brightness of this light source can be extracted and put in relation to the scintillator response. In that way, the charge determination

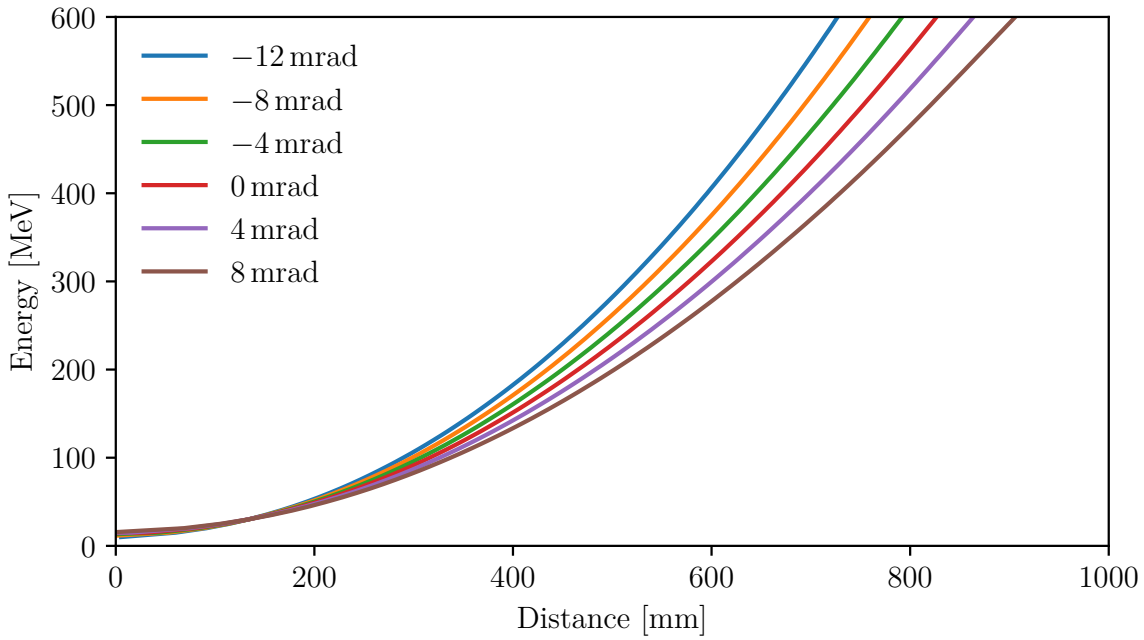

Figure 4.13.: *Pointing calibration of the energy lanex. Monoenergetic electrons entering the spectrometer's magnetic field with positive (negative) vertical momentum hit the scintillating screen at greater (smaller) distances. The distance-energy correlations for six different incidence angles were simulated and used for interpolation of pointing angles between −12 mrad and 8 mrad. By courtesy of H. Ding.*

becomes independent of the imaging optics [190]. This light source consists of a 12 mm long glass cylinder measuring 2 mm in diameter. It contains tritium gas, is hermetically sealed and is covered with scintillating material. The radioactive gas in this capsule decays exponentially and stimulates the surrounding scintillator via its beta decay [187]. The half-life of the gas together with the degradation of the scintillating material combines to a decay time of this light source of ~ 5 years [189]. The brightness reduction of this light source is measured and determined by a dedicated test setup [190]. Of course, the brightness reduction of the reference light source is taken into account when regularly recalibrating both the pointing and espec lanex[1].

In summary, the fluorescence response of the pointing and espec lanex allows us to determine several crucial beam parameters namely the divergence, pointing angle, absolute charge density, total charge, and energy spectrum[2].

[1] Details are given in Ding [183] and Kurz [190].

[2] Due to limited beam time, experimental setups to measure the remaining parameters like bunch duration and beam current were not operated ([54]) and hence need to be extracted from PIC simulations.

Chapter 5

High-Charge Electron Beams from Shock Front Injection

Advanced injection techniques offer the advantage of delivering monochromatic high-charge electron beams (cf. section 2.6.6). The shock front injection method used in our experiments provides unprecedented performance regarding the stability, total charge, spectral charge density and divergence of accelerated electron beams [38, 191]. These quantities are crucial parameters for future applications of LWFAs. Especially, the total charge which is linked to the beam current via the bunch duration is of eminent significance for the occurrence of beam loading effects, which will be discussed in the following chapter. Hence, a proper discussion of the performance of this LWFA is appropriate.

Figure 5.1(a) shows 100 consecutive angle-integrated electron spectra. The LWFA is driven by the ATLAS-300 laser system operated at 75 TW (power on target). The plateau plasma density for this run was measured[2] to be $n_0 = 3.0 \times 10^{18}\,\mathrm{cm}^{-3}$. We define the peak charge as the integrated charge density around the peak above a certain threshold relative to the maximum charge density. This threshold is often set to 0.5, corresponding to the full width at half maximum (FWHM). However, to study beam-plasma interactions, a measure that reflects the whole bunch charge more accurately is preferable. We therefore use 20 % of the peak charge density as threshold unless specified otherwise. This definition contains most of the peak charge while omitting the low charge "dark current" (see for instance Figure 5.1(b) and Figure 5.2). The mean charge within the peak is 338 pC and fluctuates by 11 % (36 pC RMS) at a mean peak energy of 216 MeV with 4 % shot-to-shot standard deviation (std) with a RMS divergence of (0.40 ± 0.09) mrad. Note that the accelerated charge is in good agreement with theoretical expectations, whereas the measured energy is a factor of ~ 3.5 lower than the predicted ideal energy gain (cf. subsection 2.6.7). We attribute the latter to a non-ideal energy gain disturbed by beam loading and an acceleration distance shorter than the depletion and dephasing length.

[2] The plasma density in this data set was determined by measuring the plasma wavelength, see subsection 4.2.1

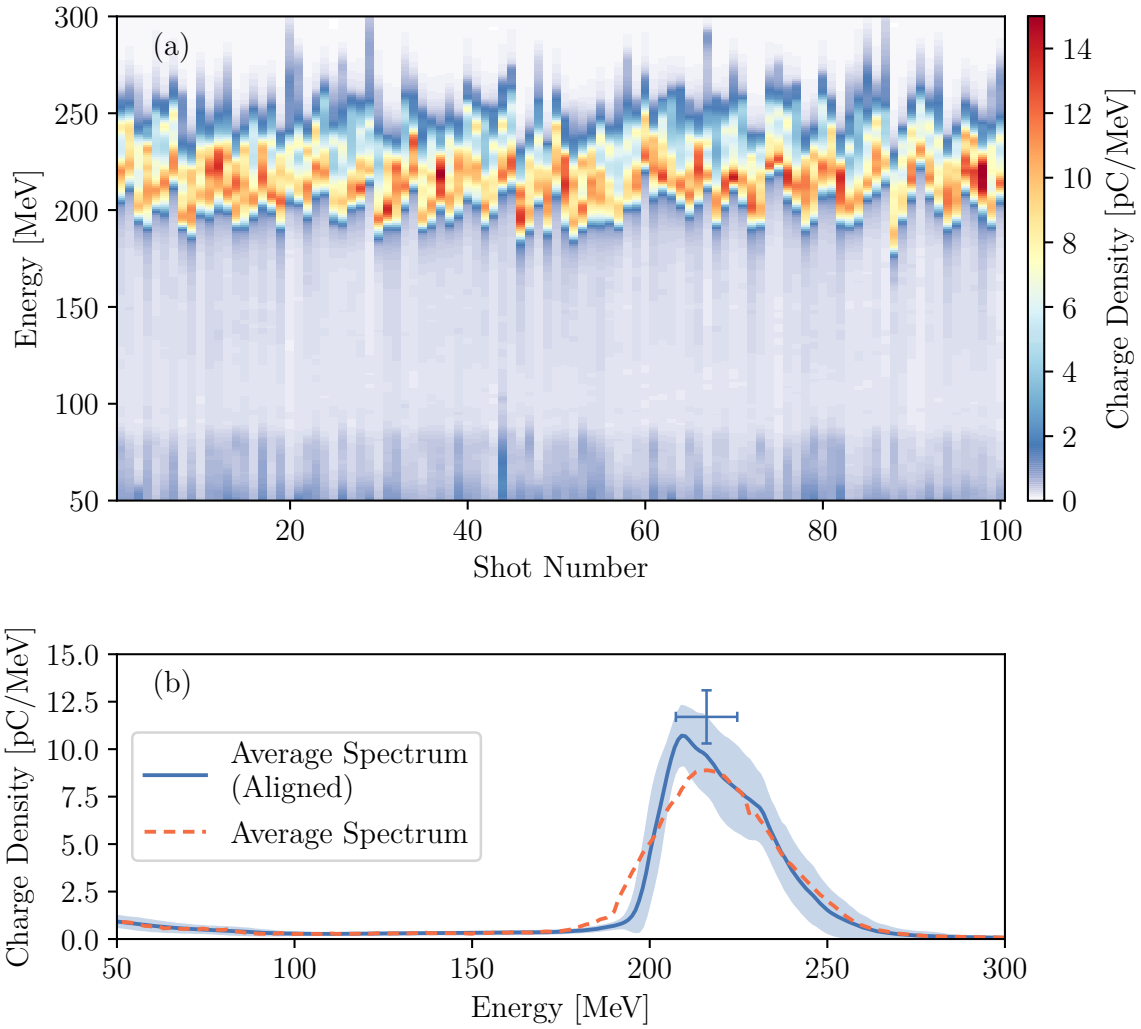

Figure 5.1.: *Shot-to-shot performance of the shock front injector driven by the 75 TW ATLAS-300 laser system. (a) The plot shows the angle integrated electron energy spectra of 100 consecutive shots with low charge and energy jittering. The spectral charge density is color-coded. A corresponding quantitative analysis is given in the text. (b) Calculated average electron spectra. The dashed orange line is the average of all shots presented in (a). Distinct features such as asymmetric charge distributions around the peak energy are obscured by shot-to-shot fluctuations. To preserve such features in the average, we have aligned the spectra according to their central energy (blue line). The error bars mark the fluctuation in energy and spectral peak charge density. Plot (b) by courtesy of A. Döpp.*

The FWHM absolute energy spread is (33.0 ± 7.2) MeV (RMS), corresponding to a relative energy spread of 15 %. The average peak charge density is $(11.7 \pm 1.4)\,\mathrm{pC\,MeV^{-1}}$, with up to $17\,\mathrm{pC\,MeV^{-1}}$ for some shots. Note that the individual shots in Figure 5.1(a) have a distinct spectral shape, with many of them being skewed towards lower energy (i.e., exhibit a tail at higher energies). These features are lost when calculating the average spectrum since shot-to-shot fluctuations naturally lead to a normally distributed average. We have therefore realigned all the spectra according to their central energy (determined via a Gaussian fit) to preserve such features – as depicted by the blue curve in Figure 5.1(b).

At the beginning of the experimental campaign, for some shots, the laser power was increased to 110 TW on target (corresponding to ~ 3 J, respectively ~ 8.5 J before the compressor). Due to the increased fluence and first appearances of damages on the compressor gratings, the laser power was later kept below 75 TW on target (~ 5.8 J before the compressor). For these high-energy shots, we observe peak charges around 440 pC and a total accelerated charge in the energy range above 100 MeV of 650 pC. The peak charge density exceeds $18\,\mathrm{pC\,MeV^{-1}}$. An exemplary 110 TW shot is shown in Figure 5.2. The one-dimensional divergence of this shot was measured on the espec lanex (since the pointing lanex was flipped out) and amounts to 0.71 mrad (RMS). The total energy of the electron beam observed on the espec lanex is 160 mJ. This corresponds to an energy transfer ratio of ~ 5.3 % from the laser pulse to the electron beam. As expected, and theoretically predicted by subsection 2.6.7, the accelerated charge increases with the laser power. A laser power scan to experimentally determine this scaling is presented in the following section.

The generated peak charges beyond 300 pC and particle beam energies above 100 mJ indicate that shock front injection has evolved to a technique capable of delivering joule-class electron beams with the benefit of a distinctly localized injection position [2, 3]. Given the total length of the acceleration stage, average accelerating fields can be deduced, which makes this advanced injection technique attractive for a quantitative analysis of beam loading effects.

5.1. Influence of Laser and Gas Target Parameters

The exact configuration of the gas jet as well as the properties of the focused laser pulse deeply influence the laser-plasma interaction and accordingly affect the outcome of the acceleration process [191]. Characteristic parameters of the driving laser pulse and the gas jet have been studied in greater detail in the scope of this work both experimentally and theoretically. These parameters are not only central to the stability of the accelerator

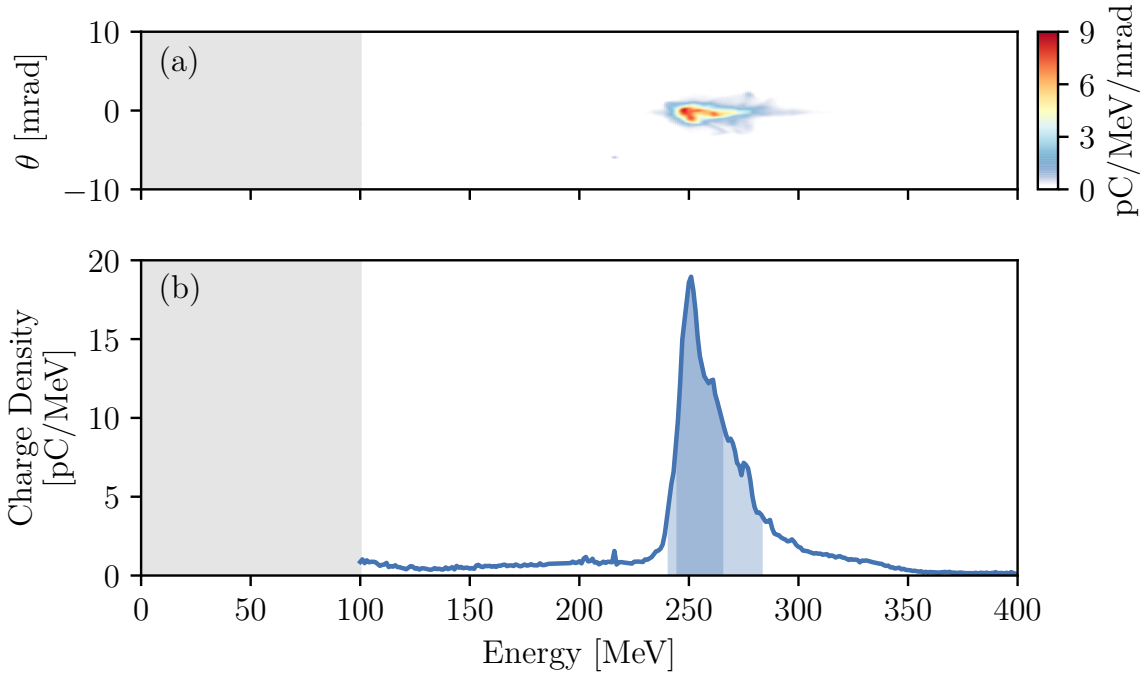

Figure 5.2.: *Electron spectrum of a 110 TW shot. The total charge above the detection threshold of 100 MeV is 665 pC. The peak charge (lightly shaded area) contains 66 % of the total charge (i.e., 440 pC). The charge within the FWHM (darker shaded area, 299 pC) lacks the higher energetic part of particle bunch and is therefore inappropriate to determine accelerated bunch charges. The spectral charge density peaks at 250 MeV with 19 pC MeV^{-1}.*

but also handy to adjust the charge and energy of the particle beam as will be shown in the following. Note that all theoretical parameter scans presented in the following span different parameter spaces which intersect at a single point characterized by the laser power $P = 50\,\mathrm{TW}$, the focus position (relative to the shock front) $z_\mathrm{f} = 0\,\mathrm{mm}$, the shock width equal to λ_p and the maximum gas density at the shock of $n_\mathrm{peak} = 2n_\mathrm{e}$.

5.1.1. Scalings with Key Laser Parameters

In the scope of this work, two key parameters characterizing the laser pulse – namely the laser power and longitudinal focal spot position – and their effect on the accelerated electron bunch are examined.

Laser Power In order to study the electrons' dependence on the laser power, we varied the laser energy from 0.5 J to 2 J by detuning the delays of the pump lasers for the final

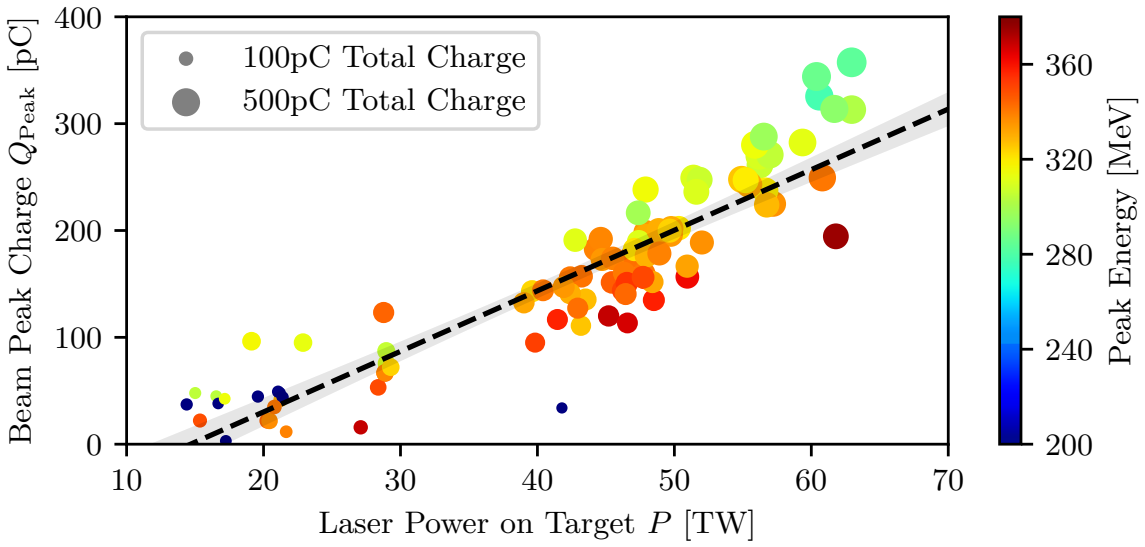

Figure 5.3.: *Measured peak charges of the electron spectra vs. laser power. The size of the dots denotes the total charge of the electron bunch and the color encodes the central energy of the peak. Note that this plot already shows beam loading as lower electron energies (greenish dots) tend to be above average peak charge, whereas higher energies (reddish dots) are generally located at lower peak charges. A linear fit (black dashed line) and its corresponding 95 % confidence interval (transparent gray area) show the correlation between laser power P and peak charge Q_{peak}.*

amplifiers. In this way, the amplifiers' gain drops while thermal lensing [192, 193] remains almost unaffected. The pulse energy for each shot was recorded by a cross-calibrated leakage diagnostic (cf. section 4.1). Figure 5.3 shows the corresponding data with 100 consecutive shots.

A linear fit correlates the laser power to the peak charge according to

$$Q_{\mathrm{Peak}} \approx 5.5\,\mathrm{pC} \times \left(P[\mathrm{TW}] - 15\,\mathrm{TW}\right), \tag{5.1}$$

where 15 TW is the minimum laser power P_{inj} for injection to occur for this driver and target configuration. The fact that for this power on target range evidently a linear correlation between laser power and peak charge is established is no contradiction to the theoretically deduced $Q_{\mathrm{peak}} \propto \sqrt{P}$ scaling (cf. Eq. (2.161)) as the latter always assumes a *fully* loaded wakefield. Our measurements at these driving powers, however, probe the regime of *partially* loaded wakefields. Corresponding simulations are plotted in Figure 5.4 and suggest that the theoretically predicted $\sqrt{P}$ scaling regime is retrieved for laser powers above $\sim$ 100 TW. Below this value, a linear correlation between the charge and laser power fits the data best.

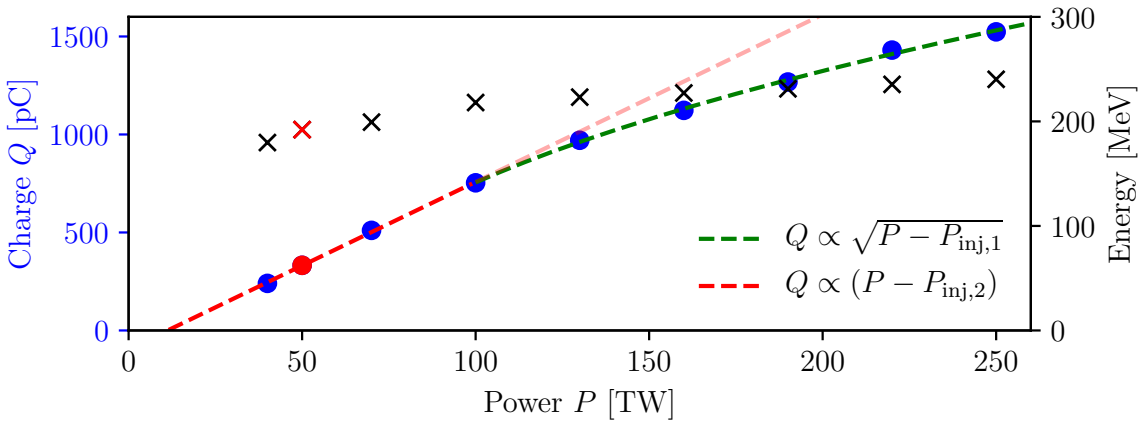

Figure 5.4.: *Simulated accelerated bunch charge (dots) and energy (crosses) for different laser powers. Below 100 TW the charge correlates linearly with the laser power as experimentally observed (dashed red line). The linear fit parameters deduce an injection threshold of $P_{inj,2} \approx 11$ TW. Above 100 TW the theoretically predicted $\sqrt{P}$ scaling fits the simulated data best (dashed green line). The simulations are in good agreement with experimental data for the accelerated charge, peak energy, and injection threshold P_{inj} (compare to Figure 5.3). The red data markers tag the intersection point of all scanned parameter spaces.*

Laser Focus Position A second method to adjust the injected charge is realized by bringing the target longitudinally in and out of focus. This is done by moving the whole target setup with the hexapod. The amount of charge that can be trapped by a sudden plasma density change depends on the bubble radius R which scales as $R \propto \sqrt{a_0/n_e}$ (cf. Eq. (2.130)). Hence, by shifting the target and hereby controlling the laser intensity at the position of the shock, the number of accelerated electrons can easily be adjusted. In order to quantify this effect, we have simulated different longitudinal focal spot positions from -1 mm to 1 mm in 20 equidistant steps relative to the shock front (cf. section B.3). Eleven of these simulations are displayed in Figure 5.5. This scan implies that the shock injection process is even sensitive to focal shifts in the range of ~ 0.2 mm, which is well below the Rayleigh length of ~ 1.1 mm. For our optical setup, such a focus shift corresponds to a wavefront curvature in the near field of $\Delta\lambda \approx 40\,\mathrm{nm} = \lambda/20$. Wavefront fluctuations on this order of magnitude can easily be induced by unsteady thermal lenses in the laser amplification stages or air turbulence in the optical beam path. Hence, these fluctuations intensify for large beams and long beam paths as is the case for the ATLAS system [194]. This insight not only supports the need for wavefront stabilization for the driving laser but might also explain one major cause for shot-to-shot fluctuations in the presented electron data.

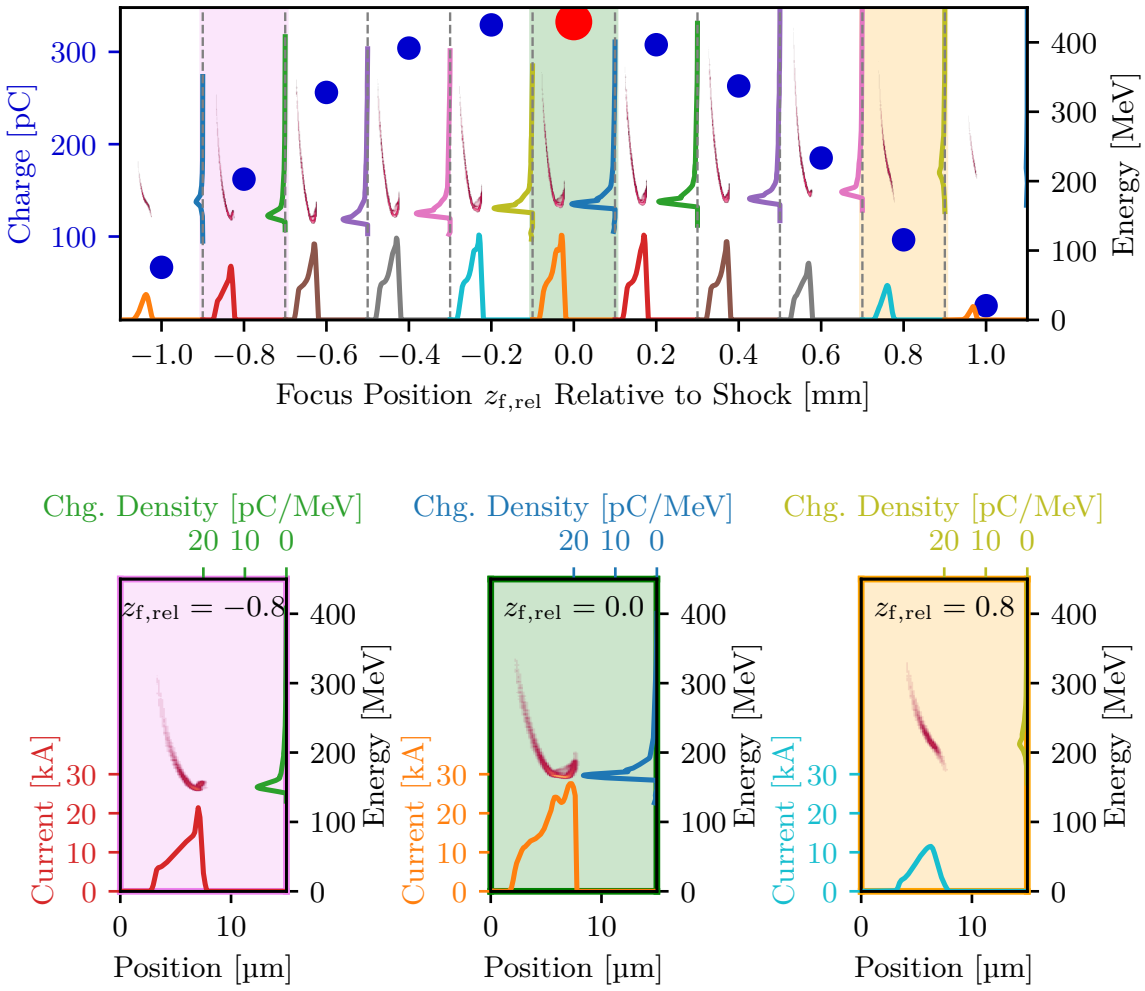

Figure 5.5.: *Simulation study of the influence of the longitudinal focus position relative to the shock front [38]. For each data point, the beam charge (blue dot), the current (bottom graph), integrated energy spectrum (right graph), and phase space are plotted. The red dot marks the position $z_{f,rel} := z_f - z_{shock} = 0$ and was used as the reference case for all other scans (cf. section B.3). The bottom row highlights the results for three distinctive laser focal positions which include further details on the current profile, electron bunch length, and spectral charge density. Note, that the shape of the electron phase space and the corresponding energy spectra change with the amount of injected charge. This beam loading effect will be discussed in chapter 6.*

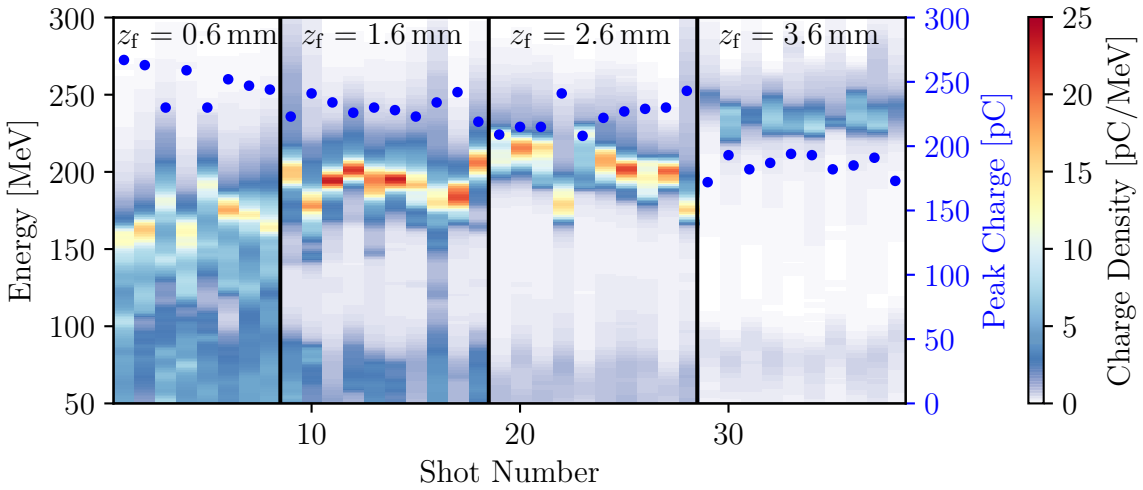

Figure 5.6.: *Experimental focus position scan. The data show 38 consecutive electron spectra with different longitudinal focal spot position. More positive (negative) values correspond to focal shifts towards the beam dump (parabola). A large focal detuning produces less charge (blue dots) but higher peak energies, which confirms the findings deduced from simulations. Note the peak spectral charge densities above 20 pC MeV^{-1} for the spectra at $z_f = 1.6$ mm. These charge densities were among the highest recorded in LEX. Unfortunately, the scan was aborted at $z_f = 0.6$ mm and does not contain negative focus positions.*

The experimental data support this theoretically deduced correlation as shown in Figure 5.6. In the $z_f = 0$ setting, the focus of the attenuated beam is at the same longitudinal position as the edge of the silicon wafer. The scan starts at $z_f = 3.6$ mm. Unfortunately, the step size of $\Delta z_f = -1$ mm is very large, and the scan was aborted when reaching $z_f = 0.6$ mm. Nevertheless, we can confirm, that the peak charge drops whereas the peak energy increases for larger longitudinal focal detuning. In contrast to simulations, the accelerated charge shows a less sensitive dependence on the focal spot position as electrons are even accelerated with a focal shift of more than ± 1 mm.

5.1.2. Scalings with Key Target Parameters

Besides varying the driver's parameters, we have also examined changing gas target parameters, namely the height and width of the shock front. To assess their respective influence experimentally, changes in the shock width or height respectively must not affect other parameters like the plateau gas density or acceleration length. This is, however, difficult to accomplish. For example, increasing the vertical distance between the focal spot position and the gas target, of course, decreases the height and increases the shock

width simultaneously, but also modifies the plateau gas density (cf. [179]). This makes it impossible to extract correlations between the accelerated electron bunch and one single target parameter. Therefore, we rely on FBPIC simulations to study the influence of changing shock front heights and widths and to determine respective correlations with the electron beam charge or energy.

Shock Width By keeping the plateau gas density and the peak density constant but varying the width of the down ramp, the density gradient and its influence on the injected charge can be studied. The simulated density profiles are plotted in Figure 5.7(b). This study is of particular interest since the width of the shock front itself cannot be derived from interferometric data. On the one hand, Abel inversion assumes axial symmetry which is violated by the non-vertical course of the shock[1]. On the other hand, the probe beam is diffracted by this density transition, which distorts the interferometric images. Hence, the density reconstruction from interferometric data for the shock front is therefore fraught with greater uncertainty. Our findings based on PIC simulations, however, suggest only a minor influence on the accelerated electrons for shock widths in the range of $0.1 \times \lambda_\mathrm{p} \approx 2\,\mu\mathrm{m}$ to $5 \times \lambda_\mathrm{p} \approx 100\,\mu\mathrm{m}$ (cf. Figure 5.7). Neither the accelerated charge nor the energy significantly depends on this parameter. It is therefore fair to assume a reasonable transition length of $\sim \lambda_\mathrm{p}$ and to generally adopt this transition width for further shock front simulations.

Shock Height To determine the LWFAs sensitivity on the absolute height of the density jump, the peak gas density n_peak at the shock was varied for nine different simulations between $1.2 \times n_\mathrm{e}$ and $4.2 \times n_\mathrm{e}$, where $n_\mathrm{e} = 3.0 \times 10^{18}\,\mathrm{cm}^{-3}$ is the plateau gas density. On the scale of one plasma wavelength, the density drops from n_peak to n_e for all these simulations. The corresponding gas densities are plotted in Figure 5.8(b). For higher gas density jumps we observe more injected charge but less final bunch energies as depicted in Figure 5.8(a). The charge dependence complies well with a $Q \propto \sqrt{n_\mathrm{peak} - n_\mathrm{peak,0}}$ scaling, where $n_\mathrm{peak,0} \approx 1.17 \times n_\mathrm{e}$ (see green fitted line in Figure 5.8(a)). These effects become clear when recapitulating the physics of shock front injection (cf. section 2.6.6). The prompt radial increase the bubble experiences when passing through the density down ramp scales as $R \propto n_\mathrm{e}^{-1/2}$ according to Eq. (2.130). Hence, larger jumps lead to a more pronounced growth of the bubble volume and thus more electrons are injected. The hereby associated effect of decreasing final bunch energies is a direct consequence of beam loading and will be elaborated on in the following chapter 6.

[1] A generalization of the Abel inversion which is less susceptible to such asymmetries is developed in Sävert [181].

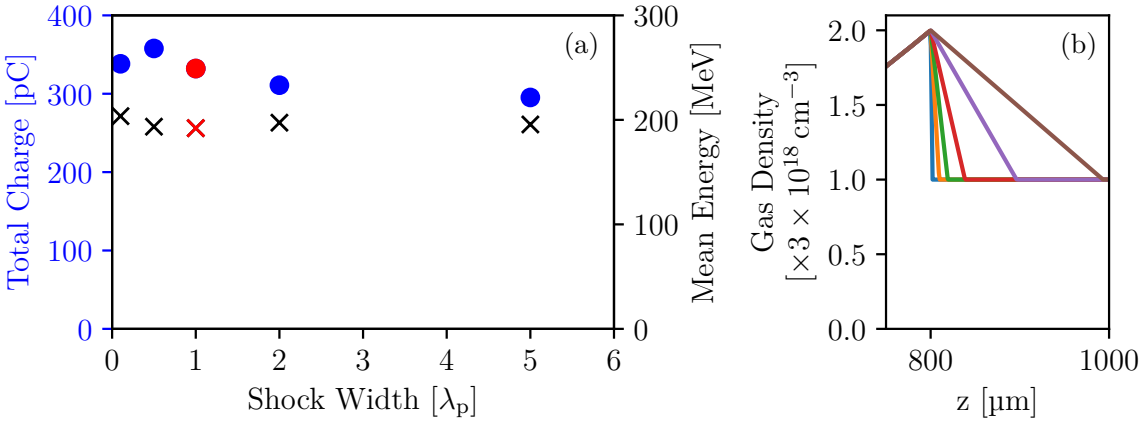

Figure 5.7.: *Simulation results of different shock widths (a) and corresponding gas density profiles plotted around the position of the shock at $z = 800\,\mu m$ (b). The peak gas density as well as the density plateau are kept constant. Neither the charge nor the energy shows a significant correlation with the gradient of the density down ramp. The red markers indicate the intersection point of all scanned parameter spaces.*

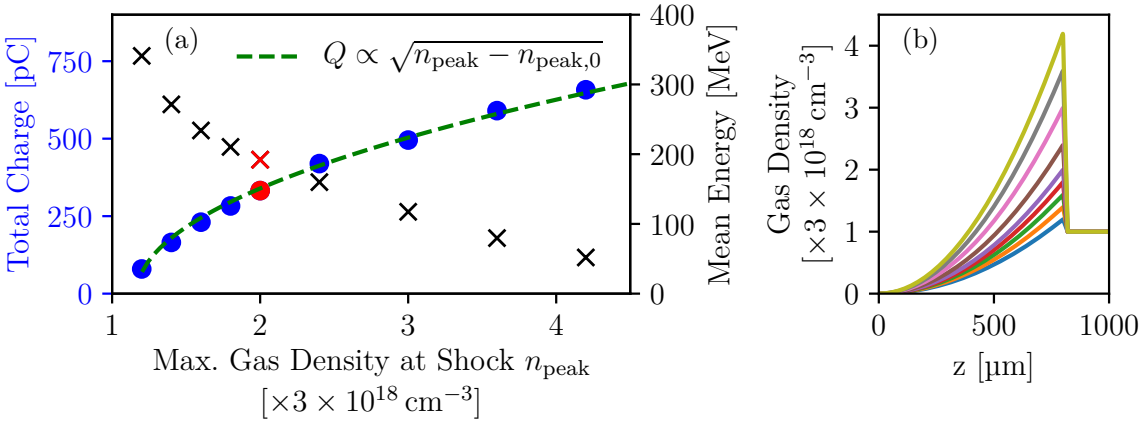

Figure 5.8.: *Simulation results of different shock heights (a) and corresponding gas density profiles plotted around the position of the shock at $z_{shock} = 800\,\mu m$ (b). The shock width as well as the density plateau are kept constant. Higher density jumps promote electron injection. Hence, the accelerated charge increases whereas the peak energy decreases. Again, the red markers indicate the intersection point of all scanned parameter spaces.*

Chapter 6

Experimental Study of Beam Loading

In this chapter, we present an in-detail experimental study of the interplay of the laser-driven wakefield with the one created by the accelerated particle bunch itself. The discussion of this so-called beam loading and its related effects in this chapter is split into two sections.

The first part of this chapter focuses on energy spectra of single electron bunches. Characteristic parameters like the peak energy, the energy spread and the skewness of the spectrum are examined relative to the peak charge. Two characteristic features for beam loading are discussed, firstly a negative correlation between beam charge and peak energy and secondly the skewness of the corresponding energy spectrum.

The second part of this chapter extends our analysis to dual-energy electron beams. Two distinct experimental setups are presented to generate longitudinally separated electron bunches in a driver-witness configuration. The two respective data sets are examined for charge-energy-correlations between the driving and witnessing electron bunch and hence allows us to analyze the accelerating fields in the first and second bubble. These intra-cavity and inter-cavity beam loading effects are explained by tailored PIC simulations.

PIC simulations which yield deeper insight into the underlying physics are provided and discussed throughout this chapter. As we present three different experiments, a separate sketch of the respective experimental setup is given at the very beginning of each section.

6.1. Effects of Beam Loading on the Energy Spectrum

To study beam loading effects, we analyze 91 consecutive shots with a plateau plasma density of $n_0 = 3.5 \times 10^{18}\,\mathrm{cm}^{-3}$. The experimental setup is similar to the one described in subsection 4.2.1. A schematic drawing of the experimental setup is given in Figure 6.1. On average, these shots contain $(123 \pm 35)\,\mathrm{pC}$ peak charge, spanning a range from 60 pC to 180 pC. Within the probed charge interval, the relative FWHM energy spread increases from $\sim 10\,\%$ for low charges to $\sim 30\,\%$ for high charges (cf. Figure 6.2). The maximum

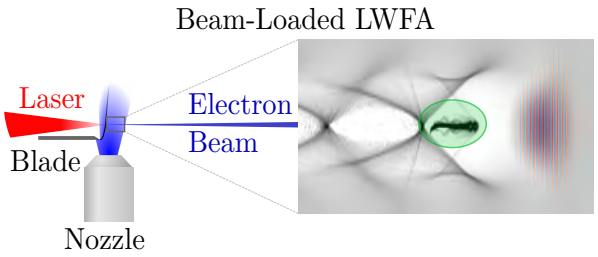

Figure 6.1.: *Experimental setup for studying beam loading effects on a single electron bunch. A corresponding simulation depicting the acceleration process in the plasma is shown on the right. The driving laser pulse is color-coded, whereas the electron density is given as gray background. The accelerated particle bunch is highlighted by the green ellipse. In this experiment, an abrupt plasma density down ramp injects electrons into the first wakefield period where this single bunch is further accelerated.*

spectral charge density was determined to be $4.5\,\mathrm{pC\,MeV^{-1}}$ measured for a shot with 162 pC peak charge. In Figure 6.3(a) the shots of this data set are binned by their peak charge. Furthermore, we observe a drop in maximum electron energy from 280 MeV at low peak charges to 200 MeV at high peak charges (cf. black dots in Figure 6.3(a)). A linear fit correlates the peak energy E_{peak} to the beam charge Q according to

$$E_{\mathrm{peak}} \approx (358 \pm 35)\,\mathrm{MeV} - (1.01 \pm 0.06)\,\mathrm{MeV} \times Q[\mathrm{pC}]. \tag{6.1}$$

Additionally to the reduction in beam energy at higher charges, which is the characteristic property of beam loading and already well-studied [45, 49], we also observe a change of the spectral shape for high charge beams (cf. Figure 6.3(b)). The spectral shape of low

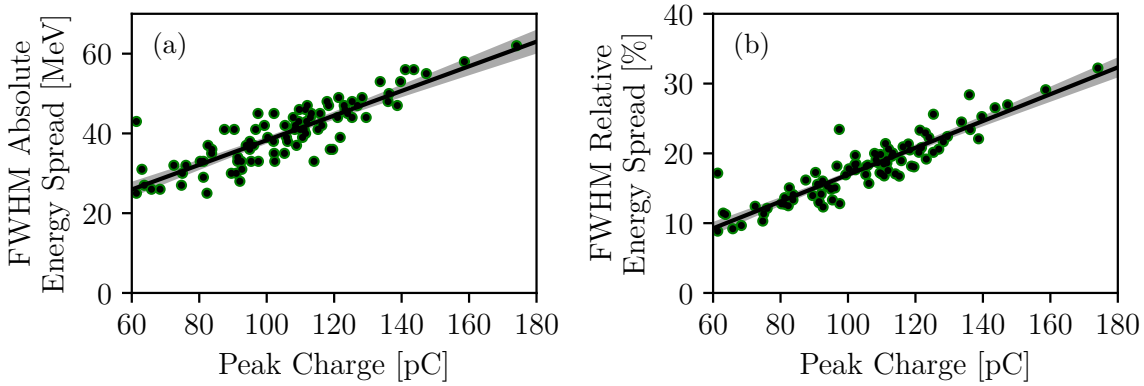

Figure 6.2.: *Absolute and relative energy spread versus peak charge. For high charges, both the absolute (a) and relative (b) FWHM energy spread increases. The 95 % confidence intervals of the linear fits are depicted by the shaded area in both cases.*

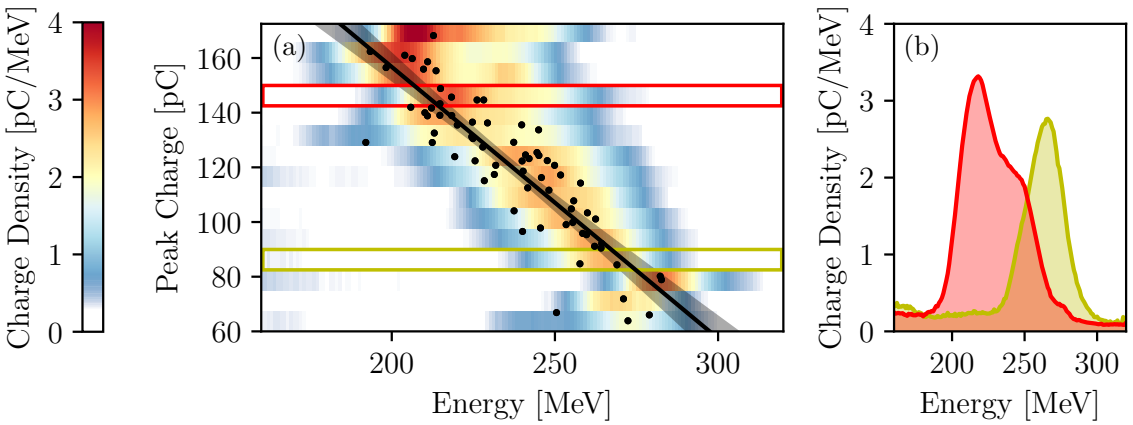

Figure 6.3.: *High shot-to-shot variations of the shock front injector. 91 consecutive shots with varying energy are binned according to their peak charge (a). The peak energy of each shot is indicated by a black dot. A linear trend is fitted to this data (black line) according to Eq. (6.1) and its corresponding 95 % confidence interval is shown as a gray-shaded area. The peak charge clearly correlates with the energy. Two individual line-outs representing the high and low charge case are highlighted in (b). A discussion of their distinct spectral shape is given in the main text.*

charge shots follows a quasi-Gaussian distribution and hence is almost symmetric around the peak, whereas the spectral peak for high charge shots shifts towards lower energies, leading to an asymmetric shape. This effect is more pronounced the higher the peak charge.

This skewness observed in our experiments may be quantified mathematically with statistical measures. The third standardized momentum γ_3, also called *moment coefficient of skewness* (or simply *skewness*), defined as

$$\gamma_3 := \mathrm{E}\left[\left(\frac{X-\mu}{\sigma}\right)^3\right] = \frac{\mu_3}{\sigma^3} = \frac{\mathrm{E}\left[(X-\mu)^3\right]}{(\mathrm{E}\left[(X-\mu)^2\right])^{3/2}} = \frac{\kappa_3}{\kappa_2^{3/2}}, \tag{6.2}$$

quantifies the lopsidedness of the random variable X (which is the energy spectrum in our case). μ is the statistical mean, E the expectation operator, μ_3 denotes the third central momentum, σ the standard deviation and κ_i is the i-th cumulant. For distributions which are symmetric around the average μ, the skewness γ_3 vanishes. If the electron spectra have a peak at higher and a tail at lower energies, γ_3 becomes negative, whereas spectra with $\gamma_3 > 0$ are shaped oppositely. The larger $|\gamma_3|$, the more pronounced this asymmetry is. A demonstrative sketch of negatively and positively skewed probability distributions is shown in Figure 6.4(a-b).

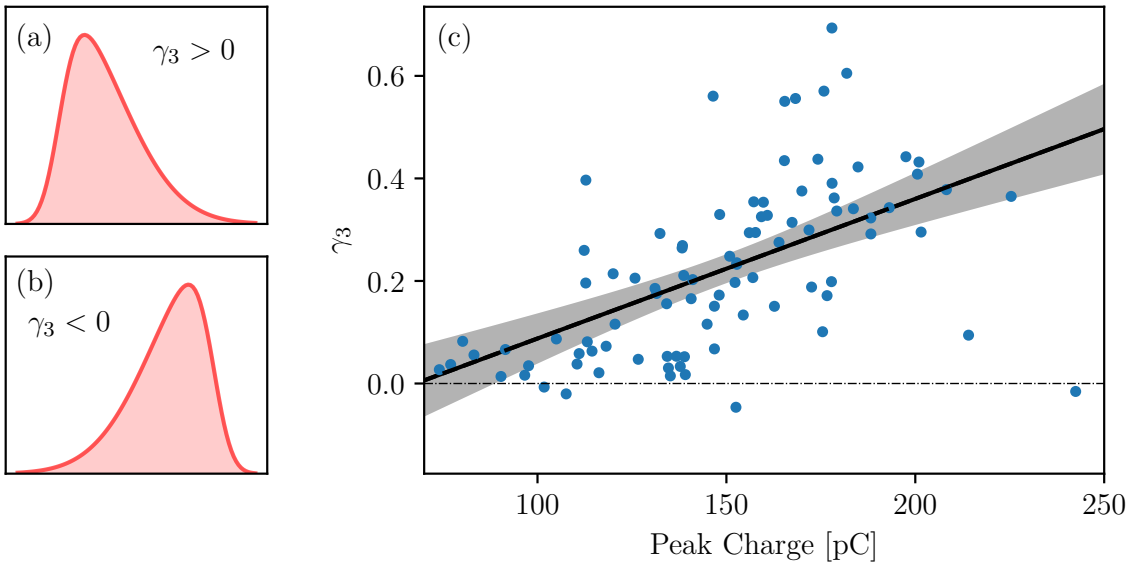

Figure 6.4.: *Calculated Skewness for beam-loaded electron spectra. The first column illustrates the difference in shape for a positively (a) and negatively (b) skewed distribution. In (c) the calculated skewness for each electron spectrum presented in Figure 6.3(a) is depicted. Almost all spectra are positively skewed. The asymmetry increases for higher peak charges which hints at beam loading effects. The 95 % confidence interval is given by the gray shaded area.*

When calculating the skewness assigned to the spectral shape of the accelerated electron bunch, special care must be taken to crop any dark current. This is accomplished by defining a threshold below which the charge density is set to zero. Only if this threshold is high enough, the analysis is confined to the main peak of interest. If dark current or secondary peaks at different energies are taken into account, the calculated skewness of the main peak may significantly change. An example of such a circumstance is given in Figure 6.5(a). This whole spectrum is negatively skewed since the secondary peak adds/increases the probability for the random variable to be left of the statistical mean. The skewness decreases and becomes negative, although the main peak of interest clearly leans towards the left and, hence, is positively skewed. The threshold must be adjusted and checked for each data set to analyze. The exact value of this threshold parameter only plays a minor role as long as all subsidiary peaks are cut away. In the analysis of Figure 6.4(c), this threshold was set to $1.25\,\mathrm{pC\,MeV^{-1}}$ which eliminates all the background except for the main peak. The slope of the fit changes by less than 25 % for thresholds in the range of $1.25\,\mathrm{pC\,MeV^{-1}}$ to $2.2\,\mathrm{pC\,MeV^{-1}}$. An application of this procedure to eliminate subsidiary peaks in the calculated skewness is shown for 20 shots in Figure 6.5(b-c).

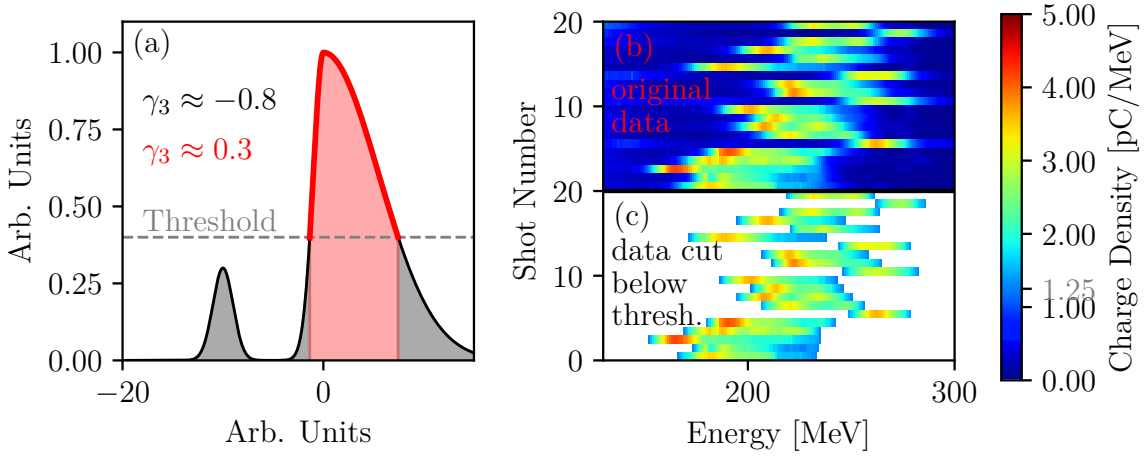

Figure 6.5.: *Caveats when calculating the skewness of an energy spectrum. An artificial distribution with noise is plotted in (a). The main peak clearly tends towards the left and hence is positively skewed ($\gamma_3 = 0.3$). Nevertheless, the secondary small peak to the left compensates for this asymmetry and the calculated skewness for the whole distribution (gray) becomes negative ($\gamma_3 = -0.8$). To avoid such distortions and to confine the analysis to the part of the distribution we are interested in – the main peak – a well-chosen threshold is employed. Only data above this threshold contribute to the calculation of skewness. In this way, the asymmetry of the main peak in (a) is preserved and the calculated skewness for the peak alone becomes positive (red). The first 20 shots from the above data set are shown in (b). In (c) these shots are modified by erasing the charge density where the threshold set to $1.25\,\mathrm{pC\,MeV^{-1}}$ is not surpassed. Hence, the function to calculate the skewness for each spectrum is confined to the main peak of the charge density.*

Indeed, when analyzing the skewness for each spectrum of the dataset shown in Figure 6.3 individually, positively skewed energy spectra strongly dominate (Figure 6.4(c)). If a linear fit is applied to the data, we find the following relation for the skewness γ_3

$$\gamma_3 \approx (2.7 \pm 0.4) \times Q[\mathrm{nC}] - (0.18 \pm 0.06)\,, \tag{6.3}$$

where Q denotes the peak charge given in nC.

In the following, we study PIC simulations and hereby identify this effect as a characteristic property of beam loading in shock-injected LWFAs. To understand how the accelerated electron bunch loads the wake and affects its energy spectrum, we have extensively simulated the interaction process for a wide range of parameters. The analysis of this theoretical data indeed explains the observed asymmetry. Two of these simulations are depicted in Figure 6.6(a) and (b). As the electron bunch is injected into *different phase* positions at nearly *the same time*, the electrons experience different accelerating fields due

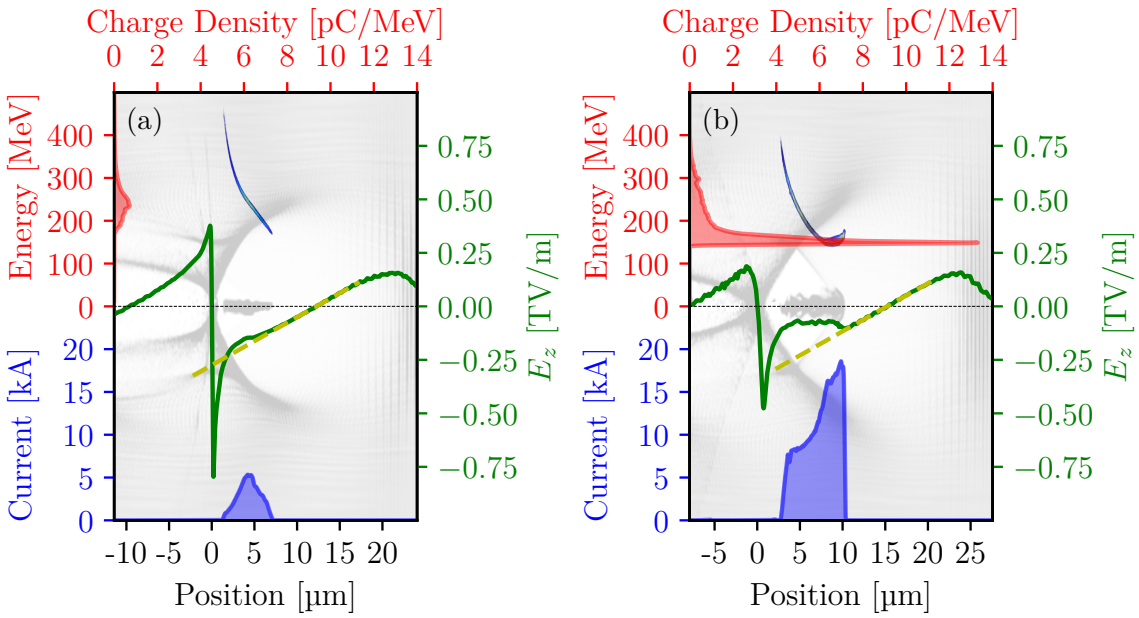

Figure 6.6.: *Simulated effects of strong and weak beam loading. The simulation parameters are matched to the ATLAS-300 LWFA whereas the injected charge was adjusted by varying the focus position as discussed in subsection 5.1.1. Into the background the simulated electron density is imprinted as a gray watermark. A colored map of the electron phase space is shown on top. The on-axis longitudinal field is plotted in green with dashed ocher lines as the linear extrapolation of the undisturbed wakefield at the front of the cavity. Deviations between these two lines show the influence of beam loading and indicate its strength. The energy spectrum is plotted on the left (shaded red) and the respective current on the bottom (shaded blue). In the low charge case ($Q_{Peak} \approx 55\,pC$) (a) the electrons only slightly disturb the accelerating fields. Hence, the phase space is linearly chirped and the energy spectrum is symmetric. However, in the high charge case ($Q_{Peak} \approx 280\,pC$) (b) with strong beam loading, the nonlinearly chirped phase space causes a very asymmetric energy spectrum.*

to the variation of the longitudinal field across the wakefield phase. This leads to a linear positive chirp in phase space which maps the current profile congruently to the energy axis, see Figure 6.6(a). In the high charge case, the self-fields of the electrons are large enough to significantly reduce the accelerating fields. The chirp at the front of the bunch where electrons of lower energy are located vanishes due to beam loading or even reverses when the wake is overloaded (cf. Figure 6.6(b)). Being the projection of the phase space onto the energy axis, the electron spectrum, therefore, exhibits a strong asymmetry with a peak at lower energies. Hence, the skewed spectra we observe in the experiment are the signature of beam loading causing a nonlinear phase space chirp. As beam loading effects become more dominant with increasing current and hence with the number of injected particles, we expect γ_3 to increase with charge, which is indeed the case for experimental data (cf. Figure 6.4(c)). Moreover, these simulations suggest that for a certain amount of injected charge, beam loading effects become strong enough to flatten the effective accelerating fields. This optimal beam loading regime leads to a minimal energetic bandwidth of the accelerated electrons and has already been identified in the past by several groups ([44, 45, 49]). For the charges probed in Figure 6.2, such optimal beam loading is not observed. We assume that scattering in the pointing lanex smears the signal on the espec lanex and by that, spectra with minimal bandwidth cannot be observed. This effect becomes stronger for smaller particle energies and hence counteracts the narrowing of energetic bandwidth due to beam loading.

As plasma wakefields are scaling-invariant, our findings are not restricted to the very specific experimental conditions presented in this context, but are valid for a much broader set of parameters [195]. Provided the scaling conditions are fulfilled, the different LWFAs behave similarly and corresponding beam loading effects like the skewed spectral shape can be generalized to all kinds of LWFAs with localized injection mechanisms operating under different experimental conditions. Indeed, our analysis can be extended to a different shock front LWFA operating regime with densities almost an order of magnitude larger and a few-cycle laser pulse as a driver[1]. Although the scaling requirements are not perfectly met (the few-cycle laser also operates at a central wavelength of 800 nm), the analysis presented in [38] suggests that the scaling invariance also holds true for beam loading.

6.2. Beam Loading in Dual-Energy Electron Beams

In previous sections, we have presented the performance of the 75 TW LWFA and highlighted its capability of delivering monochromatic electron beams via shock front injection.

[1] Further details on this LWFA are given in [48, 123]

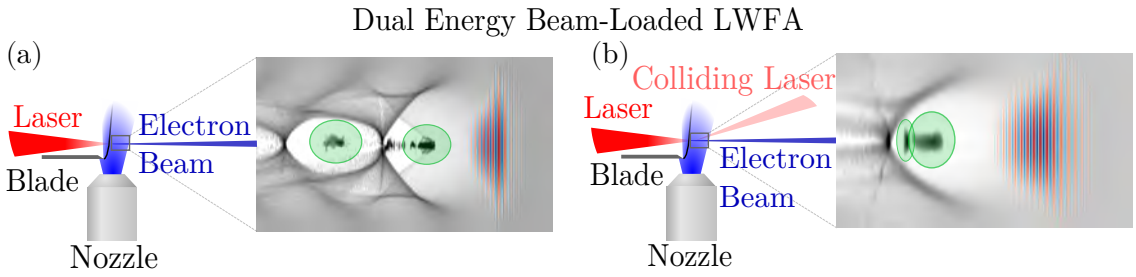

Figure 6.7.: *Experimental setups for studying beam loading effects on dual-energy electron bunches. Corresponding simulations depicting the acceleration process in the plasma are shown as well. The (main) driving laser pulse is color-coded, whereas the electron density is given as gray background. The accelerated particle bunches are highlighted by the green ellipses. In (a) the second electron bunch is generated by shock injection alone. Here, the LWFA is tuned to enable injection into the second cavity as well. Both particle beams are located in different buckets of the wake and are inherently separated by one plasma wavelength. In (b) the two separate particle bunches are created by two independent injection events, namely shock injection followed by optical injection induced by a counter-propagating laser pulse. Here, both particle beams are located in the leading bucket of the wake.*

We have investigated beam loading and how it affects the driving electron bunch. By generating two longitudinally separated electron bunches, driver and witness of beam loading effects can be decoupled. We hereby gain the possibility of directly probing the fields by measuring the final energy of the witness bunch. In the following part, we will show how dual-energy electron beams from one LWFA may be generated. We will discuss how modifications to the experimental setup lead to additional injection into the second plasma cavity or dual injection into the leading bucket of the wake. Both schemes allow for the generation of dual-energy electron bunches and complement each other as they allow for inter- and intra-cavity beam loading studies. The following sections are based on Götzfried *et al.* [38] where these results were published initially. A schematic plot of both experimental setups is given in Figure 6.7.

6.2.1. Dual Shock Injection

Up to now, we have studied how high charge electron beams modify their own accelerating fields and hereby influence their own final energy spectrum. Nevertheless, these self-fields are not restricted to their direct vicinity but also modify the wakefields in their trail. Hence, beam loading not only affects the spectrum of the leading high charge bunch but also the acceleration process of subsequent electron bunches. A method of generating

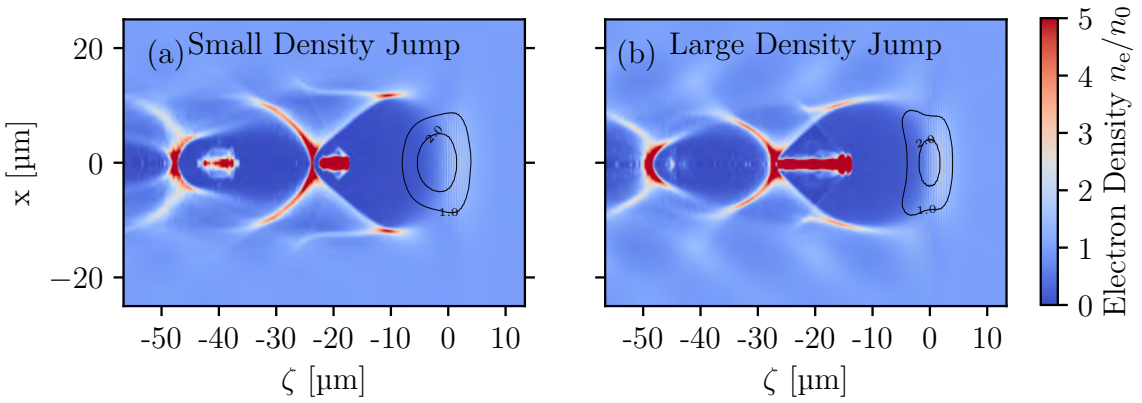

Figure 6.8.: *Two simulations differing by the amount of injected charge into the first cavity. In (a), the initialized hydrogen gas density decreases from $1.6 \times 3.0 \times 10^{18} cm^{-3}$ to $1.0 \times 3.0 \times 10^{18} cm^{-3}$ over the range of one plasma wavelength ($\sim 19\,\mu m$), whereas in (b) the density gradient is almost twice as large and drops from $3.0 \times 3.0 \times 10^{18} cm^{-3}$ to $1.0 \times 3.0 \times 10^{18} cm^{-3}$. All other parameters are identical. With 322 pC in (b) as opposed to 231 pC in (a), the injected charge in the first cavity in (b) is large enough to suppress further injection into subsequent cavities. The shape of the laser pulse in each case is displayed as contour lines in units of a_0.*

two longitudinally separated electron bunches grants the possibility to study far-reaching energy-charge correlations between two distinct electron beams.

In order to inject electrons into subsequent wakefield cavities, one has to decrease the total injected charge in the leading cavity. The space charge of these electrons increases the injection threshold and hence suppresses further injection into subsequent buckets. As discussed in previous sections, this can be achieved for example by lowering the height of the density jump at the shock (cf. Figure 5.8) and/or reducing the laser intensity at the position where injection happens (cf. Figure 5.5). In that way, the electrostatic potential in the leading cavity can be reduced sufficiently to enable injection into subsequent buckets. Two exemplary simulations with (a) and without (b) secondary injection are given in Figure 6.8. Note that the two bunches in this setup are inherently longitudinally separated by a distance of $\sim \lambda_p$.

To experimentally realize the generation of dual-energy electron bunches with a single laser pulse, we moved the wafer by ~ 0.4 mm out of the middle of the gas jet and closer to the jet entrance. This reduces the height of the density jump but also changes the angle of the shock front and increases its width (cf. [179]). The latter only plays a minor role, as has been discussed above in subsection 5.1.2. Fine-tuning the hydrogen pressure applied to the nozzle in combination with adjusting the longitudinal focal spot position eventually leads to the generation of double-bunch electron beams. Figure 6.9 shows a dataset containing

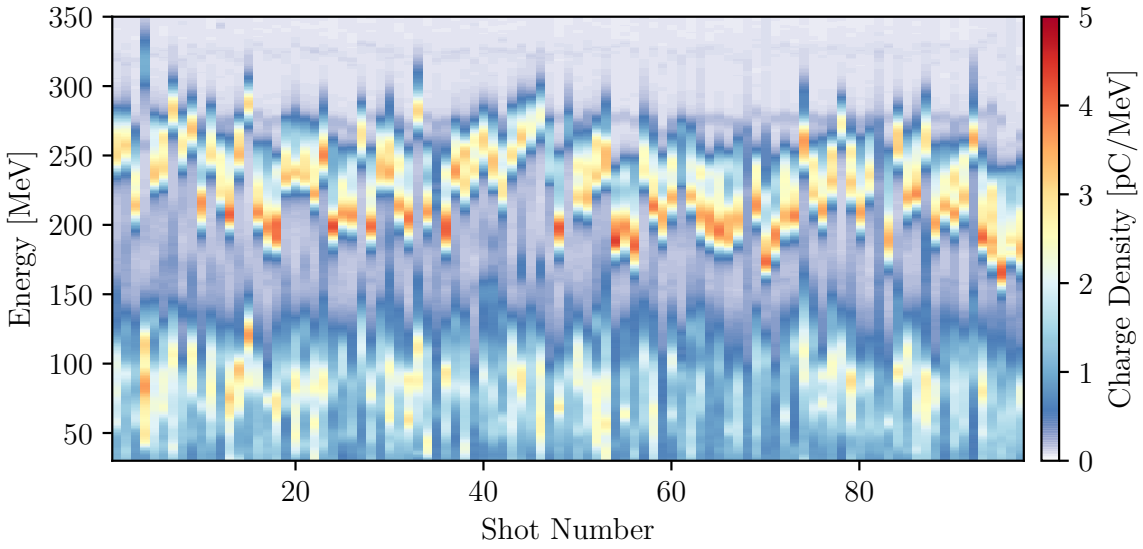

Figure 6.9.: *Dual-energy electron bunches generated with a single laser pulse using shock front injection. The plot shows 97 consecutive electron spectra where the experimental parameters have been optimized to yield a second particle beam at lower energies via injection into the second plasma period. A detailed analysis of this data set is given in the main text.*

97 consecutive shots[1] where the accelerator operates in a regime favoring injection into two successive cavities. Since the accelerating fields in the second cavity are lower, the second electron bunch gains a factor of $\sim 1/3$ less energy during the acceleration process than the leading one.

As in previous cases, we again start our analysis of the data set by sorting the electron beams according to their charge to reveal energy-charge correlations (cf. Figure 6.10(a-b)). As expected, the energy of the leading beam again depends on its own charge. A linear fit to the experimental data (cf. red dots in Figure 6.10(a)) discloses the correlation for the leading electron bunch (denoted by $E_1|Q_1$ in the following)

$$E_1 \approx (259 \pm 3)\,\mathrm{MeV} - (0.11 \pm 0.03)\,\mathrm{MeV} \times Q_1[\mathrm{pC}], \tag{6.4}$$

which differs from Eq. (6.8) due to slightly different laser and target parameters (longitudinal focus and wafer position).

The lower-energy bunch E_2, however, shows no statistically significant dependence on Q_1 (cf. blue data in Figure 6.10(a)). However, we now observe beam loading effects

[1] Three shots in this run contained no data due to DAQ failure. These shots have been cut out.

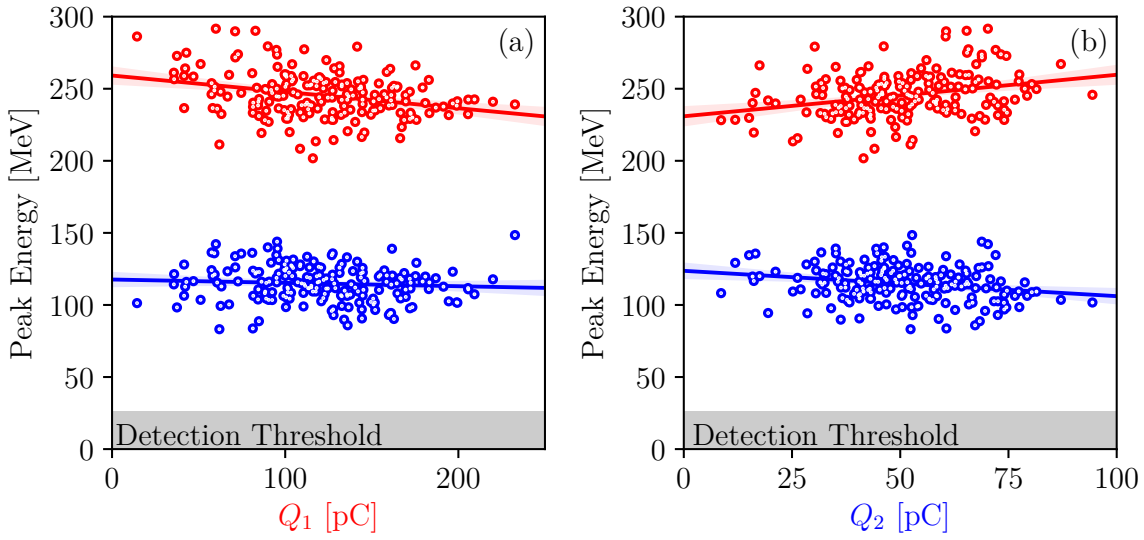

Figure 6.10.: *Experimentally observed inter-cavity beam loading effects. The dual-energy electron beams are generated by injection into subsequent wakefield cavities at a sharp plasma density down ramp. The data are sorted either by the charge in the leading, high-energy beam (denoted by Q_1) (a) or by the charge in the trailing, low-energy beam (Q_2) (b). Linear fits and their respective 95 % confidence intervals (shaded areas) are given in both cases. The data not only show beam loading effects of the respective bunches on themselves but also reveal a clear correlation between the energy of the leading bunch E_1 and the charge of the second bunch Q_2 (red dots in (b)). The latter dependence experimentally demonstrates beam loading effects between different wakefield buckets.*

of the second bunch on itself, as we clearly find the correlation $E_2|Q_2$ (cf. blue data in Figure 6.10(b)) approximated by

$$E_2 \approx (113 \pm 3)\,\mathrm{MeV} - (0.18 \pm 0.06)\,\mathrm{MeV} \times Q_2[\mathrm{pC}]. \tag{6.5}$$

Nevertheless, due to the mechanism employed to create these two separated electron bunches, we also expect E_1 to correlate with Q_2. When fewer electrons are captured by the first wakefield period, more electrons can be trapped in the second one due to the higher remaining wakefield amplitude in the second bucket. A higher energy of the leading bunch consequently correlates with a higher amount of injected charge in the second bucket (via Eq. (6.4)). Indeed, we measure (cf. red data in Figure 6.10(b))

$$E_1 \approx (231 \pm 4)\,\mathrm{MeV} + (0.28 \pm 0.07)\,\mathrm{MeV} \times Q_2[\mathrm{pC}]. \tag{6.6}$$

The FBPIC simulations to verify our experimental results are shown in Figure 6.11. As in the experimental data, the charge in the first electron bunch Q_1 changes the slope of

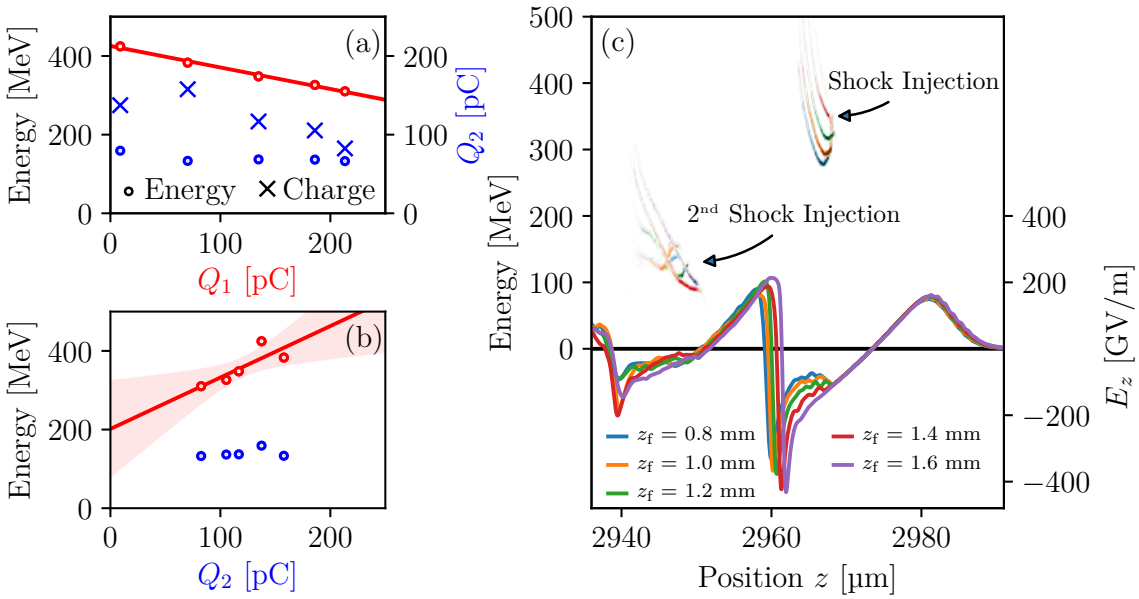

Figure 6.11.: *Simulated inter-cavity beam loading effects on dual-energy electron beams injected into two subsequent wakefield cavities. The data sets are again sorted either by the charge in the leading (Q_1) or trailing (Q_2) electron bunch (a-b). Five different PIC simulations explaining the experimentally observed inter-cavity beam loading effects are shown in (c) where their respective phase space and on-axis longitudinal field are plotted. Beams of different charges are injected into the first and second wakefield period by varying the absolute longitudinal position of the focal laser spot z_f from $z_f = z_{shock} = 0.8\,mm$ to $z_f = 1.6\,mm$, where z_{shock} is the absolute position of the shock front. The experimentally deduced effect of electron bunches influencing the acceleration process of an adjacent wakefield cavity is reproduced. For high charges Q_1 both the on-axis accelerating field E_z (blue curve in (c)) and the amount of subsequently injected electrons are reduced (blue crosses in (a)). Thus, this beam loading effect results in a higher charge Q_2 for the second particle bunch the higher E_1 (red dots in (b)). Simulations provided by courtesy of A. Döpp.*

the accelerating field in the first bucket. The higher the charge, the more suppressed the fields and hence the lower the final electron energy E_1 (red dots in Figure 6.11(a)). The correlation $E_1|Q_1$ is immediately established and identified as typical beam loading in a LPA. A linear fit to the simulated data leads to

$$E_1 \approx (426 \pm 4)\,\mathrm{MeV} - (0.55 \pm 0.03)\,\mathrm{MeV} \times Q_1[\mathrm{pC}]. \tag{6.7}$$

Compared to Eq. (6.4) beam loading effects of the first bunch on itself are more pronounced in the simulations which we trace back to higher simulated beam currents. Similar to the experimental data, this effect does not extend to the electron bunch in the second wakefield period. The field strengths and hence the energies E_2 in the second bucket are uncorrelated to the charge in the leading electron beam Q_1 – as experimentally observed (blue data points in Figure 6.11(a)). In fact, for all five different cases, the slope of the wakefield in the second period appears to be almost independent of beam loading from the first bunch and changes only due to beam loading of the second bunch on itself explaining the correlation $E_2|Q_2$ (cf. Figure 6.11(c)). The simulations also help us to verify the $E_1|Q_2$ correlation found in Eq. (6.6). High charges in the leading wakefield cavity indeed suppress injection into subsequent periods which results in a $Q_1|Q_2$ dependence [45] (cf. crosses in Figure 6.11(a)). Together with the already established $Q_1|E_1$ correlation, the $E_1|Q_2$ effect can be understood as their combination[1].

6.2.2. Shock and Optical Injection

In the previously mentioned method of creating dual-energy beams, both particle bunches are located in two different but subsequent wakefield cavities and are inherently separated by $\sim \lambda_p$. By introducing a second independent injection event, another way to generate dual-energy electron beams can be realized. With the combination of shock and optical injection, we gain the possibility to generate two particle bunches in the first wakefield cavity as optical injection inherently only loads the first bucket and shock injection can be confined to the first wakefield period as explained above. This method of combining shock front and colliding pulse injection has only recently been established [51]. The *intra-cavity* beam loading study presented in the following section hence complements the above explained *inter-cavity* interaction process.

The setup to experimentally realize two independent injection events, i.e., to clip out and focus a second counter-propagating laser beam into the perturbed gas jet has already been

[1] Note that the charge in the second bunch cannot have a direct influence on the energy of the first bunch as this would require information to travel faster than the speed of light.

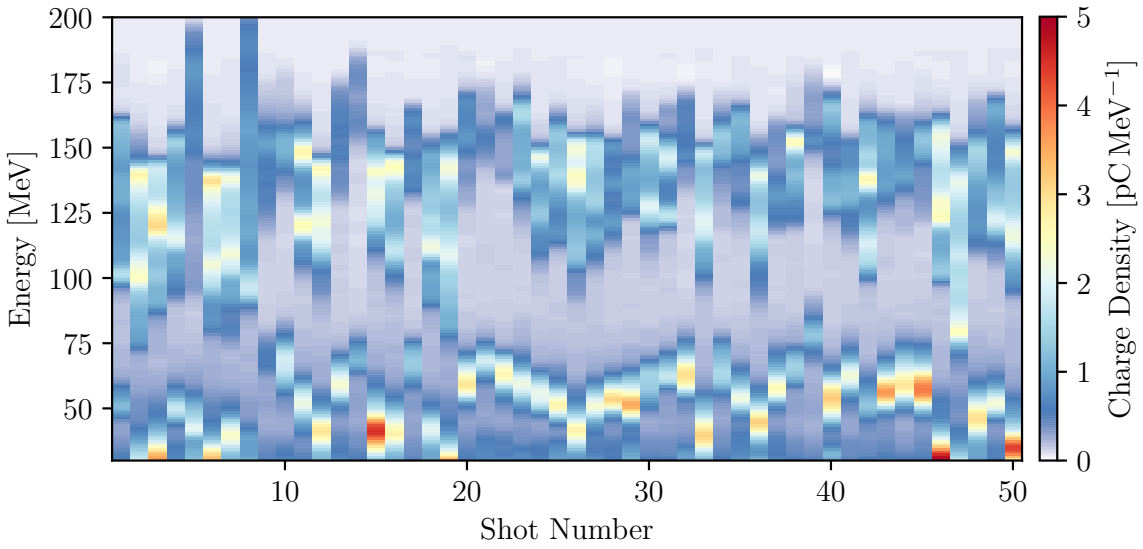

Figure 6.12.: *Combination of shock and colliding pulse injection. This data set shows 50 consecutive shots of dual-energy electron beams. The high-energy bunches stem from shock injection, whereas the lower-energetic ones are optically injected. A detailed analysis of this data set is given in the main text.*

described above (cf. chapter 4). A corresponding sketch of the target setup is given in Figure 6.7(b). The sharp density down ramp at the shock constitutes the first injection event. The target and laser parameters (wafer and focal spot position) are fine-tuned to generate a single accelerated particle bunch and shock injection into subsequent buckets – as described in the previous section – is suppressed. Optical injection in the gas density up ramp (before the shock) is inhibited due to increasing phase velocity. Hence, the counter-propagating laser pulse is adjusted such that the second optical injection takes place at the density plateau and happens after the injection induced by the shock front. Both the sharp gas density down ramp and the collision with the counter-propagating laser pulse lead to a mutually independent injection of electrons into the leading bucket of the wake but at different positions along the propagation. As the optical injection occurs later, the accelerating distance for this electron bunch is shorter and hence its energy is lower[1]. This "driver-witness" configuration is ideally suited to study intra-cavity beam loading effects since the second optically injected electron bunch ("witness") probes the effective fields within the first wakefield period modified by the leading shock-injected bunch ("driver"). In Figure 6.12 a data set of 50 angle-integrated consecutive electron spectra is shown where this method of generating dual-energy electron beams has been applied.

[1]This is easily verified during the experiment simply by blocking the counter-propagating laser pulse.

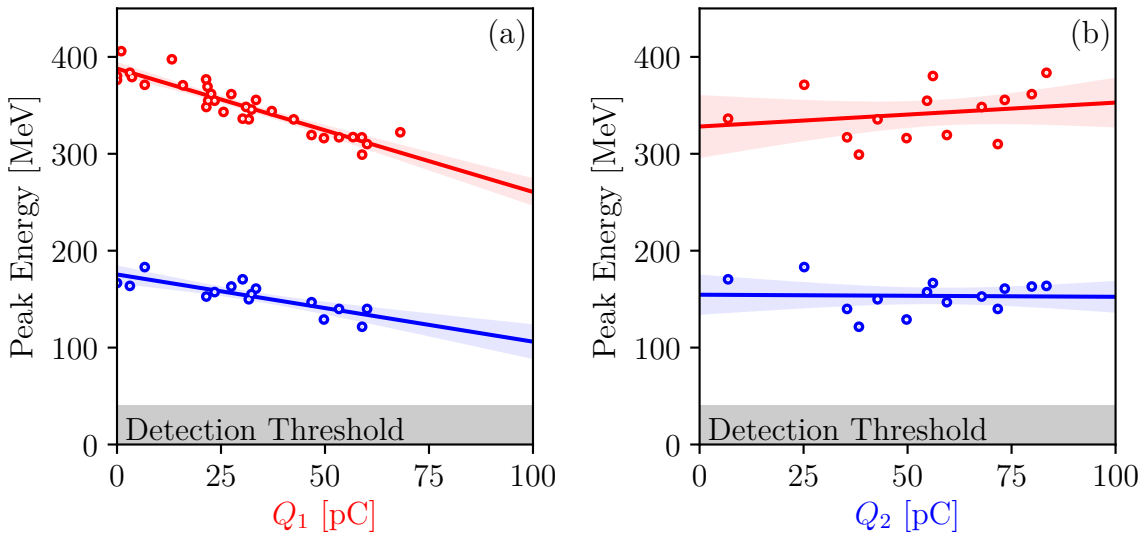

Figure 6.13.: *Experimentally observed intra-cavity beam loading effects. The dual-energy electron beams are generated by a sharp density down ramp (shock injection) and a counter-propagating laser pulse (optical injection). They are accelerated in the same wakefield period. The data are sorted either by the charge in the leading, shock-injected high-energy beam (denoted by Q_1) (a) or by the charge in the trailing, optically-injected low-energy beam (Q_2) (b). Linear fits and their respective 95% confidence intervals (shaded areas) are given in both cases. The data not only show beam loading effects of the first bunch on itself but also discloses a clear correlation between the energy of the trailing bunch E_2 and the charge of the leading bunch Q_1 (blue dots in (a)). This dependence experimentally demonstrates beam loading effects between different bunches in the same wakefield bucket.*

In this data set, we again observe beam loading as the energy E_1 of the first bunch depends on its own charge Q_1 according to

$$E_1 \approx (387 \pm 4)\,\mathrm{MeV} - (1.3 \pm 0.1)\,\mathrm{MeV} \times Q_1[\mathrm{pC}]. \tag{6.8}$$

This correlation is clearly visible when sorting the data set by the first bunch's charge (Figure 6.13(a), red dots). In contrast, the second bunch's charge Q_2 shows no statistically significant correlation to the energy E_1 of the leading bunch (Figure 6.13(b), red dots). This is unexpected since high charges Q_1 not only reduce the accelerating fields in the cavity (E_1 decreases) but also increase the threshold for further particle injection (Q_2 decreases). We therefore attribute this effect to the rather low statistics of our data set, especially as PIC simulations hint at a $Q_2|E_1$ correlation (cf. Figure 6.14(b), red dots). However, the

optically injected beam is clearly influenced by the leading one as E_2 significantly depends on Q_1 (cf. Figure 6.13(a), blue dots)

$$E_2 \approx (175 \pm 5)\,\mathrm{MeV} - (0.7 \pm 0.1)\,\mathrm{MeV} \times Q_1\,[\mathrm{pC}]. \tag{6.9}$$

For high charges in Q_1, the on-axis accelerating fields are suppressed due to beam loading which leads to a lower peak energy E_2 of the second electron beam experiencing these fields. Surprisingly, we do not observe beam loading effects of the second bunch on itself as delineated by Figure 6.13(b, blue) where the data is sorted by Q_2. This circumstance can be explained by the combination of already described effects. On the one hand, high charges Q_1 lower the accelerating fields in the cavity via beam loading (smaller E_2) but also increase the injection threshold, and hence Q_2 is decreased. On the other hand, small secondary charges Q_2 lead to less beam loading of this bunch on itself (E_2 increases). For the combination of charges in our experiment, these two opposing effects cancel each other, which is why a correlation $E_2|Q_2$ is not observed experimentally.

To gain better insight into the underlying physics, we have simulated the whole interaction process. Based on our findings in subsection 5.1.1 the charge of the leading bunch was adjusted by changing the longitudinal focus position z_f in the range of $z_\mathrm{f} = z_\mathrm{shock} = 0.8\,\mathrm{mm}$ to $z_\mathrm{f} = 1.6\,\mathrm{mm}$ in four equidistant steps, where z_shock is the absolute position of the shock and remains constant. In this way, the first bunch's charge decreases whereas its energy increases the larger z_f gets (cf. section 5.1.1). The counter-propagating laser pulse was initialized with a FWHM spot size of $\sim 18\,\mu\mathrm{m}$ and a vacuum normalized vector potential of $a_1 = 0.5$. It collides on the gas density plateau with the main laser pulse at its focal position $z_\mathrm{collision} = z_{2,\mathrm{f}} = 1.9\,\mathrm{mm} > z_\mathrm{f}$. The final charges and energies of both simulated electron beams sorted by Q_1 and Q_2 are given in Figure 6.14(a) and (b). Simulated phase spaces of both electron bunches in combination with the longitudinal electric fields E_z are plotted in Figure 6.14(c). The phase spaces show a clear dependence on the scanned focus position z_f and the experimentally deduced $E_1|Q_1$ beam loading effect is clearly reproduced by the simulations (Figure 6.14(a), red). For the simulated beam loading effect, we deduce an identical relation to Eq. (6.7)

$$E_1 \approx (426 \pm 4)\,\mathrm{MeV} - (0.55 \pm 0.03)\,\mathrm{MeV} \times Q_1\,[\mathrm{pC}]. \tag{6.10}$$

Moreover, the simulated on-axis fields in Figure 6.14(c) show, that beam loading effects induced by the first bunch also extend to the second bunch. A linear fit leads to

$$E_2 \approx (210 \pm 5)\,\mathrm{MeV} - (0.46 \pm 0.03)\,\mathrm{MeV} \times Q_1\,[\mathrm{pC}] \tag{6.11}$$

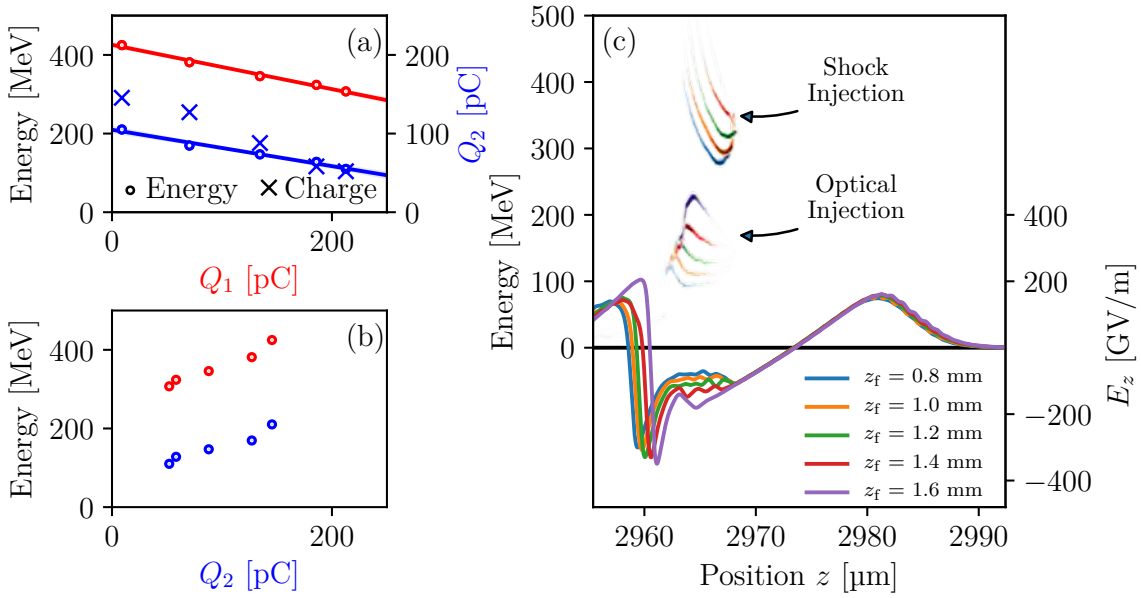

Figure 6.14.: *Simulated intra-cavity beam loading effects on dual-energy electron beams injected into the same wakefield cavity. The data sets are again sorted either by the charge in the leading (Q_1) or trailing (Q_2) electron bunch (a-b). Five different PIC simulations explaining the experimentally observed intra-cavity beam loading effects are shown in (c) where their respective phase space and on-axis longitudinal field are plotted. Beams of different charges are injected into the first wakefield period by two independent injection events. By varying the absolute longitudinal position of the main focal laser spot z_f in the range of $z_f = z_{shock} = 0.8\,mm$ to $z_f = 1.6\,mm$, where z_{shock} is the absolute position of the shock front, the charge in the first electron bunch can be adjusted. A counter-propagating laser pulse with $a_1 = 0.5$ collides with the main pulse at an absolute position of $z_{collison} = z_{2,f} = 1.9\,mm > z_f$. For high charges Q_1 both the on-axis accelerating field E_z (blue curve in (c)) and the amount of subsequently injected electrons are reduced (crosses in (a)). The simulations not only show beam loading effects of the first bunch on itself but also disclose a clear correlation between the charge of the shock-injected bunch Q_1 and the energy of the optically injected bunch E_2. The experimentally deduced effects of electron bunches influencing the acceleration process of the second bunch in the same cavity are hereby reproduced and the correlation between E_2 and Q_1 is established. Simulations provided by courtesy of A. Döpp.*

which is in fair agreement with the experimentally deduced correlation in Eq. (6.9). The $E_2|Q_1$ correlation can therefore be explained by the different amount of beam loading the second bunch witnesses for varying charges in the leading bunch (Figure 6.11(a), blue). As opposed to the experimental data we indeed find the $E_1|Q_2$ dependence (Figure 6.14(b), red) based on the fact, that the threshold for optical injection is modified by E_z and hence by Q_1 (cf. blue crosses in Figure 6.14(a)). In the simulations, the on-axis fields E_z at the position of the optically injected bunch are clearly dominated by the electrostatic potential of the shock-injected particle beam, i.e., the modification to E_z by the first beam is much more significant than the beam loading effect of the second bunch on itself. This explains the positive correlation $E_2|Q_2$ which we only observe in the simulations (cf. Figure 6.14(b), blue) but not in the experimental data.

6.3. Conclusion

In this chapter, we have described experimentally and by simulations, how the charge and the energy of a single electron bunch are correlated. The cause of this correlation was identified as the beam loading effect. Experimental data suggest that beam loading also leads to a specific asymmetric shape of the energy spectrum. By statistical measures, these deviations from symmetry can be boiled down and parametrized by a single scalar quantity – coined by the mathematical expression of "skewness". Taking PIC simulations as a starting point, we have developed a thorough understanding of how the phase space of accelerated electrons evolves under beam loading effects. The skewed spectra are indeed identified as a signature of beam loading causing a nonlinear chirp in phase space. The notion of skewness allows for simple quantification of the strength of beam loading effects and may serve as a tool to distinguish between pure and beam-loaded but laser-dominated LWFA [38]. In the second part of this chapter, two ways of generating dual-energy electron bunches were presented. We extended our analysis of beam loading to these dual bunches. Here we distinguished between inter-cavity and intra-cavity beam loading effects. In the first case, both bunches are located in two separate but subsequent wakefield periods. Via its space charge, the first electron bunch not only reduces its own final energy by beam loading but also inhibits injection into the second wakefield bucket. This effect was reproduced by simulations. An analogous effect is discovered for intra-cavity beam loading, where both electron bunches sit in the same wakefield period. The modifications to the accelerating field induced by the leading electron bunch extend to the trailing particle beam and hereby reduce its energy gain. Beam loading effects hence not only extend to trailing electron bunches in separate plasma cavities but also alter the acceleration dynamics of a subsequent electron bunch in the same wakefield period.

Chapter 7

Summary and Outlook

Within the scope of this work, a state-of-the-art LWFA has been presented producing high-charge electron beams beyond 300 pC peak charge with exceptionally low divergences of less than 0.5 mrad and a relative energy spread of $\sim 15\,\%$ (FWHM), respectively 6.5 % (RMS). The tailored gas density profile enables stable operation over a wide set of parameter ranges. In contrast to many other injection schemes, hundreds of pC can be loaded into the wakefield. With these results, the ATLAS-300 accelerator joins the rank of only a handful of LWFAs being capable of delivering joule-class quasi-monochromatic electron beams with less than 15 % bandwidth (RMS) [33, 34, 49, 196, 197].

Nonetheless, for many applications of these joule-class electron beams in high-energy physics, especially for the development of compact radiation sources [33], energy spreads of 1 % or even less are necessary. Andriyash *et al.* [198] for example propose an ultra-compact coherent X-ray source based on betatron amplification in an optical lattice. However, the stringent demand on the spectral bandwidth of less than 1 % defies the current experimental realization. The same demands currently hinder the development of tabletop ultra-brilliant X-ray FELs. With spectral filters, the electrons' bandwidth can of course be reduced at the expense of the total charge throughput. With such a setup, soft-X-ray undulator generation with laser-plasma-based electron beams has already been shown by Fuchs *et al.* [5]. Here the bandwidth was reduced from $\sim 40\,\%$ (FWHM) to 6 % (FWHM) by a magnetic lens doublet. Simulations with table-top LPA parameters suggest that micro bunching in the undulator – a necessary effect to reach the high gain regime – however requires an electrons' energy spread below 1 % (RMS) for beams of some pC peak charge [4, 199–201]. Hence, with the unprecedented peak charge densities presented in this thesis and even smaller band-pass filters, detectable FEL gain driven by compact LPAs comes into reach.

Besides introducing energy filters to reduce the bandwidth, alternative ways to directly generate even more monochromatic plasma-based beams may be pursued. Lehe *et al.* [129] for example identified a new optical injection regime combining both high charge and low

energy spread ($\sim 100\,\mathrm{pC}$ at a final bandwidth of $\sim 2\,\%$). The required laser parameters are well met with current Ti:Sa laser technology and it remains to be seen if these expectations defy experimental validation.

Another way to tackle electron beams of the lowest energy bandwidths uses beam loading effects to flatten the longitudinal accelerating fields. The theoretical foundation for this technique was developed by Tzoufras *et al.* [42] in 2008 (cf. chapter 1). In this work it was shown, that trapezoidal beam currents with the appropriate total charge may flatten the accelerating fields in a LWFA via beam loading (cf. subsection 2.7.3). However, to access this intermediary regime between LWFA and PWFA, beam currents in the range of tens of kA are necessary. As shown in the final theoretical chapter of this work, charges around hundreds of pC are necessary in the case of the ATLAS-300 accelerator to enter the optimal beam loading regime. These high demands are the reason why this intermediary regime has only been scarcely studied yet.

The data presented in chapter 6 show that we reach this beam loading regime in the case of highly-loaded quasi-monoenergetic wakefields. Here, we use single and dual-energy electron bunches to probe the accelerating fields in the first and second wakefield cavity (cf. section 6.2) and assess their dependence on the accelerated charge. The first hints for such inter-cavity beam loading effects were discovered by Rechatin *et al.* [44] who extended their analysis also to the 'dark current' of the accelerator. This background charge originates in the injection of electrons into trailing buckets of the wakefield. The dark current they measure decreases the higher the trapped charge in the first bucket. This observation is in agreement with our measurements (cf. section 6.2) – even though they are dealing with lower peak charges in the range of 1 pC to 40 pC. Based on our studies with dual-energy electron bunches, we find that beam loading effects extend to trailing electron bunches in the same and also subsequent plasma cavity. Fine-tuning the injected charge (with methods shown in chapter 5) bears the potential of reducing the effective fields such that they become flat (cf. Figure 6.6(b)). Instead of probing the fields, a subsequently injected electron bunch may thus be used as "witness" experiencing the fields flattened by a preceding "escort" bunch [38]. Proof-of-principle studies conducted by Manahan *et al.* [202] showed that by this mechanism the energy spread of the witness can be reduced by an order of magnitude. In this way, beam loading can be utilized to minimize the bunch's energy spread and offers the possibility for future experiments to tailor electron beams of extremely small emittance, needed for example to seed next-generation FELs [4, 203].

To take advantage of such beam loading effects in future experiments, a thorough understanding of the underlying physics is mandatory. Supported by extensive PIC simulations, beam loading effects are comprehended in our work much more fundamentally and are recognized as the development of a nonlinear chirp in the evolving phase space. This chirp

expresses itself in a skewed energy spectrum which is indeed observed in experimental data. The effect of smaller energy spread is a direct consequence of this behavior. Hence, this work delivers a fundamental picture of beam loading as a critical phenomenon in plasma acceleration and constitutes another step towards compact high-brightness electron beam sources for quality-demanding applications [4].

Besides the capability to significantly reduce the energy spread, these beam loading studies open up the way to examine wakefields generated by the self-fields of electron beams [204]. In such PWFAs stages, injection schemes can be employed which are expected to provide electron bunches of superior beam quality in terms of energy spread and normalized emittance [205]. Furthermore, this type of accelerators are not limited by dephasing inherent to pure LWFAs (cf. subsection 2.6.7). Indeed, Blumenfeld *et al.* [206] showed potentially very high acceleration fields of PWFAs by doubling the energy of parts of a conventionally accelerated 42 GeV electron bunch in a 85 cm long PWFA stage.

With the generation of a driver-witness electron bunch pair by the methods described in section 6.2, the advantages unique to both LWFA and PWFA can be combined and might culminate in the development of a new accelerator type. In so-called hybrid plasma accelerators, ultra-cold electron beams may be generated by the interaction between two locally separated electron bunches as studied in this work. A first LWFA stage acts as compact source for high-brightness electron beams. These particle bunches excite their own trailing plasma density wave in a subsequent PWFA stage located some mm to cm behind the first LWFA target. In common LWFA scenarios, the electrons' beta function – the equivalent to the Rayleigh length z_R for optical beams[39] – is typically an order of magnitude larger than the laser's z_R. Hence, due to laser diffraction, the self-fields of the driving bunch causing beam loading in the first LWFA stage take over as the dominant driving force in the second plasma target realizing the PWFA stage [39]. The dephasing-free second stage offers new possibilities to boost the particles' energies [207, 208] and enables novel ultra-cold PWFA injection schemes appropriate to generate ultra-low-emittance particle beams [205, 209–211]. Moreover, hybrid compact accelerators comprise an ideal platform for studying PWFA physics complementary to large-scale RF-based PWFA facilities [212]

In order to develop such hybrid accelerators, the interplay between laser- and particle-driven wakes needs to be well understood and utilized to generate particle beams of suitable properties. The beam loading studies in this thesis contribute to this understanding for sub-nanocoulomb particle beams and by that support the development of this novel type of particle accelerators.

In future experiments, these beam loading studies will be extended to joule-class LPAs in the newly built Centre for Advanced Laser Applications (CALA) housing the upgraded version of the ATLAS-300 laser now being capable of delivering $\sim 2\,\mathrm{PW}$ on target[1]. Ultimately, these beam loading studies may pave the way to lowest bandwidth GeV electron beams and by that culminate in the development of laboratory-scale ultra-brilliant X-ray sources with potentially high impact on material characterization and medical imaging applications [3, 213, 214].

[1] First LWFA results with the ATLAS-3000 laser system in CALA with a pulse power of 300 TW on target are presented in [38].

Appendix A

Theoretical details and in-depth derivations

This part of the appendix provides supplementary material to the theory chapter. In particular, in-depth mathematical derivations too technical for the main theory chapter are given. Nevertheless, the following sections contain results crucial for the stringent mathematical derivations in chapter 2 and thus complete the theory part where references to the corresponding sections in this appendix are given. The following derivations are based upon [57–59, 63].

A.1. Poynting Vector

Starting from Poynting's theorem, two basic quantities of electrodynamics - the Poynting vector $\boldsymbol{S}$ and the energy density u - will be derived in the following.

Poynting's theorem is a direct consequence of the conservation of energy extended to electromagnetic fields. It states that the decrease in the electromagnetic energy per unit volume equals the energy flow out of this volume $\nabla \cdot \boldsymbol{S}$ plus the work done by the fields on a charged object $\boldsymbol{j} \cdot \boldsymbol{E}$

$$-\frac{\partial u}{\partial t} = \nabla \cdot \boldsymbol{S} + \boldsymbol{j} \cdot \boldsymbol{E}. \qquad \text{(Poynting's theorem)} \tag{A.1}$$

Multiplying Eq. (2.4) with $\boldsymbol{E}$ and making use of the identity

$$\nabla (\boldsymbol{B} \times \boldsymbol{E}) = \boldsymbol{E} (\nabla \times \boldsymbol{B}) - \boldsymbol{B} (\nabla \times \boldsymbol{E}) \tag{A.2}$$

leads to

$$\boldsymbol{E} \cdot \boldsymbol{j} = \varepsilon_0 c^2 \nabla \cdot (\boldsymbol{B} \times \boldsymbol{E}) + \varepsilon_0 c^2 \boldsymbol{B} \cdot (\nabla \times \boldsymbol{E}) - \frac{\partial}{\partial t} \left(\frac{1}{2} \varepsilon_0 \boldsymbol{E} \cdot \boldsymbol{E} \right). \tag{A.3}$$

With Eq. (2.2) and reversing the cross product, we get

$$\boldsymbol{E}\cdot\boldsymbol{j} = -\nabla\left(\varepsilon_0 c^2 \boldsymbol{E}\times\boldsymbol{B}\right) - \frac{\partial}{\partial t}\left(\frac{1}{2}\varepsilon_0 c^2 \boldsymbol{B}\cdot\boldsymbol{B} + \frac{1}{2}\varepsilon_0 \boldsymbol{E}\cdot\boldsymbol{E}\right). \tag{A.4}$$

Therefore, we have

$$\boldsymbol{S} := \varepsilon_0 c^2 \boldsymbol{E}\times\boldsymbol{B}, \tag{A.5}$$

$$u := \frac{1}{2}\varepsilon_0 c^2 \boldsymbol{B}\cdot\boldsymbol{B} + \frac{1}{2}\varepsilon_0 \boldsymbol{E}\cdot\boldsymbol{E}. \tag{A.6}$$

The intensity I of an electromagnetic wave is given by the cycle averaged Poynting vector $\boldsymbol{S}$ and can be expressed via Eq. (2.17) and Eq. (2.18) as

$$I := \left\langle|\boldsymbol{S}|\right\rangle = \varepsilon_0 c \left\langle \boldsymbol{E}^2\right\rangle. \tag{A.7}$$

A.2. Relativistic Equation of Motion

In this section, the motion of a relativistic electron interacting with a linearly polarized plane wave will be derived. Plots of this trajectory in the laboratory and co-moving frame can be found in the main part of this work in subsection 2.2.2.

In contrast to the classical treatment in subsection 2.2.1, both terms the electric and the magnetic field contribute significantly to the Lorentz force in the relativistic case. Hence, the electron's momentum is given by

$$\frac{\mathrm{d}\boldsymbol{p}}{\mathrm{d}t} = \frac{\mathrm{d}}{\mathrm{d}t}\left(\gamma m_\mathrm{e}\boldsymbol{v}\right) = \boldsymbol{F}_\mathrm{L} = -e\left(\boldsymbol{E}+\boldsymbol{v}\times\boldsymbol{B}\right) \tag{A.8}$$

with

$$\gamma := \frac{1}{\sqrt{1-\frac{v^2}{c^2}}} = \sqrt{1+\left(\frac{\boldsymbol{p}}{m_\mathrm{e}c}\right)^2} \tag{A.9}$$

being the relativistic Lorentz factor.

Noting that

$$\frac{1}{2}\frac{\mathrm{d}\boldsymbol{p}^2}{\mathrm{d}t} = \boldsymbol{p}\frac{\mathrm{d}\boldsymbol{p}}{\mathrm{d}t} = -e\boldsymbol{p}\cdot\boldsymbol{E} - e\boldsymbol{p}\cdot\left(\boldsymbol{v}\times\boldsymbol{B}\right) = -e\boldsymbol{p}\cdot\boldsymbol{E}, \tag{A.10}$$

where we have used $\boldsymbol{p}\cdot(\boldsymbol{v}\times\boldsymbol{B})=0$, we can calculate

$$\frac{\mathrm{d}\gamma}{\mathrm{d}t}=\frac{\mathrm{d}}{\mathrm{d}t}\sqrt{1+\left(\frac{\boldsymbol{p}}{m_\mathrm{e}c}\right)^2}=\frac{1}{2\gamma(m_\mathrm{e}c)^2}2\boldsymbol{p}\frac{\mathrm{d}\boldsymbol{p}}{\mathrm{d}t}=\frac{1}{2\gamma(m_\mathrm{e}c)^2}\frac{\mathrm{d}\boldsymbol{p}^2}{\mathrm{d}t}=-\frac{e}{m_\mathrm{e}c^2}\boldsymbol{v}\cdot\boldsymbol{E}. \quad \text{(A.11)}$$

The kinetic energy of the electron directly follows as

$$\frac{\mathrm{d}E_\mathrm{kin}}{\mathrm{d}t}=\frac{\mathrm{d}\left((\gamma-1)m_\mathrm{e}c^2\right)}{\mathrm{d}t}=m_\mathrm{e}c^2\frac{\mathrm{d}\gamma}{\mathrm{d}t}=-e\boldsymbol{v}\cdot\boldsymbol{E}. \quad \text{(A.12)}$$

Applying the identities

$$\frac{\mathrm{d}\boldsymbol{A}}{\mathrm{d}t}=\frac{\partial\boldsymbol{A}}{\partial t}+(\boldsymbol{v}\cdot\nabla)\boldsymbol{A}, \quad \text{(A.13)}$$

$$\boldsymbol{v}\times(\nabla\times\boldsymbol{A})=\nabla_{\boldsymbol{A}}(\boldsymbol{v}\cdot\boldsymbol{A})-(\boldsymbol{v}\cdot\nabla)\boldsymbol{A}, \quad \text{(A.14)}$$

– where $\nabla_{\boldsymbol{A}}$ means, that the nabla-operator only acts on the $\boldsymbol{A}$-component – to Eq. (2.7), we get

$$\boldsymbol{E}=-\frac{\partial\boldsymbol{A}}{\partial t}=-\frac{\mathrm{d}\boldsymbol{A}}{\mathrm{d}t}+(\boldsymbol{v}\cdot\nabla)\boldsymbol{A} \quad \text{(A.15)}$$

and

$$\boldsymbol{v}\times\boldsymbol{B}=\boldsymbol{v}\times(\nabla\times\boldsymbol{A})=\nabla_{\boldsymbol{A}}(\boldsymbol{v}\cdot\boldsymbol{A})-(\boldsymbol{v}\cdot\nabla)\boldsymbol{A}. \quad \text{(A.16)}$$

Inserting into Eq. (2.20) leads to

$$\frac{\mathrm{d}\boldsymbol{p}}{\mathrm{d}t}=-e\left(-\frac{\mathrm{d}\boldsymbol{A}}{\mathrm{d}t}+(\boldsymbol{v}\cdot\nabla)\boldsymbol{A}+\nabla_{\boldsymbol{A}}(\boldsymbol{v}\cdot\boldsymbol{A})-(\boldsymbol{v}\cdot\nabla)\boldsymbol{A}\right)=e\frac{\mathrm{d}\boldsymbol{A}}{\mathrm{d}t}-e\nabla_{\boldsymbol{A}}(\boldsymbol{v}\cdot\boldsymbol{A}). \quad \text{(A.17)}$$

Let us again consider a plane linearly polarized electromagnetic wave traveling in x-direction via $\boldsymbol{A}=\boldsymbol{A}_\perp=\boldsymbol{e}_y A_0\sin(\tilde{\phi})$, with $\boldsymbol{e}_v$ being the unit vector in v-direction and $\phi=\boldsymbol{k}\cdot\boldsymbol{r}-\omega t+\tilde{\phi}=kx-\omega t+\tilde{\phi}$. $\tilde{\phi}$ is a constant phase offset and can be set to zero. Hence, according to Eq. (2.7) and Eq. (2.6), we have $\boldsymbol{E}=\boldsymbol{e}_y E_\mathrm{max}\cos(\phi)$ and $\boldsymbol{B}=\boldsymbol{e}_z B_0\cos(\phi)$.

Now, we split the momentum from Eq. (A.17) into components transverse and longitudinal to the plane wave

$$\boldsymbol{p} = \boldsymbol{p}_\perp + \boldsymbol{p}_\parallel \tag{A.18}$$

and solve Eq. (A.17) for the transversal component $\boldsymbol{p}_\perp$.

$\boldsymbol{A}$ only depends on the longitudinal component and is uniform in the transverse direction, therefore $0 = \nabla_{\boldsymbol{A}} (\boldsymbol{v} \cdot \boldsymbol{A}_\perp) = \nabla_{\boldsymbol{A}} (\boldsymbol{v} \cdot \boldsymbol{A})$ and hence

$$\frac{\mathrm{d}\boldsymbol{p}_\perp}{\mathrm{d}t} = e \frac{\mathrm{d}\boldsymbol{A}}{\mathrm{d}t}. \tag{A.19}$$

Integration of the last equation with the boundary condition, that the electron is initially at rest $\left(\boldsymbol{p}|_{\phi=0} \stackrel{!}{=} \boldsymbol{0} \right)$, leads to

$$\boldsymbol{p}_\perp = e\boldsymbol{A}. \tag{A.20}$$

In the case of a plane wave, it is $\boldsymbol{p}_\perp = p_y = eA_0 \sin(\phi) =: eA$. Eq. (A.11) then simplifies to

$$\frac{\mathrm{d}\gamma}{\mathrm{d}t} = -\frac{eE_{\max}}{m_\mathrm{e} c^2} v_y \cos(\phi) \tag{A.21}$$

and the relativistic equation of motion becomes

$$\begin{aligned} \frac{\mathrm{d}\boldsymbol{p}}{\mathrm{d}t} &= -e \left(\boldsymbol{e_y} E_{\max} + \boldsymbol{v} \times \boldsymbol{e_z} B_0 \right) \cos(\phi) = -e \left[\begin{pmatrix} 0 \\ E_{\max} \\ 0 \end{pmatrix} + \begin{pmatrix} v_y B_0 \\ -v_x B_0 \\ 0 \end{pmatrix} \right] \cos(\theta) \\ &= -eE_{\max} \begin{pmatrix} v_y/c \\ 1 - v_x/c \\ 0 \end{pmatrix} \cos(\phi). \end{aligned} \tag{A.22}$$

Comparing the longitudinal x-component of the momentum to Eq. (A.21) leads to

$$\frac{\mathrm{d}p_x}{\mathrm{d}t} = -\frac{eE_{\max}}{c} v_y \cos(\phi) = -m_\mathrm{e} c \frac{e}{m_\mathrm{e} c^2} \boldsymbol{v}\boldsymbol{E} = m_\mathrm{e} c \frac{\mathrm{d}\gamma}{\mathrm{d}t}. \tag{A.23}$$

Integration of both sides with respect to the formerly mentioned boundary condition $\left(\boldsymbol{p}(\phi=0) \stackrel{!}{=} \mathbf{0} \rightarrow \gamma(\phi=0)=1\right)$ leads to

$$p_x = m_\mathrm{e} c\,(\gamma - 1)\,. \tag{A.24}$$

Since $p_z = 0$ for all times t (cf. Eq. (A.17)), we may simplify $\boldsymbol{p}^2 = p_x^2 + p_y^2$. Therefore, by inserting Eq. (A.24) into Eq. (2.29) and making use of the definition given in Eq. (2.23) we get

$$\begin{aligned}
(p_x + m_\mathrm{e} c)^2 = \gamma^2 (m_\mathrm{e} c)^2 = (m_\mathrm{e} c)^2 \left(1 + \frac{p_x^2 + p_y^2}{(m_\mathrm{e} c)^2}\right) &= (m_\mathrm{e} c)^2 + p_x^2 + p_y^2 \\
\Rightarrow 2 p_x m_\mathrm{e} c &= p_y^2 \\
\Rightarrow p_x = \frac{1}{2}\frac{p_y^2}{m_\mathrm{e} c} = \frac{e^2 A^2}{m_\mathrm{e}^2 c^2}\frac{m_\mathrm{e} c}{2} &= a^2 \frac{m_\mathrm{e} c}{2}.
\end{aligned} \tag{A.25}$$

In the highly relativistic case $(\gamma \gg 1)$ the forward momentum p_y dominates, whereas in the classical regime $(\gamma \ll 1)$ the transverse momentum p_x determines the motion of the electron.

From Eq. (A.24) and Eq. (A.25) we get for a linearly polarized plane wave

$$p_y = (m_\mathrm{e} c)\sqrt{2\,(\gamma - 1)}, \tag{A.26}$$

$$\gamma = 1 + \frac{p_x}{m_\mathrm{e} c} = 1 + \frac{a^2}{2}. \tag{A.27}$$

The propagation angle θ of the accelerated charge with respect to the traveling direction of the plane wave is given by

$$\tan(\theta) = \frac{p_y}{p_x} = \frac{m_\mathrm{e} c\sqrt{2\,(\gamma-1)}}{m_\mathrm{e} c\,(\gamma - 1)} = \sqrt{\frac{2}{\gamma - 1}}. \tag{A.28}$$

With Eq. (A.27) and Eq. (A.25) the kinetic energy in Eq. (A.12) becomes

$$E_\mathrm{kin} = (\gamma - 1)\, m_\mathrm{e} c^2 = c p_x = \frac{a^2}{2} m_\mathrm{e} c^2. \tag{A.29}$$

Eq. (A.19) and Eq. (A.29) can also be obtained directly from Noether's theorem [215]. The twofold symmetry (invariance under translation and invariance under $t \rightarrow t - \boldsymbol{x}/c$) of the incident plane wave corresponds to two conservation laws of the electron motion:

The transverse canonical momentum $\boldsymbol{p}_\perp - e\boldsymbol{A}$ as well as $E - cp_x$ are conserved over time. Integration regarding the boundary conditions yields Eq. (A.19) and Eq. (A.29).

To summarize, the following equations derived above completely describe the electron motion driven by a plane wave

$$\begin{aligned} p_x &= \frac{a^2}{2} m_\mathrm{e} c, \\ p_y &= eA = a m_\mathrm{e} c, \\ p_z &= 0. \end{aligned}$$

In accordance with Eq. (2.24) it therefore makes sense to define *normalized momenta* $\tilde{p}$ via $\tilde{p} = p/(m_\mathrm{e} c)$ to simplify these equations to

$$\tilde{p}_x = \frac{a^2}{2}, \tag{A.30}$$

$$\tilde{p}_y = a, \tag{A.31}$$

$$\tilde{p}_z = 0. \tag{A.32}$$

The electron trajectory can easily be calculated by integrating these equations after transforming the parameter $t \to \tau' = t - x/c \Rightarrow \phi \to -\omega\tau'$.

Remembering $\boldsymbol{A} = \boldsymbol{e_y} A_0 \sin(\phi) \Rightarrow \boldsymbol{a} = \boldsymbol{e_y} a_0 \sin(\phi) \to \boldsymbol{a}(\tau') = -\boldsymbol{e_y} a_0 \sin(\omega\tau')$ and using

$$\gamma \frac{\mathrm{d}}{\mathrm{d}t} = \gamma \frac{\mathrm{d}\tau'}{\mathrm{d}t} \frac{\mathrm{d}}{\mathrm{d}\tau'} = (\gamma - \tilde{p}_x) \frac{\mathrm{d}}{\mathrm{d}\tau'} = \frac{\mathrm{d}}{\mathrm{d}\tau'}, \tag{A.33}$$

the above equations transform to

$$p_x = \gamma m_\mathrm{e} \frac{\mathrm{d}x}{\mathrm{d}t} = \frac{a^2}{2} m_\mathrm{e} c \quad \Rightarrow \quad \frac{\mathrm{d}x}{\mathrm{d}\tau'} = \gamma \frac{\mathrm{d}x}{\mathrm{d}t} = \frac{a^2}{2} c, \tag{A.34}$$

$$p_y = \gamma m_\mathrm{e} \frac{\mathrm{d}y}{\mathrm{d}t} = a m_\mathrm{e} c \quad \Rightarrow \quad \frac{\mathrm{d}y}{\mathrm{d}\tau} = \gamma \frac{\mathrm{d}y}{\mathrm{d}t} = ac, \tag{A.35}$$

$$p_z = 0 \quad \Rightarrow \quad \frac{\mathrm{d}z}{\mathrm{d}\tau'} = 0. \tag{A.36}$$

Therefore, we get (with $x(\tau'=0) \stackrel{!}{=} 0$, $y(\tau'=0) \stackrel{!}{=} 0$, $z(\tau'=0) \stackrel{!}{=} 0$)

$$x(\tau') = \frac{c}{4} a_0^2 \left(\tau' - \frac{1}{2\omega} \sin(2\omega\tau') \right), \tag{A.37}$$

$$y(\tau') = \frac{c}{\omega} a_0 \left(1 - \cos(\omega\tau') \right), \tag{A.38}$$

$$z(\tau') = 0. \tag{A.39}$$

The trajectory of the electron is composed of transverse oscillation with the laser frequency and a longitudinal oscillation with double the frequency superimposed by a drift motion v_{drift}

$$v_{\text{drift}} = \left\langle \frac{\mathrm{d}x(\tau')}{\mathrm{d}t} \right\rangle = \frac{c a_0^2}{4} \left\langle \frac{1}{\gamma} \right\rangle = \frac{c a_0^2}{4 + a_0^2}. \tag{A.40}$$

Subtracting the longitudinal drift from the above equations, the quivering motion of the electron in the drift frame $\left(x', y'\right)$ can be extracted

$$kx' = \frac{a_0^2}{8} \sin(2\omega\tau'), \tag{A.41}$$

$$ky' = a_0 \cos(\omega\tau'). \tag{A.42}$$

The frequency difference between the two components leads to the typical figure-8 motion (cf. Figure 2.1). Whereas the x-component scales with $\sim a_0^2$, the y-component depends linearly on a_0. Therefore, the trajectory gets stretched in the longitudinal direction the higher the normalized vector potential.

A.3. Ponderomotive Force Derivation

The ponderomotive force is the cycle-averaged Lorentz force which charged particles experience in an inhomogeneous electromagnetic field. An expression of its first order will be derived in the following by a perturbative ansatz.

Starting from the equation of motion given by Eq. (2.20) we decompose the electric field into a spatial and a temporal component

$$\boldsymbol{E}(\boldsymbol{x},t) = \tilde{\boldsymbol{E}}(\boldsymbol{x}) \cos(\omega t). \tag{A.43}$$

For convenience, the following indices denote the order of the appearing terms.

Taylor expansion leads to

$$\tilde{\boldsymbol{E}}(\boldsymbol{x}) = \tilde{\boldsymbol{E}}_{\boldsymbol{1}}(\boldsymbol{x}) + \tilde{\boldsymbol{E}}_{\boldsymbol{2}}(\boldsymbol{x}) + \cdots = \tilde{\boldsymbol{E}}(\boldsymbol{x_0}) + (\Delta \boldsymbol{x_1} \cdot \nabla) \cdot \tilde{\boldsymbol{E}}(\boldsymbol{x_0}) + \cdots . \tag{A.44}$$

To the lowest order, the equation of motion Eq. (2.20) reads

$$m_\mathrm{e} \frac{\mathrm{d}\boldsymbol{v}_1}{\mathrm{d}t} = -e\boldsymbol{E}_{\boldsymbol{1}}(\boldsymbol{x},t) = -e\tilde{\boldsymbol{E}}_{\boldsymbol{1}}(\boldsymbol{x})\cos(\omega t) = -e\tilde{\boldsymbol{E}}(\boldsymbol{x_0})\cos(\omega t). \tag{A.45}$$

This differential equation is solved by

$$\boldsymbol{v_1} = -\frac{e}{m_\mathrm{e}\omega}\tilde{\boldsymbol{E}}(\boldsymbol{x_0})\sin(\omega t), \tag{A.46}$$

$$\Delta\boldsymbol{x_1} = \frac{e}{m_\mathrm{e}\omega^2}\tilde{\boldsymbol{E}}(\boldsymbol{x_0})\cos(\omega t). \tag{A.47}$$

To the lowest (first) order, only the E-field accounts for the electron motion. Note, that the average over this motion in the lowest order vanishes.

Considering the non-linear part of the equation of motion (second order terms) and Taylor expanding the electric fields leads to

$$m_\mathrm{e} \frac{\mathrm{d}\boldsymbol{v_2}}{\mathrm{d}t} = -e\left(\boldsymbol{E_2}(\boldsymbol{x},t) + \boldsymbol{v_1} \times \boldsymbol{B_1}(\boldsymbol{x},t)\right). \tag{A.48}$$

The first order magnetic field $\boldsymbol{B_1}$ can be found by integrating Eq. (2.2), which leads to

$$\boldsymbol{B_1}(\boldsymbol{x},t) = -\frac{1}{\omega}\nabla \times \boldsymbol{E_1}(\boldsymbol{x},t) = -\frac{1}{\omega}\nabla \times \tilde{\boldsymbol{E}}(\boldsymbol{x_0})\sin(\omega t). \tag{A.49}$$

Inserting Eq. (A.46) and Eq. (A.47) into the non-linear part of the equation of motion, i.e., into Eq. (A.48), we get

$$\begin{aligned} m_\mathrm{e} \frac{\mathrm{d}\boldsymbol{v_2}}{\mathrm{d}t} &= -e\left((\Delta\boldsymbol{x_1} \cdot \nabla) \cdot \boldsymbol{E}(\boldsymbol{x_0},t) + \boldsymbol{v_1} \times \boldsymbol{B_1}(\boldsymbol{x},t)\right) \\ &= -\frac{e^2}{m_\mathrm{e}\omega^2}\left(\cos^2(\omega t)\left(\tilde{\boldsymbol{E}}(\boldsymbol{x_0}) \cdot \nabla\right) \cdot \tilde{\boldsymbol{E}}(\boldsymbol{x_0}) + \sin^2(\omega t)\,\tilde{\boldsymbol{E}}(\boldsymbol{x_0}) \cdot \left(\nabla \times \tilde{\boldsymbol{E}}(\boldsymbol{x_0})\right)\right). \end{aligned} \tag{A.50}$$

Averaging over the fast oscillations of the carrier, this expression simplifies to

$$\begin{aligned} \boldsymbol{F}_{\mathrm{Pond}} &= m_{\mathrm{e}} \left\langle \frac{\mathrm{d}\boldsymbol{v}}{\mathrm{d}t} \right\rangle = m_{\mathrm{e}} \frac{\mathrm{d}\left\langle \boldsymbol{v_2} \right\rangle}{\mathrm{d}t} \\ &= -\frac{e^2}{2m_{\mathrm{e}}\omega^2} \left(\left(\tilde{\boldsymbol{E}}(\boldsymbol{x_0}) \cdot \nabla \right) \cdot \tilde{\boldsymbol{E}}(\boldsymbol{x_0}) + \tilde{\boldsymbol{E}}(\boldsymbol{x_0}) \times \left(\nabla \times \tilde{\boldsymbol{E}}(\boldsymbol{x_0}) \right) \right), \end{aligned} \tag{A.51}$$

since $\langle \sin^2(\omega t) \rangle = \langle \cos^2(\omega t) \rangle = 1/2$.

Making use of the already above-introduced vector calculus identity (cf. Eq. (A.14)), the last part can be rewritten as

$$\boldsymbol{E} \times (\nabla \times \boldsymbol{E}) = \frac{1}{2} \nabla (\boldsymbol{E} \cdot \boldsymbol{E}) - (\boldsymbol{E} \cdot \nabla) \boldsymbol{E}. \tag{A.52}$$

Therefore, the ponderomotive force – to first order – becomes

$$\boldsymbol{F}_{\mathrm{Pond}} = -\frac{e^2}{4m_{\mathrm{e}}\omega^2} \nabla \tilde{\boldsymbol{E}}^2 = -\frac{m_{\mathrm{e}}c^2}{4} \nabla \tilde{\boldsymbol{a}}^2 = -\frac{e^2}{2m_{\mathrm{e}}\omega^2 \varepsilon_0 c} \nabla I. \tag{A.53}$$

Since the ponderomotive force is conservative, a potential ϕ_{Pond} fulfilling $\boldsymbol{F}_{\mathrm{Pond}} = -\nabla \phi_{\mathrm{Pond}}$ can be found

$$\phi_{\mathrm{Pond}} = \frac{e^2}{4m_{\mathrm{e}}\omega^2} \tilde{\boldsymbol{E}}^2. \tag{A.54}$$

The ponderomotive potential equals the mean kinetic energy of the electrons, since with Eq. (A.46)

$$\langle E_{\mathrm{kin}} \rangle = \frac{1}{2} m_{\mathrm{e}} \langle \boldsymbol{v}^2 \rangle = \frac{1}{2} m_{\mathrm{e}} \frac{e^2}{m_{\mathrm{e}}^2 \omega^2} \tilde{\boldsymbol{E}}^2 \frac{1}{2} = \frac{e^2}{4m_{\mathrm{e}}\omega^2} \tilde{\boldsymbol{E}}^2 = \phi_{\mathrm{Pond}}. \tag{A.55}$$

The pressure p exerted by the electric field onto the surrounding gas can be calculated via the force density $\boldsymbol{f}$ as

$$\begin{aligned} -\nabla p = \boldsymbol{f} = \frac{\mathrm{d}\boldsymbol{F}}{\mathrm{d}V} = \boldsymbol{F}_{\mathrm{Pond}} \frac{\mathrm{d}N}{\mathrm{d}V} = n_{\mathrm{e}} \boldsymbol{F}_{\mathrm{Pond}} \\ \Rightarrow p = \frac{n_{\mathrm{e}} e^2}{2m_{\mathrm{e}} c \varepsilon_0 \omega^2} I. \end{aligned} \tag{A.56}$$

For typical parameters of $I = 7 \times 10^{18}\,\mathrm{W\,cm^{-2}}$, $n_{\mathrm{e}} = 3.0 \times 10^{18}\,\mathrm{cm^{-3}}$, $\lambda = 800\,\mathrm{nm}$ the exerted ponderomotive pressure is $\sim 2.0 \times 10^6\,\mathrm{bar}$.

A.4. Debye Length and Shielded Coulomb Potential

In the following, we will derive the typical distance at which the electric potential is significantly suppressed in ideal plasmas, the so-called Debye length. Moreover, the screened Coulomb potential will be examined quantitatively.

Assume a test particle with charge $q = -e$ at the origin of the coordinate system in a hydrogen plasma $Z_\mathrm{i} = 1$. Introducing the electric potential ϕ via $\nabla\phi = -\boldsymbol{E}$ and exploiting the radial symmetry, we have to solve the Poisson equation emerging from Eq. (2.1) in spherical coordinates

$$\nabla^2\phi(r) = \frac{1}{r^2}\frac{\mathrm{d}}{\mathrm{d}r}\left(r^2\frac{\mathrm{d}\phi(r)}{\mathrm{d}r}\right) = -\frac{\rho(r)}{\varepsilon_0}. \tag{A.57}$$

The charge density on the right-hand side is composed of the test charge represented by the δ-function and the plasma background

$$\rho(r) = q\delta(r) - e(n_\mathrm{e}(r) - n_\mathrm{i}(r)). \tag{A.58}$$

The density distribution of each particle species depends on the potential energy and – provided that both species are in thermal equilibrium[1] – is given by the Boltzmann distribution

$$n(r) = n_0 \exp\left(-\frac{q\phi(r)}{k_\mathrm{B}T}\right), \tag{A.59}$$

where k_B denotes the Boltzmann constant and T stands for the thermodynamic temperature.

Using the plasma approximation $n_\mathrm{e} \approx n_\mathrm{i} \approx: n$ and exploiting the fact that the kinetic energy is much larger than the potential energy ($e\phi \ll k_\mathrm{B}T$), we can write

$$\begin{aligned} n_\mathrm{e}(r) - n_\mathrm{i}(r) =& n_0\left(\exp\left(\frac{e\phi(r)}{k_\mathrm{B}T}\right) - \exp\left(-\frac{e\phi(r)}{k_\mathrm{B}T}\right)\right) \\ \approx& n_0\left(1 + \frac{e\phi(r)}{k_\mathrm{B}T} - 1 + \frac{e\phi(r)}{k_\mathrm{B}T}\right) = 2n_0\frac{e\phi(r)}{k_\mathrm{B}T}. \end{aligned} \tag{A.60}$$

[1] In thermal equilibrium the kinetic energy between the different components (T_e stands for the temperature of the electrons, T_i for the ion temperature) of the plasma equalizes through collisions and therefore $T := T_\mathrm{i} = T_\mathrm{e}$.

For $r \neq 0$ the Poisson equation Eq. (A.57) becomes

$$\nabla^2 \phi(r) = \frac{2n_0 e^2}{\varepsilon_0 k_\mathrm{B} T} \phi(r). \tag{A.61}$$

Defining

$$\lambda_\mathrm{D} := \sqrt{\frac{\varepsilon_0 k_\mathrm{B} T}{n_0 e^2}} \tag{A.62}$$

we therefore get for $r \neq 0$

$$\frac{1}{r^2} \frac{\mathrm{d}}{\mathrm{d}r} \left(r^2 \frac{\mathrm{d}\phi(r)}{\mathrm{d}r} \right) = 2\lambda_\mathrm{D}^{-2} \phi(r). \tag{A.63}$$

The solution to this differential equation with the boundary conditions $\phi(r) \xrightarrow[r\to\infty]{} 0$ and $\phi(r) \xrightarrow[r\to 0]{} -e/(4\pi\varepsilon_0 r)$ is given by

$$\phi(r) = -\frac{e}{4\pi\varepsilon_0 r} \exp\left(-\frac{\sqrt{2}r}{\lambda_\mathrm{D}} \right) \tag{A.64}$$

and is composed of the typical $1/r$ Coulomb potential multiplied by an exponential shielding term, which depresses the potential much faster for large radii than the vacuum term[1]. The parameter λ_D is called *Debye length*. For $r \ll \lambda_\mathrm{D}$ the shielding term is negligible, and we get the normal Coulomb potential. For $r \gg \lambda_\mathrm{D}$ the potential drops exponentially and hence the test charge is shielded at distances greater than the Debye length.

[1] If we assume a constant ion background $n_\mathrm{i}(r) = n_0$, justified by the larger response time of the ions to external perturbations due to their much higher mass, we retrieve the Debye-Hückel potential

$$\phi(r) = -e/(4\pi\varepsilon_0 r) \exp\left(-r/\lambda_\mathrm{D}\right)$$

in the very same way.

Appendix B

Set Up and Analysis of FBPIC Simulations

This part of the appendix covers technical details of FBPIC simulations and elaborates on the parameters and physical quantities chosen for the input file. An exemplary python input file adapted to our experimental conditions is given at the very end of this chapter.

B.1. Technical Details on Simulation Parameters

In order to accurately model the laser-plasma interaction and extract decent estimates for accelerated charges and energies, all relevant structures for the underlying physical process must be resolved in these simulations. In FBPIC, the parameters to adjust are

1. the longitudinal and radial size of the simulation box given by $z_{\min}$, $z_{\max}$ and $r_{\max}$ (the respective variables in the input file are called `zmin`, `zmax`, `rmax`)
2. the number of grid points along the radial r and longitudinal dimension z denoted by N_r and N_z (`Nr`, `Nz`)
3. the simulation time step δt (`dt`)
4. the number of modes used N_m (`Nm`)
5. the number of macroparticles per cell along each dimension z, r and θ denoted by pn_z, pn_r and pn_t (`p_nz`, `p_nr`, `p_nt`)

These parameters are chosen as follows

1. the simulation box size must contain all physical relevant structures. In the longitudinal direction, this is the laser pulse and at least one plasma wavelength of gas behind the laser pulse. The radial size must be chosen large enough such that numerical back reflections of the laser from the radial boundary do not interfere with the acceleration process (this is a typical problem in PIC simulations and even happens for absorbing boundary conditions). A typical value for propagation lengths

of some mm is $r_{\max} \approx 3w_{\max}$, where $w_{\max}$ is the largest radial size of the laser pulse during the simulation (typically, the laser pulse is focused into the plasma, hence, the pulse radius is maximum at the very beginning of the simulation).

2. The longitudinal and radial resolution must be chosen fine enough to resolve all physically meaningful length scales. In the longitudinal direction, this is the laser wavelength, whereas in the transverse direction we only need to resolve the plasma dynamics which takes place on the scale of the plasma wavelength. The Nyquist criterion sets lower limits for the resolution in both directions [216]. Since the parameters N_z and N_r crucially influence the numerical cost of PIC simulations, an extensive study on these two parameters has been performed in the course of this work. Both parameters have been scanned independently whilst keeping the remaining quantities unchanged. It was found that longitudinal resolutions δz higher than

$$\delta z < \lambda/30 \tag{B.1}$$

do neither significantly change the accelerated charge nor the energy gain (the respective change is less than 1 %). For the transverse dimension, we find that charge and energy change by less than $\sim 1\,\%$ for resolutions δr finer than[1]

$$\delta r < \lambda_{\mathrm{p}}/120. \tag{B.2}$$

To keep the numerical cost as low as possible (the Fourier transform scales as $N_z \log(N_z)$, the Hankel transform as N_r^2), we have therefore chosen in all the simulations presented in the scope of this thesis $N_z \approx (z_{\max} - z_{\min})/(\lambda/30)$ and $N_r \approx r_{\max}/(\lambda_{\mathrm{p}}/120)$. Typically we've set $z_{\max} = 0$, $z_{\min} = -70 \times 10^{-6}\,\mathrm{m}$, $r_{\max} = 80 \times 10^{-6}\,\mathrm{m}$. With $\lambda \approx 800\,\mathrm{nm}$ and $\lambda_{\mathrm{p}} \approx 19\,\mu\mathrm{m}$, Eq. (B.1) and Eq. (B.2) correspond to $N_z \approx 2500$ and $N_r \approx 500$.

3. Due to solving the fields in spectral coordinates, FBPIC is free of numerical dispersion. Hence, the time step δt can be chosen freely without taking the Courant limit into account. In practice, it is common to choose $\delta t = \delta z/c$.

4. As mentioned in the main part, FBPIC exploits the quasi radial symmetry of LPA scenarios. Higher-order azimuthal modes ($m \geq 1$) cover the deviations from rotational symmetry by representing fields proportional to $\cos(m\theta)$ and $\sin(m\theta)$ [143]. The number of higher-order modes to consider depends on the physical conditions

[1] Parameter studies for the OSIRIS code show that the error based on inadequate resolution becomes small and the wakefields converge for roughly the same resolution [217, 218].

of the respective simulation and their degree of asymmetry. The initialization of a linearly polarized laser pulse for example demands $m \geq 1$ and hence $N_m \geq 2$ [152]. It must be made sure that the number of modes is sufficient to resolve the involved physics. In typical LWFA two modes are enough, whereas non-linear effects like self-injection may require three modes [143]. In our studies, no significant difference for shock-injected LWFA simulations with varying $N_m \geq 2$ was found. Since the computational costs of course increase with N_m, we have set $N_m = 2$ for our simulations.

5. As the particle pusher has to act on each macroparticle separately, in many simulations, this step is the most time-consuming one. Hence, on the one hand, it is favorable to keep the total number of macroparticles as low as possible. On the other hand, especially for simulations where injection happens locally, the sampling rate in each dimension must be high enough to obtain a precise modeling of the total accelerated charge. To unite both requirements, we have identified the parts of the simulation where injection happens and increased the macroparticle density locally for these specific areas. To implement this adaptive macroparticle sampling, several shock-injected LWFA simulations were analyzed and the initial spatial coordinates of the finally injected and accelerated electrons were retraced. An example of such a simulation, where the initial coordinates of the accelerated particles are identified, is given in Figure 2.12. Basically, all electrons ending up in the accelerating fields of the bubble stem from the plasma surrounding the gas density down ramp extended to a radial extension of $\sim w$, where w is the actual radial size of the driving laser pulse. It is therefore sufficient to sample only the plasma around the shock very finely to gain a decent modeling of the accelerated charge. We have therefore split the total plasma volume into five separate regions with different sampling rates (cf. Figure B.1). The outer regions I, II, and III do not provide any electrons to accelerate and were therefore only sampled with four particles per cell. The plasma around the shock (region IV and V) where injection happens was sampled with 64 macroparticles per cell[1].

All the simulations conducted in the scope of this work were set up and run on an *NVIDIA Tesla V100 GPU*. To guarantee comparability between the various simulations, the underlying FBPIC code remained unchanged and was not upgraded from version 0.9.4. With this setup, a full quasi-3D LWFA simulation can be performed on the order of a few hours. Newer versions of the code support advanced techniques like *boosted-frame simulations*,

[1] The distinction between region IV and V is obsolete. It was implemented to offer the opportunity of an even higher sampling of the central region V of the laser plasma interaction which turned out to be not necessary.

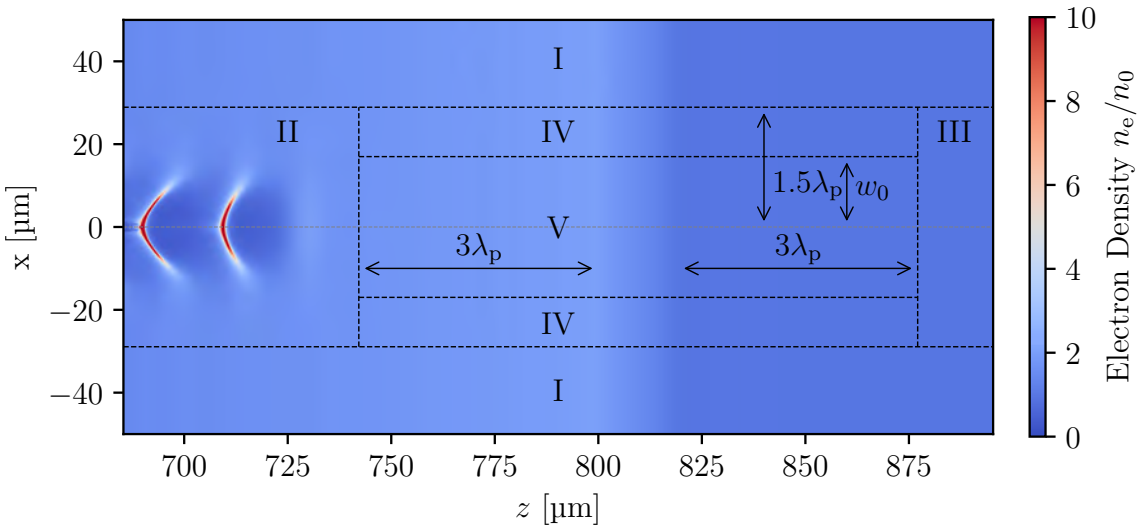

Figure B.1.: *Adaptive macroparticle sampling. Varying sampling rates were applied to different regions of the plasma depending on their respective significance to the acceleration process. Only the regions IV and V significantly deliver electrons that are injected and eventually accelerated. To keep the numerical cost of such simulations low while maintaining a decent modeling for the accelerated charge, it is beneficial to reduce the sampling rate of the outer regions I, II, and III.*

where all parameters are converted from the laboratory frame to a numerical more favorable Lorentz frame [219, 220]. This allows for the speed-up of at least one order of magnitude for such simulations.

B.2. Physical Parameters

As mentioned in the main text, the physical parameters appearing in the input file have been measured and accordingly adopted to tailor these simulations to our experimental data. These quantities characterize the laser pulse as well as the plasma density and profile. To do so, the laser pulses have been fully characterized by frequency-resolved optical gating (FROG). The pulse energy on target was calculated by determining the pulse energy before compression and measuring the transmission through the optical compressor and beamline ($\sim 35\,\%$). The focal width of the laser spot was determined by an infinity-corrected microscope objective whose magnification was calibrated to a well-known diffraction pattern (cf- chapter 4). The laser pulse was initialized with a Gaussian profile defined by these measured parameters [143].

Table B.1.: *Overview of the laser parameters used for simulations in this work. Some parameters still need to be converted to fit the needs of FBPIC, e.g., FWHM to RMS. The relative focal spot position $z_{f,rel}$ is defined as $z_{f,rel} := z_f - z_{shock}$, where z_{shock} denotes the location of the shock front and z_f stands for the absolute longitudinal position of the focal spot.*

Parameter	Value
Laser power P [TW]	0 to 250
Laser FWHM duration τ [fs]	30
Focal waist radius w_0 [µm]	17
Relative focal spot position $z_{\mathrm{f,rel}}$ [mm]	-1 to 1

The adopted gas density profile itself was measured interferometrically [177, 221] and crosschecked by measuring the plasma wavelength (cf. subsection 4.2.1). The retrieved plasma density profile which accordingly was entered into the simulations is plotted in Figure 4.7(b). Nevertheless, the width of the shock is too small to be resolved, therefore, we have chosen a reasonable transition length of λ_{p}. Simulations suggest that this quantity is of minor importance for the injection and acceleration process (cf. subsection 5.1.2). The exact longitudinal position of the focal spot z_{f} cannot be determined experimentally, as it critically depends on the interaction between laser and plasma (cf. subsection 2.5.2). Hence, we have extensively studied the influence of this quantity and the effects of possible shot-to-shot jittering by scanning this simulation parameter over a wide range around the position of the shock (cf. section 5.1). If not stated otherwise, the absolute focal spot position z_{f} in the simulations was set to the beginning of the density down ramp (z_{shock}), hence $z_{\mathrm{f,rel}} := z_{\mathrm{f}} - z_{\mathrm{shock}} = 0$.

B.3. Analysis of PIC Simulations

The developers of FBPIC offer a wide set of routines and predefined functions to analyze the generated HDF5 data. An additionally offered package called *openPMD-viewer* [222] contains a set of tools to load and visualize these data. These visualization tools are very handy to quickly assess the quality of the respective simulation, but cannot replace a thorough analysis. The analysis of the simulated data in the scope of this work was done in Python. Details on where to find all these macros, scripts, and notebooks may be found at the very end of this thesis.

B.4. Complete FBPIC Input Deck

Example for a complete FBPIC input file simulating a LWFA scenario with ATLAS-300 parameters. Short explanations of the respective parameters are given as comments in the Python code.

```
# -------
# Imports
# -------
import numpy as np
from scipy.constants import c, e, m_e, m_p
from fbpic.main import Simulation
from fbpic.lpa_utils.laser import add_laser
from fbpic.openpmd_diag import FieldDiagnostic, ParticleDiagnostic,\
set_periodic_checkpoint, restart_from_checkpoint
import scipy
import scipy.io as sio
import scipy.constants as const
import scipy.interpolate as interpolate



# -------
# Basic functions and parameters
# -------
def lambda_p(n_e): #plasma wavelength
return(2*np.pi*const.c*np.sqrt(const.m_e*\
const.epsilon_0/(const.e**2*n_e)))
def k_p(n_e): #wave number
return(1./(const.c*np.sqrt(const.m_e*\
const.epsilon_0/(const.e**2*n_e))))
def n_elec(lambda_p): #plasma density
return((2*np.pi*const.c/lambda_p)**2*\
(const.m_e*const.epsilon_0/(const.e**2)))
n_c = n_elec(0.8e-6) #critical density
r_e = const.e**2/(4*np.pi*const.epsilon_0*\
const.m_e*const.c**2) #classical electron radius
def P_c(n_e): #critical power
return(2*const.m_e*const.c**3*n_c/(r_e*n_e))
def matched_a0(P,n_e): #matched laser strength parameter
return(2*(P/P_c(n_e))**(1./3))
def matched_waist(P,n_e): #matched laser waist
return(2*np.sqrt(matched_a0(P,n_e))/k_p(n_e))
def v_g(n_e): #group velocity
return(const.c*np.sqrt(1-n_e/n_c))
def calc_a0(P,w0,lambda_0): #strength parameter
I0 = 2*P/(np.pi*w0**2)
E0 = np.sqrt(2*I0/(const.epsilon_0*const.c))
a0 = E0*(lambda_0/(2*np.pi))/(const.m_e*const.c**2/const.e)
return(a0)
```

```
# ----------
# Parameters
# ----------
use_cuda = True #Whether to use the GPU

# The simulation box
Nz = 2500          # Number of gridpoints along z
zmax = 0.e-6     # Right end of the simulation box (meters)
zmin = -70.e-6   # Left end of the simulation box (meters)
Nr = 500           # Number of gridpoints along r
rmax = 80.e-6     # Length of the box along r (meters)
Nm = 2             # Number of modes used
diag_steps=1000 # Period of the diagnostics (timesteps)

# The simulation timestep
dt = (zmax-zmin)/Nz/c    # Timestep (seconds)
end_of_simulation = 3.5e-3
N_step = int(np.ceil(end_of_simulation/(dt*c)/ \
float(diag_steps))*diag_steps+1)  # Number of iterations to perform
n_order = -1

# Plasma profile
n_e = 3e18*1e6 #plateu density
peakDensity = 2 #relative peak density
plateauDensity = 1 #relative plateau density
uprampLength = 800e-6 #length of density upramp till shock
lengthparameter=1 #relative length density down ramp
lp = lambda_p(plateauDensity*n_e) #plasma wavelength
downrampLength = lengthparameter*lp #shock length

# The particles
p_zmin = 0.e-6  # Position of the beginning of the plasma (meters)
p_zmax = 5.e-3  # Position of the end of the plasma (meters)
p_rmin = 0.       # Minimal radial position of the plasma (meters)
p_rmax = 78.e-6  # Maximal radial position of the plasma (meters)
p_nz = 1          # Number of particles per cell along z
p_nr = 1          # Number of particles per cell along r
p_nt = 4          # Number of particles per cell along theta

# The laser parameters
P = 50*1e12 #laser power
lambda_0=8e-7 #laser central wavelength
FWHM_size=20e-6 #Intensity FWHM transverse size
conv=1.177 #conversion paramter from FWHM to rms
w0=FWHM_size/conv
a0 = calc_a0(P,w0,lambda_0) #normalized vector potential
```

```
FWHM_time=30e-15 #laser duration
ctau = FWHM_time*const.c/conv
z0 = -15e-6        # Laser centroid positoin

#gas density profile
def dens_func(x):
upramp = x[x<uprampLength]
uprampDens = upramp**2*(peakDensity/uprampLength**2)
downramp = x[x>uprampLength]
downramp = downramp[downramp<uprampLength+downrampLength]
downrampDens = (uprampLength-downramp)*\
(peakDensity-plateauDensity)/downrampLength+peakDensity
plateau = x[x>uprampLength+downrampLength]
plateauDens = np.ones_like(plateau)*plateauDensity
density = np.concatenate((uprampDens,downrampDens,\
plateauDens), axis=0)
return(density)
uprampEnd=uprampLength
downrampStart=uprampEnd
downrampEnd=downrampStart+downrampLength

#longitudinal laser focal spot position
focshift = 0.0 #position relative to downramp
z_foc =downrampStart+focshift

#interpolate density function
position = np.linspace(0,end_of_simulation+1e-6,5000)
f = interpolate.interp1d(position, dens_func(position),\
bounds_error=False,fill_value=(0,plateauDensity))

#function to avoid simulation artifacts when populating
#neighboring regions of the simulation
def roundToCell(pos, dpos):
return round(pos/dpos) * dpos

#define boundaries for different regions to sample
innerboundary=roundToCell(1.5*lp, rmax/Nr)
beforeboundary=roundToCell(uprampEnd-3*lp,(zmax-zmin)/Nz)
shockboundary=roundToCell(w0,rmax/Nr)
downrampboundary=roundToCell(downrampStart-3*lp,(zmax-zmin)/Nz)
downrampendboundary=roundToCell(downrampEnd+3*lp,(zmax-zmin)/Nz)

#function to separate region (II-IV) from region I
def dens_func_inner( z, r ) :
n=f(z)*(1-np.heaviside(r-innerboundary,0))
return(n)
```

```
#function region I
def dens_func_outer( z, r ) :
n=f(z)*(1-np.heaviside(r-p_rmax,0))*\
np.heaviside(r-innerboundary,0)
return(n)
#function region II
def dens_func_before( z, r ) :
n=dens_func_inner(z,r)*(1-np.heaviside(z-beforeboundary,0))
return(n)
#function region V
def dens_func_shock( z, r ) :
n=f(z)*(1-np.heaviside(r-shockboundary,0))*\
(np.heaviside(z-downrampboundary,0))*\
np.heaviside(downrampendboundary-z,0)
return(n)
#function region IV
def dens_func_shock2( z, r ) :
n=f(z)*(1-np.heaviside(r-innerboundary,0))*\
np.heaviside(r-shockboundary,0)*\
(np.heaviside(z-downrampboundary,0))*\
np.heaviside(downrampendboundary-z,0)
return(n)
#function region III
def dens_func_after( z, r ) :
n=dens_func_inner(z,r)*\
(np.heaviside(z-downrampendboundary,0))
return(n)

# The moving window
vg = v_g(plateauDensity*n_e)
v_window = vg       # Speed of the window

# The diagnostics and the checkpoints/restarts
diag_period = diag_steps # Period of the diagnostics
diag_fields = diag_steps # Period of the diagnostics
save_checkpoints = False # Whether to write checkpoint files
checkpoint_period = 80000  # Period for writing the checkpoints
use_restart = False # Whether to restart from a previous checkpoint
track_electrons = True  # Whether to track and write particle ids


# ----------------------------
# Carrying out the simulation
# ----------------------------
if __name__ == '__main__':
```

```
# Initialize the simulation object
sim = Simulation(Nz, zmax, Nr, rmax, Nm, dt,
zmin=zmin, boundaries='open', initialize_ions=True,
n_order=n_order, use_cuda=use_cuda)
sim.ptcl = []

#populate regions with different macroparticle densities
#populate region V
elec = sim.add_new_species(q=-e, m=m_e, n=n_e,
dens_func=dens_func_shock, p_nz=2*p_nz,\
p_nr=4*p_nr,p_nt=2*p_nt, p_zmin=p_zmin)
#populate region IV
elec2 = sim.add_new_species(q=-e, m=m_e, n=n_e,
dens_func=dens_func_shock2, p_nz=2*p_nz,\
p_nr=4*p_nr,p_nt=2*p_nt, p_zmin=p_zmin)
#populate region I
elec_out = sim.add_new_species(q=-e, m=m_e, n=n_e,
dens_func=dens_func_outer, p_nz=p_nz,\
p_nr=p_nr,p_nt=p_nt, p_zmin=p_zmin)
#populate region II
elec_before = sim.add_new_species(q=-e, m=m_e, n=n_e,
dens_func=dens_func_before, p_nz=p_nz,\
p_nr=p_nr,p_nt=p_nt, p_zmin=p_zmin)
#populate region III
elec_after = sim.add_new_species(q=-e, m=m_e, n=n_e,
dens_func=dens_func_after, p_nz=p_nz,\
p_nr=p_nr,p_nt=p_nt, p_zmin=p_zmin)

add_laser(sim, a0, w0, ctau, z0, zf=z_foc) # Add laser pulse

if use_restart is False:
if track_electrons: # Track electrons if required
elec.track(sim.comm)
elec2.track(sim.comm)
elec_out.track(sim.comm)
elec_before.track(sim.comm)
elec_after.track(sim.comm)
else:
restart_from_checkpoint(sim)

sim.set_moving_window(v=v_window) #Configure the moving window

# Add diagnostics
write_dir='diags'+str(0.0)
sim.diags = [FieldDiagnostic(diag_fields,sim.fld,\
comm=sim.comm, write_dir=write_dir),\
```

```
ParticleDiagnostic(diag_period,{"elec":elec,\
"elec_before":elec_before,"elec2":elec2,\
"elec_out":elec_out,"elec_after":elec_after},\
comm=sim.comm, write_dir=write_dir)]

# Add checkpoints
if save_checkpoints:
set_periodic_checkpoint(sim, checkpoint_period)

### Run the simulation
sim.step(N_step)
```

Bibliography

[1] Walker, P. A. *et al.* Horizon 2020 EuPRAXIA design study. *Journal of Physics: Conference Series* **874,** 012029. https://doi.org/10.1088%2F1742-6596%2F874%2F1%2F012029 (2017).

[2] Döpp, A. *et al.* Quick x-ray microtomography using a laser-driven betatron source. *Optica* **5,** 199–203. http://www.osapublishing.org/optica/abstract.cfm?URI=optica-5-2-199 (2018).

[3] Götzfried, J. *et al.* Research towards high-repetition rate laser-driven X-ray sources for imaging applications. *Nuclear Instruments and Methods in Physics Research Section A: Accelerators, Spectrometers, Detectors and Associated Equipment* **909.** 3rd European Advanced Accelerator Concepts workshop (EAAC2017), 286–289. ISSN: 0168-9002. http://www.sciencedirect.com/science/article/pii/S0168900218303115 (2018).

[4] Maier, A. R. *et al.* Demonstration Scheme for a Laser-Plasma-Driven Free-Electron Laser. *Phys. Rev. X* **2,** 031019. https://link.aps.org/doi/10.1103/PhysRevX.2.031019 (3 2012).

[5] Fuchs, M. *et al.* Laser-driven soft-X-ray undulator source. *Nature Physics* **5,** 826–829. ISSN: 1745-2481. https://doi.org/10.1038/nphys1404 (2009).

[6] Khrennikov, K. *et al.* Tunable All-Optical Quasimonochromatic Thomson X-Ray Source in the Nonlinear Regime. *Phys. Rev. Lett.* **114,** 195003. https://link.aps.org/doi/10.1103/PhysRevLett.114.195003 (19 2015).

[7] Rutherford, E. ATOMIC PROJECTILES AND THEIR COLLISIONS WITH LIGHT ATOMS. *Science* **50,** 467–473. ISSN: 0036-8075. https://science.sciencemag.org/content/50/1299/467 (1919).

[8] Cockcroft, J. D., Walton, E. T. S. & Rutherford, E. Experiments with high velocity positive ions. - (I) Further developments in the method of obtaining high velocity positive ions. *Proceedings of the Royal Society of London. Series A, Containing Papers of a Mathematical and Physical Character* **136,** 619–630. https://royalsocietypublishing.org/doi/abs/10.1098/rspa.1932.0107 (1932).

[9] Van de Graaff, R. J., Compton, K. T. & Van Atta, L. C. The Electrostatic Production of High Voltage for Nuclear Investigations. *Phys. Rev.* **43,** 149–157. https://link.aps.org/doi/10.1103/PhysRev.43.149 (3 1933).

[10] NobelPrize.org. *The Nobel Prize in Physics 1951 - Award Ceremony Speech* https://www.nobelprize.org/prizes/physics/1951/ceremony-speech/ (2021).

[11] Wideröe, R. Über ein neues Prinzip zur Herstellung hoher Spannungen. *Archiv für Elektrotechnik* **21,** 387–406. ISSN: 1432-0487. https://doi.org/10.1007/BF01656341 (1928).

[12] Lawrence, E. O. & Livingston, M. S. The Production of High Speed Light Ions Without the Use of High Voltages. *Phys. Rev.* **40,** 19–35. https://link.aps.org/doi/10.1103/PhysRev.40.19 (1 1932).

[13] Lawrence, E. O. The evolution of the cyclotron. *Nobel Lecture.* https://www.nobelprize.org/prizes/physics/1939/lawrence/lecture/ (1951).

[14] Aad, G. *et al.* Observation of a new particle in the search for the Standard Model Higgs boson with the ATLAS detector at the LHC. *Physics Letters B* **716,** 1–29. ISSN: 0370-2693. https://www.sciencedirect.com/science/article/pii/S037026931200857X (2012).

[15] Charles, T. K. *et al.* The Compact Linear Collider (CLIC) - 2018 Summary Report. **2/2018** (eds Burrows, P. N. *et al.*) arXiv: 1812.06018 [physics.acc-ph] (2018).

[16] Wuensch, W. *et al.* Statistics of vacuum breakdown in the high-gradient and low-rate regime. *Phys. Rev. Accel. Beams* **20,** 011007. https://link.aps.org/doi/10.1103/PhysRevAccelBeams.20.011007 (1 2017).

[17] Gerigk, F. Cavity types. arXiv: 1111.4897 [physics.acc-ph] (2011).

[18] Wuensch, W. High-Gradient Breakdown in Normal-Conducting RF Cavities. https://cds.cern.ch/record/559337 (2002).

[19] Xu, X. *et al.* RF breakdown studies in X-band klystron cavities. **3,** 3045–3047 vol.3. https://ieeexplore.ieee.org/document/753103 (1997).

[20] Barengolts, S. A. *et al.* Mechanism of vacuum breakdown in radio-frequency accelerating structures. *Phys. Rev. Accel. Beams* **21,** 061004. https://link.aps.org/doi/10.1103/PhysRevAccelBeams.21.061004 (6 2018).

[21] Tajima, T. & Dawson, J. M. Laser Electron Accelerator. *Phys. Rev. Lett.* **43,** 267–270. https://link.aps.org/doi/10.1103/PhysRevLett.43.267 (4 1979).

[22] Chen, P. *et al.* Acceleration of Electrons by the Interaction of a Bunched Electron Beam with a Plasma. *Phys. Rev. Lett.* **54,** 693–696. https://link.aps.org/doi/10.1103/PhysRevLett.54.693 (7 1985).

[23] Joshi, C. *et al.* Ultrahigh gradient particle acceleration by intense laser-driven plasma density waves. *Nature* **311,** 525–529. ISSN: 1476-4687. https://doi.org/10.1038/311525a0 (1984).

[24] Joshi, C. Plasma-based accelerators: then and now. *Plasma Physics and Controlled Fusion* **61,** 104001. https://doi.org/10.1088%2F1361-6587%2Fab396a (2019).

[25] Clayton, C. E. *et al.* Ultrahigh-gradient acceleration of injected electrons by laser-excited relativistic electron plasma waves. *Phys. Rev. Lett.* **70,** 37–40. https://link.aps.org/doi/10.1103/PhysRevLett.70.37 (1 1993).

[26] Everett, M. *et al.* Trapped electron acceleration by a laser-driven relativistic plasma wave. *Nature* **368,** 527–529. ISSN: 1476-4687. https://doi.org/10.1038/368527a0 (1994).

[27] Strickland, D. & Mourou, G. Compression of amplified chirped optical pulses. *Optics Communications* **55,** 447–449. ISSN: 0030-4018. http://www.sciencedirect.com/science/article/pii/0030401885901518 (1985).

[28] Gorbunov, L. & Kirsanov, V. Excitation of plasma waves by an electromagnetic wave packet. *Sov. Phys. JETP* **66,** 290–294. http://www.jetp.ac.ru/cgi-bin/e/index/e/66/2/p290?a=list (1987).

[29] Sprangle, P. *et al.* Laser wakefield acceleration and relativstic optical guiding. *AIP Conference Proceedings* **175,** 231–239. https://aip.scitation.org/doi/abs/10.1063/1.37621 (1988).

[30] Amiranoff, F. *et al.* Observation of Laser Wakefield Acceleration of Electrons. *Phys. Rev. Lett.* **81,** 995–998. https://link.aps.org/doi/10.1103/PhysRevLett.81.995 (5 1998).

[31] Pukhov, A. & Meyer-ter-Vehn, J. Laser wake field acceleration: the highly non-linear broken-wave regime. *Applied Physics B* **74,** 355–361. ISSN: 1432-0649. https://doi.org/10.1007/s003400200795 (2002).

[32] Mangles, S. P. D. *et al.* Monoenergetic beams of relativistic electrons from intense laser-plasma interactions. *Nature* **431,** 535–538. ISSN: 1476-4687. https://doi.org/10.1038/nature02939 (2004).

[33] Geddes, C. G. R. *et al.* High-quality electron beams from a laser wakefield accelerator using plasma-channel guiding. *Nature* **431,** 538–541. ISSN: 1476-4687. https://doi.org/10.1038/nature02900 (2004).

[34] Faure, J. *et al.* A laser-plasma accelerator producing monoenergetic electron beams. *Nature* **431,** 541–544. ISSN: 1476-4687. https://doi.org/10.1038/nature02963 (2004).

[35] Leemans, W. P. *et al.* GeV electron beams from a centimetre-scale accelerator. *Nature Physics* **2,** 696–699. ISSN: 1745-2481. https://doi.org/10.1038/nphys418 (2006).

[36] Yoon, J. W. *et al.* Achieving the laser intensity of 5.5×10^{22} W/cm2 with a wavefront-corrected multi-PW laser. *Opt. Express* **27,** 20412–20420. http://www.opticsexpress.org/abstract.cfm?URI=oe-27-15-20412 (2019).

[37] Gonsalves, A. J. *et al.* Petawatt Laser Guiding and Electron Beam Acceleration to 8 GeV in a Laser-Heated Capillary Discharge Waveguide. *Phys. Rev. Lett.* **122,** 084801. https://link.aps.org/doi/10.1103/PhysRevLett.122.084801 (8 2019).

[38] Götzfried, J. *et al.* Physics of High-Charge Electron Beams in Laser-Plasma Wakefields. *Phys. Rev. X* **10,** 041015. https://link.aps.org/doi/10.1103/PhysRevX.10.041015 (4 2020, © 2020 American Physical Society).

[39] Hidding, B. *et al.* Fundamentals and Applications of Hybrid LWFA-PWFA. *Applied Sciences* **9.** ISSN: 2076-3417. https://www.mdpi.com/2076-3417/9/13/2626 (2019).

[40] Katsouleas, T. *et al.* Beam loading in plasma accelerators. *Particle Accelerators* **22,** 81–99. ISSN: 0031-2460. http://inis.iaea.org/search/search.aspx?orig_q=RN:18090527 (1987).

[41] Lu, W. *et al.* Generating multi-GeV electron bunches using single stage laser wakefield acceleration in a 3D nonlinear regime. *Phys. Rev. ST Accel. Beams* **10,** 061301. https://link.aps.org/doi/10.1103/PhysRevSTAB.10.061301 (6 2007).

[42] Tzoufras, M. *et al.* Beam Loading in the Nonlinear Regime of Plasma-Based Acceleration. *Phys. Rev. Lett.* **101,** 145002. https://link.aps.org/doi/10.1103/PhysRevLett.101.145002 (14 2008).

[43] Tzoufras, M. *et al.* Beam loading by electrons in nonlinear plasma wakes. *Physics of Plasmas* **16,** 056705. https://doi.org/10.1063/1.3118628 (2009).

[44] Rechatin, C. *et al.* Observation of Beam Loading in a Laser-Plasma Accelerator. *Phys. Rev. Lett.* **103,** 194804. https://link.aps.org/doi/10.1103/PhysRevLett.103.194804 (19 2009).

[45] Rechatin, C. *et al.* Characterization of the beam loading effects in a laser plasma accelerator. *New Journal of Physics* **12,** 045023. https://doi.org/10.1088%2F1367-2630%2F12%2F4%2F045023 (2010).

[46] Mirzaie, M. *et al.* Demonstration of self-truncated ionization injection for GeV electron beams. *Scientific Reports* **5,** 14659. ISSN: 2045-2322. https://doi.org/10.1038/srep14659 (2015).

[47] Zeng, M. *et al.* Self-truncated ionization injection and consequent monoenergetic electron bunches in laser wakefield acceleration. *Physics of Plasmas* **21,** 030701. eprint: https://doi.org/10.1063/1.4868404. https://doi.org/10.1063/1.4868404 (2014).

[48] Buck, A. *et al.* Shock-Front Injector for High-Quality Laser-Plasma Acceleration. *Phys. Rev. Lett.* **110,** 185006. https://link.aps.org/doi/10.1103/PhysRevLett.110.185006 (18 2013).

[49] Couperus, J. P. *et al.* Demonstration of a beam loaded nanocoulomb-class laser wakefield accelerator. *Nature Communications* **8,** 487. ISSN: 2041-1723. https://doi.org/10.1038/s41467-017-00592-7 (2017).

[50] Guillaume, E. *et al.* Physics of fully-loaded laser-plasma accelerators. *Phys. Rev. ST Accel. Beams* **18,** 061301. https://link.aps.org/doi/10.1103/PhysRevSTAB.18.061301 (6 2015).

[51] Wenz, J. *et al.* Dual-energy electron beams from a compact laser-driven accelerator. *Nature Photonics* **13,** 263–269. ISSN: 1749-4893. https://doi.org/10.1038/s41566-019-0356-z (2019).

[52] Lehe, R. *et al.* A spectral, quasi-cylindrical and dispersion-free Particle-In-Cell algorithm. *Computer Physics Communications* **203,** 66–82. ISSN: 0010-4655. http://www.sciencedirect.com/science/article/pii/S0010465516300224 (2016).

[53] Maxwell, J. C. VIII. A dynamical theory of the electromagnetic field. *Philosophical Transactions of the Royal Society of London* **155,** 459–512. https://royalsocietypublishing.org/doi/abs/10.1098/rstl.1865.0008 (1865).

[54] Heigoldt, M. *Temporal dynamics of the longitudinal bunch profile in a laser wakefield accelerator* PhD thesis (Ludwig-Maximilians-Universität München, 2017). http://nbn-resolving.de/urn:nbn:de:bvb:19-208879.

[55] Mehrling, T. J. *Theoretical and numerical studies on the transport of transverse beam quality in plasma-based accelerators* PhD thesis (Universität Hamburg, 2014). https://ediss.sub.uni-hamburg.de/handle/ediss/5644.

[56] Esarey, E., Schroeder, C. B. & Leemans, W. P. Physics of laser-driven plasma-based electron accelerators. *Rev. Mod. Phys.* **81,** 1229–1285. https://link.aps.org/doi/10.1103/RevModPhys.81.1229 (3 2009).

[57] Karsch, S. Lecture Notes: Applications of High-Intensity Laser-Pulses. *Ludwig-Maximilians-Universität München, Fakultät für Physik.* https://www.physik.uni-muenchen.de/lehre/vorlesungen/sose_18/applications_of_high-intensity_laser-pulses/vorlesung/index.html (2018).

[58] Jackson, J. D. *Klassische Elektrodynamik* 3rd ed. ISBN: 3-11-016502-3. https://www.degruyter.com/view/product/36733 (De Gruyter, 2002).

[59] Gibbon, P. *Short Pulse Laser Interactions with Matter* ISBN: 978-1-86094-135-1. https://www.fz-juelich.de/ias/jsc/EN/AboutUs/Organisation/ComputationalScience/Simlabs/slpp/Teaching/SPLIM/_node.html (Imperial College Press, 2005).

[60] Quesnel, B. & Mora, P. Theory and simulation of the interaction of ultraintense laser pulses with electrons in vacuum. *Phys. Rev. E* **58,** 3719–3732. https://link.aps.org/doi/10.1103/PhysRevE.58.3719 (3 1998).

[61] Liu, C. S., Tripathi, V. K. & Eliasson, B. *High-Power Laser-Plasma Interaction* https://www.cambridge.org/core/books/highpower-laserplasma-interaction/5C2399EEEF8E259BBD13BA56B954B89A (Cambridge University Press, 2019).

[62] Mulser, P. & Bauer, D. *High power laser-matter interaction* https://www.springer.com/de/book/9783540506690 (Springer, 2010).

[63] Zohm, H. Plasmaphysik. *Ludwig-Maximilians-Universität München, Fakultät für Physik.* https://www.physik.uni-muenchen.de/lehre/vorlesungen/wise_11_12/A_Plasmaphysik/vorlesung/skript.pdf (2010).

[64] Kruer, W. *The physics of laser plasma interactions* (Westview Press, 2003).

[65] Rae, S. Ionization-induced defocusing of intense laser pulses in high-pressure gases. *Optics Communications* **97,** 25–28. ISSN: 0030-4018. http://www.sciencedirect.com/science/article/pii/0030401893906118 (1993).

[66] Fill, E. E. Focusing limits of ultrashort laser pulses: analytical theory. *J. Opt. Soc. Am. B* **11,** 2241–2245. http://josab.osa.org/abstract.cfm?URI=josab-11-11-2241 (1994).

[67] Del Pizzo, V., Luther-Davies, B. & Siegrist, M. R. Self-focussing of a laser beam in a multiply ionized, absorbing plasma. *Applied physics* **18,** 199–204. ISSN: 1432-0630. https://doi.org/10.1007/BF00934416 (1979).

[68] Mori, W. B. *et al.* Evolution of self-focusing of intense electromagnetic waves in plasma. *Phys. Rev. Lett.* **60,** 1298–1301. https://link.aps.org/doi/10.1103/PhysRevLett.60.1298 (13 1988).

[69] Sharma, A. & Kourakis, I. Relativistic laser pulse compression in plasmas with a linear axial density gradient. *Plasma Physics and Controlled Fusion* **52,** 065002. https://doi.org/10.1088%2F0741-3335%2F52%2F6%2F065002 (2010).

[70] Karle, C. & Spatschek, K. H. Relativistic laser pulse focusing and self-compression in stratified plasma-vacuum systems. *Physics of Plasmas* **15,** 123102. https://doi.org/10.1063/1.3023154 (2008).

[71] Lefebvre, E. & Bonnaud, G. Transparency/Opacity of a Solid Target Illuminated by an Ultrahigh-Intensity Laser Pulse. *Phys. Rev. Lett.* **74,** 2002–2005. https://link.aps.org/doi/10.1103/PhysRevLett.74.2002 (11 1995).

[72] Sprangle, P., Tang, C. & Esarey, E. Relativistic Self-Focusing of Short-Pulse Radiation Beams in Plasmas. *IEEE Transactions on Plasma Science* **15,** 145–153. ISSN: 1939-9375. https://ieeexplore.ieee.org/document/4316677 (1987).

[73] Mori, W. B. The physics of the nonlinear optics of plasmas at relativistic intensities for short-pulse lasers. *IEEE Journal of Quantum Electronics* **33,** 1942–1953. ISSN: 1558-1713. https://ieeexplore.ieee.org/abstract/document/641309 (1997).

[74] Hora, H. Theory of relativistic self-focusing of laser radiation in plasmas. *J. Opt. Soc. Am.* **65,** 882–886. http://www.osapublishing.org/abstract.cfm?URI=josa-65-8-882 (1975).

[75] Hora, H. Self-focusing of laser beams in a plasma by ponderomotive forces. *Zeitschrift für Physik A Hadrons and nuclei* **226,** 156–159. ISSN: 0939-7922. https://doi.org/10.1007/BF01392018 (1969).

[76] Siegrist, M. Self-focusing in a plasma due to ponderomotive forces and relativistic effects. *Optics Communications* **16,** 402–407. ISSN: 0030-4018. http://www.sciencedirect.com/science/article/pii/0030401876900286 (1976).

[77] Streeter, M. J. V. *et al.* Observation of Laser Power Amplification in a Self-Injecting Laser Wakefield Accelerator. *Phys. Rev. Lett.* **120,** 254801. https://link.aps.org/doi/10.1103/PhysRevLett.120.254801 (25 2018).

[78] Leemans, W. P. *et al.* Experiments and simulations of tunnel-ionized plasmas. *Phys. Rev. A* **46,** 1091–1105. https://link.aps.org/doi/10.1103/PhysRevA.46.1091 (2 1992).

[79] Esarey, E. *et al.* Overview of plasma-based accelerator concepts. *IEEE Transactions on Plasma Science* **24,** 252–288. ISSN: 1939-9375. https://ieeexplore.ieee.org/document/509991 (1996).

[80] Sun, G.-Z. *et al.* Self-focusing of short intense pulses in plasmas. *The Physics of Fluids* **30,** 526–532. https://aip.scitation.org/doi/abs/10.1063/1.866349 (1987).

[81] Sprangle, P., Esarey, E. & Ting, A. Nonlinear theory of intense laser-plasma interactions. *Phys. Rev. Lett.* **64,** 2011–2014. https://link.aps.org/doi/10.1103/PhysRevLett.64.2011 (17 1990).

[82] Faure, J. *et al.* Observation of Laser-Pulse Shortening in Nonlinear Plasma Waves. *Phys. Rev. Lett.* **95,** 205003. https://link.aps.org/doi/10.1103/PhysRevLett.95.205003 (20 2005).

[83] Najmudin, Z. Laser Wakefield Accelerators. *CERN Yellow Reports* **1,** 109. https://e-publishing.cern.ch/index.php/CYR/article/view/216 (2016).

[84] Schreiber, J. *et al.* Complete Temporal Characterization of Asymmetric Pulse Compression in a Laser Wakefield. *Phys. Rev. Lett.* **105,** 235003. https://link.aps.org/doi/10.1103/PhysRevLett.105.235003 (23 2010).

[85] Kaluza, M. C. *Characterisation of Laser-Accelerated Proton Beams* Dissertation (Technische Universität München, München, 2004). http://mediatum.ub.tum.de/node?id=603032.

[86] Meyer-ter-Vehn, J., Pukhov, A. & Sheng, Z.-M. *Relativistic Laser Plasma Interaction* in *Atoms, Solids, and Plasmas in Super-Intense Laser Fields* (eds Batani, D. *et al.*) 167–192 (Springer US, Boston, MA, 2001). ISBN: 978-1-4615-1351-3. https://doi.org/10.1007/978-1-4615-1351-3_9.

[87] Chen, X. L. & Sudan, R. N. Two-dimensional self-focusing of short intense laser pulse in underdense plasma. *Physics of Fluids B: Plasma Physics* **5,** 1336–1348. https://doi.org/10.1063/1.860923 (1993).

[88] Bulanov, S. V. *et al.* Nonlinear depletion of ultrashort and relativistically strong laser pulses in an underdense plasma. *Physics of Fluids B: Plasma Physics* **4,** 1935–1942. https://doi.org/10.1063/1.860046 (1992).

[89] Berezhiani, V. & Murusidze, I. Relativistic wake-field generation by an intense laser pulse in a plasma. *Physics Letters A* **148,** 338–340. ISSN: 0375-9601. http://www.sciencedirect.com/science/article/pii/0375960190908134 (1990).

[90] Sprangle, P., Esarey, E. & Ting, A. Nonlinear interaction of intense laser pulses in plasmas. *Phys. Rev. A* **41,** 4463–4469. https://link.aps.org/doi/10.1103/PhysRevA.41.4463 (8 1990).

[91] Sprangle, P. *et al.* Laser wakefield acceleration and relativistic optical guiding. *Applied Physics Letters* **53,** 2146–2148. https://doi.org/10.1063/1.100300 (1988).

[92] Ruth, R. *et al.* A PLASMA WAKE FIELD ACCELERATOR. *Part. Accel.* **17,** 171. https://www-public.slac.stanford.edu/sciDoc/docMeta.aspx?slacPubNumber=SLAC-PUB-3374 (1985).

[93] Schroeder, C. B. *et al.* Trapping, dark current, and wave breaking in nonlinear plasma waves. *Physics of Plasmas* **13,** 033103. https://doi.org/10.1063/1.2173960 (2006).

[94] Ting, A., Esarey, E. & Sprangle, P. Nonlinear wake-field generation and relativistic focusing of intense laser pulses in plasmas. *Physics of Fluids B: Plasma Physics* **2,** 1390–1394. https://doi.org/10.1063/1.859561 (1990).

[95] Shadwick, B. A., Schroeder, C. B. & Esarey, E. Nonlinear laser energy depletion in laser-plasma accelerators. *Physics of Plasmas* **16,** 056704. https://doi.org/10.1063/1.3124185 (2009).

[96] Ding, H. *et al.* Nonlinear plasma wavelength scalings in a laser wakefield accelerator. *Phys. Rev. E* **101,** 023209. https://link.aps.org/doi/10.1103/PhysRevE.101.023209 (2 2020).

[97] Dawson, J. M. Nonlinear Electron Oscillations in a Cold Plasma. *Phys. Rev.* **113,** 383–387. https://link.aps.org/doi/10.1103/PhysRev.113.383 (2 1959).

[98] Akhiezer, A. & Polovin, R. Theory of Wave Motion of an Electron Plasma. *Soviet Phys. JETP* **3.** http://www.jetp.ac.ru/cgi-bin/e/index/e/3/5/p696?a=list (1956).

[99] Sheng, Z. M. & Meyer-ter-Vehn, J. Relativistic wave breaking in warm plasmas. *Physics of Plasmas* **4,** 493–495. https://doi.org/10.1063/1.872116 (1997).

[100] Coffey, T. P. Breaking of Large Amplitude Plasma Oscillations. *The Physics of Fluids* **14,** 1402–1406. https://aip.scitation.org/doi/abs/10.1063/1.1693620 (1971).

[101] Katsouleas, T. & Mori, W. B. Wave-Breaking Amplitude of Relativistic Oscillations in a Thermal Plasma. *Phys. Rev. Lett.* **61,** 90–93. https://link.aps.org/doi/10.1103/PhysRevLett.61.90 (1 1988).

[102] Trines, R. M. G. M. & Norreys, P. A. Wave-breaking limits for relativistic electrostatic waves in a one-dimensional warm plasma. *Physics of Plasmas* **13,** 123102. https://doi.org/10.1063/1.2398927 (2006).

[103] Schroeder, C. B., Esarey, E. & Shadwick, B. A. Warm wave breaking of nonlinear plasma waves with arbitrary phase velocities. *Phys. Rev. E* **72,** 055401. https://link.aps.org/doi/10.1103/PhysRevE.72.055401 (5 2005).

[104] Kim, J. K. & Umstadter, D. Cold relativistic wavebreaking threshold of two-dimensional plasma waves. *AIP Conference Proceedings* **472,** 404–412. https://aip.scitation.org/doi/abs/10.1063/1.58859 (1999).

[105] Bulanov, S. V. *et al.* Transverse-Wake Wave Breaking. *Phys. Rev. Lett.* **78,** 4205–4208. https://link.aps.org/doi/10.1103/PhysRevLett.78.4205 (22 1997).

[106] Rosenzweig, J. B. *et al.* Acceleration and focusing of electrons in two-dimensional nonlinear plasma wake fields. *Phys. Rev. A* **44,** R6189–R6192. https://link.aps.org/doi/10.1103/PhysRevA.44.R6189 (10 1991).

[107] Lu, W. *Nonlinear plasma wakefield theory and optimum scaling for laser wakefield acceleration in the blowout regime* PhD thesis (University of California, Los Angeles, 2006). https://ui.adsabs.harvard.edu/abs/2006PhDT.......245L.

[108] Lu, W. *et al.* Nonlinear Theory for Relativistic Plasma Wakefields in the Blowout Regime. *Phys. Rev. Lett.* **96,** 165002. https://link.aps.org/doi/10.1103/PhysRevLett.96.165002 (16 2006).

[109] Lu, W. *et al.* A nonlinear theory for multidimensional relativistic plasma wave wakefields. *Physics of Plasmas* **13,** 056709. https://doi.org/10.1063/1.2203364 (2006).

[110] Vieira, J., Fonseca, R. & Silva, L. Multidimensional Plasma Wake Excitation in the Non-linear Blowout Regime. Comments: presented at the CERN Accelerator School- CAS 2014: Plasma Wake Acceleration, Geneva, Switzerland, 23-29 November 2014, 79–107. 29 p. https://cds.cern.ch/record/2199067 (2016).

[111] Kostyukov, I., Pukhov, A. & Kiselev, S. Phenomenological theory of laser-plasma interaction in “bubble” regime. *Physics of Plasmas* **11,** 5256–5264. https://doi.org/10.1063/1.1799371 (2004).

[112] Esirkepov, T. *et al.* Electron, Positron, and Photon Wakefield Acceleration: Trapping, Wake Overtaking, and Ponderomotive Acceleration. *Phys. Rev. Lett.* **96,** 014803. https://link.aps.org/doi/10.1103/PhysRevLett.96.014803 (1 2006).

[113] Esarey, E. & Pilloff, M. Trapping and acceleration in nonlinear plasma waves. *Physics of Plasmas* **2,** 1432–1436. https://doi.org/10.1063/1.871358 (1995).

[114] Corde, S. *et al.* Observation of longitudinal and transverse self-injections in laser-plasma accelerators. *Nature Communications* **4,** 1501. ISSN: 2041-1723. https://doi.org/10.1038/ncomms2528 (2013).

[115] Thomas, A. G. R. Scalings for radiation from plasma bubbles. *Physics of Plasmas* **17,** 056708. https://doi.org/10.1063/1.3368678 (2010).

[116] Mangles, S. P. D. *et al.* Self-injection threshold in self-guided laser wakefield accelerators. *Phys. Rev. ST Accel. Beams* **15,** 011302. https://link.aps.org/doi/10.1103/PhysRevSTAB.15.011302 (1 2012).

[117] Umstadter, D., Kim, J. K. & Dodd, E. Laser Injection of Ultrashort Electron Pulses into Wakefield Plasma Waves. *Phys. Rev. Lett.* **76,** 2073–2076. https://link.aps.org/doi/10.1103/PhysRevLett.76.2073 (12 1996).

[118] Bulanov, S. *et al.* Particle injection into the wave acceleration phase due to nonlinear wake wave breaking. *Phys. Rev. E* **58,** R5257–R5260. https://link.aps.org/doi/10.1103/PhysRevE.58.R5257 (5 1998).

[119] Pak, A. *et al.* Injection and Trapping of Tunnel-Ionized Electrons into Laser-Produced Wakes. *Phys. Rev. Lett.* **104,** 025003. https://link.aps.org/doi/10.1103/PhysRevLett.104.025003 (2 2010).

[120] Wenz, J. & Karsch, S. *Physics of Laser-Wakefield Accelerators (LWFA)* in *CAS - CERN Accelerator School 2019: High Gradient Wakefield Accelerators* (2020). arXiv: 2007.04622 [physics.acc-ph].

[121] Suk, H. *et al. Plasma electron trapping and acceleration in a plasma wake field using a density transition* in *The Physics of High Brightness Beams* (World Scientific, 2000), 404–417. https://www.worldscientific.com/doi/abs/10.1142/9789812792181_0026.

[122] Swanson, K. K. *et al.* Control of tunable, monoenergetic laser-plasma-accelerated electron beams using a shock-induced density downramp injector. *Phys. Rev. Accel. Beams* **20,** 051301. https://link.aps.org/doi/10.1103/PhysRevAccelBeams.20.051301 (5 2017).

[123] Schmid, K. *et al.* Density-transition based electron injector for laser driven wakefield accelerators. *Phys. Rev. ST Accel. Beams* **13,** 091301. https://link.aps.org/doi/10.1103/PhysRevSTAB.13.091301 (9 2010).

[124] Esarey, E. *et al.* Electron Injection into Plasma Wakefields by Colliding Laser Pulses. *Phys. Rev. Lett.* **79,** 2682–2685. https://link.aps.org/doi/10.1103/PhysRevLett.79.2682 (14 1997).

[125] Faure, J. *et al.* Controlled injection and acceleration of electrons in plasma wakefields by colliding laser pulses. *Nature* **444,** 737–739. ISSN: 1476-4687. https://doi.org/10.1038/nature05393 (2006).

[126] Davoine, X. *et al.* Cold Optical Injection Producing Monoenergetic, Multi-GeV Electron Bunches. *Phys. Rev. Lett.* **102,** 065001. https://link.aps.org/doi/10.1103/PhysRevLett.102.065001 (6 2009).

[127] Fubiani, G. *et al.* Beat wave injection of electrons into plasma waves using two interfering laser pulses. *Phys. Rev. E* **70,** 016402. https://link.aps.org/doi/10.1103/PhysRevE.70.016402 (1 2004).

[128] Rechatin, C. *et al.* Controlling the Phase-Space Volume of Injected Electrons in a Laser-Plasma Accelerator. *Phys. Rev. Lett.* **102,** 164801. https://link.aps.org/doi/10.1103/PhysRevLett.102.164801 (16 2009).

[129] Lehe, R. *et al.* Optical Transverse Injection in Laser-Plasma Acceleration. *Phys. Rev. Lett.* **111,** 085005. https://link.aps.org/doi/10.1103/PhysRevLett.111.085005 (8 2013).

[130] Esarey, E. *et al.* Nonlinear Pump Depletion and Electron Dephasing in Laser Wakefield Accelerators. *AIP Conference Proceedings* **737,** 578–584. https://aip.scitation.org/doi/abs/10.1063/1.1842594 (2004).

[131] Sainte-Marie, A., Gobert, O. & Quéré, F. Controlling the velocity of ultrashort light pulses in vacuum through spatio-temporal couplings. *Optica* **4,** 1298–1304. http://www.osapublishing.org/optica/abstract.cfm?URI=optica-4-10-1298 (2017).

[132] Froula, D. H. *et al.* Flying focus: Spatial and temporal control of intensity for laser-based applications. *Physics of Plasmas* **26,** 032109. eprint: https://doi.org/10.1063/1.5086308. https://doi.org/10.1063/1.5086308 (2019).

[133] Froula, D. H. *et al.* Spatiotemporal control of laser intensity. *Nature Photonics* **12,** 262–265. ISSN: 1749-4893. https://doi.org/10.1038/s41566-018-0121-8 (2018).

[134] Steinke, S. *et al.* Multistage coupling of independent laser-plasma accelerators. *Nature* **530,** 190–193. ISSN: 1476-4687. https://doi.org/10.1038/nature16525 (2016).

[135] Chen, P. *et al.* Energy Transfer in the Plasma Wake-Field Accelerator. *Phys. Rev. Lett.* **56,** 1252–1255. https://link.aps.org/doi/10.1103/PhysRevLett.56.1252 (12 1986).

[136] Panasenko, D. *et al.* Staging Laser Plasma Accelerators for Increased Beam Energy. *AIP Conference Proceedings* **1086,** 215–220. https://aip.scitation.org/doi/abs/10.1063/1.3080907 (2009).

[137] Decker, C. D. *et al.* The evolution of ultra-intense, short-pulse lasers in underdense plasmas. *Physics of Plasmas* **3,** 2047–2056. https://doi.org/10.1063/1.872001 (1996).

[138] Gordienko, S. & Pukhov, A. Scalings for ultrarelativistic laser plasmas and quasi-monoenergetic electrons. *Physics of Plasmas* **12,** 043109. https://doi.org/10.1063/1.1884126 (2005).

[139] Heigoldt, M. *et al.* Temporal evolution of longitudinal bunch profile in a laser wakefield accelerator. *Phys. Rev. ST Accel. Beams* **18,** 121302. https://link.aps.org/doi/10.1103/PhysRevSTAB.18.121302 (12 2015).

[140] Couperus, J. P. *Optimal beam loading in a nanocoulomb-class laser wakefield accelerator* PhD thesis (Helmholtz-Zentrum Dresden-Rossendorf, Germany, 2018). https://www.hzdr.de/publications/Publ-28080.

[141] Birdsall, C. K. & Langdon, A. B. *Plasma Physics via Computer Simulation* ISBN: 0-07-005371-5. https://www.taylorfrancis.com/books/mono/10.1201/9781315275048/plasma-physics-via-computer-simulation-langdon-birdsall (IOP Publishing, 1991).

[142] Hockney, R. W. & Eastwood, J. W. *Computer Simulation Using Particles* ISBN: 0852743920. https://www.taylorfrancis.com/books/mono/10.1201/9780367806934/computer-simulation-using-particles-hockney-eastwood (IOP Publishing, 1988).

[143] Lehe, R. *FBPIC* https://fbpic.github.io/overview/pic_algorithm.html (2020).

[144] Dawson, J. M. Particle simulation of plasmas. *Rev. Mod. Phys.* **55,** 403–447. https://link.aps.org/doi/10.1103/RevModPhys.55.403 (2 1983).

[145] Grigoryev, Y. N., Vshivkov, V. & Fedoruk, M. P. *Numerical "Particle-in-Cell" Methods: Theory and Applications* https://doi.org/10.1515/9783110916706 (Walter de Gruyter, 2002).

[146] Buneman, O. Dissipation of Currents in Ionized Media. *Phys. Rev.* **115,** 503–517. https://link.aps.org/doi/10.1103/PhysRev.115.503 (3 1959).

[147] Dawson, J. One-Dimensional Plasma Model. *The Physics of Fluids* **5,** 445–459. https://aip.scitation.org/doi/abs/10.1063/1.1706638 (1962).

[148] Qin, H. *et al.* Why is Boris algorithm so good? *Physics of Plasmas* **20,** 084503. https://doi.org/10.1063/1.4818428 (2013).

[149] Fonseca, R. A. *et al. OSIRIS: A Three-Dimensional, Fully Relativistic Particle in Cell Code for Modeling Plasma Based Accelerators* in *Computational Science — ICCS 2002* (eds Sloot, P. M. A. *et al.*) (Springer Berlin Heidelberg, Berlin, Heidelberg, 2002), 342–351. ISBN: 978-3-540-47789-1. https://link.springer.com/chapter/10.1007/3-540-47789-6_36.

[150] Arber, T. D. *et al.* Contemporary particle-in-cell approach to laser-plasma modelling. *Plasma Physics and Controlled Fusion* **57,** 113001. https://doi.org/10.1088%2F0741-3335%2F57%2F11%2F113001 (2015).

[151] Friedman, A., Grote, D. P. & Haber, I. Three-dimensional particle simulation of heavy-ion fusion beams*. *Physics of Fluids B: Plasma Physics* **4,** 2203–2210. https://doi.org/10.1063/1.860024 (1992).

[152] Lifschitz, A. *et al.* Particle-in-Cell modelling of laser–plasma interaction using Fourier decomposition. *Journal of Computational Physics* **228,** 1803–1814. ISSN: 0021-9991. http://www.sciencedirect.com/science/article/pii/S0021999108005950 (2009).

[153] Burau, H. *et al.* PIConGPU: A Fully Relativistic Particle-in-Cell Code for a GPU Cluster. *IEEE Transactions on Plasma Science* **38,** 2831–2839. https://ieeexplore.ieee.org/document/5556015 (2010).

[154] Cowan, B. M. *et al.* Generalized algorithm for control of numerical dispersion in explicit time-domain electromagnetic simulations. *Phys. Rev. ST Accel. Beams* **16,** 041303. https://link.aps.org/doi/10.1103/PhysRevSTAB.16.041303 (4 2013).

[155] Lehe, R. *et al.* Numerical growth of emittance in simulations of laser-wakefield acceleration. *Phys. Rev. ST Accel. Beams* **16,** 021301. https://link.aps.org/doi/10.1103/PhysRevSTAB.16.021301 (2 2013).

[156] Godfrey, B. B. Numerical Cherenkov instabilities in electromagnetic particle codes. *Journal of Computational Physics* **15,** 504–521. ISSN: 0021-9991. http://www.sciencedirect.com/science/article/pii/002199917490076X (1974).

[157] Courant, R., Friedrichs, K. & Lewy, H. Über die partiellen Differenzengleichungen der mathematischen Physik. *Mathematische Annalen* **100,** 32–74. ISSN: 1432-1807. https://doi.org/10.1007/BF01448839 (1928).

[158] Guizar-Sicairos, M. & Gutiérrez-Vega, J. C. Computation of quasi-discrete Hankel transforms of integer order for propagating optical wave fields. *J. Opt. Soc. Am. A* **21,** 53–58. http://josaa.osa.org/abstract.cfm?URI=josaa-21-1-53 (2004).

[159] *openPMD* https://www.openpmd.org (2020).

[160] Moulton, P. Ti-doped sapphire: tunable solid-state laser. *Optics News* **8,** 9–9. http://www.optica-opn.org/abstract.cfm?URI=on-8-6-9 (1982).

[161] Moulton, P. F. Spectroscopic and laser characteristics of Ti:Al2O3. *J. Opt. Soc. Am. B* **3,** 125–133. http://josab.osa.org/abstract.cfm?URI=josab-3-1-125 (1986).

[162] Günther, B. *Design, implementation and characterisation of the 300TW-upgrade of the ATLAS laser system* MA thesis (Ludwig-Maximilians-Universität München, 2014).

[163] Heider, T. *Upgrade des Hochkontrast-Frontends des ATLAS-300 Laser Systems* MA thesis (Ludwig-Maximilians-Universität München, 2016).

[164] Cheriaux, G. *et al.* Aberration-free stretcher design for ultrashort-pulse amplification. *Opt. Lett.* **21,** 414–416. http://ol.osa.org/abstract.cfm?URI=ol-21-6-414 (1996).

[165] Tournois, P. Acousto-optic programmable dispersive filter for adaptive compensation of group delay time dispersion in laser systems. *Optics Communications* **140,** 245–249. ISSN: 0030-4018. http://www.sciencedirect.com/science/article/pii/S0030401897001533 (1997).

[166] Oksenhendler, T. *et al.* Intracavity acousto-optic programmable gain control for ultra-wide-band regenerative amplifiers. *Applied Physics B* **83,** 491. ISSN: 1432-0649. https://doi.org/10.1007/s00340-006-2231-0 (2006).

[167] Amplitude. *Amplitude-Laser* https://amplitude-laser.com/ (2021).

[168] Pretzler, G., Kasper, A. & Witte, K. J. Angular chirp and tilted light pulses in CPA lasers. *Applied Physics B* **70,** 1–9. ISSN: 1432-0649. https://doi.org/10.1007/s003400050001 (2000).

[169] SWAMP. *Swamp Optics* http://www.swampoptics.com/pulse-measurement.html (2021).

[170] Amplitude. *Amplitude-Laser* https://amplitude-laser.com/add_ons/metrology/sequoia/ (2021).

[171] Fastlite. *Fastlite* https://fastlite.com/produits/wizzler-ultrafast-pulse-measurement/ (2021).

[172] Oksenhendler, T. *et al.* Self-referenced spectral interferometry. *Applied Physics B* **99,** 7–12. ISSN: 1432-0649. https://doi.org/10.1007/s00340-010-3916-y (2010).

[173] Moulet, A. *et al.* Single-shot, high-dynamic-range measurement of sub-15 fs pulses by self-referenced spectral interferometry. *Opt. Lett.* **35,** 3856–3858. http://ol.osa.org/abstract.cfm?URI=ol-35-22-3856 (2010).

[174] Daiber, F. M. *Generation of Few Cycle Pulses for Direct Observation of the Plasma Wave* MA thesis (Ludwig-Maximilians-Universität München, 2015).

[175] Schwab, M. B. *et al.* Few-cycle optical probe-pulse for investigation of relativistic laser-plasma interactions. *Applied Physics Letters* **103,** 191118. https://doi.org/10.1063/1.4829489 (2013).

[176] Sävert, A. *et al.* Direct Observation of the Injection Dynamics of a Laser Wakefield Accelerator Using Few-Femtosecond Shadowgraphy. *Phys. Rev. Lett.* **115,** 055002. https://link.aps.org/doi/10.1103/PhysRevLett.115.055002 (5 2015).

[177] Benattar, R., Popovics, C. & Sigel, R. Polarized light interferometer for laser fusion studies. *Review of Scientific Instruments* **50,** 1583–1586. https://doi.org/10.1063/1.1135764 (1979).

[178] Goers, A. J. *et al.* Multi-MeV Electron Acceleration by Subterawatt Laser Pulses. *Phys. Rev. Lett.* **115,** 194802. https://link.aps.org/doi/10.1103/PhysRevLett.115.194802 (19 2015).

[179] Hüther, M. J. *Design and Characterisation of Supersonic Nozzles for Shock Front Electron Injection in Laser Wakefield Acceleration* MA thesis (Ludwig-Maximilians-Universität München, 2015).

[180] Koschitzki, C. *Injection mechanisms in Laser Wakefield Acceleration* PhD thesis (Humboldt-Universität zu Berlin, Mathematisch-Naturwissenschaftliche Fakultät, 2017). http://edoc.hu-berlin.de/18452/18412.

[181] Sävert, A. *Few-cycle microscopy of a laser wakefield accelerator* en. Dissertation, Friedrich-Schiller-Universität Jena, 2016. PhD thesis (Jena, 2016). http://uri.gbv.de/document/gvk:ppn:869877348.

[182] Wildgruber, L. *Few-cycle probing of high-power laser induced plasma* MA thesis (Ludwig-Maximilians-Universität München, 2017).

[183] Ding, H. *LWFA diagnostics development for ATLAS-300 and Nonlinear Plasma Wavelength Scalings* PhD thesis (Ludwig-Maximilians-Universität München, 2021).

[184] Schindler, S. *et al. Tunable X-ray source by Thomson scattering during laser-wakefield acceleration* in *Laser Acceleration of Electrons, Protons, and Ions V* (eds Esarey, E., Schroeder, C. B. & Schreiber, J.) **11037** (SPIE, 2019), 48–56. https://doi.org/10.1117/12.2520354.

[185] CAWO. *CAWO Solutions* https://www.cawo.com/products/intensifying-screens/green-emitting/ (2021).

[186] Morlotti, R. *et al.* Intrinsic conversion efficiency of X-rays to light in Gd2O2S : Tb3+ powder phosphors. *Journal of Luminescence* **72-74.** Luminescence and Optical Spectroscopy of Condensed Matter, 772–774. ISSN: 0022-2313. http://www.sciencedirect.com/science/article/pii/S0022231396003304 (1997).

[187] Kurz, T. *et al.* Calibration and cross-laboratory implementation of scintillating screens for electron bunch charge determination. *Review of Scientific Instruments* **89,** 093303. https://doi.org/10.1063/1.5041755 (2018).

[188] Pulsar Physics. *General Particle Tracer (GPT)* http://www.pulsar.nl/gpt/index.html (2021).

[189] Buck, A. *et al.* Absolute charge calibration of scintillating screens for relativistic electron detection. *Review of Scientific Instruments* **81,** 033301. https://doi.org/10.1063/1.3310275 (2010).

[190] Kurz, T. *Calibration of scintillation screens for bunch charge determination in laser wakefield acceleration* MA thesis (Ludwig-Maximilians-Universität München, 2016).

[191] Maier, A. R. *et al.* Decoding Sources of Energy Variability in a Laser-Plasma Accelerator. *Phys. Rev. X* **10,** 031039. https://link.aps.org/doi/10.1103/PhysRevX.10.031039 (3 2020).

[192] Bendow, B. & Gianino, P. D. Optics of Thermal Lensing in Solids. *Appl. Opt.* **12,** 710–718. http://ao.osa.org/abstract.cfm?URI=ao-12-4-710 (1973).

[193] Wagner, G., Shiler, M. & Wulfmeyer, V. Simulations of thermal lensing of a Ti:Sapphire crystal end-pumped with high average power. *Opt. Express* **13,** 8045–8055. http://www.opticsexpress.org/abstract.cfm?URI=oe-13-20-8045 (2005).

[194] Kirchen, M. *et al.* Optimal Beam Loading in a Laser-Plasma Accelerator. *Phys. Rev. Lett.* **126,** 174801. https://link.aps.org/doi/10.1103/PhysRevLett.126.174801 (17 2021).

[195] Pukhov, A. *et al.* The bubble regime of laser–plasma acceleration: monoenergetic electrons and the scalability. *Plasma Physics and Controlled Fusion* **46,** B179–B186. https://doi.org/10.1088%2F0741-3335%2F46%2F12b%2F016 (2004).

[196] Hsieh, C.-T. *et al.* Tomography of Injection and Acceleration of Monoenergetic Electrons in a Laser-Wakefield Accelerator. *Phys. Rev. Lett.* **96,** 095001. https://link.aps.org/doi/10.1103/PhysRevLett.96.095001 (9 2006).

[197] Kneip, S. *et al.* Near-GeV Acceleration of Electrons by a Nonlinear Plasma Wave Driven by a Self-Guided Laser Pulse. *Phys. Rev. Lett.* **103,** 035002. https://link.aps.org/doi/10.1103/PhysRevLett.103.035002 (3 2009).

[198] Andriyash, I. A. *et al.* X-Ray Amplification from a Raman Free-Electron Laser. *Phys. Rev. Lett.* **109,** 244802. https://link.aps.org/doi/10.1103/PhysRevLett.109.244802 (24 2012).

[199] Seggebrock, T. *Conceptual design of a laser-plasma accelerator driven free-electron laser demonstration experiment* PhD thesis (Ludwig-Maximilians-Universität München, 2015). http://nbn-resolving.de/urn:nbn:de:bvb:19-184314.

[200] Petrillo, V., Serafini, L. & Tomassini, P. Ultrahigh brightness electron beams by plasma-based injectors for driving all-optical free-electron lasers. *Phys. Rev. ST Accel. Beams* **11,** 070703. https://link.aps.org/doi/10.1103/PhysRevSTAB.11.070703 (7 2008).

[201] Bacci, A. *et al.* Compact X-ray free-electron laser based on an optical undulator. *Nuclear Instruments and Methods in Physics Research Section A: Accelerators, Spectrometers, Detectors and Associated Equipment* **587,** 388–397. ISSN: 0168-9002. https://www.sciencedirect.com/science/article/pii/S0168900207025053 (2008).

[202] Manahan, G. G. *et al.* Single-stage plasma-based correlated energy spread compensation for ultrahigh 6D brightness electron beams. *Nature Communications* **8,** 15705. ISSN: 2041-1723. https://doi.org/10.1038/ncomms15705 (2017).

[203] Schlenvoigt, H.-P. *et al.* A compact synchrotron radiation source driven by a laser-plasma wakefield accelerator. *Nature Physics* **4,** 130–133. ISSN: 1745-2481. https://doi.org/10.1038/nphys811 (2008).

[204] Gilljohann, M. F. *et al.* Direct Observation of Plasma Waves and Dynamics Induced by Laser-Accelerated Electron Beams. *Phys. Rev. X* **9,** 011046. https://link.aps.org/doi/10.1103/PhysRevX.9.011046 (1 2019).

[205] Martinez de la Ossa, A. *et al.* High-Quality Electron Beams from Beam-Driven Plasma Accelerators by Wakefield-Induced Ionization Injection. *Phys. Rev. Lett.* **111,** 245003. https://link.aps.org/doi/10.1103/PhysRevLett.111.245003 (24 2013).

[206] Blumenfeld, I. *et al.* Energy doubling of 42 GeV electrons in a metre-scale plasma wakefield accelerator. *Nature* **445,** 741–744. ISSN: 1476-4687. https://doi.org/10.1038/nature05538 (2007).

[207] Hidding, B. *et al.* Monoenergetic Energy Doubling in a Hybrid Laser-Plasma Wakefield Accelerator. *Phys. Rev. Lett.* **104,** 195002. https://link.aps.org/doi/10.1103/PhysRevLett.104.195002 (19 2010).

[208] Heinemann, T. *et al. Investigating the Key Parameters of a staged Laser- and Particle Driven Plasma Wakefield Accelerator Experiment* in *Proc. of International Particle Accelerator Conference (IPAC17)* (JACoW, Geneva, Switzerland, 2017), 1703–1706. ISBN: 978-3-95450-182-3. https://accelconf.web.cern.ch/ipac2017/papers/tupik010.pdf.

[209] Martinez de la Ossa, A. *et al.* Hybrid LWFA–PWFA staging as a beam energy and brightness transformer: conceptual design and simulations. *Philosophical Transactions of the Royal Society A* **377,** 20180175. https://doi.org/10.1098/rsta.2018.0175 (2019).

[210] Hidding, B. *et al.* Ultracold Electron Bunch Generation via Plasma Photocathode Emission and Acceleration in a Beam-Driven Plasma Blowout. *Phys. Rev. Lett.* **108,** 035001. https://link.aps.org/doi/10.1103/PhysRevLett.108.035001 (3 2012).

[211] Martinez de la Ossa, A. *et al.* Wakefield-induced ionization injection in beam-driven plasma accelerators. *Physics of Plasmas* **22,** 093107. https://doi.org/10.1063/1.4929921 (2015).

[212] Kurz, T. *et al.* Demonstration of a compact plasma accelerator powered by laser-accelerated electron beams. *Nature Communications* **12,** 2895. ISSN: 2041-1723. https://doi.org/10.1038/s41467-021-23000-7 (2021).

[213] Wenz, J. *et al.* Quantitative X-ray phase-contrast microtomography from a compact laser-driven betatron source. *Nature Communications* **6,** 7568. ISSN: 2041-1723. https://doi.org/10.1038/ncomms8568 (2015).

[214] Cole, J. M. *et al.* Laser-wakefield accelerators as hard x-ray sources for 3D medical imaging of human bone. *Scientific Reports* **5,** 13244. ISSN: 2045-2322. https://doi.org/10.1038/srep13244 (2015).

[215] Noether, E. Invariante Variationsprobleme. ger. *Nachrichten von der Gesellschaft der Wissenschaften zu Göttingen, Mathematisch-Physikalische Klasse* **1918,** 235–257. http://eudml.org/doc/59024 (1918).

[216] Shannon, C. Communication in the Presence of Noise. *Proceedings of the IRE* **37,** 10–21. https://doi.org/10.1109/JRPROC.1949.232969 (1949).

[217] Tsung, F. S. *et al.* Simulation of monoenergetic electron generation via laser wakefield accelerators for 5–25 TW lasers. *Physics of Plasmas* **13,** 056708. https://doi.org/10.1063/1.2198535 (2006).

[218] Shaw, J. L. *et al.* Estimation of direct laser acceleration in laser wakefield accelerators using particle-in-cell simulations. *Plasma Physics and Controlled Fusion* **58,** 034008. https://doi.org/10.1088%2F0741-3335%2F58%2F3%2F034008 (2016).

[219] Vay, J.-L. Noninvariance of Space- and Time-Scale Ranges under a Lorentz Transformation and the Implications for the Study of Relativistic Interactions. *Phys. Rev. Lett.* **98,** 130405. https://link.aps.org/doi/10.1103/PhysRevLett.98.130405 (13 2007).

[220] Vay, J.-L. *et al.* Modeling of 10 GeV-1 TeV laser-plasma accelerators using Lorentz boosted simulations. *Physics of Plasmas* **18,** 123103. https://doi.org/10.1063/1.3663841 (2011).

[221] Adelmann, A. *et al.* Real-Time Tomography of Gas-Jets with a Wollaston Interferometer. *Applied Sciences* **8,** 443. https://www.mdpi.com/2076-3417/8/3/443 (2018).

[222] Lehe, R. *openPMD-viewer* https://github.com/openPMD/openPMD-viewer (2020).

[228] Kurz, T. *et al.* Demonstration of a compact plasma accelerator powered by laser-accelerated electron beams. *Nature Communications* **12,** 2895. ISSN: 2041-1723. https://doi.org/10.1038/s41467-021-23000-7 (2021).

Glossary

AOPDF	acousto-optic programmable dispersive filter
ASE	amplified spontaneous emission
ATLAS	Advanced Titanium Sapphire Laser System
BSI	barrier-suppression ionization
CAD	computer-aided design
CALA	Centre for Advanced Laser Applications
CCD	charge-coupled device
CERN	European Organization for Nuclear Research
CPA	chirped pulse amplification
CPU	central processing unit
CTR	coherent transition radiation
DAQ	data acquisition
DC	direct current
FBPIC	Fourier-Bessel Particle-In-Cell
FEL	free-electron laser
FROG	frequency-resolved optical gating
FWHM	full width at half maximum
GPU	graphics processing unit
HDF5	Hierarchical Data Format 5
LEX	Laboratory for EXtreme Photonics
LHC	Large Hadron Collider
LPA	laser plasma accelerator

LWFA	laser wakefield accelerator
ND	neutral-density
Nd:YAG	neodymium-doped yttrium aluminum garnet
OAP	off-axis parabolic mirror
openPMD	open standard for particle-mesh data files
PIC	particle-in-cell
PtV	peak to valley
PWFA	plasma wakefield accelerator
RF	radio frequency
RMS	root mean square
SPM	self-phase modulation
SRSI	self-referenced spectral interferometry
std	standard deviation
STII	self-truncated ionization injection
Ti:Sa	titanium-sapphire

Data Archiving

The experimental and simulated raw data, corresponding evaluation files, and notebooks to generate the figures are stored on the Data Archive Server of the Laboratory for Attosecond Physics at the Max Planck Institute of Quantum Optics accessible under

`/afs/ipp-garching.mpg.de/mpq/lap/publication_archive/Theses/2023/Götzfried,Johannes(PhD)`.

The list of figures in the next section contains a comment for each plot indicating the specific paths relative to the base directory where the files necessary to generate the individual plot can be found. Typically, the experimental raw data are stored as .png or .txt. Input files to set up the respective simulations (.py) and generate the simulated raw data (.h5) are given in each case. The processing of all the raw data is either done in Matlab or Python. If appropriate, intermediate data files are stored as .mat or .npy/.npz respectively. The final plots (.pdf) are either generated from this intermediate data or directly via Jupyter notebooks (.ipynb). If no file is given, the image is an Inkscape drawing. Where necessary, *ReadMe.txt* files located in the respective folders provide further explanations and information.

List of Figures

List of Tables

List of Symbols and Constants

$z_{\text{collision}}$	absolute longitudinal laser collision position	[mm]
z_{f}	absolute longitudinal laser focus position	[mm]
z_{shock}	absolute shock front position	[mm]
L_{acc}	acceleration length	[m]
Γ	accelerator efficiency	[ ]
ω	angular frequency of the laser	$[\text{rad}\,\text{s}^{-1}]$
ω_{p}	angular plasma frequency	$[\text{rad}\,\text{s}^{-1}]$
k_{B}	Boltzmann constant	$1.380\,65 \times 10^{-23}\,\text{J}\,\text{K}^{-1}$
R	bubble radius	[m]
ρ	charge density	$[\text{C}\,\text{m}^{-3}]$
q	charge of a particle	[C]
n_{crit}	critical electron density	$[\text{cm}^{-3}]$
P_{crit}	critical laser power	[W]
E_0	cold non-relativistic wave breaking field	$[\text{V}\,\text{m}^{-1}]$
E_{WB}	cold relativistic wave breaking field	$[\text{V}\,\text{m}^{-1}]$
λ_{D}	Debye length	[m]
L_{d}	dephasing length in 1D	[m]
$L_{\text{d,3D}}$	dephasing length in 3D	[m]
$\boldsymbol{j}$	electric current density	$[\text{A}\,\text{m}^{-2}]$
$\boldsymbol{E}$	electric field strength	$[\text{V}\,\text{m}^{-1}]$
χ_{e}	electric susceptibility	[ ]
n_{b}	electron bunch density	$[\text{cm}^{-3}]$
n_{e}	electron density	$[\text{cm}^{-3}]$
m_{e}	electron mass	$9.109\,38 \times 10^{-31}\,\text{kg}$
Q_{Peak}	electron peak charge	[C]
E_{Peak}	electron peak energy	[eV]
e	elementary charge	$1.602\,18 \times 10^{-19}\,\text{C}$
Q_{s}	flat field beam loading charge	[C]
E_{s}	flat on-axis longitudinal beam loading field	$[\text{V}\,\text{m}^{-1}]$
$\boldsymbol{F}$	force	[N]
w	Gaussian beam radius (field amplitude drops to 1/e)	[m]

v_{gr}	group velocity of laser pulse	$[\mathrm{m\,s^{-1}}]$
W	ideal accelerated electron energy	[eV]
γ_{thres}	injection threshold	[ ]
I	intensity	$[\mathrm{W\,m^{-2}}]$
Z_i	ion charge	[ ]
n_i	ion density	$[\mathrm{cm^{-3}}]$
E_{kin}	kinetic energy	[eV]
Δ	Laplace operator	$\Delta := \nabla^2$
P	laser power	[W]
τ	laser pulse duration	[fs]
E_L	laser pulse energy	[J]
λ	laser wavelength	[m]
$z_{f,rel}$	long. laser focus pos. relative to shock front[1]	[mm]
ζ,ξ	longitudinal position in co-moving frame	[m]
γ	Lorentz factor	$\gamma = (1 - \boldsymbol{v}^2/\mathrm{c}^2)^{-1/2}$
$\boldsymbol{F}_L$	Lorentz force	[N]
$\boldsymbol{B}$	magnetic flux density	[T]
χ_m	magnetic susceptibility	[ ]
w_{match}	matched beam spot size	[m]
P_{match}	matched laser power	[W]
$\boldsymbol{p}$	momentum	[N s]
∇	nabla operator	$\nabla := (\partial_{x_1}, \ldots, \partial_{x_n})$
φ	normalized electric potential	[ ]
$\boldsymbol{a}^2$	normalized laser intensity	[ ]
β_p	normalized phase velocity of plasma wave	[ ]
a_0	normalized vector potential	[ ]
$\boldsymbol{\beta}$	normalized velocity	$\boldsymbol{\beta} = \boldsymbol{v}/c$
∂_ν	partial derivative with respect to ν	$\partial_\nu := \partial/\partial\nu$
v_{ph}	phase velocity of laser pulse	$[\mathrm{m\,s^{-1}}]$
v_g	phase velocity of plasma wave	$[\mathrm{m\,s^{-1}}]$
λ_p	plasma wavelength	[m]
$\boldsymbol{F}_{Pond}$	ponderomotive force	[N]
ϕ_{Pond}	ponderomotive potential	[J]
$\boldsymbol{x}$, $\boldsymbol{r}$	position	[m]
$\boldsymbol{S}$	Poynting vector	$[\mathrm{W\,m^{-2}}]$
L_{pd}	pump depletion length in 1D	[m]

[1] $z_{f,rel} := z_f - z_{shock}$

$L_{\mathrm{pd,3D}}$	pump depletion length in 3D	[m]
w_0	radial focal spot size	[m]
z_R	Rayleigh length	[m]
n	refractive index	[ ]
η	refractive index of plasma	[ ]
μ_r	relative permeability	[ ]
ε_r	relative permittivity	[ ]
ϕ	scalar electric potential	V
γ_3	skewness of electron spectrum	[ ]
c	speed of light	$2.997\,92 \times 10^{8}\,\mathrm{m\,s^{-1}}$
T	temperature	[K]
t	time	[s]
W_tot	total electron beam energy	[J]
Q_tot	totally accelerated charge	[C]
r_b	transverse bubble radius	[m]
n_0	unperturbed electron density	$[\mathrm{cm^{-3}}]$
μ_0	vacuum permeability	$1.256\,64 \times 10^{-6}\,\mathrm{N\,A^{-2}}$
ε_0	vacuum permittivity	$8.854\,19 \times 10^{-12}\,\mathrm{F\,m^{-1}}$
$\boldsymbol{A}$	vector or magnetic potential	[T m]
$\boldsymbol{v}$	velocity	$[\mathrm{m\,s^{-1}}]$
$\boldsymbol{k}$	wave vector	$[\mathrm{m^{-1}}]$

List of Publications by the Author

During the work for this thesis, the following articles have been published in peer-reviewed journals. In some of these articles parts of the work presented in this thesis are mentioned or discussed:

- **Götzfried, J.,** Döpp, A., Gilljohann, M. F., Foerster, F. M., Ding, H., Schindler, S., Schilling, G., Buck, A., Veisz, L. & Karsch, S. Physics of High-Charge Electron Beams in Laser-Plasma Wakefields. *Phys. Rev. X* **10,** 041015. https://link.aps.org/doi/10.1103/PhysRevX.10.041015 (4 2020, © 2020 American Physical Society)
- Ding, H., Döpp, A., Gilljohann, M., **Götzfried, J.,** Schindler, S., Wildgruber, L., Cheung, G., Hooker, S. M. & Karsch, S. Nonlinear plasma wavelength scalings in a laser wakefield accelerator. *Phys. Rev. E* **101,** 023209. https://link.aps.org/doi/10.1103/PhysRevE.101.023209 (2 2020)
- Schindler, S., Döpp, A., Ding, H., Gilljohann, M., **Götzfried, J.** & Karsch, S. *Tunable X-ray source by Thomson scattering during laser-wakefield acceleration* in *Laser Acceleration of Electrons, Protons, and Ions V* (eds Esarey, E., Schroeder, C. B. & Schreiber, J.) **11037** (SPIE, 2019), 48–56. https://doi.org/10.1117/12.2520354
- Gilljohann, M. F., Ding, H., Döpp, A., **Götzfried, J.,** Schindler, S., Schilling, G., Corde, S., Debus, A., Heinemann, T., Hidding, B., Hooker, S. M., Irman, A., Kononenko, O., Kurz, T., Martinez de la Ossa, A., Schramm, U. & Karsch, S. Direct Observation of Plasma Waves and Dynamics Induced by Laser-Accelerated Electron Beams. *Phys. Rev. X* **9,** 011046. https://link.aps.org/doi/10.1103/PhysRevX.9.011046 (1 2019)
- Haffa, D., Yang, R., Bin, J., Lehrack, S., Brack, F.-E., Ding, H., Englbrecht, F. S., Gao, Y., Gebhard, J., Gilljohann, M., **Götzfried, J.,** Hartmann, J., Herr, S., Hilz, P., Kraft, S. D., Kreuzer, C., Kroll, F., Lindner, F. H., Metzkes-Ng, J., Ostermayr, T. M., Ridente, E., Rösch, T. F., Schilling, G., Schlenvoigt, H.-P., Speicher, M., Taray, D., Würl, M., Zeil, K., Schramm, U., Karsch, S., Parodi, K., Bolton, P. R., Assmann, W. & Schreiber, J. I-BEAT: Ultrasonic method for online measurement of the energy

distribution of a single ion bunch. *Scientific Reports* **9,** 6714. ISSN: 2045-2322. https://doi.org/10.1038/s41598-019-42920-5 (2019)

- Kurz, T., Heinemann, T., Gilljohann, M. F., Chang, Y. Y., Couperus Cabadağ, J. P., Debus, A., Kononenko, O., Pausch, R., Schöbel, S., Assmann, R. W., Bussmann, M., Ding, H., **Götzfried, J.,** Köhler, A., Raj, G., Schindler, S., Steiniger, K., Zarini, O., Corde, S., Döpp, A., Hidding, B., Karsch, S., Schramm, U., Martinez de la Ossa, A. & Irman, A. Demonstration of a compact plasma accelerator powered by laser-accelerated electron beams. *Nature Communications* **12,** 2895. ISSN: 2041-1723. https://doi.org/10.1038/s41467-021-23000-7 (2021)
- Wenz, J., Döpp, A., Khrennikov, K., Schindler, S., Gilljohann, M. F., Ding, H., **Götzfried, J.,** Buck, A., Xu, J., Heigoldt, M., Helml, W., Veisz, L. & Karsch, S. Dual-energy electron beams from a compact laser-driven accelerator. *Nature Photonics* **13,** 263–269. ISSN: 1749-4893. https://doi.org/10.1038/s41566-019-0356-z (2019)
- Döpp, A., Hehn, L., **Götzfried, J.,** Wenz, J., Gilljohann, M., Ding, H., Schindler, S., Pfeiffer, F. & Karsch, S. Quick x-ray microtomography using a laser-driven betatron source. *Optica* **5,** 199–203. http://www.osapublishing.org/optica/abstract.cfm?URI=optica-5-2-199 (2018)
- **Götzfried, J.,** Döpp, A., Gilljohann, M., Ding, H., Schindler, S., Wenz, J., Hehn, L., Pfeiffer, F. & Karsch, S. Research towards high-repetition rate laser-driven X-ray sources for imaging applications. *Nuclear Instruments and Methods in Physics Research Section A: Accelerators, Spectrometers, Detectors and Associated Equipment* **909.** 3rd European Advanced Accelerator Concepts workshop (EAAC2017), 286–289. ISSN: 0168-9002. http://www.sciencedirect.com/science/article/pii/S0168900218303115 (2018)

The following articles are unrelated to this thesis but nevertheless worth reading:

- Krauth, J. J., Schuhmann, K., Ahmed, M. A., Amaro, F. D., Amaro, P., Biraben, F., Chen, T.-L., Covita, D. S., Dax, A. J., Diepold, M., Fernandes, L. M. P., Franke, B., Galtier, S., Gouvea, A. L., **Götzfried, J.,** Graf, T., Hänsch, T. W., Hartmann, J., Hildebrandt, M., Indelicato, P., Julien, L., Kirch, K., Knecht, A., Liu, Y.-W., Machado, J., Monteiro, C. M. B., Mulhauser, F., Naar, B., Nebel, T., Nez, F., dos Santos, J. M. F., Santos, J. P., Szabo, C. I., Taqqu, D., Veloso, J. F. C. A., Vogelsang, J., Voss, A., Weichelt, B., Pohl, R., Antognini, A. & Kottmann, F. Measuring the α-particle charge radius with muonic helium-4 ions. *Nature* **589,** 527–531. https://doi.org/10.1038/s41586-021-03183-1 (2021)

- Monteiro, C., Amaro, F., Sousa, M., Abdou-Ahmed, M., Amaro, P., Biraben, F., Chen, T., Covita, D., Dax, A., Diepold, M., Fernandes, L., Franke, B., Galtier, S., Gouvea, A., **Götzfried, J.,** Graf, T., Hänsch, T., Hildebrandt, M., Indelicato, P., Julien, L., Kirch, K., Knecht, A., Kottmann, F., Krauth, J., Liu, Y., Machado, J., Mulhauser, F., Naar, B., Nebel, T., Nez, F., Pohl, R., Santos, J., dos Santos, J., Schuhmann, K., Szabo, C., Taqqu, D., Veloso, J. & Antognini, A. On the double peak structure of avalanche photodiode response to monoenergetic x-rays at various temperatures and bias voltages. *Journal of Instrumentation* **13,** C01033–C01033. https://doi.org/10.1088%2F1748-0221%2F13%2F01%2Fc01033 (2018)
- Krauth, J. J., Schuhmann, K., Abdou Ahmed, M., Amaro, F. D., Amaro, P., Biraben, F., Cardoso, J. M. R., Carvalho, M. L., Covita, D. S., Dax, A., Dhawan, S., Diepold, M., Fernandes, L. M. P., Franke, B., Galtier, S., Giesen, A., Gouvea, A. L., **Götzfried, J.,** Graf, T., Guerra, M., Haack, J., Hänsch, T. W., Hildebrandt, M., Indelicato, P., Julien, L., Kirch, K., Knecht, A., Knowles, P., Kottmann, F., Le Bigot, E. .-O., Liu, Y. .-W., Lopes, J. A. M., Ludhova, L., Machado, J., Monteiro, C. M. B., Mulhauser, F., Nebel, T., Nez, F., Rabinowitz, P., Rapisarda, E., dos Santos, J. M. F., Santos, J. P., Schaller, L. A., Schwob, C., Szabo, C. I., Taqqu, D., Veloso, J. F. C. A., Voss, A., Weichelt, B., Willig, M., Pohl, R. & Antognini, A. The proton radius puzzle. *arXiv e-prints,* arXiv:1706.00696. arXiv: 1706.00696 [physics.atom-ph] (2017)
- Antognini, A., Schuhmann, K., Amaro, F. D., Amaro, P., Abdou-Ahmed, M., Biraben, F., Chen, T.-L., Covita, D. S., Dax, A. J., Diepold, M., Fernandes, L. M. P., Franke, B., Galtier, S., Gouvea, A. L., **Götzfried, J.,** Graf, T., Hänsch, T. W., Hildebrandt, M., Indelicato, P., Julien, L., Kirch, K., Knecht, A., Kottmann, F., Krauth, J. J., Liu, Y.-W., Machado, J., Monteiro, C. M. B., Mulhauser, F., Nez, F., Santos, J. P., dos Santos, J. M. F., Szabo, C. I., Taqqu, D., Veloso, J. F. C. A., Voss, A., Weichelt, B. & Pohl, R. Experiments towards resolving the proton charge radius puzzle. *EPJ Web of Conferences* **113,** 01006. https://doi.org/10.1051/epjconf/201611301006 (2016)
- Pohl, R., Nez, F., Fernandes, L. M. P., Ahmed, M. A., Amaro, F. D., Amaro, P., Biraben, F., Cardoso, J. M. R., Covita, D. S., Dax, A., Dhawan, S., Diepold, M., Franke, B., Galtier, S., Giesen, A., Gouvea, A. L., **Götzfried, J.,** Graf, T., Hänsch, T. W., Hildebrandt, M., Indelicato, P., Julien, L., Kirch, K., Knecht, A., Knowles, P., Kottmann, F., Krauth, J. J., Bigot, E.-O. L., Liu, Y.-W., Lopes, J. A. M., Ludhova, L., Machado, J., Monteiro, C. M. B., Mulhauser, F., Nebel, T., Rabinowitz, P., dos Santos, J. M. F., Santos, J. P., Schaller, L. A., Schuhmann, K., Schwob, C., Szabo, C. I., Taqqu, D., Veloso, J. F. C. A., Voss, A., Weichelt, B. & Antognini, A. *Laser Spectroscopy of Muonic Atoms and Ions* in *Proceedings of the 12th International*

Conference on Low Energy Antiproton Physics (LEAP2016) (Journal of the Physical Society of Japan, 2017). eprint: https://journals.jps.jp/doi/pdf/10.7566/JPSCP.18.011021. https://journals.jps.jp/doi/abs/10.7566/JPSCP.18.011021

- Diepold, M., Fernandes, L. M. P., Machado, J., Amaro, P., Abdou-Ahmed, M., Amaro, F. D., Antognini, A., Biraben, F., Chen, T.-L., Covita, D. S., Dax, A. J., Franke, B., Galtier, S., Gouvea, A. L., **Götzfried, J.,** Graf, T., Hänsch, T. W., Hildebrandt, M., Indelicato, P., Julien, L., Kirch, K., Knecht, A., Kottmann, F., Krauth, J. J., Liu, Y.-W., Monteiro, C. M. B., Mulhauser, F., Naar, B., Nebel, T., Nez, F., Santos, J. P., dos Santos, J. M. F., Schuhmann, K., Szabo, C. I., Taqqu, D., Veloso, J. F. C. A., Voss, A., Weichelt, B. & Pohl, R. Improved x-ray detection and particle identification with avalanche photodiodes. *Review of Scientific Instruments* **86,** 053102. eprint: https://doi.org/10.1063/1.4921195. https://doi.org/10.1063/1.4921195 (2015)
- Vogelsang, J., Diepold, M., Antognini, A., Dax, A., **Götzfried, J.,** Hänsch, T. W., Kottmann, F., Krauth, J. J., Liu, Y.-W., Nebel, T., Nez, F., Schuhmann, K., Taqqu, D. & Pohl, R. Multipass laser cavity for efficient transverse illumination of an elongated volume. *Opt. Express* **22,** 13050–13062. http://www.opticsexpress.org/abstract.cfm?URI=oe-22-11-13050 (2014)

Acknowledgments

First, I would like to thank my doctoral advisor **Prof. Dr. Stefan Karsch** for accepting me as his Ph.D. student. His outstanding technical skills in the lab and his profound knowledge of lasers, in general, were often crucial for the success of the experiments. His support especially by acquiring a decent amount of computing capacity was a prerequisite for the extensive simulation studies which made up a great deal of my work.

Furthermore, I am indebted to **Prof. Dr. Ferenc Krausz** who gave me the opportunity to pursue my Ph.D. at his chair and group at the Max Planck Institute of Quantum Optics. Only the excellent research environment provided here makes experiments of such scale possible.

I am very grateful to **Prof. Dr. Laszlo Veisz** not only for constructive discussions and his data contribution to our beam loading studies, but also for acting as the second referee of this thesis.

Many thanks to our postdoc **Dr. Andreas Döpp**. His guidance over the years, the fruitful discussions, and above all his help with the analysis and publication of the experimental data are invaluable.

I also want to thank **Max Gilljohann** with whom I not only shared the office but also many night shifts during the experimental campaign. In my very first year, it was he who introduced me to wakefield acceleration and showed me how to tame such a complex laser system. His exceptional skills and abilities concerning any technical issue are truly remarkable. I don't know if there is any programming language he hasn't mastered yet. Special thanks are also addressed to the rest of my colleagues who were directly involved in the success of the experiments. These are **Hao Ding**, **Gregor Schilling** and **Sabine Schindler**. Without your enthusiasm, efforts, and dedication this work would not have been possible. Moreover, I am very grateful to **Olga Jahn** for all her support and help. With her fascinating expertise and as the main driving force behind "Schrödingers Käuze" she also contributed essentially to the success of our group aside from the physics of laser-matter interaction.

I also want to thank **David Campbell**, **Christoph Eberle**, **Moritz Förster**, **Katinka von Grafenstein**, **Florian Haberstroh**, **Faran Irshad**, **Albert Schletter** and **Enes Travac**

for the good cooperation during the last year and wish them all the best for their future experiments in CALA.

Furthermore, I am also very grateful to my former colleagues **Konstantin Khrennikov** and **Johannes Wenz** for their support not only during my very first year as a Ph.D. student. The daily discussions in the canteen are not the same since you left. Many thanks also go to **Dr. Matthias Heigoldt** and **Andreas Münzer**, especially for the great mountain hikes in the Bavarian Alps and Dolomites.

The group around **Prof. Dr. Jörg Schreiber** was always available when help was needed. I am very thankful to **Lenny Doyle**, **Dr. Daniel Haffa**, **Jens Hartmann**, **Dr. Christian Kreuzer** and **Thomas Rösch**. Your support, especially during the weeks when the whole lab in LEX was dismantled to be moved to CALA was priceless, and I will miss working with you. Special thanks go to **Johannes Gebhard** and **Martin Speicher** with whom I often had the joy to debug the ZEUS laser and help to put it into operation.

Dr. Martin Groß also deserves to be mentioned here. Without him and his administrative team, the countless extensions of my contract would not have been feasible.

Finally, and above all, I want to thank my **family** for their constant and unconditional support over all these years.